Title
Probing for Extended Gamma-ray Emission Within and Beyond the Virial Radius from the Coma Galaxy Cluster

Author
Stevenson, Thomas Brandon

Publication Date
2020

Peer reviewed|Thesis/dissertation

UNIVERSITY OF CALIFORNIA
Los Angeles

Probing for Extended Gamma-ray Emission Within and Beyond the Virial Radius from the Coma Galaxy Cluster

A dissertation submitted in partial satisfaction
of the requirements for the degree
Doctor of Philosophy in Physics

by

Thomas Brandon Stevenson

2020

ABSTRACT OF THE DISSERTATION

Probing for Extended Gamma-ray Emission
Within and Beyond the Virial Radius
from the Coma Galaxy Cluster

by

Thomas Brandon Stevenson
Doctor of Philosophy in Physics
University of California, Los Angeles, 2020
Professor Vladimir V. Vassiliev, Chair

Galaxy Clusters (GCls) are the largest known virialized objects in the Universe. About one-third of GCls exhibit an extended radio halo associated with a population of nonthermal electrons emitting synchrotron radiation in a $\sim \mu$G level magnetic field. The cooling time for the nonthermal electrons is about two orders of magnitude below the diffusion time needed to explain the radio halo, indicating that the electrons are created locally. The electrons may either be accelerated directly in the turbulent cluster medium or created as secondary products from nonthermal protons colliding with the intracluster medium. Observed gamma-ray emission can therefore resolve the contribution from these two mechanisms. Despite the empirical and theoretical motivation for the existence of gamma-ray emission from GCls, so far it remains undetected. In this talk VERITAS observations are used to analyze a $6^\circ \times 8^\circ$ field of the Coma GCl and evaluate the existence of possible extended gamma-ray emission. To achieve this, a method is developed which utilizes cosmic rays as a calibration source to determine a background measurement across the full field of view. The resulting

excess demonstrates a small significance of 2.7σ in the central 1.5° radius of the cluster. This observed central excess, while alone is not significant, has an angular extent in agreement with simulations and corresponds to a similar significance level seen by Fermi-LAT in the same region, and hence I discuss the potential for further investigation by VERITAS and future instruments such as CTA.

The dissertation of Thomas Brandon Stevenson is approved.

Rene Ong

David Saltzberg

Michael Fitzgerald

Vladimir V. Vassiliev, Committee Chair

University of California, Los Angeles

2020

TABLE OF CONTENTS

1 Introduction **1**

2 Scientific Motivation **5**

2.1 Coma Galaxy Cluster 5

2.1.1 Galaxy Clusters 5

2.1.2 γ-ray Observations of Galaxy Clusters 16

2.2 Dragonfly 44 23

2.2.1 Brief Summary of Dark Matter Evidence 23

2.2.2 WIMP as DM candidate 27

2.2.3 Indirect detection of the WIMP 29

2.2.4 Ultra Diffuse Galaxies 31

3 Cherenkov Imaging Technique and Instruments **34**

3.1 Detecting VHE Radiation 34

3.1.1 Extensive Air Showers 35

3.1.2 Cherenkov Radiation 37

3.1.3 Imaging Atmospheric Cherenkov Telescopes 39

3.1.4 Detection Significance and Upper Limits 40

3.2 VERITAS 43

3.2.1 Hardware 44

3.2.2 Observations and Analysis 48

4 Data Analysis of the Coma Galaxy Cluster Extended Field **57**

4.1 Analysis of Extended Emission in the Coma GCl 60
4.1.1 Data Selection 64
4.1.2 Data Calibration 71
4.1.3 Angular Acceptance Treatment 81
4.1.4 Excess Counts Significance Computation 84
4.1.5 Results 91
4.2 Dragonfly44 114

5 The Schwarzschild-Couder Telescope Optical Alignment System 117
5.1 The Cherenkov Telescope Array 117
5.2 pSCT Introduction 123
5.3 pSCT Optical System Hardware 126
5.3.1 Mirror Panel Alignment Hardware 128
5.3.2 Global Alignment Hardware 134
5.4 pSCT Optical System Software and Calibrations 138
5.4.1 Mirror Panel Controller Board Software 139
5.4.2 Actuator Software and Calibration 141
5.4.3 Platform Software 146
5.4.4 Telescope Software 149
5.5 pSCT Status and Future 152

6 Discussion 159

References 168

LIST OF FIGURES

2.1 The Coma GCl SZ signal amplitude (colored) with X-ray contours overlaid on a $3^\circ \times 3^\circ$ grid, displaying excellent spatial overlap. Each Image taken from [PAA11]. 7

2.2 Stellar mass vs ICM mass within R_{500}. Red circles correspond to local clusters ($z < 0.1$) and blue squares correspond to farther clusters ($0.1 < z < 0.6$). The dotted line corresponds to the stellar-to-gas mass ratio of 0.1, while the dashed lines correspond to ratios of 0.05 and 0.2. Image taken from [KB12]. 8

2.3 The electron number density n_e measured at three different radii (defined by $\rho_c(z)$, the critical mass overdensity at its redshift) as functions of ICM temperature (and thus mass). Since the radii are defined by the critical density, $\rho_c(z) = \rho_0 E^2(z)$, the values of n_e are rescaled by $E^{-2}(z)$, where $E(z) = H(z)/H_0$. Note the densities are approximately flat across a range of masses for the largest of the three radii shown, R_{500}. Image taken from [KB12]. 9

2.4 Chandra X-ray image of galaxy cluster RBS 797 with Very Large Array radio contours overlaid in green (1.4 GHz) and blue (5 GHz). Radio lobes coincident with X-ray cavities can be seen protruding east and west of the central bright galaxy. Image taken from [Git16]. 10

2.5 A plot of the frequency-weighted differential power emitted by radio mini halos at 1.4 GHz and the power from the cooling flow required to explain the core temperature for a sample of 21 GCls observed to have mini halos. A best-fit relation is given in red for the 12 GCls without upper limits. Image taken from [BGB16]. 12

2.6 Distribution of radio power (1.4 GHz) vs X-ray luminosity (0.1-2.4 keV) for a number of GCls showing that GCls branch into two populations: radio-on and radio-off. Upper limits are provided for GCls with no observed radio emission. Image taken from [BCD09]. 13

2.7 Examples of radio relic emission (red) and X-ray emission (blue) in the "Sausage" cluster and "Toothbrush" cluster. Image taken from [WGA19]. 15

2.8 Left: Simulated radiation spectrum produced by the different emission processes: inverse Compton (dotted) and non-thermal bremsstrahlung (dash-dotted) from shock accelerated electrons, inverse Compton emission from secondary $e^{\pm}$ (dashed) and π^0 decay (solid) produced by accelerated protons. Right: Also simulated, integrated photon luminosities above 100 MeV vs distance from the cluster core for the same processes. The simulated core temperature for this plot was $T_x \approx 2 - 4$ keV, a factor of a few smaller than the Coma GCl. Image taken from [Min03]. 18

2.9 The simulated γ-ray emission above 100 GeV for a Coma-like cluster from pion decay originating from cosmic-ray protons interacting with the ICM (left), and inverse Compton emission from primary and secondary cosmic-ray electrons (right). The pion decay emission demonstrates a regular morphology with a strong central peak where the ICM density is largest, while the inverse Compton emission traces the structure formation shock waves. The extension for the pion decay emission is mostly contained within a 2 Mpc radius, equivalent to 1.5° for the Coma GCl. Image taken from [PP10]. 19

2.10 Test Statistic (TS) map of Coma GCl from Fermi-LAT observations. Left: 100 MeV-1 GeV emission in the Coma GCl. There appears to be extended, diffuse signal associated with the radio halo. Right: 1 GeV-10 GeV emission in the Coma GCl. The dashed lines indicate the virial radius. Image taken from [Ack16]. . . 20

2.11 The smoothed significance map of the Coma GCl published by VERITAS, with radio contours overlaid. The color scale corresponds to the determined significance from measured excess counts, where the background counts were derived using a ring-background model. The integration radius of 0.2° and 0.4° are shown by the dashed cyan curves. Image taken from [AAB12]. 21

2.12 The proposed virial shock region outlined by the dashed thick green lines, created from the original VERITAS skymap (see Figure 2.11). The proposed region is contained within two ellipse with semi-minor axis of $1^\circ \lesssim b \lesssim 1.6^\circ$ with the elongation ratio of $a/b = 2$, and angular orientation of $\phi = -0.5^\circ$. Image taken from [KKL17]. 22

2.13 The rotational velocity measurements of sixty seven emission regions in M31. The velocities stay flat for increasing radius. Image taken from the original Rubin. et. al. paper published in 1970 ([RF70]). 24

2.14 The rotational velocities of 967 spiral galaxies, with origins shifted proportionally to the average velocity (1-10 kpc). Image taken from [Sof17]. 25

2.15 Optical (left) and X-ray (right) images of the Bullet Cluster. The green contours correspond to increasing surface mass density, as derived from the gravitational lensing signal. Image taken from [CBG06]. 26

2.16 The temperature perturbations power spectrum of the CMB, measured by the *Planck* instrument. The amplitudes and locations of the peaks are used to determine the energy density of baryonic matter and cold dark matter. Image taken from [PAA18]. 27

2.17 The M/L ratio vs dynamical mass of Dragonfly44 is anomalous compared to other dispersion-dominated galaxies. Image taken from [vAB16]. 32

3.1 Monte Carlo simulated particle constituents for a γ-ray shower (left) and hadronic shower (right) with their widths stretched by a factor of four. The γ-ray shower has a narrower development, while the hadronic shower has larger transverse momentum transfer. Image taken from [Feg97]. 36

3.2 Left: The simulated Cherenkov light density distribution for γ-rays with a variety of energies. The photon density is relatively flat in a "pool" of $\sim$ 130 m radius before decaying at large distances from the shower center. Right: The two dimensional photon density profile for a simulated 300 GeV γ-ray with a log-scale colorbar. Image taken from [Hol15]. 39

3.3 Depiction of the stereoscopic IACT technique. The Cherenkov flash is captured by multiple IACTs which can triangulate the direction of the shower core by intersecting the major axes of the images in the sky. Image taken from [Hol15]. . 41

3.4 The VERITAS array at Fred Lawrence Whipple Observatory in Tucson, Arizona before (top) and after (bottom) the relocation of a telescope. Image taken from [Hol11]. 43

3.5 The VERITAS DC optical system with segmented mirror facets. 45

3.6 An example of a triggered shower before (left) and after (right) image cleaning. The color scale of the pre-cleaned pixels displays the digital counts for that pixel, while the post-cleaned pixels have a color corresponding to whether the pixel is an image (red) or border (yellow) pixel. 50

3.7 A cleaned telescope image which has been cleaned and parameterized. The PMT trace for a single pixel is shown in the sub plot. The vertical dashed line represents the T_0 point, and the voltage is integrated over the shaded region to determine the pixel's charge. Image taken from [Hol15]. 51

3.8 Left: The arrival direction of the shower is determined by superimposing the parameterized ellipses and intersecting the major axes. Right: The location where the shower core would have impacted the ground is determined by intersecting the major axes of the ellipses in the shower plane coordinates. Image taken from [DHH97]. 52

3.9 Distribution of mean-scaled widths for γ-rays and hadrons from simulated and real data. Events outside of the shaded region are discarded. A similar cut is also performed in the length parameter space. Image taken from [Hol15]. 53

3.10 The ring-background (left) and reflected region (right) background prediction methods depicted on the γ-ray source PKS 2155-304. The solid angle contained within the solid red lines are the regions where background measurements are made, and the source region is contained in the dashed white line. Image taken from [BFH07]. 56

4.1 Available Coma GCl exposure by VERITAS for the V4 (top) and V6 (bottom) epochs with four operating telescopes and A or B weather. The x and y axes correspond to the pointing azimuth and elevation in degrees, respectively, where the VERITAS azimuth coordinate system runs clockwise from the North direction. The bin increments for elevation and azimuth are 1° and 5°, respectively. The red boxes highlight the telescope pointing cuts made, such that the selected observations are constrained to have similar observing conditions without the loss of excessive exposure. 66

4.2 The resulting pedestal variance (pedvar) distributions of V4 (top) and V6 (bottom) Coma GCl observations after performing the elevation and azimuth selection. Since the distributions are already well constrained, therefore no additional pedvar selection is made on the Coma GCl observations. The background data selection requires V4 and V6 runs to have pedvars within the ranges shown. . . 68

4.3 A scatter plot of the mean γ-ray-like event rates (in Hz) above 215 GeV for individual V4 runs passing the selection criteria after calibrations (described later) are performed. Energies below 215 GeV are not considered in this analysis because of their sensitivity to trigger effects. Coma GCl runs are shown in blue, while the source-free runs are shown in red. A jump in the calibrated rates can be seen between the runs before and after 39500 (marked by the dashed line) when significant hardware changes to the VERITAS array occurred, and therefore the runs before this date are removed from the source-free dataset. Note the gap in the data points is because these runs have an increased night-sky brightness (pedvar) value at the selected elevation and azimuth range. 69

4.4 Histograms of the γ-ray-like event rates for V4 runs after calibrations (described later) are performed, before (top) and after (bottom) the outlier runs (runs before 39500) are removed. The event rate mean and standard deviation is determined for the dataset containing both Coma GCl and source-free runs, and the histogram is created in reference to these parameters with the red line displaying the normal distribution. The Coma GCl observations are shown in orange and the combined Coma GCl and source-free runs are shown in blue. The distribution of source-free runs is more representative of the Coma GCl distribution after the outlier runs are removed. Note that the mean and standard deviation changes between plots, since it is computed before and after the outlier runs are removed. 70

4.5 Top: A scatter plot of the mean γ-ray-like event rates (in Hz) above 215 GeV for individual V6 runs passing the selection criteria after calibrations (described later) are performed. Coma GCl runs are shown in blue, while the source-free runs are shown in red. Bottom: Histogram of the γ-ray-like event rates for V6 runs after calibrations are performed. The event rate mean and standard deviation is determined for the dataset containing both Coma GCl and source-free runs, and the histogram is created in reference to these parameters with the red line displaying the normal distribution. The Coma GCl observations are shown in orange and the combined Coma GCl and source-free runs are shown in blue. The distribution of rates of the source-free runs are approximately centered with respect to the Coma GCl runs, however the dispersion is not the same. While the variances of the Coma GCl and source-free runs are expected to match with more data, the discrepancy seen here may result in an overestimation of the significances later calculated which are based on a likelihood ratio with one degree of freedom. 72

4.6 Top: A scatter plot of the CR event rates above 460 GeV vs pointing elevation for all selected V6 runs before gain calibration is performed. Since the cosmic-ray calibration of gain later performed uses only high energy cosmic-ray events, the elevation correction is determined for events with approximately the same energy range (above 460 GeV). A negative correlation is observed which is fitted by the maximum likelihood estimator (MLE) function described in the text. Bottom: After applying the fitted slope to correct the run exposures, the correlation is removed. 75

4.7 The resulting Crab energy spectrum for V4 (top) and V6 (bottom) after iterative gain adjustment. Both spectrums have an integrated flux above 1 TeV of 2.1×10^{-11} cm^{-2} s^{-1}, in agreement with the Crab's integrated flux published in [Hil98]. 77

4.8 The distribution of the V6 event rates for cosmic-ray events of the 206 individual runs before (top) and after (bottom) gain calibration is performed. The cutoff energy for V6 (670 GeV) is shown by the dashed vertical line, and the energy range considered in the analysis is enclosed in the solid vertical lines ($0.2 - 4.6$ TeV). The mean rate is shown by the bold black line with the 3σ Poisson error bars for a ~ 20 minute exposure. The V4 data appears similar and are not shown. 79

4.9 The distribution of the V6 event rates for γ-ray-like cosmic-ray events of the 164 individual **source-free** runs before (top) and after (bottom) gain calibration is performed. The cutoff energy for V6 (670 GeV) is shown by the dashed vertical line, and the energy range used in the analysis is enclosed in the solid vertical lines ($0.2 - 4.6$ TeV). The mean rate is shown by the bold black line with the 3σ error bars shown for the Poisson error for a 15 minute exposure. The dispersion in the rates is significantly reduced after the gain calibration procedure, especially at lower energies. The V4 data appears similar and are not shown. 80

4.10 A plot of the relative difference (above and below the pointing direction) of γ-ray-like events as a function of the angular Y-position. The mean and 1-σ error bars of the distribution of the source-free runs is shown in black, with the linear fit shown by the blue line. A 0.25° bin size is used. For larger Y-positions where the effect is larger, the decreasing field of view compounded with the decreased radial acceptance significantly diminishes the effect's impact. The plot shown is for V6 source-free runs with events in the $220 - 460$ GeV range as an example. . 83

4.11 Exposure profile partitioning example showing two pointings and using four radial bins for simplicity of illustration. The region of interest is outlined by the red box. The field of view of the pointings are divided into equal area radial bins and the exposure profile q_{ji} is partioned into each bin for each run. Numbers are not shown in the exposure profile, but nonzero values are colored red while zero values are colored blue. 85

4.12 Top: An exposure profile consisting of 14 runs whose order has been rearranged in order to overlap their assembly. The used and unused radial bins are colored red and cyan, respectively. Bottom: An example of the above exposure profile being assembled into four sets of data (identified by the four shades of blue, where the red bins are unused). The x-axis corresponds to the source-free run index l, while the y-axis is the radial bin number. Four off sets with 14 runs each are able to be created from only 36 source-free runs. Source-free data within a radial bin are not used more than once. 89

4.13 The significance skymap (left) and distribution of significance bins (right) for the V4 Coma GCl dataset over the full energy range (220 GeV−4.6 TeV) for three tested regions. Bins contained in the full skymap are shown in the first row, while only those contained in the tested virial shock ring and central 1.5° radius are shown in the second and third rows, respectively. 93

4.14 The significance skymap (left) and distribution of significance bins (right) for the V6 Coma GCl dataset over the full energy range (220 GeV−4.6 TeV) for three tested regions. Bins contained in the full skymap are shown in the first row, while only those contained in the tested virial shock ring and central 1.5° radius are shown in the second and third rows, respectively. 94

4.15 The significance skymap (left) and distribution of significance bins (right) for the V6 mimic #1 dataset over the full energy range (220 GeV−4.6 TeV) for three tested regions. Bins contained in the full skymap are shown in the first row, while only those contained in the tested virial shock ring and central 1.5° radius are shown in the second and third rows, respectively. 95

4.16 The significance skymap (left) and distribution of significance bins (right) for the V6 mimic #2 dataset over the full energy range (220 GeV−4.6 TeV) for three tested regions. Bins contained in the full skymap are shown in the first row, while only those contained in the tested virial shock ring and central 1.5° radius are shown in the second and third rows, respectively. 96

4.17 Histograms of 100 iterations determining the integrated-region significance of the ring and circle regions for different datasets over the full energy range (220 GeV−4.6 TeV). First row: V4 Coma GCl data. Second row: V6 Coma GCl data. Third row: V6 mimic dataset one. Fourth row: V6 mimic dataset two. 100

4.18 Histograms of 100 iterations determining the integrated significance of the ring and circle regions for the V6 Coma GCl dataset in different energy bins. First row: 220 GeV−460 GeV. Second row: 460 GeV−1 TeV. Third row: 1 TeV−2.2 TeV. Fourth row: 2.2 TeV−4.6 TeV. 102

4.19 The significance skymap (left) and distribution of significance bins (right) for the V4 Coma GCl dataset over the energy range 220 GeV−460 GeV for three tested regions. Bins contained in the full skymap are shown in the first row, while only those contained in the tested virial shock ring and central 1.5° radius are shown in the second and third rows, respectively. 103

4.20 The significance skymap (left) and distribution of significance bins (right) for the V4 Coma GCl dataset over the energy range 460 GeV−1 TeV for three tested regions. Bins contained in the full skymap are shown in the first row, while only those contained in the tested virial shock ring and central 1.5° radius are shown in the second and third rows, respectively. 104

4.21 The significance skymap (left) and distribution of significance bins (right) for the V6 Coma GCl dataset over the energy range 220 GeV−460 GeV for three tested regions. Bins contained in the full skymap are shown in the first row, while only those contained in the tested virial shock ring and central 1.5° radius are shown in the second and third rows, respectively. 105

4.22 The significance skymap (left) and distribution of significance bins (right) for the V6 Coma GCl dataset over the energy range 460 GeV−1 TeV for three tested regions. Bins contained in the full skymap are shown in the first row, while only those contained in the tested virial shock ring and central 1.5° radius are shown in the second and third rows, respectively. 106

4.23 The significance skymap (left) and distribution of significance bins (right) for the V6 Coma GCl dataset over the energy range 1 TeV−2.2 TeV for three tested regions. Bins contained in the full skymap are shown in the first row, while only those contained in the tested virial shock ring and central 1.5° radius are shown in the second and third rows, respectively. 107

4.24 The significance skymap (left) and distribution of significance bins (right) for the V6 mimic #1 dataset over the energy range 220 GeV−460 GeV for three tested regions. Bins contained in the full skymap are shown in the first row, while only those contained in the tested virial shock ring and central 1.5° radius are shown in the second and third rows, respectively. 108

4.25 The significance skymap (left) and distribution of significance bins (right) for the V6 mimic #1 dataset over the energy range 460 GeV−1 TeV for three tested regions. Bins contained in the full skymap are shown in the first row, while only those contained in the tested virial shock ring and central 1.5° radius are shown in the second and third rows, respectively. 109

4.26 The significance skymap (left) and distribution of significance bins (right) for the V6 mimic #1 dataset over the energy range 1 TeV−2.2 TeV for three tested regions. Bins contained in the full skymap are shown in the first row, while only those contained in the tested virial shock ring and central 1.5° radius are shown in the second and third rows, respectively. 110

4.27 The significance skymap (left) and distribution of significance bins (right) for the V6 mimic #2 dataset over the energy range 220 GeV−460 GeV for three tested regions. Bins contained in the full skymap are shown in the first row, while only those contained in the tested virial shock ring and central 1.5° radius are shown in the second and third rows, respectively. 111

4.28 The significance skymap (left) and distribution of significance bins (right) for the V6 mimic #2 dataset over the energy range 460 GeV−1 TeV for three tested regions. Bins contained in the full skymap are shown in the first row, while only those contained in the tested virial shock ring and central 1.5° radius are shown in the second and third rows, respectively. 112

4.29 The significance skymap (left) and distribution of significance bins (right) for the V6 mimic #2 dataset over the energy range 1 TeV−2.2 TeV for three tested regions. Bins contained in the full skymap are shown in the first row, while only those contained in the tested virial shock ring and central 1.5° radius are shown in the second and third rows, respectively. 113

4.30 V6 upper limits on the differential flux are shown for an 0.1° integration radius around Dragonfly 44. 115

5.1 An artist's rendition of the CTA southern (top) and northern (bottom) sites which includes the various telescope candidates shown in the south, including the pSCT. Image taken from the CTA webpage (https://www.cta-observatory.org/). 118

5.2 The proposed layouts of the southern and northern hemisphere CTA sites. The red circles are LSTs, the black square are MSTs, and the blue dots are SSTs. Both sites are designed to host MSTs, the workhorse telescope of the CTA observatory. The LSTs and MSTs are spaced apart approximately the radius of the Cherenkov light pool in order to ensure that contained events are sensitively observed by multiple telescopes. Image taken from [Ong18] 119

5.3 The simulated differential flux sensitivity of the CTA northern and southern arrays compared to other instruments. MAGIC and H.E.S.S. are IACT arrays like VERITAS, and HAWC is an array of water Cherenkov detectors. Only a rough comparison between IACTs & LAT and HAWC instruments is possible since the method of calculation and the criteria applied are not identical between different γ-ray detection technologies. For CTA, the differential sensitivity is defined as the minimum flux needed to obtain a 5-standard-deviation detection of a point-like source, calculated in five logarithmic energy bins per decade. At least ten detected γ-rays per energy bin are also required. Image taken from the CTA webpage (https://www.cta-observatory.org/). 120

5.4 The simulated angular resolution of the CTA southern array vs. the reconstructed energy, where angular resolution here is defined to be the angle within which 68% of γ-ray events are reconstructed. Image taken from the CTA webpage (https://www.cta-observatory.org/). 122

5.5 Left: The ratio of differential point source sensitivities simulated for the CTA southern array layout with the 25 MSTs as either DCTs or SCTs. The SCT configuration demonstrates significantly improved off-axis point source sensitivity at low energies. Right: The ratio of angular resolutions of different instruments compared to the CTA southern array layout with DCTs. The use of SCTs instead of DCTs offers an improvement in angular resolution similar to the CTA improvement over current generation IACT arrays. 124

5.6 The constructed prototype Schwarzschild-Couder Telescope at the Fred Lawrence Whipple Observatory near Tucson, Arizona. Image provided by photographer Deivid Ribeiro. 127

5.7 Comparison between the simulated focal plane images of the Davies-Cotton (left) and Schwarzschild-Couder (right) telescopes for 1 TeV γ-ray (top) and 3 TeV proton (bottom) primary particles. Images based on simulations performed in [WJD16]. 129

5.8 Left: Schematic showing the orientation and numbering of MPES mounted on the backside of the primary mirror panels. Blue circles correspond to the camera side of the MPES, while red circles correspond to the laser side. Right: Image of a long edge between two mirror panels. The MPES are oriented in mutually orthogonal directions, such that all six degrees of freedom between the panel positions are sensitively measured. 133

5.9 Left: A schematic of the pSCT Global Alignment System with all relevant devices as described in the text. Right: The performance of the autocollimator's ability to determine the tilt using a 5 cm circular mirror located 8 m away. The accuracy has a residual of $\lesssim 50$ μm, below the tolerance requirement of 150 μm 136

5.10 Optical Tables being calibrated in the UCLA laboratory. Each table contains a SP which enables motion for alignment. Three CCD cameras and one AC are located on each table (located in the white enclosures). The primary OT laser can be seen at the center of the far table. Not shown is the secondary OT rangefinder, PSD enclosure, and the sky camera. 137

5.11 The alignment branch of the pSCT software structure. The Central Alignment computer aggregates the platform and GAS alignment status, processes this information and determines how the individual platforms should move to achieve alignment. The platform objects, corresponding to each SP in the optical system, consist of one Controller Board Computer (CBC) object, six actuator objects, and four to five MPES objects depending on the location of the platform. The actuator and MPES objects communicate with the local CBC object in order to read and move the actuators via the actuator ports, as well as read the MPES position via the USB ports. 140

5.12 Schematic demonstrating how an actuator's Home position is defined. An actuator is extended until the hardware limit is reached (green line). At this mechanical position, the encoder is fixed at a rotation angle such that the corresponding voltage of the extension limit position is roughly in the central half of the range of voltages ($\sim 1.2 - 2.4$ V). The actuator is then retracted until it observes three discontinuity jumps of the encoder, at which point it is in the Home position. Further retraction increments the angular position until another discontinuity is reached, and then the angular position is reset to zero and the revolution position is incremented by one. 143

5.13 The actuator calibration setup at the UCLA lab. Once an actuator is assembled, the Home position is found and the actuator's length at this position is measured using a caliper with 10μm resolution. The actuator is then unfixed and finishes its calibration procedure. 145

5.14 The magnitude of hysteresis present in the P2PAS alignment as measured by MPES position (44 μm per pixel). The red dots demonstrate the position of an MPES without moving actuators. The actuators are then moved in random directions and return to the original positions, at which point a measurement is made. These measurements are shown by the blue dots. 148

5.15 Camera snapshot of a single event for the pSCT's first light. The white square in the center is because the COM is temporary replacing the front end electronics module. The module left of the center is dark because it did not connect after the prototype SCT camera was turned on the first time. The optical system of the SCT in this image is only coarsely aligned. The data shown in this picture do not include pedestal subtraction or data processing and has only historical value. 153

5.16 Left: The de-focused image of a star on-axis to the pSCT optical system. The individual points correspond to focused light by pairs of individual primary (annotated) and secondary mirror panels. Right: Each mirror panel is adjusted to bring the points into focus, producing a rough alignment of the optical system. Further improvements are expected when including higher order corrections to the alignment algorithm and structure deformations are accounted for. These images were taken by a CCD camera placed near the focal plane. 154

5.17 Left: GAS CCD determination of a panel's position along one direction. Right: The CCD sky camera FOV center position as determined by astrometry, demonstrating the stability of the pointing. Image taken from [AAA19]. 156

5.18 The preliminary map of γ-ray events recorded by the pSCT from the direction of the Crab Nebula, marked with the cross at the center of the map. The data analysis was optimized on a few hours of joint observations with the VERITAS observatory and applied to an independent 20-hour dataset with the pSCT operating in stand-alone mode. 157

6.1 Top: The significance map determined in this analysis on the V6 Coma GCl dataset. Bottom: The simulated secondary acceleration γ-ray emission (above 100 GeV) for a Coma-like cluster scaled to match the top figure (see Figure 2.9 for the original). The central 1.5° (approximately 2.5 Mpc) radius region (circled) demonstrates a median significance of 2.7σ for the V6 Coma GCl dataset, which approximately corresponds to the simulated emission central extension in the secondary acceleration model shown in the bottom figure, as well as the hadronic model shown in Figure 2.9. 163

6.2 The predicted intensity of the γ-ray emission of hadronic origin in the Perseus GCl integrated within a 0.15° radius from the center. The centrally peaked (solid line) and extended (dashed line) models of the cosmic-ray profile is taken from [PP10]. Intensities for central magnetic field strengths of 10 μG and 20 μG are shown by the red and yellow lines, respectively. The grey band shows the current upper limits from MAGIC observations. The dark blue band is an estimate of the 95% CL upper limit from 300 hours of observation by CTA, while the black band is an estimate of the corresponding detectability level. The light blue line is an estimate of the minimum γ-ray flux for a nonthermal proton spectral index of 2.3. Image taken from [CAA19] 166

LIST OF TABLES

4.1 Observing Condition Selections 73

4.2 Standard cuts used in this analysis 74

4.3 The cut values made on triggered events for γ-ray-like events. Cosmic-ray-like events have the same cut parameters but with the complement values of MSCW and MSCL (which define the shape cut). At least two telescopes are required to have observed an event to activate stereoscopic reconstruction. Events landing far from the telescope array have poor stereoscopic reconstruction sensitivity, hence the distance to shower core cut. The size second max cut is a requirement that the second brightest pixel has a minimum number of digital counts. A minimum emission height is required, defined as the height of the air shower which contains the maximum number of Cherenkov emitting particles. 74

4.4 Median Integrated-Region Significances 99

4.5 Dragonfly 44 Results 116

5.1 Stewart Platform Hardware Elements 130

5.2 A list of the isolated transformations of pSCT optical system elements corresponding to an increase in the PSF to 1 arcmin on-axis. The most sensitive degrees of freedom are the tip and tilt of the individual panels in both M1 & M2, and also the tip and tilt of M2 as a whole. 131

ACKNOWLEDGMENTS

I would like to thank my advisor Vladimir V. Vassiliev for his patient guidance not only in the development of this work, but also in my development as a scientist. Leading by example, Vladimir has instilled in me a standard of excellence which I am grateful for. Thank you to my committee, Rene Ong, David Saltzberg, and Michael Fitzgerald for imparting your significant advice and input in helping me complete this dissertation. To the members of the pSCT optics group, whose collaboration and comradery has been invaluable, especially Ruo-Yu Shang, Julien Rousselle, Andriy Petrashyk, Qi Feng, Bryan Kim, Daniel Nieto, Deivid Ribeiro, and Peter Yu. Thank you to my parents, my brother, and the rest of my family and friends for your endless support. Thank you to Victoria for being a constant source of encouragement.

I would also like to thank the staff at Fred Lawrence Whipple Observatory and collaborating institutions in the construction and operation of the VERITAS and pSCT projects. This research has been supported by NSF funding under the awards 1913798, 1607491, 1229792 and 1307171.

VITA

2010 University of California at San Diego

Bachelor of Science, Physics

Minor, Philosophy

Minor, Psychology

CHAPTER 1

Introduction

Very High Energy (VHE) γ-ray astronomy is a relatively young field, with the first detection occurring at the Whipple Observatory in 1989 when a TeV signal was seen coming from the Crab Nebula [WCF89]. Since then over 150 γ-ray sources have been detected, and many more are expected in the near future when the next generation Cherenkov Telescope Array (CTA) is completed. CTA is designed to provide an order of magnitude improvement in sensitivity over current generation instruments. VHE astronomy utilizes ground-based imaging telescopes which capture the Cherenkov emission created when a very energetic (> 100 GeV) photon interacts with the Earth's atmosphere.

Photons are detected in VHE astronomy with energies of up to a few hundred TeV, considerably larger than the terrestrial particle accelerators can produce. Therefore ground-based VHE astronomy makes capable the utilization of the Universe as a laboratory to study particle physics at otherwise inaccessible energies. The VHE γ-rays have energies which are orders of magnitude greater than the black-body radiation of the hottest objects known to exist in the Universe, meaning that VHE γ-rays are a byproduct of non-thermal, dynamic processes. Therefore the observation and study of VHE γ-rays offer a probe of energetic, time-dependent mechanisms occurring in astrophysical sources which are capable of accelerating particles to energies greater than 100 GeV.

Galaxy clusters (GCls) are the largest gravitationally bound structures known in the Universe, containing hundreds to thousands of galaxies acquired through hierarchal mergers and accretion. Many galaxy clusters demonstrate non-thermal particle acceleration processes

which are revealed by radio and X-ray observations, which suggests that γ-ray emission may also accompany them. As of now γ-ray emission has not been detected from a galaxy cluster. Claims of evidence of a γ-ray signal have been made, however, using observations of the Coma GCl, a relatively nearby ($\sim$ 100 Mpc), large galaxy cluster which is believed to have undergone a recent merger event and has ongoing accretion of matter from large structure filaments [KKL17]. Analyzing this possible γ-ray emission coming from the Coma GCl is a major focus of this dissertation.

Within the field of view of Coma GCl observations exists an ultra diffuse galaxy (UDG) Dragonfly 44. This UDG is a member galaxy of the Coma GCl, and is an exceptional source which is thought to be almost entirely composed ($> 98\%$) of dark matter (DM). There is strong evidence for the existence of dark matter, which is thought to make up $\sim 85\%$ of all matter in the Universe, yet it has eluded detection. A dense source of dark matter is most capable of DM-DM self-annihilation processes (where the expected flux is proportional to the DM density squared), which may produce γ-rays that can be observed to indirectly detect dark matter. Since the exposure of Dragonfly 44 overlaps the obtained Coma GCl exposure, an analysis of Dragonfly 44 is also performed in this dissertation to determine its γ-ray flux upper limits.

The data used in this work are obtained by the VERITAS imaging atmospheric Cherenkov telescope (IACT) array, an array of four Cherenkov telescopes located near Mt. Hopkins in Arizona. When a VHE photon enters the Earth's atmosphere, it pair produces to create an electron and positron which produce energetic photons of their own via bremsstrahlung. The secondary photons in turn pair produce again. The result is a cascade of secondary charged particles which move faster than the speed of light in the medium of the Earth's atmosphere, producing a flash of Cherenkov radiation. IACTs image the Cherenkov flash and reconstruct the primary γ-ray's energy and direction from the image properties. VERITAS is one of three major IACT observatories operating at the present time which utilizes stereoscopic reconstruction into the technique to greatly improve the angular reconstruction and energy

sensitivity.

The ground-based operation of the IACT technique allows for a cost-effective method of producing large collecting areas to observe the relatively low flux γ-rays, however a large level of background exists in this technique. Over 99% of the Cherenkov events detected by IACTs are created by the isotropic cosmic-ray (CR) background, charged hadrons which have been deflected by magnetic fields and therefore carry no directional information about their sources. In order to isolate the number of events created by primary γ-rays, an estimate of the number of background events is required. This estimate is commonly made by simultaneously measuring an area of the field of view away from the targeted source, avoiding systematic errors which would be introduced from using separate observations with different observing conditions. However, for sources with large angular extensions, an accurate background measurement cannot be made in the same field of view. In order to evaluate evidence of an extended ($\sim 5^\circ$) γ-ray emission in the Coma GCl, a custom background measurement procedure is developed and presented in this dissertation.

With the construction of CTA, the next generation ground-based γ-ray observatory, the γ-ray Universe will be observed with an unprecedented sensitivity. Among other improvements, the field of view of CTA is expected to more than double that of VERITAS in diameter ($\sim 8^\circ$ vs 3.5°), with an enhanced angular resolution as well. These particular advancements are especially suitable for the detection and morphological study of extended sources, potentially including the Coma GCl. The novel Schwarzschild-Couder Telescope (SCT) is a candidate design for the medium sized telescopes in CTA. The SCT is designed to achieve a performance near the theoretical limit of the IACT technique in the CTA installation, with dramatic improvements in off-axis sensitivity, imaging resolution and γ-ray angular resolution compared to the conventional Davies-Cotton telescope design. Therefore the SCT is an especially suitable telescope design for studying extended astrophysical objects like the Coma GCl. A prototype SCT (pSCT) has been constructed, co-located with the VERITAS observatory. I have been fortunate to contribute to in both hardware and software, and

hence I also document my work on the pSCT in this dissertation.

The dissertation layout is as follows. In chapter 2, I review and examine the non-thermal emission mechanisms thought to occur in galaxy clusters, including the possible evidence for γ-ray emission in the Coma GCl. I also discuss the evidence of dark matter and the potential of the ultra diffuse galaxy Dragonfly 44 as an indirect detection candidate. In chapter 3, I outline details of the ground-based γ-ray IACT technique, describe the VERITAS hardware, and explain the datasets and the standard VHE γ-ray analysis methods. In chapter 4, I present a non-conventional procedure to analyze an extended region around the Coma GCl, and then evaluate the existence of an extended signal. I also produce analysis results for Dragonfly 44, including energy differential flux upper limits. In chapter 5, I discuss CTA as the next generation array for ground-based γ-ray astronomy and describe the Schwarzschild-Couder Telescope (SCT), a candidate medium-sized telescope for CTA. The pSCT is currently in the advanced stages of commissioning and beginning of operation with a prototype camera, which has already detected the Crab Nebula. I explain my specific contributions to the development of the pSCT in this chapter as well. In chapter 6, I make concluding remarks on the analysis results of the Coma GCl and its outlook in the context of the upcoming CTA.

CHAPTER 2

Scientific Motivation

2.1 Coma Galaxy Cluster

2.1.1 Galaxy Clusters

The largest virialized objects in the Universe are galaxy clusters (GCls), with typical masses of $10^{14} - 10^{15} M_{\odot}$. GCls consist of a large number of galaxies (ranging from 100s to $1,000$s) which account for only a few percent of its mass. The majority of GCl mass ($\sim 80\%$) is made up of dark matter (DM), as evidenced by gravitational lensing and velocity dispersion measurements of individual member galaxies, the latter of which being one of the earliest sources of evidence for the existence of DM. The remaining $\sim 15\%$ of mass exists in the form of an extended intracluster medium (ICM), which is a hot ($T \sim 10^8 K$), low-density plasma ($n_{gas} \approx 10^{-1} - 10^{-4}$ cm^{-3}) which emits X-ray radiation by thermal bremsstrahlung. Situated at the nodes of the cosmic web, GCls are believed to be the result of DM-driven hierarchal mergers of smaller systems and accretion of matter along the cosmic filaments. The enormous amount of gravitational binding energy of GCls is dissipated along accretion shocks which heats the ICM to the observed temperatures and settles into hydrostatic equilibrium with the potential well, producing large-scale ICM motions in the process [RKC08]. Many clusters exhibit diffuse synchrotron radio emission which encodes information about the dynamical state of the cluster and its evolutionary stage. Therefore GCls offer not only a laboratory to understand the dissipation of enormous amounts of gravitational energy at microphysical scales, but also a probe into the evolution of the large scale structure in the Universe.

The formation and evolution of GCls are complex, involving physical processes at spatial scales spanning many orders of magnitude, from the size of the cluster to the size of supermassive black holes in the centers of powerful active galactic nuclei frequently found in GCls. However, despite their diverse environment and evolution history there is a strong amount of regularity among observed clusters. The implied thermal energy of ICM temperatures, deduced from X-ray observations, is consistent with the implied kinetic energy determined from velocities of member galaxies, which indicates that they have been virialized by the large gravitational well of the cluster. The hot ICM electrons also inverse Compton scatters ambient cosmic microwave background (CMB) photons, leaving an imprint on the CMB blackbody spectrum on the scale of temperature variations on the order of $\sim 10^{-4} - 10^{-5}$, called the Sunyaev-Zel'dovich (SZ) effect (see Figure 2.1) [PAA11]. The combination of X-ray and millimeter observations constrain the ICM density and temperature, which demonstrates a level of regularity between clusters. Clusters display a tight correlation between the mass of the ICM gas within R_{500}, defined as the radius which contains a mean overdensity of $500\rho_c(z)$, and the stellar mass within the same radius even though the stellar and ICM content are not directly related (see Figure 2.2). The critical density $\rho_c(z)$ here is defined by the Hubble constant, H, through the following expression, $\rho_c(z) = 3H(z)^2/8\pi G$, where G is the gravitational constant. The radial density profile of the ICM in GCls also appears to be relatively stable at distances far from the core for clusters of various sizes (Figure 2.3). The GCl regularities appear to confirm the thermalization of matter being pulled into the cluster's gravitational well with much of the evolutionary history of the cluster erased.

Many clusters deviate from the common regularities in some way and reveal information about the cluster's individual evolution history. One such distinction between GCls lies in their core properties; some relaxed clusters contain a lower temperature core region with strongly peaked X-ray emissivity associated with its high density. The cooled gas in the core is expected to cause a "cooling flow" where the hot ICM exterior gas flows inward [Fab94]. Temperature measurements performed on cool cores indicate that the gas does not cool

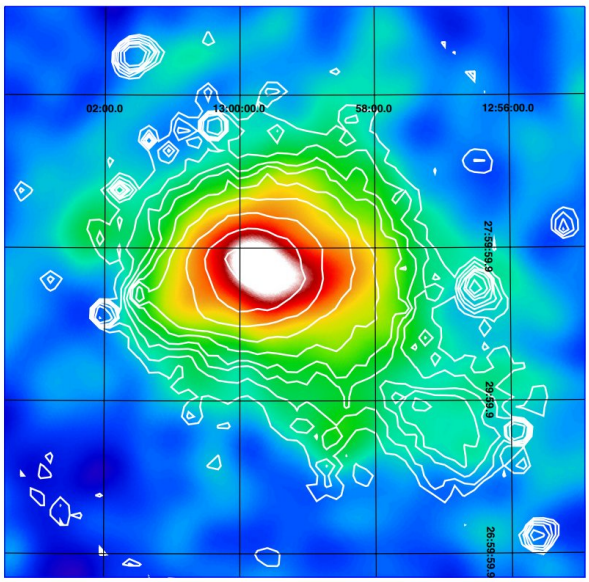

Figure 2.1: The Coma GCl SZ signal amplitude (colored) with X-ray contours overlaid on a $3° \times 3°$ grid, displaying excellent spatial overlap. Each Image taken from [PAA11].

down to temperatures as low as expected, an observation supported by the low level of star formation in bright GCls [MVR11]. This cooling flow problem seen in some clusters suggests that an unknown heating element is present in the core region which prevents or limits the cooling flow. Most cool-core clusters have radio-loud central active galactic nucleus (AGN) which deposit large amounts of mechanical energy into the cluster in the form of radio-emitting jets, and this is thought to be a promising source for the core heating. Roughly a quarter of clusters have been observed to contain AGN-associated radio lobes which are coincident with X-ray cavities, where the expelled AGN plasma forms a buoyant bubble and displaces the X-ray gas (see Figure 2.4). These cavities provide a good estimate for the total power output by AGN, which has been shown to be comparable to the amount needed to account for the cool core heating element [MN07]. If the AGN jets are indeed the source of feedback heating however, it is still not fully understood how the jet energy is converted to heat or how the feedback process is regulated.

Many of the cool-core clusters have been observed to contain diffuse, steep-spectrum

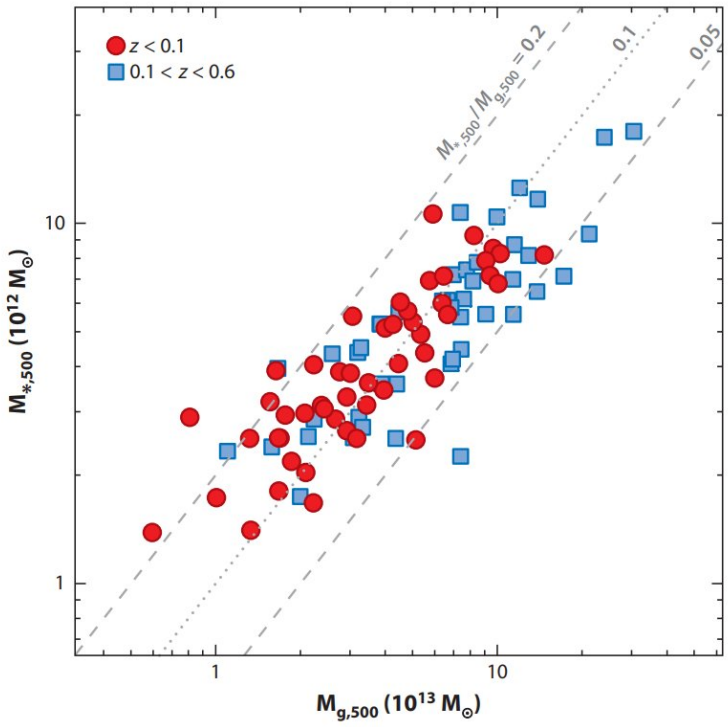

Figure 2.2: Stellar mass vs ICM mass within R_{500}. Red circles correspond to local clusters ($z < 0.1$) and blue squares correspond to farther clusters ($0.1 < z < 0.6$). The dotted line corresponds to the stellar-to-gas mass ratio of 0.1, while the dashed lines correspond to ratios of 0.05 and 0.2. Image taken from [KB12].

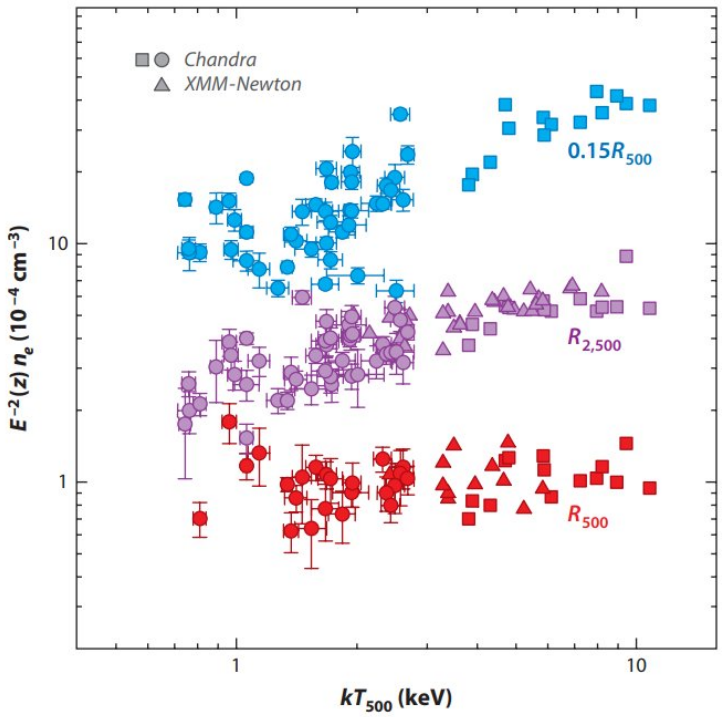

Figure 2.3: The electron number density n_e measured at three different radii (defined by $\rho_c(z)$, the critical mass overdensity at its redshift) as functions of ICM temperature (and thus mass). Since the radii are defined by the critical density, $\rho_c(z) = \rho_0 E^2(z)$, the values of n_e are rescaled by $E^{-2}(z)$, where $E(z) = H(z)/H_0$. Note the densities are approximately flat across a range of masses for the largest of the three radii shown, R_{500}. Image taken from [KB12].

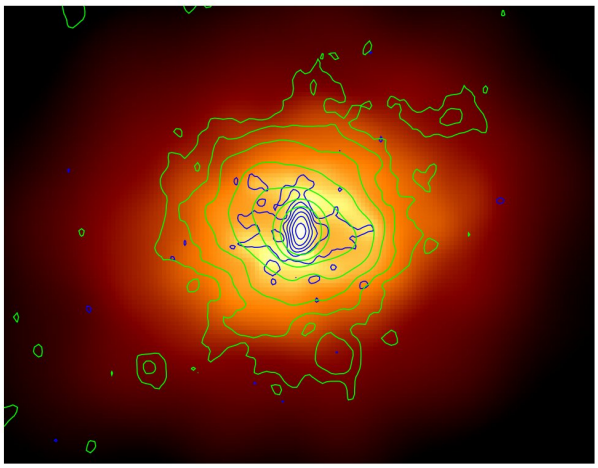

Figure 2.4: Chandra X-ray image of galaxy cluster RBS 797 with Very Large Array radio contours overlaid in green (1.4 GHz) and blue (5 GHz). Radio lobes coincident with X-ray cavities can be seen protruding east and west of the central bright galaxy. Image taken from [Git16].

synchrotron radio emission in the central $\sim 100 - 500$ kpc, called radio mini halos, which may further elucidate the processes occurring in relaxed clusters. While the central AGN could be the origin of the synchrotron-producing electrons, they alone cannot fully explain the diffuse halo. Specifically, the cooling time for the cosmic-ray electrons in the ICM's measured μG-level magnetic field is much shorter than the diffusion time necessary to reach the > 100 kpc distances which the halo spans. This leaves the conclusion that the high energy electrons must be generated *in situ*. Unlike the radio lobes of AGN which do not emit in the X-ray band, the radio mini halos overlay the ICM radiation, indicating that physics involving the ICM may be responsible for the acceleration of electrons. A study of 21 GCls observed to have mini halos (see Figure 2.5) has found a correlation between the frequency-weighted power of radio halos and the power required to heat the cluster core [BGB16]. If the existence of the radio halo is related to the heating mechanism as suggested, then turbulence may play a vital role. In particular, an analysis of deep X-ray *Chandra* data of the Perseus and Virgo clusters demonstrated that AGN-generated turbulence can account for

the necessary heating required locally at each radius and can also explain the radio mini halos if the magnetic field is large enough ($B > 0.5\mu$G) [ZCS14]. In this model, local seed electrons are re-accelerated via turbulent motion of the ICM plasma. Alternatively, spiral-shaped cold fronts have been observed in many cool-core clusters which could be generated by sloshing of cold gas in the core [MV07]. This sloshing could also produce the necessary turbulence required to re-accelerate electrons as well as strengthen magnetic fields, and is supported by simulations as well as evidence showing a connection between cold fronts and radio mini halos [ZMB13, MG08]. It is also possible that these re-accelerated cosmic-ray electrons are secondary particles generated by cosmic-ray protons inelastically colliding with ICM protons. The energetic protons, possibly expelled from central AGN, have significantly longer lifetimes than the electrons and are able to naturally explain the diffuse property of the radio mini halo [ZPP14]. There is some evidence against the electrons being secondary particles, as attempts to explain the core heating via Coulomb and hadronic interactions overestimate the proton energies and are ruled out by γ-ray observations [HTE13]. However, it is argued that if the cooling flow is explained by invoking ICM heating via proton streaming, then the low X-ray and γ-ray observed fluxes are acceptable [FO13].

While relaxed, cool-core clusters have been discussed so far, merging clusters can also contain diffuse, steep-spectrum radio emission but with a cluster-wide ($\sim$ Mpc) extent, called giant radio halos. Approximately one-third of X-ray luminous GCls have giant radio halos, significantly more common than their mini-halo counterpart [BJ14]. The emission of giant radio halos, like the mini halos, is observed to have strong coincidence with the ICM X-ray emission. However, giant radio halos are exclusively associated with merging cluster systems while the mini halos are only observed in relaxed clusters. Like in radio mini halos, the synchrotron-emitting cosmic-ray electrons are thought to be accelerated directly or produced as secondary products from hadronic interactions. Under the direct acceleration scenario, the spatial extent of the radio emission requires, to an even stronger degree than in mini halos, that the electrons are re-accelerated *in situ*. The turbulent re-

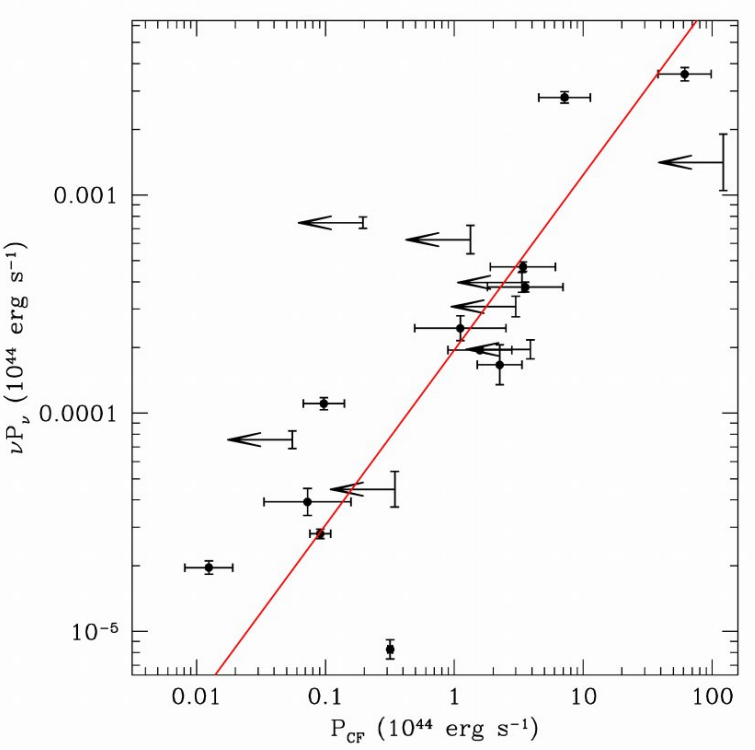

Figure 2.5: A plot of the frequency-weighted differential power emitted by radio mini halos at 1.4 GHz and the power from the cooling flow required to explain the core temperature for a sample of 21 GCls observed to have mini halos. A best-fit relation is given in red for the 12 GCls without upper limits. Image taken from [BGB16].

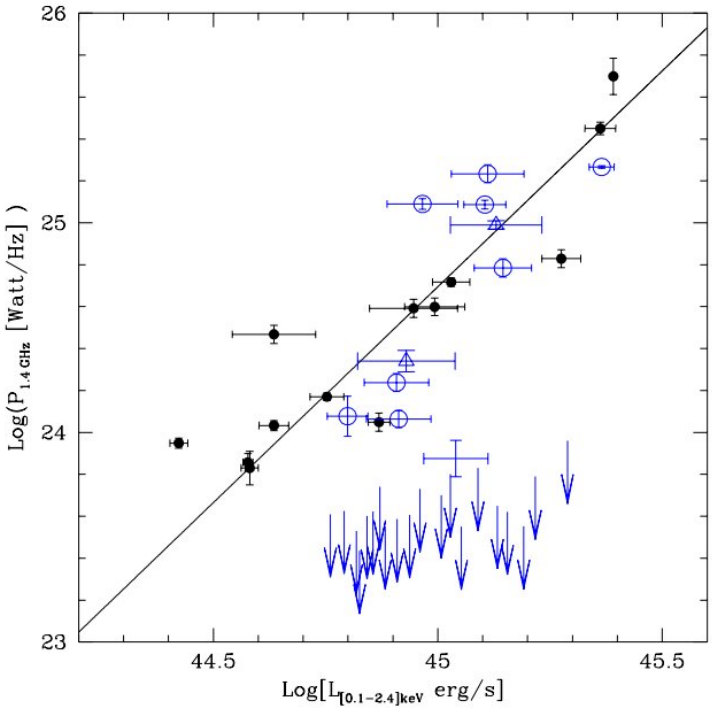

Figure 2.6: Distribution of radio power (1.4 GHz) vs X-ray luminosity (0.1-2.4 keV) for a number of GCls showing that GCls branch into two populations: radio-on and radio-off. Upper limits are provided for GCls with no observed radio emission. Image taken from [BCD09].

acceleration model is commonly invoked as the most likely direct acceleration scenario, where relativistic seed electrons are accelerated in ICM merger-induced turbulence to energies great enough to produce the giant synchrotron radio halos in the $\sim \mu$G level magnetic fields of the cluster [BGC08]. Alternatively in the hadronic scenario, cosmic-ray protons with a long enough lifetime to diffuse to the $\sim$ Mpc scale generate secondary electron-positron pairs through inelastic collisions with the ICM protons.

Relaxed clusters with mini radio halos and merging systems with giant radio halos both share similar emission features, namely a steep spectrum and a tight correlation with the ICM X-ray luminosity (see Figure 2.6). A common question is whether the two sources of emission have different acceleration mechanisms. It has been proposed that the electrons producing the mini halos are primarily secondary particles generated from hadronic interactions near the dense cluster core while those producing the giant radio halos are directly re-accelerated via merger induced turbulence [ZPP14]. The merging of clusters may then power the giant radio halo emission, possibly by transporting cosmic-ray protons from the core outwards, subsequently producing secondary energetic seed electrons. Some observed clusters appear to be in a transitioning state, as they have relaxed cool cores yet also generate radio emission with a spatial extent much greater than mini halos, further indicating that mini and giant radio halos may be related [KSP19, SBB18]. Observations of the cluster Abell 2142 suggests that the two classes of radio halos are generated from separate acceleration mechanisms, as the radio emission appears to have two components: a compact mini halo and an extended steeper-spectrum emission [Ven17].

Some clusters also have been observed to host Mpc-size elongated radio emission called radio relics (see Figure 2.7). This relic emission differs from halo emission in that it is located at the periphery of the cluster, sometimes observed in pairs on opposite sides of the cluster along the merger axis, and is partially polarized. The consensus is that the relic emission traces cosmic-ray electrons which are locally accelerated by accretion (or merger) shocks, in agreement with the elongated morphology of relics which appears to be tracing shock regions

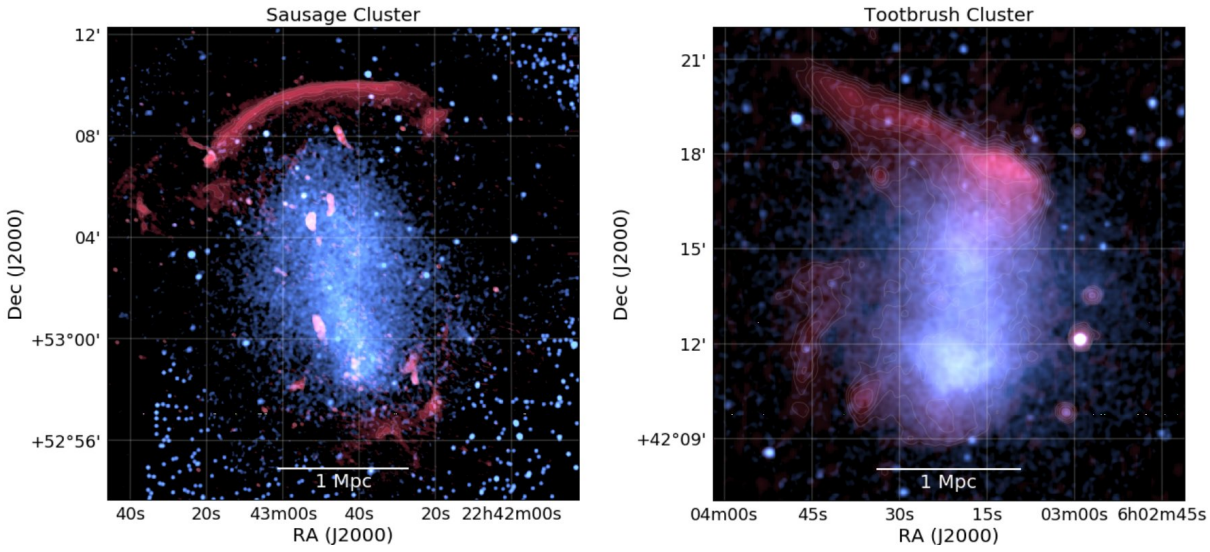

Figure 2.7: Examples of radio relic emission (red) and X-ray emission (blue) in the "Sausage" cluster and "Toothbrush" cluster. Image taken from [WGA19].

edge-on. The polarization orientation implies that the magnetic field is confined to the shock plane [BBR12]. This theory is also supported by observations of relics which have X-ray evidence of shocks spatially coincident with the cluster's radio relics [OB13, Mar10, RSM94]. The shocks are believed to be weak, possibly requiring seed electrons more energetic than the ICM provides in order to generate the radio relic emission. If seed electrons are necessary, a direct connection between the radio relic and a radio galaxy in the merging clusters Abell 3411-3412 suggests that local AGN could be the seed source [vAD17].

Non-thermal emission must exist in GCls as evidenced by the varieties of synchrotron radio emission. The proposed acceleration mechanisms have been discussed, which can generally be separated into mechanisms which accelerate protons and those which accelerate electrons directly, where the relative contribution from each mechanism can be constrained by observing the cluster non-thermal emission. Cosmic-ray protons will inelastically collide with ICM protons, producing pions which will decay into secondary cosmic-ray electrons, positrons, and γ-rays. Cosmic-ray electrons, secondary and primary, are expected to produce hard X-rays and γ-rays via supra-thermal bremsstrahlung and inverse Compton scattering

with the CMB. Simulations predict (see Figure 2.8) that the two primary contributions to γ-ray emission above 1 GeV are π^0 decay and inverse Compton scattering of primary accelerated electrons [Min03]. Since the high density core has many collision targets for the energized protons, it is expected to be dominated by π^0 decay emission. Conversely, the fast cooling times of energized electrons mean that the inverse Compton emission is expected to be in the vicinity of strong shocks at the cluster edges where the electrons are accelerated and, in general, it traces the morphology of regions with intense shocks. A simulation of the γ-ray emission from these two components for a Coma-like cluster is shown in Figure 2.9.

2.1.2 γ-ray Observations of Galaxy Clusters

To date, diffuse γ-ray emission associated with the ICM has not been conclusively observed. The emission most expected is from protons via neutral pion decay in the high density GCl core region, as the protons can accumulate over cosmological times. While no detection has been made, observations have constrained predicted models. A joint likelihood analysis of Fermi-LAT data on 50 X-ray bright GCls, which specifically investigated a purely hadronic origin of the γ-ray emission, found no detection but provided upper limits on the cosmic-ray-to-thermal pressure ratio $\langle X_{CR} \rangle \lesssim 2\%$ as well as the hadronic injection efficiency in shocks $\zeta_{p,inj} \lesssim 20\%$ [Ack14]. Observations of the nearby Perseus and Coma GCls, the prototypical clusters containing mini and giant radio halos, respectively, have provided the most important γ-ray emission limits due to their nearby proximity, high mass, and bright radio emission. The Perseus Cluster, due to its high density cool core, may be the most promising galaxy cluster to detect γ-ray emission of hadronic origin by future observatories [PP10]. Current observations of the Perseus Cluster by the MAGIC Cherenkov telescopes found a lower limit on the central magnetic field strength which conflicts with a hard ($\alpha \lesssim 2.1$) hadronic interpretation of the radio mini halo [Ahn16]. VERITAS observations of the analyzed the central 0.4° radius region and found no significant excess (see Figure 2.11 [AAB12]. Fermi-LAT 6-year observations of the Coma GCl under the hadronic interpretation have found a

lower limit on the magnetic field $\sim$ 5 times greater than Faraday rotation measurements give, rejecting the purely hadronic interpretation of the giant radio halo [BZZ17]. The same observations also concluded that the cosmic-ray proton energy budget is less than 10% of the thermal ICM mostly independently (within a factor of two) of the emission model and magnetic field strength. A recent Fermi-LAT analysis of the Coma GCl using enhanced event-level sensitivity found an excess ($\sim$ 3 standard deviations) of diffuse emission in the cluster central $\sim$ 1 Mpc region (see Figure 2.10), as well as higher energy (1-10 GeV) emission extending beyond the virial radius, but not enough to claim a detection [Ack16]. Since hadronic γ-ray production via π^0 decay strongly depends on the spectral index of accelerated hadrons, which may not be immediately coupled to the synchrotron radio emission if it is dominated by primary electrons accelerated *in situ*, it may be possible to reconcile all observations of the Coma GCl in radio, X-ray and HE bands, and still allow VHE γ-ray radiation to be detectable by current ground-based γ-ray observatories.

Searches for γ-ray emission have also occurred in peripheral regions of clusters where the radio relics associated with shock acceleration are observed, but no detection has been made so far. A thorough examination involving a stacked analysis of ten clusters, each with a pair of merger radio relics, obtained strict γ-ray upper limits in tension with the expected γ-ray flux from shock acceleration, suggesting that the proton to electron acceleration efficiency ratio may be much smaller than expected [VEB15]. This could be explained by the magnetic fields at the shocks being perpendicular to the shock normal, which simulations show to be able to suppress the proton acceleration efficiency [CS14].

Evidence of γ-ray emission associated with peripheral shock acceleration in the Coma GCl has been suggested in literature [KKL17]. An analysis by independent researchers of a published VERITAS Coma GCl skymap (Figure 2.11) found a nominal significance (2.7σ) for integrated γ-ray emission in a $\sim$ 5 Mpc minor axis ring elongated towards the large scale filament connecting Abell 1367 (see Figure 2.12). Some cross correlation ($\sim 3\sigma$) was also found between the VERITAS significance map and both SZ and synchrotron signals

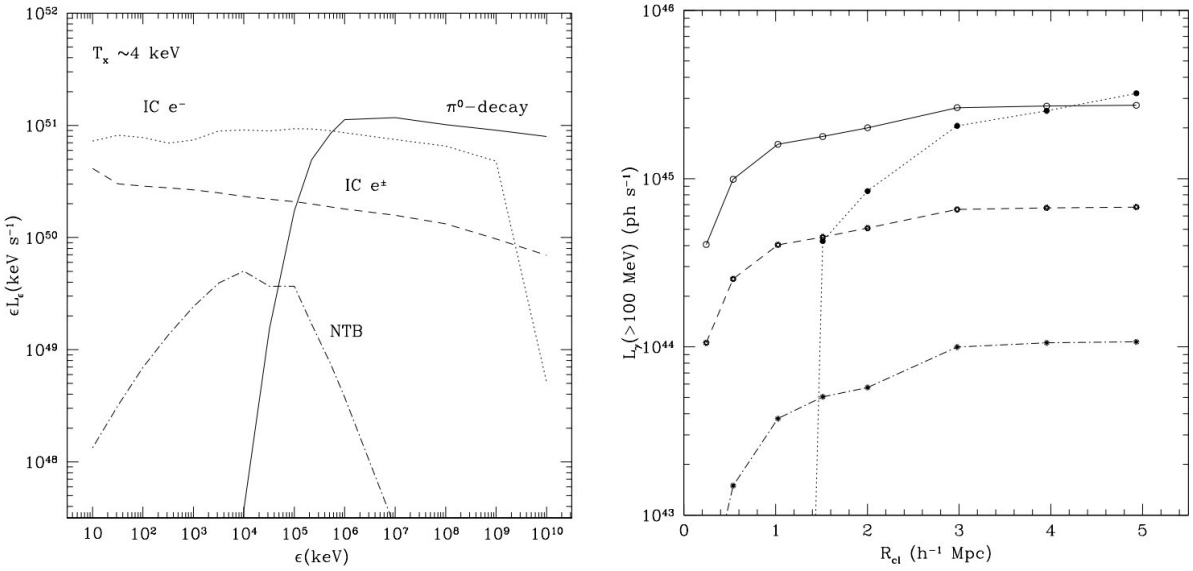

Figure 2.8: Left: Simulated radiation spectrum produced by the different emission processes: inverse Compton (dotted) and non-thermal bremsstrahlung (dash-dotted) from shock accelerated electrons, inverse Compton emission from secondary $e^{\pm}$ (dashed) and π^0 decay (solid) produced by accelerated protons. Right: Also simulated, integrated photon luminosities above 100 MeV vs distance from the cluster core for the same processes. The simulated core temperature for this plot was $T_x \approx 2-4$ keV, a factor of a few smaller than the Coma GCl. Image taken from [Min03].

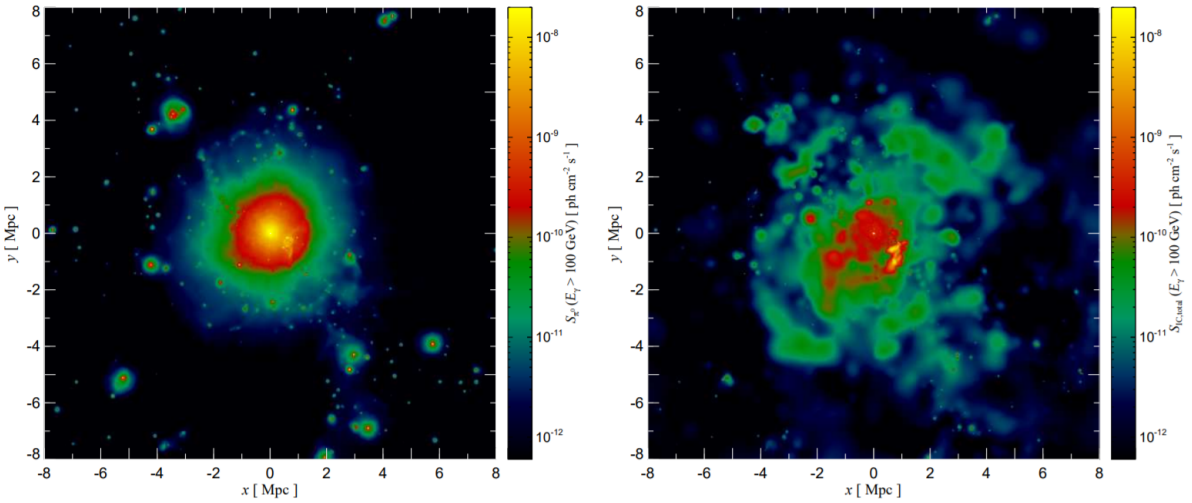

Figure 2.9: The simulated γ-ray emission above 100 GeV for a Coma-like cluster from pion decay originating from cosmic-ray protons interacting with the ICM (left), and inverse Compton emission from primary and secondary cosmic-ray electrons (right). The pion decay emission demonstrates a regular morphology with a strong central peak where the ICM density is largest, while the inverse Compton emission traces the structure formation shock waves. The extension for the pion decay emission is mostly contained within a 2 Mpc radius, equivalent to 1.5° for the Coma GCl. Image taken from [PP10].

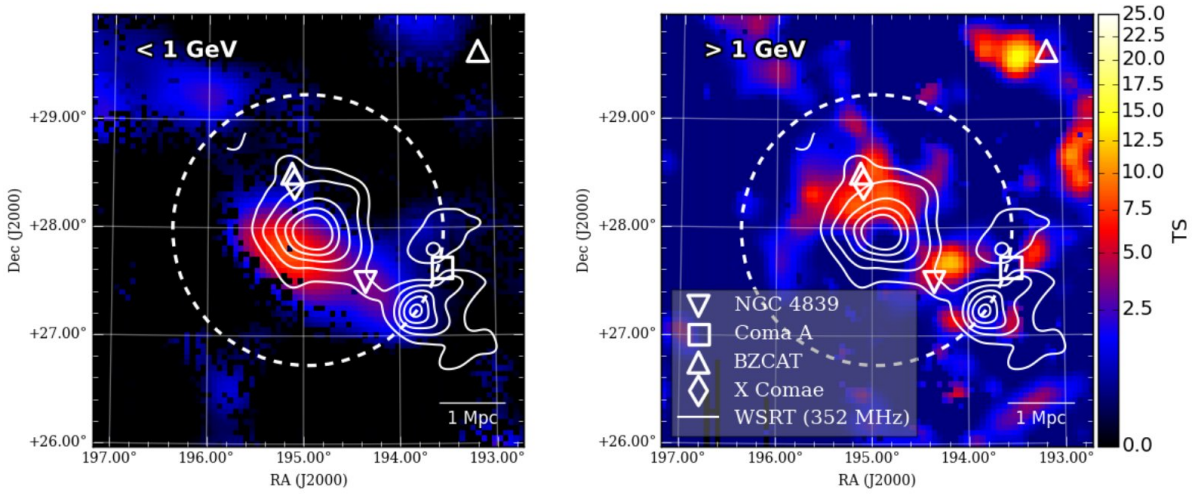

Figure 2.10: Test Statistic (TS) map of Coma GCl from Fermi-LAT observations. Left: 100 MeV-1 GeV emission in the Coma GCl. There appears to be extended, diffuse signal associated with the radio halo. Right: 1 GeV-10 GeV emission in the Coma GCl. The dashed lines indicate the virial radius. Image taken from [Ack16].

in the claimed virial shock ring region. A follow up analysis using five years of Fermi-LAT data tested for a 100 MeV$-$100 GeV γ-ray signal in the declared ring structure and found a flux upper limit, which contradicted originally claimed fluxes if they are extrapolated into the high energy regime [ZA14]. However, this contradiction may be expected as the point spread function (PSF) of Fermi-LAT at lower energies is significantly larger ($> 5^\circ$ for 68% containment) than the expected shock ring width ($\sim 0.6^\circ$) [AAB13]. A more recent analysis of Fermi-LAT data with high energy γ-rays ($>$ 1 GeV) tested a variety of ring sizes and orientations, finding a moderate significance (3.4σ) for integrated emission along a proposed virial shock ring [Kes17]. Furthermore, a soft X-ray emission excess is also claimed to be observed in a ring-like structure in the Coma GCl, which is likely indicative of the presence of primary re-accelerated electrons. This interpretation in combination with the VERITAS and Fermi-LAT shock emissions, gives a cosmic-ray electron spectrum that is approximately flat ($p \equiv -\frac{d \ln N}{d \ln E} \simeq 2.0 - 2.2$). The photon spectrum should be similarly flat, making observations

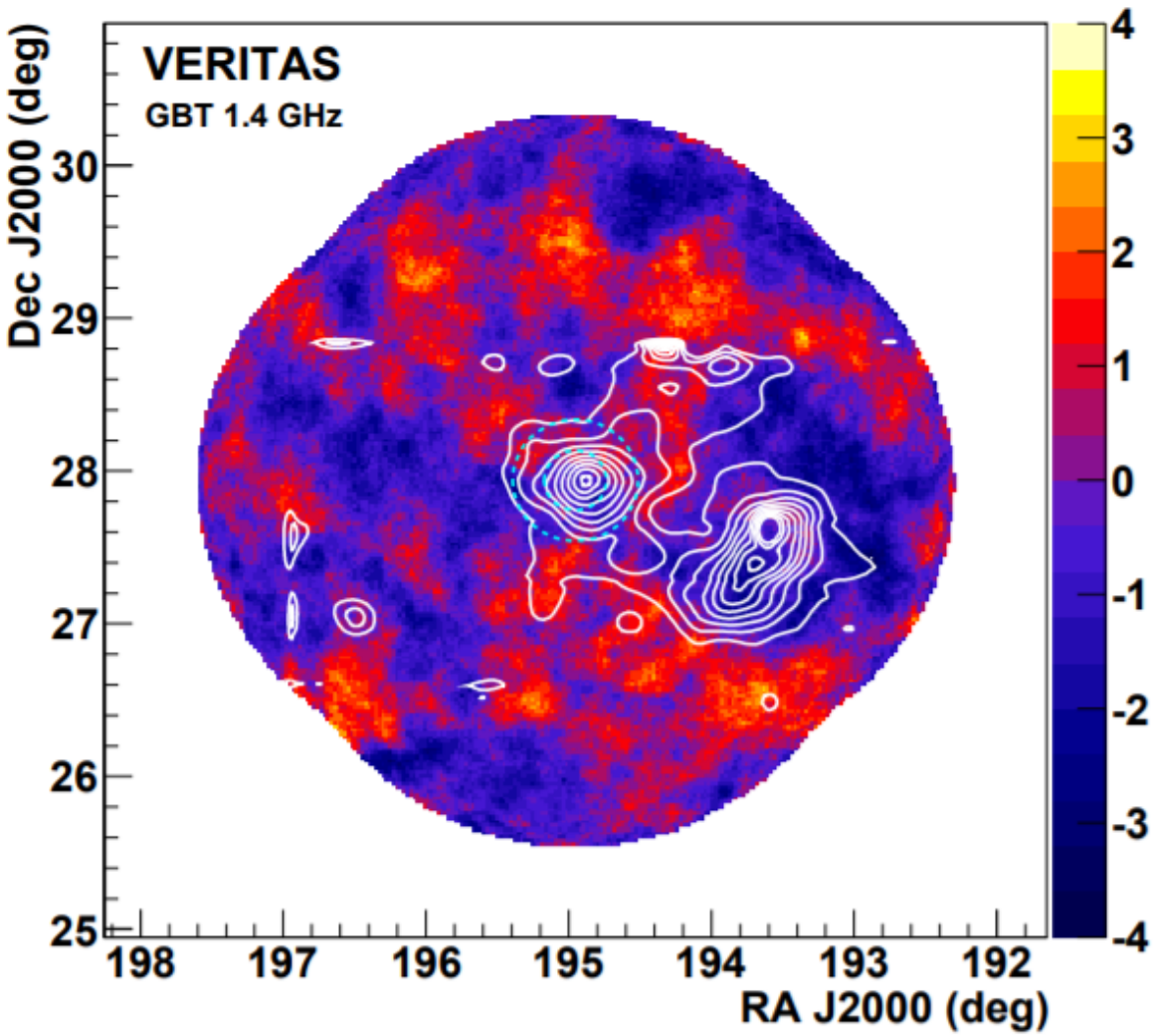

Figure 2.11: The smoothed significance map of the Coma GCl published by VERITAS, with radio contours overlaid. The color scale corresponds to the determined significance from measured excess counts, where the background counts were derived using a ring-background model. The integration radius of 0.2° and 0.4° are shown by the dashed cyan curves. Image taken from [AAB12].

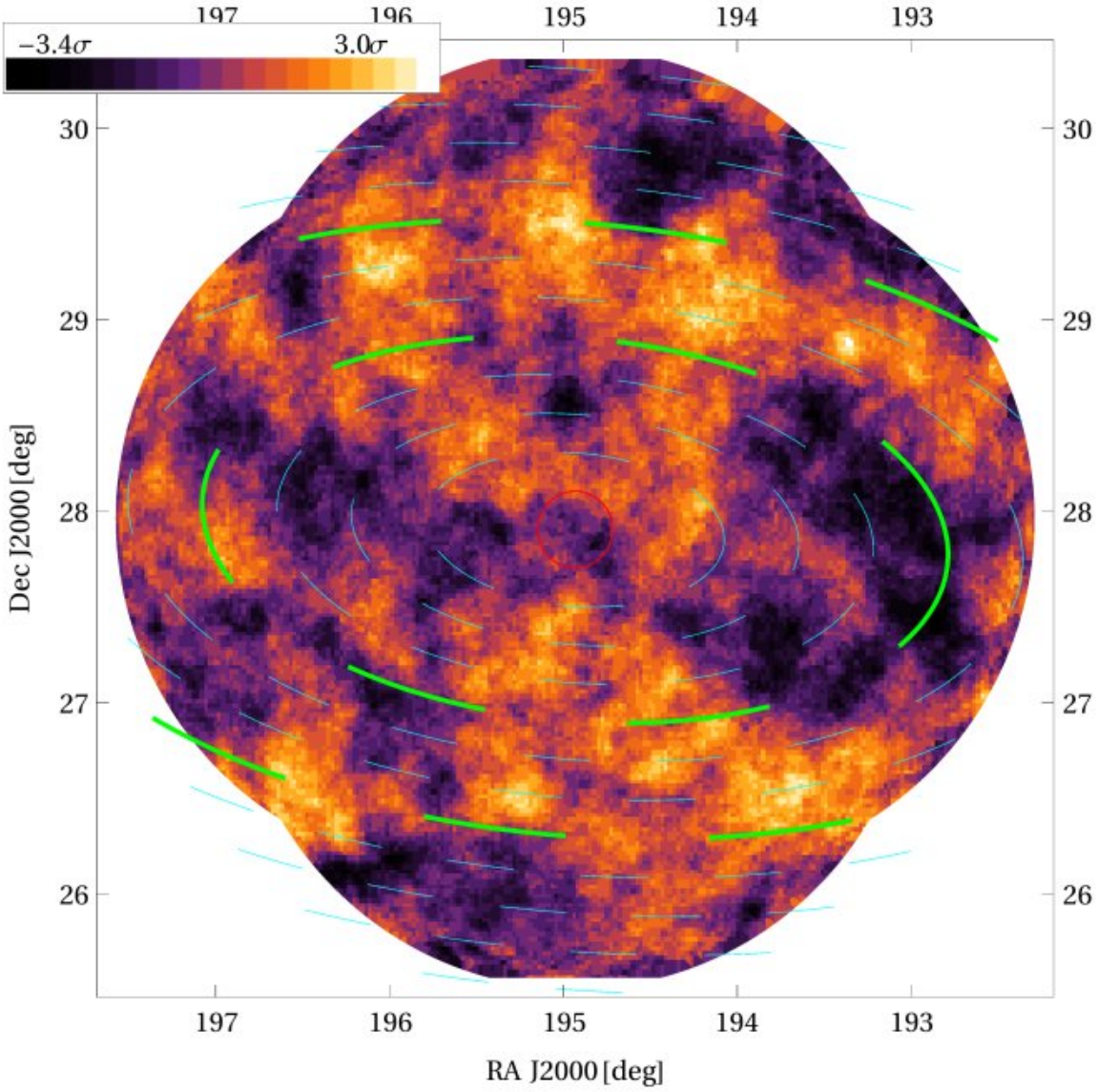

Figure 2.12: The proposed virial shock region outlined by the dashed thick green lines, created from the original VERITAS skymap (see Figure 2.11). The proposed region is contained within two ellipse with semi-minor axis of $1^\circ \lesssim b \lesssim 1.6^\circ$ with the elongation ratio of $a/b = 2$, and angular orientation of $\phi = -0.5^\circ$. Image taken from [KKL17].

for energies above 100 GeV with IACTs like VERITAS sensitive to the virial shock emission. In this dissertation an analysis of the extended Coma GCl region is performed to investigate the evidence of an extended γ-ray emission with the proposed ring morphology determined from the VERITAS published skymap.

2.2 Dragonfly 44

2.2.1 Brief Summary of Dark Matter Evidence

The first prominent observation of dark matter came in the 1930s, when Fritz Zwicky studied the redshifts of galaxy clusters and found a large velocity dispersion of eight galaxies within the Coma GCl. Applying the virial theorem to these velocities to estimate the mass of the Coma GCl, Zwicky found it to be approximately an order of magnitude greater than the mass from light estimation alone [Zwi37]. Further development occured in 1970, when Rubin et. al. published observations on the velocities of stars in the Andromeda spiral galaxy M31 [RF70]. The velocities were determined by Doppler shifting measurements of 21 cm radio and Hα optical emission lines of hydrogen. The velocity dispersion of stars in a spiral galaxy, with a central mass and flat disk, can be estimated by Newtonian dynamics. For a simple two dimensional disk rotation, assuming circular motion, for radius r far from the central mass (where M is does not change much)

$$v(r) \propto r^{-1/2}$$

However the velocities found by Rubin et. al. flattened out for large r, suggesting a significant non-luminous mass content at large r with density $\rho(r) \propto r^{-2}$, called a dark matter halo (see Figure 2.13). Currently, the rotation curves of over one thousand spiral galaxies have been observed and found to share a similar flatness to them at large radius [Sof17]. These curves provide one of the strongest pieces of evidence for dark matter (see Figure 2.14).

Galaxy clusters provide further evidence for the existence of dark matter. The mass

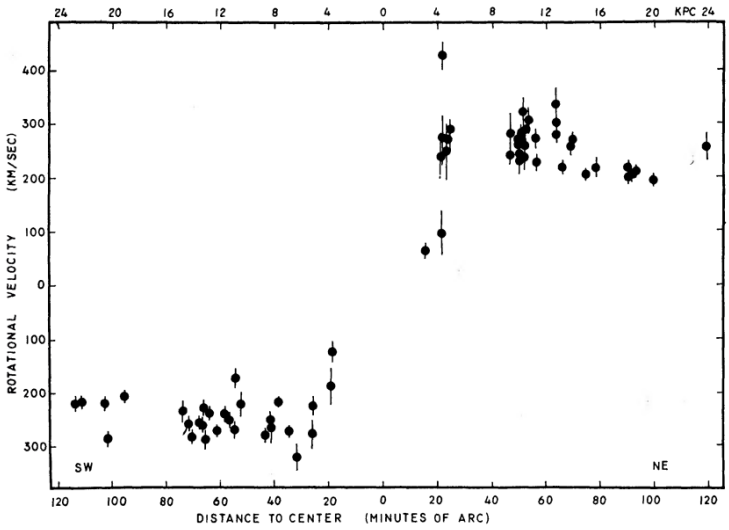

Figure 2.13: The rotational velocity measurements of sixty seven emission regions in M31. The velocities stay flat for increasing radius. Image taken from the original Rubin. et. al. paper published in 1970 ([RF70]).

distribution of galaxy clusters can be probed by observing objects which are gravitationally lensed by the galaxy cluster. Clowe et. al. observed the gravitational lensing of 1E 0657-558, named the "Bullet Cluster", and found the mass distribution to have two separate peaks spaced over 500 kpc apart. However, observations in X-ray reveal a baryonic plasma more central to the cluster, approximately 200 kpc apart (see Figure 2.15). The discrepancy between the gas distribution and mass distribution suggests that the Bullet Cluster is the result of two separate clusters colliding, with the baryonic components heating up via collision friction and losing momentum while the massive dark matter components passed through with little interaction [CBG06]. Another example of this observation can be seen in the cluster MACSJ0025.4-1222 [BAT08].

There is a variety of cosmological evidence for dark matter as well. The standard Big Bang model has the Universe beginning approximately fourteen billion years ago in a hot, dense state in thermodynamical equilibrium. As the Universe expanded this hot plasma

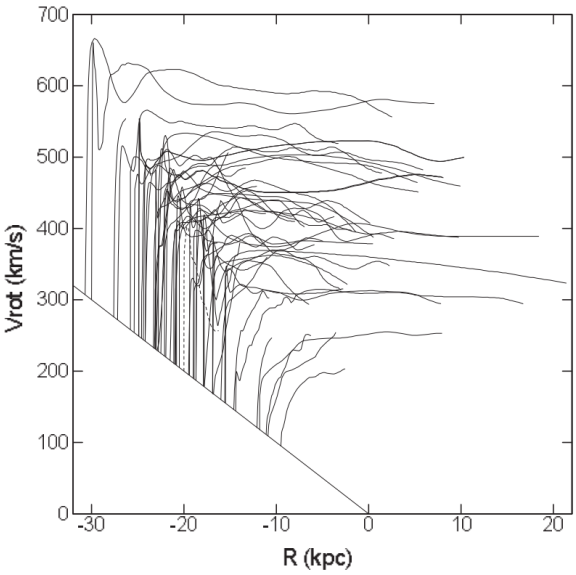

Figure 2.14: The rotational velocities of 967 spiral galaxies, with origins shifted proportionally to the average velocity (1-10 kpc). Image taken from [Sof17].

cooled, causing protons and electrons to form neutral Hydrogen which was transparent to the thermal radiation, allowing photons to escape. Observation of this thermal radiation, called the cosmic microwave background (CMB), first occurred in the 1960s by Penzias and Wilson [PW65], who found it to be isotropic and approximately corresponding to the blackbody thermal spectrum of $\approx$ 3K. In 1990 the experiment Cosmic Background Explorer (COBE) confirmed that the CMB radiation corresponded to a temperature of 2.73K with anisotropies on the order of 10^{-5} [MCE90]. The anisotropies reveal gravitational perturbations in the matter-radiation plasma at the moment of decoupling. Under ΛCDM, the most widely accepted cosmological model, the current energy density budget of the Universe is divided between baryonic matter, cold dark matter (CDM), and dark energy. The measured angular power spectrum of the CMB temperature perturbations on the sky has clear peaks and troughs which can be used to determine the relative energy densities (see Figure 2.16). The latest results by the Planck instrument gives the energy density of cold dark matter ($\Omega_c h^2 \approx 0.12$) and of baryonic matter ($\Omega_b h^2 \approx 0.0224$). The ratio of these energy densities

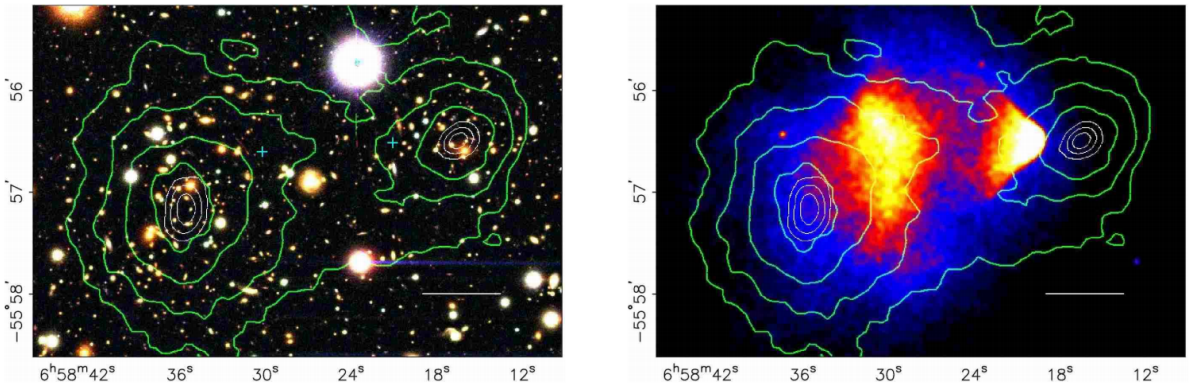

Figure 2.15: Optical (left) and X-ray (right) images of the Bullet Cluster. The green contours correspond to increasing surface mass density, as derived from the gravitational lensing signal. Image taken from [CBG06].

is $\frac{\Omega_c}{\Omega_b} \approx 5.4$, suggesting that there is over five times as much dark matter as visible matter in the Universe [PAA18].

Further support for dark matter comes from studies of Big Bang nucleosynthesis. In the early Universe the quantities of light elements (^{2}H, ^{3}He, ^{4}He, ^{7}Li) produced depended on the neutron lifetime and on the baryon-photon number density ratio, $\eta = n_b/n_\gamma$. The measured present day abundances of these elements, primarily obtained from low metallicity stars and from the absorption spectra of quasars, constrains the value of this ratio to $\eta \approx 6 \times 10^{-10}$ [CFO16]. Combining this value with the CMB-observed photon number density, the energy density of baryons is determined to be $\Omega_b h^2 \approx 0.022$. Since the Universe appears approximately flat ($\Omega_0 \approx 1$) from CMB measurements, a large amount of missing energy density must exist in the form of dark energy and dark matter.

Observations of the large scale structure of the Universe also support the need for a dark matter component. The standard theory of structure formation accounts for the present day relative density distribution of matter, $\delta(\vec{r}) = [\rho(\vec{r}, t) - \bar{\rho}(t)]\,/\bar{\rho}(t)$, as the evolution of initial perturbations in the gravitational potential of the early Universe. Before recombination, the amplitude of these relative density perturbations for baryonic matter was limited to

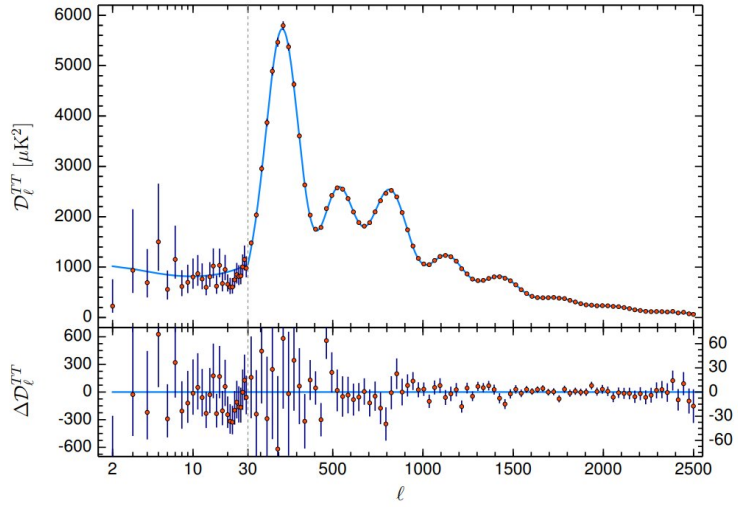

Figure 2.16: The temperature perturbations power spectrum of the CMB, measured by the *Planck* instrument. The amplitudes and locations of the peaks are used to determine the energy density of baryonic matter and cold dark matter. Image taken from [PAA18].

10^{-5} according to CMB measurements. After photon decoupling, the relative densities grow according to $\delta \propto [1+z]^{-1}$, resulting in the expectation of observed relative densities on the order of 10^{-2}. However the actual observed value is $\delta \geq 1$, two orders of magnitude above what is expected. This discrepancy could be resolved with the inclusion of dark matter in the early Universe. Since dark matter decouples from photons much earlier than baryonic matter, density perturbations significantly larger than 10^{-5} could be developed by the time of recombination. After recombination, the baryonic matter could then fall into these dark matter gravitational wells, speeding up the growth of relative density perturbations to be developed faster than $[1+z]^{-1}$.

2.2.2 WIMP as DM candidate

The collection of observational evidence for dark matter provides constraints on a theoretical DM particle. The DM particle is expected to be charge neutral, since it does not appear to interact via electromagnetic channels as evidence shows it is collisionless in comparison with

electromagnetic and hadronic cross-sections and it does not create or absorb light. Since the current energy density of DM in the Universe is $\Omega_c h^2 \approx 0.12$, the DM candidate must be stable on timescales on the order of the age of the Universe. If the DM candidate particle interacts non-gravitationally, then the strength of this interaction must be relatively weak. The candidate that adheres to these requirements is generally termed the weakly interacting massive particle (WIMP). While there are alternative hypothetical DM candidates, the scope of this dissertation will only contain the WIMP.

In the high temperature thermal equilibrium of the early Universe, DM particles were created and destroyed at equal rates. As the Universe expanded and the temperature cooled, DM decoupled from the other matter and was no longer being created, but a population of DM particles remained. The rate of DM self-annihilation is proportional to the number density squared, and is also dependent on the expansion rate of the Universe, and on the DM's self-annihilation cross section. After the period of efficient self-annihilating, the DM particle number density decreased until eventually the rate of the Universe's expansion became greater than the rate of self-annihilation, at which point the amount of time for a DM particle to find another DM particle was roughly the age of the Universe. At this point the number of DM particles was "frozen out", and the remaining population became stable. If one assumes that the density of particles is equal and the mass of the particle is around 100 GeV, which is of the order of the mass of the weak interaction bosons $W^{\pm}$ and Z, then in calculating the relic abundance of DM, using the present-day DM relic energy density, the velocity-averaged cross section for DM self-annihilation is found to be:

$$\langle \sigma v \rangle \approx 3 \times 10^{-26} \text{ cm}^3 \text{ s}^{-1}$$

. This cross section "miraculously" happens to be of the order of the weak interactions scale which is dubbed the "WIMP Miracle" for its natural fit into the standard model of particle physics, making a massive DM particle which interacts via the weak force, the WIMP, a naturally appealing candidate. One of the most favorite WIMP candidates, the neutralino, is the lightest stable weakly interacting Majorana particle. The possible mass

range of the neutralino for its potential indirect detection utilizing the self-annihilation signal in astrophysical regions of high DM density is 100 GeV-100 TeV.

2.2.3 Indirect detection of the WIMP

Evidence for the WIMP can be obtained through one of four methods: astrophysical probes, collider detection, direct detection, or indirect detection. Astrophysical probes constrain properties of dark matter through its impact on astrophysical observables. Collider detection makes use of particle accelerators like the Large Hadron Collider (LHC) to discover or to set limits on theoretical DM particles. A WIMP that is produced in a collider (direct production) would be seen only through the missing transverse momentum from an event. Direct detection experiments look for a signature of DM interacting with a standard model particle, such as the nuclear recoil caused by the scattering of a DM particle. Indirect detection searches look for the byproducts of WIMP self-annihilations in the Universe. The indirect detection method is the one relevant for this dissertation.

While the self-annihilation rate of the WIMP on the scale of the Universe is very low, regions with a large concentration of DM will have significantly higher self-annihilation rates. Among the potential self-annihilation byproducts, photons are especially promising because they travel in straight lines from the annihilation location. A photon signal of self-annihilation can be measured from a restricted solid angle in the sky, significantly reducing background contamination for compact DM sources. For a region with WIMP number density n, the rate of self-annihilation per unit volume is

$$\frac{\Gamma}{V} = \frac{\langle \sigma v \rangle n^2}{2}$$

where the factor of 2 is there to avoid double counting for the case of Majorana fermions such as the neutralino. The total γ-ray spectrum per unit volume-time from this region for a single annihilation spectrum of $\frac{dN}{dE}$ is

$$\frac{dN}{dV dE dt} = \frac{dN}{dE} \frac{\langle \sigma v \rangle n^2}{2}$$

The differential flux observed on Earth from the WIMP self-annihilations is equal to

$$\frac{dN}{dEdAdt} = \frac{dN}{dE}\frac{\langle\sigma v\rangle}{2m_\chi^2}\int_S \frac{\rho_\chi^2 dV}{4\pi r_s^2}$$

where the volume integral is over the DM source at a distance $\sim r_s$ from the Earth. For a source observed over the angular extent $\Delta\Omega$, the differential flux is equal to

$$\frac{dN}{dEdAdt} = \frac{dN}{dE}\frac{\langle\sigma v\rangle}{8\pi m_\chi^2}\int_{\Delta\Omega}\int_{\Delta\lambda}\rho_\chi^2(\lambda,\Omega)d\lambda d\Omega$$

This flux is typically separated into two components: a particle physics term dependent on the dark matter candidate's cross section, mass, and energy spectrum, and an astrophysical term, called the J-factor, which is the line-of-sight integral of the source's DM density squared.

Searches for γ-ray evidence of the WIMP over the GeV-TeV mass range have been performed by space telescopes (such as Fermi-LAT) and ground-based telescopes (such as the IACT arrays of VERITAS, HESS, and MAGIC) [AAA13b, AAB17, AAA18a, AAA20]. Since the J-factor scales quadratically by the WIMP density and linearly by solid angle, objects that are large, nearby, and have a high DM density are the most promising sources to investigate. The Galactic Center (GC) has by far the largest J-factor of any source because of its local proximity and significant DM density [SB87]. A GeV excess has been measured by the Fermi-LAT instrument in the GC, however there is much disagreement over the source of this excess and whether it can be attributed to DM annihilation [Ack17]. Bright non-thermal astrophysical processes exist in the region which create an often disputed background that could account for the excess [ACH14, DFH16, CCW15]. HESS observations of the GC have seen no significant excess for masses above 300 GeV [Rin19]. Dwarf Spheroidal Galaxies (dSph) are believed to be a much cleaner DM target. DSphs have low astrophysical γ-ray backgrounds and large mass to luminosity ratios (M/L), suggesting a dominant DM density. However, dSph have much smaller J-factors compared to the GC [GKW15]. A combined analysis of Fermi-LAT observations of nearby dSphs has found no significant detection of WIMP annihilation, and corresponding cross section upper limits have being produced, some

of which are below the thermal relic level [Ack15, Alb15]. Similar results have been obtained by IACT arrays for higher mass WIMPs by stacked analysis of dSphs (VERITAS, HESS) and long exposure of a single dSph (MAGIC), with no detection being found and upper limits produced [Zit16, Abr14, Ale13].

Galaxy clusters (GCl) are believed to have been formed over the age of the Universe through baryonic matter accreting towards the gravitational sink from a large amount of DM. Therefore, GCls are expected to have a large amount of DM, making them a target for a WIMP annihilation signal. Despite this high DM content, GCl are both observationally and theoretically challenging targets. Although even the closest GCls are 10^2 - 10^3 Mpc away, their DM masses are two to three orders of magnitude larger than a typical mass of Milky-Way-like galaxy, which may end up producing a competitive J-factor albeit one with significant uncertainty due to unknown density profiles. For most nearby GCls, such as Virgo, Perseus and Coma, the large several degrees angular extension in the sky makes them observationally challenging sources for IACT technology due to large cosmic-ray backgrounds. GCl are also expected to contain a significant amount of γ-ray emitting astrophysical sources, obscuring a potential DM annihilation signal. An initial analysis of Fermi-LAT data of GCls initially resulted in evidence of a DM signal, which has since been shown to be accounted for by unmodeled point sources in the cluster [MGB12]. Continued searches by Fermi-LAT have resulted in no γ-ray detection in GCls [Zim15]. IACT searches have also found no γ-ray detection in GCls so far, with upper limits on the DM annihilation cross section being produced [AAA18b, AAA12, AAB12].

2.2.4 Ultra Diffuse Galaxies

Additional promising DM self-annihilation sources are the potentially new class of astrophysical objects called ultra diffuse galaxies (UDGs). UDGs are roughly defined as galaxies having a half-light radius larger than 1.5 kpc and a central surface brightness of more than 24 mag arcsec^{-2}. There is much debate over the mechanism by which UDGs are created.

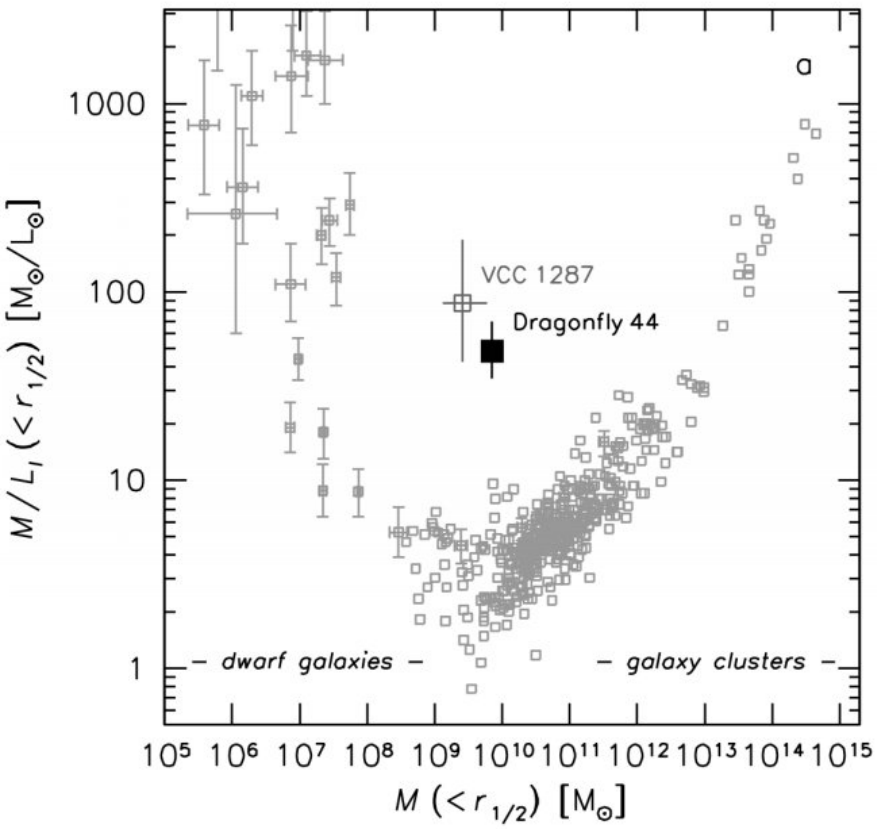

Figure 2.17: The M/L ratio vs dynamical mass of Dragonfly44 is anomalous compared to other dispersion-dominated galaxies. Image taken from [vAB16].

Some argue that because UDGs are frequently found in GCls and have a wide range of ages, they are simply a tail population of a continuous distribution of low surface brightness galaxies formed through cluster processes [Con18, vHM17]. Others claim that UDGs are "failed" galaxies which were stripped of gas during collisions and unable to form stellar populations while retaining a significant DM content, evidenced by the typical accompaniment of globular clusters [vAM15]. UDGs therefore may have significant DM content, making them an excellent source for indirect detection since the natural astrophysical backgrounds are expected to be low.

One such UDG, Dragonfly 44 (DF44), stands out as a particularly unusual source (see

Figure 2.17). Measurement of the velocity dispersion and effective radius constrains the dynamical mass to be $M(< r_{1/2}) = 0.71^{+0.26}_{-0.17} \times 10^{10} M_{\odot}$ and a relatively high mass-to-light ratio within $r_{1/2}$ of $M/L\left(< r_{1/2}\right) = 48^{+21}_{-14} M_{\odot}/L_{\odot}$ [vAB16], where $r_{1/2}$ is the deprojected half-light radius. Furthermore, DF44 is accompanied by approximately an order of magnitude more globular clusters than galaxies with similar luminosities. The anomalously large dynamical mass and globular cluster population for its luminosity suggests the presence of a dominant DM concentration in DF44. Ignoring mass from gas, and estimating the luminous mass to be $M_* = 3 \times 10^8 M_{\odot}$, the DM fraction is estimated to be $M_{DM}(< r_{1/2}) \approx 98\%$.

DF44 is a member of the Coma GCl (which has been spectroscopically confirmed) and, hence, it is located at a distance of $\sim$ 100 Mpc away. It is instructive to compare this object as an indirect detection candidate with the classical Draco dSph which is 80 kpc away. Although there is a difference in distance of three orders of magnitude, there is also nearly three orders of magnitude in difference of the estimated DM masses of these objects, which may to a significant degree cancel each other out in determination of a J-factor. Both Draco and DF44 are point sources for VERITAS, however, the DM density profile in the DF44 remains largely unknown and therefore the J-factor is highly uncertain, limiting the constraining ability of observations of DF44 for indirect detection. Since it is located within the Coma field of view, observation of DF44 comes at no additional cost of observing time, and an analysis of a possible γ-ray signal from this galaxy is undertaken in this dissertation.

CHAPTER 3

Cherenkov Imaging Technique and Instruments

3.1 Detecting VHE Radiation

The Earth is constantly being bombarded by astrophysical particles with very high energies. When such a particle enters and interacts with the Earth's atmosphere, it produces secondary particles. If the secondary particles have sufficiently high enough energy they produce secondaries of their own, and so on, until an atmospheric cascade progresses through many generations of particles, called an extensive air shower (EAS). Further details of the development of an EAS in the atmosphere is discussed in Section 3.1.1. The charged, relativistic secondary particles produce Cherenkov radiation in the atmosphere, which can be imaged on the Earth's surface. In Section 3.1.2 the properties of the EAS-induced Cherenkov radiation are examined. Section 3.1.3 describes how the imaged Cherenkov light is used to deduce the primary VHE particle's energy, direction, and to determine the particle type. This is the essence of the imaging atmospheric Cherenkov telescope (IACT) technique. The majority of observed air showers are caused by isotropic cosmic rays (CRs), which obscure the γ-ray showers originating from VHE sources. Therefore, in order to estimate a γ-ray signal, the IACT technique requires a sampling of CR-generated "background" events which are then subtracted, leaving an excess of γ-ray events. The general approach for calculating a significance and upper limits of a signal detection in the presence of a background, utilizing a likelihood-ratio test, is explained in Section 3.1.4.

3.1.1 Extensive Air Showers

There are two types of extensive air showers depending on the primary particle: electromagnetic and hadronic. Electromagnetic showers are generated by primary photons, electrons and positrons that interact with the atmosphere mainly through quantum electrodynamics (QED) processes such as pair production ($\gamma + \gamma \rightarrow e^- + e^+$) and bremsstrahlung ($e^{\pm}$+nuclei $\rightarrow \gamma + e^{\pm}$). The resulting secondary particles, made up of predominantly electrons and photons, generate more electrons and photons through the same QED interactions. As the shower continues to develop while penetrating the atmosphere, the number of secondary particles grows exponentially while the energy per particle decreases until it reaches the point where the energy lost by electrons from ionization becomes greater than the energy lost by bremsstrahlung ($\sim$85 MeV) [Mat05]. This point is where the number of shower particles is at a maximum, labeled the shower maximum, a value which, as will be described in Section 3.1.3, is used in determining the energy of the primary particle. The shower constituents then begin to decrease in number of particles as the lower energy photons are absorbed by the atmosphere and lower energy electrons quickly dissipate their energy through ionization. Due to the light particle masses and QED nature of the electromagnetic interactions, the overall cascade of secondary particles produced in an electromagnetic shower has a relatively narrow lateral spread.

The vast majority of extensive air showers are hadronic showers, generated by cosmic rays interacting with the atmosphere. These cosmic rays consist primarily ($\sim 99\%$) of protons and heavier nuclei which have traveled from various astrophysical sources to the Earth, appearing isotropic due to their deflection in magnetic fields. Hadronic showers are more complex than electromagnetic showers since the hadrons interact inelastically via strong interaction channels with atmospheric nucleons to produce mesons and unstable nuclei. The mesons produced, composed mostly of pions, go on to create a sub shower of its own. The charged pions decay into muons and neutrinos, with some muons created early enough decaying to electrons and neutrinos before reaching the Earth's surface. The neutral pions quickly

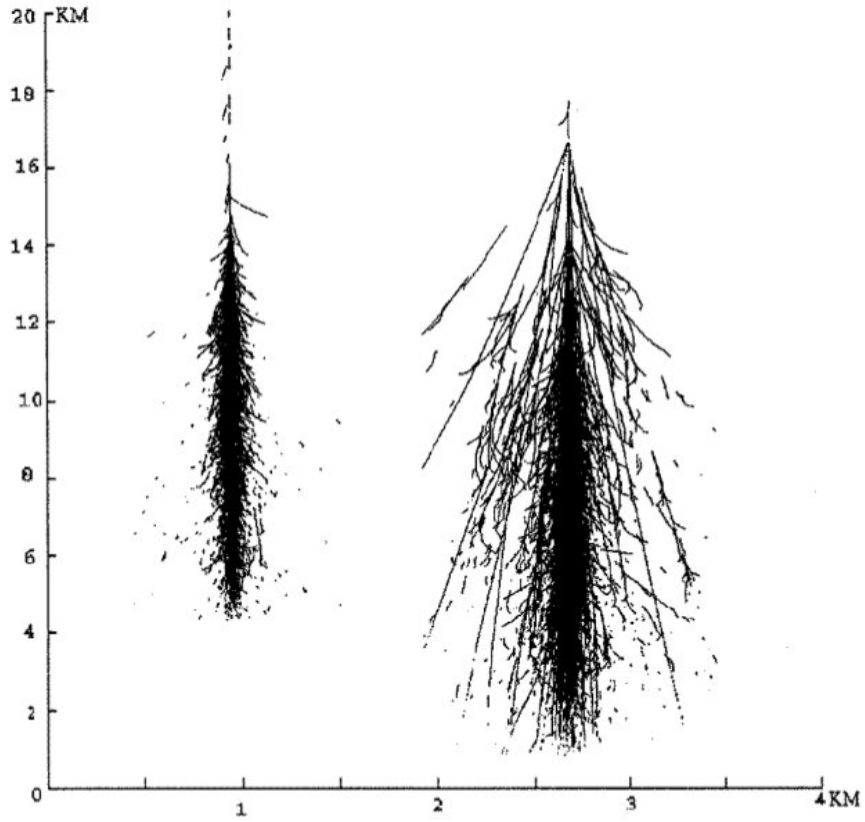

Figure 3.1: Monte Carlo simulated particle constituents for a γ-ray shower (left) and hadronic shower (right) with their widths stretched by a factor of four. The γ-ray shower has a narrower development, while the hadronic shower has larger transverse momentum transfer. Image taken from [Feg97].

decay into a pair of photons, which initiate an electromagnetic cascade. Hadronic showers therefore consist of three components: the original nuclear core, a muonic shower, and an electromagnetic shower. The lateral spread of a hadronic shower is significantly wider than an electromagnetic shower because of the large transverse momentum generated in the hadronic interactions (see Figure 3.1).

3.1.2 Cherenkov Radiation

When a charged particle travels faster than the speed of light in a medium, Cherenkov radiation is produced. This radiation is the result of constructively interfering polarization waves in the atmosphere, which acts as a a dielectric medium. The condition for constructive interference requires that the charged particle moves faster than the field, which results in the generation of a shock wave of light, analogous to a wake generated by a boat moving through water. The Cherenkov angle, θ_C, the angle of the normal to the Cherenkov wavefront with respect to the direction of the charged particle, depends on the particle's velocity ($v = \beta c$, $\gamma = [1 - \beta^2]^{-1/2}$) and the index of refraction ($n = 1 + \delta$, where $\delta \ll 1$ is proportional to the density of the Earth's atmosphere and, hence, changes with altitude).

$$\theta_C = \cos^{-1}\left(\frac{1}{\beta n}\right) \approx \sqrt{\frac{2\delta - \gamma^{-2}}{1 - \gamma^{-2}}}$$

The minimum energy required for Cherenkov radiation to be produced can be found by setting $\beta = \frac{1}{n}$ or $\gamma^{-1} = \frac{mc^2}{E_{min}} = \sqrt{2\delta}$ resulting in

$$E_{min} = \frac{mc^2}{\sqrt{1 - \frac{1}{n^2}}} \approx \frac{mc^2}{\sqrt{2\delta}}.$$

At this minimum energy the Cherenkov angle is zero ($\theta_C = 0$). When the particle's energy becomes much greater than this minimum energy, then the Cherenkov angle can be approximated as

$$\theta_C \approx \sqrt{2\delta} \qquad (E \gg E_{min})$$

Electrons and positrons make up the most numerous particles in extensive air showers with energies above E_{min}, and they therefore dominate the Cherenkov radiation of the cascade. At sea level the index of refraction is very close to one ($n - 1 = \delta = \approx 2.9 \times 10^{-4}$), setting the energy lower limit for electrons and positrons to be $E_{min} \approx 21$ MeV and $\theta_C(E \gg E_{min}) = 2.4 \times 10^{-2}$ rad or 1.4°.

To understand the structure of Cherenkov radiation from an EAS it is instructive to follow a single highly relativistic muon ($\gamma \gg 1$) as it propagates from the top of the atmosphere

≈ 25 km vertically down to the Earth's surface without interactions. It is important to note the Cherenkov light emitted at the highest altitudes arrives last to the observation surface since the relativistic muon outruns the Cherenkov photons by ~ 13 ns, which is the time depth of the Earth's atmosphere. As the muon travels deeper into the Earth's atmosphere, the Cherenkov angle increases with the thickening of the atmosphere. Once the Cherenkov light is being produced near enough to the Earth's surface, even though the Cherenkov angle is broadening, the radius of the emission cone on the ground begins to decrease because it has less time to propagate. Therefore this geometrical effect results in the ring of radiation gradually shrinking as it becomes closer to the Earth's surface. The end result is a "pool" of Cherenkov light with a radius of ≈ 130 m arriving at the observation surface in a flash lasting an average duration of 6 ns with all of the Cherenkov photons distributed in a 13 ns time window.

Examples of the resulting Cherenkov photon density from extensive air showers generated by primary γ-rays of various energies is shown in Figure 3.2. A prominent "pool" of light with the characteristic radius of ≈ 130 m is filled by the Cherenkov photons with a nearly constant density. These photons are produced by the high energy core particles of an EAS which move along the direction of the primary γ-ray. As the energy of secondary electrons and positrons is reduced to below a few hundred MeV, they begin to deflect significantly from the primary direction due to multiple Coulomb scatterings and emit Cherenkov photons towards a radius larger than the characteristic 130 m. As these particles decrease in energy through cascading and ionization, they reach a minimal threshold energy for Cherenkov light production and stop radiating photons, and hence the photon density rapidly declines. While the photons inside of the Cherenkov light "pool" arrive to the observing surface within a short period of a few nanoseconds, the photons outside the pool are distributed over an increasingly wider period of time, up to a few hundred nanoseconds, due to the geometrical effect of a greater travel distance and consequentially a longer travel time before reaching the ground. The quickest distribution of photons occurs in the vicinity of the "pool" of

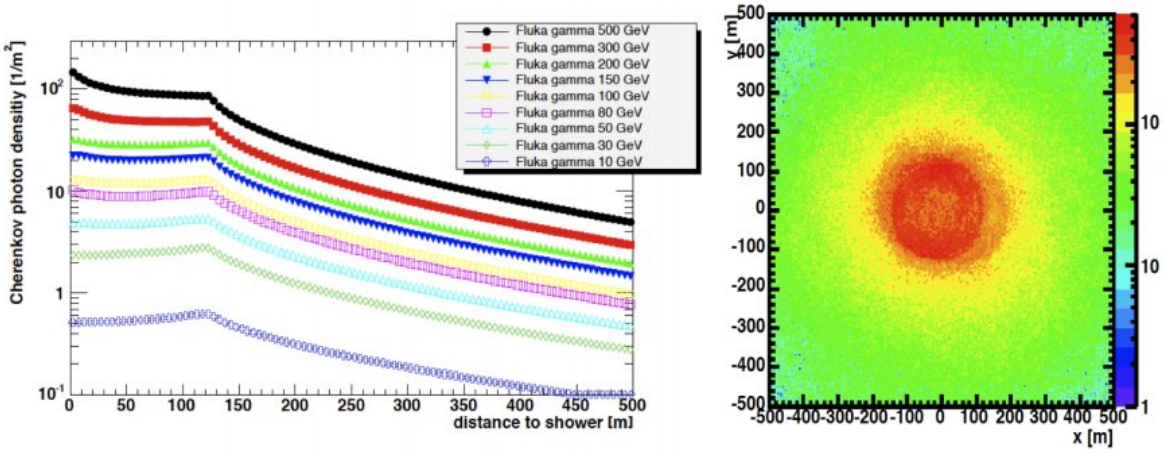

Figure 3.2: Left: The simulated Cherenkov light density distribution for γ-rays with a variety of energies. The photon density is relatively flat in a "pool" of $\sim$ 130 m radius before decaying at large distances from the shower center. Right: The two dimensional photon density profile for a simulated 300 GeV γ-ray with a log-scale colorbar. Image taken from [Hol15].

characteristic distance 130 m.

While hadronic showers also generate Cherenkov radiation from their secondary components, including electromagnetic sub showers, the radiation is typically broader in shape, has a less prominent Cherenkov "ring" photon density, and arrives in the "pool" over a longer period of time ($\sim 10-15$) ns. These distinctions between the Cherenkov radiation produced in electromagnetic and hadronic extensive air showers are used to discriminate CRs from γ-rays.

3.1.3 Imaging Atmospheric Cherenkov Telescopes

Imaging atmospheric Cherenkov telescopes (IACTs) use the flash of Cherenkov light from an EAS in order to classify and reconstruct the energy and direction of the primary particle that generated the shower. IACTs have an image-forming optical system in combination with fast photo detectors and electronics which can capture the brief ($6-20$ ns) Cherenkov

flash with minimal contamination from the night-sky background (NSB) light. For electromagnetic cascades, the Cherenkov flashes which are imaged on the telescope camera's focal plane resemble narrow elliptical shapes with a relatively smooth distribution of light in them. In distinction, the imaged flashes from hadronic cascades are relatively broader, and more frequently contain multiple sub-shower elements. These deviating characteristics allow for the "shape" classification of showers as either electromagnetic or hadronic, with the goal of removing hadronic showers and retaining only events originated by γ-rays. The suppression factor of the CR background by this shape selection is energy dependent, changing from a few to several hundred at larger energies. In addition to providing a criteria for particle classification, the imaged elliptical distribution of light contains information about the direction and energy of the primary. The major axis of the ellipse points in the direction of the shower core, allowing for the triangulation and improved angular reconstruction of events observed by multiple telescopes (see Figure 3.3). Furthermore, the brightness of the image, in combination with geometrical information about the EAS, can be used to estimate the energy of the primary particle that generated the cascade. A further detailed account of event reconstruction techniques is given in Section 3.2.

3.1.4 Detection Significance and Upper Limits

The majority of observed atmospheric cascades are caused by isotropic CRs. While a significant percentage of the hadronic showers can be filtered out, there still remains a small fraction which appear as γ-ray-like electromagnetic EAS events, in addition to the virtually indistinguishable electromagnetic cascades originated by CR electrons and positrons. Therefore, in order to estimate a genuine γ-ray signal, a sampling of a "background" is made, with excess events above this anticipated background attributed to a γ-ray signal. The source and background regions which are sampled from are referred to as "ON" and "OFF" regions, respectively. The commonly adopted method for determining a detection significance in VHE astrophysics from ON and OFF observations is given in the 1983 paper by Li & Ma [LM83].

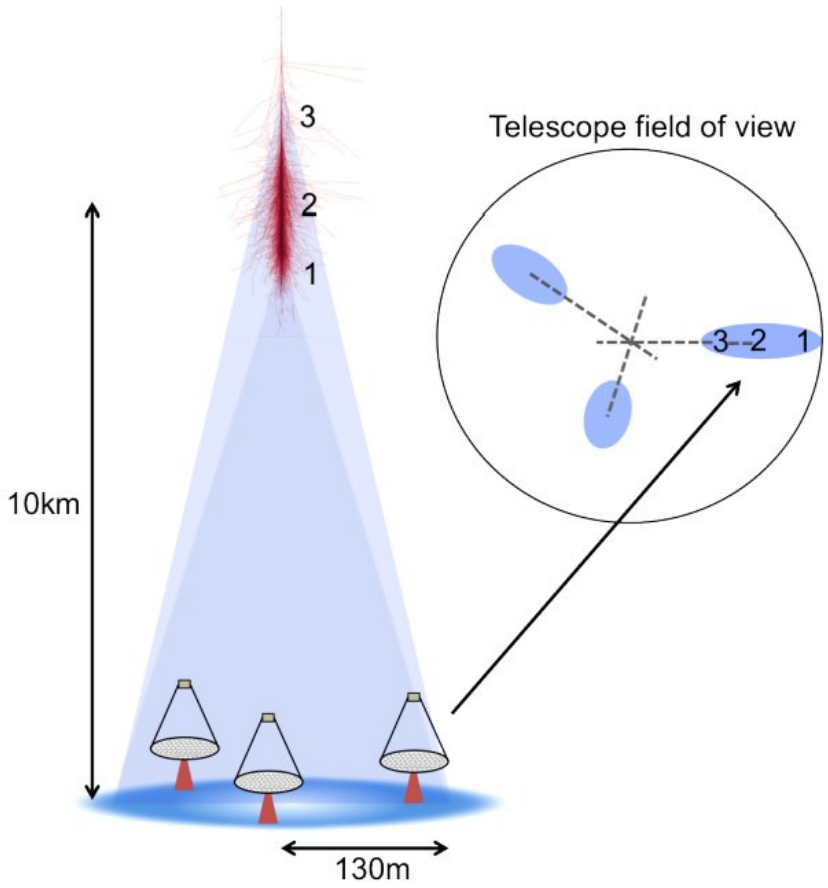

Figure 3.3: Depiction of the stereoscopic IACT technique. The Cherenkov flash is captured by multiple IACTs which can triangulate the direction of the shower core by intersecting the major axes of the images in the sky. Image taken from [Hol15].

For an observation of a source region of angular extent Ω_{ON} with exposure t_{ON}, the number of events captured which appear γ-ray-like is N_{ON}. In addition, for an observation of a background region of angular extent Ω_{OFF} with exposure t_{OFF}, the number of captured events appearing γ-ray-like is N_{OFF}. Both N_{ON} and N_{OFF} are sampled from Poisson distributions with expectation values λ_{ON} and λ_{OFF}, respectively, e.g. $P(N_{ON}|\lambda_{ON}) = e^{-\lambda_{ON}}\frac{(\lambda_{ON})^{N_{ON}}}{N_{ON}!}$. A likelihood function is defined $\mathcal{L}(N_{ON}, N_{OFF}|\lambda_{ON}, \lambda_{OFF})$ as a product of two Poisson distributions and the parameters λ_{OFF} and N_γ are estimated by maximizing the likelihood for the two hypotheses, where N_γ corresponds to the number of γ-rays observed. A null hypothesis, $N_\gamma = 0$, assumes that $\tilde{\lambda}_{ON} = \alpha\tilde{\lambda}_{OFF}$, where $\alpha = \frac{t_{ON}\Omega_{ON}}{t_{OFF}\Omega_{OFF}}$. The alternative hypothesis implies that $N_\gamma \neq 0$ and $\lambda_{ON} = N_S + \alpha\lambda_{OFF}$. A test statistic is constructed based on the likelihood ratio

$$TS = -2\ln\left(\frac{\mathcal{L}(N_{ON}, N_{OFF}|\alpha\tilde{\lambda}_{OFF}, \tilde{\lambda}_{OFF})}{\mathcal{L}(N_{ON}, N_{OFF}|N_\gamma + \alpha\lambda_{OFF}, \lambda_{OFF})}\right)$$

in which $\tilde{\lambda}_{OFF}$ maximizes the numerator under the condition ($N_\gamma = 0$), while N_γ and λ_{OFF} unconditionally maximizes the denominator (allowing for $N_\gamma < 0$). A detection significance, $S = \sqrt{TS}$, is then produced through the use of Wilks' theorem, which states that the TS is asymptotically distributed as a $\chi^2(1)$ with one degree of freedom [Wil38]. Throughout this dissertation variations of this method of significance determination will be used, in which the probability density functions are not necessarily Poisson distributions and the number of nuisance parameters, such as λ_{OFF}, can vary.

For the case of the Li & Ma application, which is formulated for a single free parameter N_γ as described above, the calculations can be carried out analytically and result in

$$S = \sqrt{2}\left[N_{ON}\ln\left(\frac{1+\alpha}{\alpha}\left(\frac{N_{ON}}{N_{ON}+N_{OFF}}\right)\right) + N_{OFF}\ln\left((1+\alpha)\left(\frac{N_{OFF}}{N_{ON}+N_{OFF}}\right)\right)\right]^{1/2}.$$

In the regime of large numbers for N_{ON} and N_{OFF} counts, where the asymptotic condition of Wilks' theorem is satisfied, the null hypothesis can be rejected with a confidence $\beta \times 100\%$ where

$$1 - \beta = \sqrt{\frac{2}{\pi}}\int_S^\infty e^{-\frac{-x^2}{2}}dx = \frac{1}{\sqrt{2\pi}}\int_{TS}^\infty y^{-\frac{1}{2}}e^{-\frac{y}{2}}dy.$$

Figure 3.4: The VERITAS array at Fred Lawrence Whipple Observatory in Tucson, Arizona before (top) and after (bottom) the relocation of a telescope. Image taken from [Hol11].

Limits for a parameter of a one sided confidence region can also be determined, in particular, upper limits on the N_γ counts coming from the source. To acquire an upper limit of a parameter with a confidence level of $1-\beta$, the parameter is fixed to a value (the new null hypothesis) and a corresponding TS value is found. The parameter is then adjusted with a new TS value found until the corresponding significance satisfies the confidence level [RLC05].

3.2 VERITAS

The Very Energetic Radiation Imaging Telescope Array System (VERITAS) project consists of four 12m IACTs located at the Fred Lawrence Whipple Observatory (FLWO) on Mount Hopkins in Arizona (see Figure 3.4) [WBB02]. The VERITAS instrument response functions (IRFs) have changed across six qualitatively different epochs reflecting its construction and hardware state. To denote this evolution, VERITAS datasets are labeled from V1 to V6. For example, the datasets V1, V2 and V3 correspond to the construction and early operation

epoch of the observatory when telescopes were being added and commissioned. The first epoch of a fully constructed VERITAS with four telescopes, denoted as V4, began in Sep 2007 and lasted through Aug 2009. In 2009, one of the telescopes was relocated in order to expand the array collecting area and improve the stereoscopic reconstruction of events. This epoch, labeled V5, ended in Aug 2012 when the photo-multiplier tubes (PMTs) of cameras were upgraded to have a higher quantum efficiency, which increased photon collection by 50%. Since Sep 2012 VERITAS has operated in this state, denoted as V6.

The VERITAS IRF depends on the primary γ-ray energy as well as the various observing conditions such as telescope azimuth, elevation and night-sky background (NSB). VERITAS performs a stereoscopic reconstruction of VHE events in the energy range of approximately 100 GeV-30 TeV. For a 1 TeV primary γ-ray observed at an elevation of 70°, the array has an angular resolution of approximately 0.1°, an energy resolution of under 20%, and an effective area of $100,000$ m^2. The VERITAS sensitivity is such that a point source with a strength of 1% of the Crab Nebula, which is the standard candle in VHE astrophysics, can be detected at the 5σ level in less than 50 hours for the V4 epoch, and in less than 25 hours for the V6 epoch.

3.2.1 Hardware

3.2.1.1 Optical System

Each VERITAS telescope consists of a positioner which points the telescope to a given elevation and azimuth with an accuracy of 0.01° [Hol06]. Installed on the positioner is an optical support structure (OSS), which provides a base for the optical system to attach to. The telescopes employ a segmented Davies-Cotton (DC) optical system composed of 345 hexagonal mirror facets (see Figure 3.5). The mirrors have a spherical curvature with focal length 2F, arranged on a spherical surface of radius F and aligned towards the point 2F, where F is the focal length of the OS [DC57]. The DC configuration, which was originally

Figure 3.5: The VERITAS DC optical system with segmented mirror facets.

designed as a solar light concentrator, is convenient in that it utilizes identical, segmented, spherical mirror facets which are relatively inexpensive to produce, and the alignment of the mirror segments is simple. However, the design suffers from off-axis comatic aberrations and an asynchronous arrival time of photons. The time dispersion becomes significant when it is comparable to the quick Cherenkov flash; therefore the DC design limits the mirror diameter to roughly <15 m. The VERITAS telescopes have a mirror diameter of 12 m and a focal length of 12 m. Each segmented mirror has an area of approximately 0.322 m^2, resulting in a total mirror area of approximately 110 m^2. The mirror facets are aluminized and anodized to protect them from degradation [RIP08]. The resulting reflectivity curve of the mirrors is reasonably well matched to the transmission curve of the Cherenkov light, after accounting for absorption in the atmosphere. After alignment of the mirror segments, the optical point spread function (PSF) achieves an 80% containment radius of around 0.05° (10.5 mm) [MHK10].

3.2.1.2 Camera and Electronics

The VERITAS camera, located at the focal plane 12m from the mirror, consists of 499 pixels containing PMTs, each with an individual field of view of 0.15° resulting in a total camera field of view of 3.5° diameter. Dead space between PMTs is reduced with the use of Winston light concentrating cones. A PMT consists of a photocathode and a series of dynodes in order to generate a measurable signal in response to an incident photon. The peak quantum efficiency of the camera PMTs for the V4 and V5 array states was 18-22%, before being upgraded in 2012 to have an increased peak quantum efficiency of 32-34% [Kie13]. The analog output voltage from the PMTs is sent through an AC coupled preamplifier integrated with the PMT to increase the signal to noise ratio before it is sent through a long coaxial cable to the Flash Analog to Digital Converter (FADC) boards where it is sampled at a rate of 500 MHz (2ns digitization step size). The nominal conversion ratio is 0.128 digital counts per mV, where a single photoelectron has a pulse size corresponding to $4-5$ digital counts. In order to capture fluctuations about zero from caused by the variable NSB, a small baseline DC voltage is added ($\sim$ 16 digital counts) to the signal before digitization. This voltage is set to be just large enough to capture the expected negative fluctuations while retaining as much room as possible to avoid saturation in the FADC and achieve the maximum dynamic range. The signal is continuously digitized and temporarily stored in a circular buffer of size 64 μs, where it awaits instructions from the trigger system on whether the readout should be sent for storage or discarded. The relative PMT gains and pixel time delays are calibrated on a nightly basis for all four telescopes [Han07].

3.2.1.3 Trigger System

The VERITAS array has a three level trigger system which is designed to filter out light from sources other than γ-ray induced Cherenkov light [Wei08]. The frequent sources of noise include: the night-sky background (NSB), muon-generated local Cherenkov light, pedestrian

lighting, and electronics noise. The level one (L1) trigger occurs at the individual pixel level, and is designed to trigger when a PMT's output voltage quickly rises in correspondence with a Cherenkov flash of light. This is done with the use of a constant fraction discriminator (CFD) board, which accompanies each PMT pixel. The CFD uses three copies of the analog PMT output voltage. The first copy determines if the pixel should trigger by checking if the voltage pulse crosses a set threshold ($\sim$ 50mV) and fires if it does. The second and third copies determine the timing of the pulse. One copy is attenuated and the other is time delayed and inverted; then the two copies are combined and sent into to a zero crossing discriminator (ZCD) to extract the timing of the pulse.

The second level (L2) trigger is at the telescope level. The L1 triggers for each camera are monitored, and when a number of adjacent pixels (usually three) have an L1 trigger occur within a coincidence window of about six nanoseconds, an L2 trigger is made for that telescope. This trigger filters out NSB and individual PMT noise, since the triggering of these events are unlikely to be grouped on the camera.

The third level (L3) trigger occurs at the array scale, requiring at least two telescope L2 triggers to occur within some coincidence window, usually 50-100 ns. Timing delays from the shower geometry and signal travel time to the L3 trigger system are taken into account. This trigger provides a strong filter for muon-generated Cherenkov light since such events typically have a small spatial footprint. An L3 trigger then instigates a readout of the data buffer from the FADC boards for all telescopes to be saved to the database and later analyzed. During this readout time the telescopes stop taking data which results in a deadtime window, stressing the importance of the trigger system. The typical deadtime percentage for the VERITAS array is around 10% at an L3 trigger rate of 325 Hz.

The camera pixels are artificially triggered at a rate of 1 Hz in order to sample the baseline digital counts and quantify the light contamination. The average of these samples (the pedestal) and the RMS (the pedestal variance, or pedvar) are determined and incorporated into the event reconstruction.

3.2.2 Observations and Analysis

Standard VERITAS observations occur during the night either when the Moon is below the horizon, or dim ($< 10\mu$A in the PMTs). Non-standard modes of observation which account for a bright moon also exist, but are not used in the collection of data for this dissertation. Nightly observations are broken up into a series of runs customarily 30 minutes long. The weather can affect the event rate observed by the telescopes, and as such it is important to monitor the weather conditions. This is achieved with the use of a set of three far infrared (FIR) cameras and a light detection and ranging (LIDAR) system. Ultimately the observers who collect the data on site make an assessment of the weather in the form of a letter grade (A-F). Further quality control of the data is performed the next day, where instrument diagnostics are monitored and the weather status is reassessed.

The data analysis process begins by selecting quality runs to analyze. The standard criteria for a run to be considered quality is to have at least three functioning telescopes and a weather grade of B or higher. Once a set of runs is determined, the data must undergo a process of cleaning, reconstruction, and analysis to measure γ-ray counts from ON and OFF regions and determine a γ-ray detection significance or limits. The Eventdisplay software package is used for data analysis in this dissertation [MH18]. The processing and reconstruction of events is performed on individual runs with the output saved and usable for further high level analysis.

3.2.2.1 Event Processing and Cleaning

The FADC trace for a pixel is processed to determine the charge, a quantity which represents the amount of Cherenkov light which the pixel captured for the event. The profile of the FADC trace from the Cherenkov pulse has a steep climb and then decays quickly, all occurring within 12 ns after factoring in delays from asynchronous optics and geometrical effects. The pulses are processed in two steps. First, the pedestal is subtracted and the T_0 point is

found, defined as the 2 ns interval where the digital counts of the pulse rises above the half maximimum of the pulse. Second, the digital counts are integrated over six intervals (12 ns) starting from just before the T_0 point, resulting in the event charge. Alternative dynamical methods of charge determination relevant to the reconstruction of higher energy events with large impact parameter on the ground (which can last up to 100 ns or longer) exist but are not used in this dissertation.

Each triggered event in a run is "cleaned" before being reconstructed. Cleaning removes pixels that are not pertinent to the Cherenkov reconstruction, or events which cannot be reconstructed well. In order to identify these pixels, cleaning is done in steps. First the image pixels are identified, defined as the pixels with a charge greater than 5 pedvars above the pedestal. Then the border pixels are determined, defined as the pixels that are adjacent to an image pixel and with a charge greater than 2.5 pedvars above the pedestal. Image pixels without at least one associated border pixel are removed and the remaining image and border pixels make up the cleaned shower image (see Figure 3.6). A quality check is then made on the cleaned shower image to determine if it should be used for the event reconstruction. If the image is too dim, that is if the total charge of all pixels in the cleaned image is below a threshold value, typically 100-400 digital counts, it is not used. A second check is to remove images that have been truncated by the camera and result in a misguided reconstruction. If greater than 20% of the total charge is contributed from pixels on the border of the camera, the image is not used. This truncation and removal of events due to the finite camera size results in a nonuniform probability of events being observed which depends on both an event's energy and distance from the pointing direction.

3.2.2.2 Event Reconstruction

After the Cherenkov images have been cleaned and filtered, a moment analysis is performed on the surviving camera pixels following Hillas' method (see Figure 3.7) [Hil85]. The zeroth moment, called the image size, is the sum of charges in the surviving pixels. The first moment

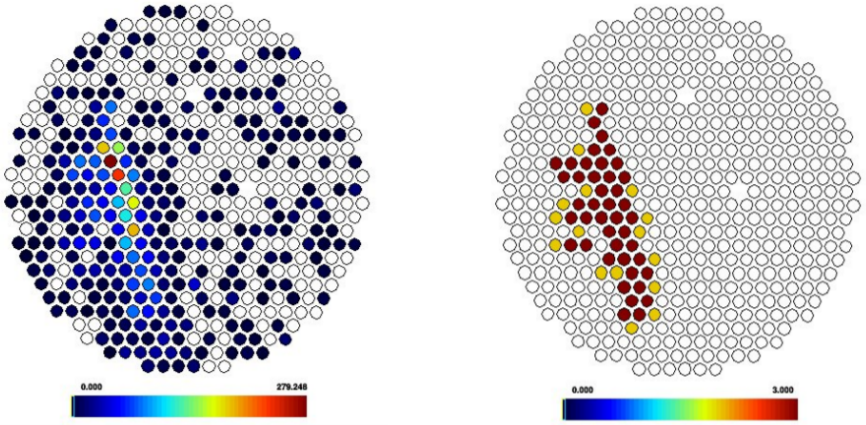

Figure 3.6: An example of a triggered shower before (left) and after (right) image cleaning. The color scale of the pre-cleaned pixels displays the digital counts for that pixel, while the post-cleaned pixels have a color corresponding to whether the pixel is an image (red) or border (yellow) pixel.

gives the centroid position of the image, and the distance is defined as the separation between the centroid and the camera center. The image pixels are fit to the shape of a two dimensional ellipse, and the second moments are determined with respect to the major and minor axis of this ellipse, called the length and width, respectively. The angle of the major axis of the ellipse is then used by multiple telescopes to perform a stereo reconstruction of the Cherenkov shower. The arrival direction of the shower is determined by superimposing the ellipses determined for each telescope onto the camera coordinates and tracing the intersection points of the major axis. Since there are $\binom{N}{2}$ intersection points for N included telescopes, a weighted average is performed. The weight factor for the intersection of telescopes i and j typically used is

$$w_{ij} = \sin(\theta_{ij}) \left(\frac{1}{S_i} + \frac{1}{S_j} \right)^{-1} \left(\frac{w_i}{l_i} + \frac{w_j}{l_j} \right)^{-1}$$

where θ_{ij} is the angle between the major axes of telescopes i and j, S_i is the size for telescope i, and w_i, l_i are the width and length, respectively, for telescope i. The shower core position,

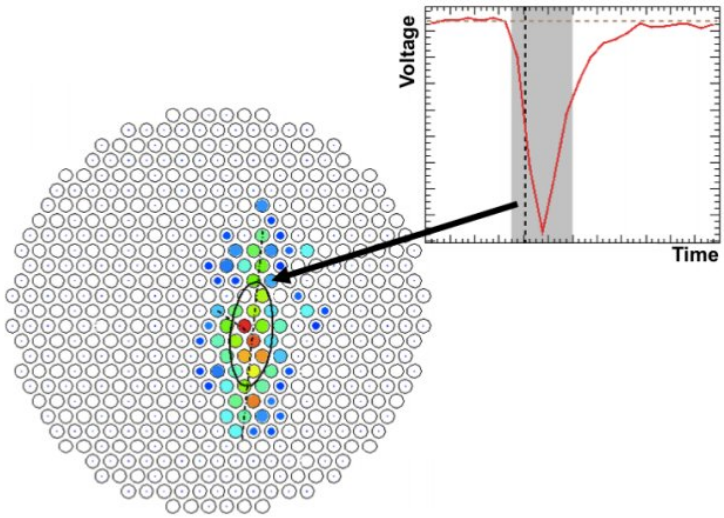

Figure 3.7: A cleaned telescope image which has been cleaned and parameterized. The PMT trace for a single pixel is shown in the sub plot. The vertical dashed line represents the T_0 point, and the voltage is integrated over the shaded region to determine the pixel's charge. Image taken from [Hol15].

the location on the ground that the primary γ-ray photon would have hit had it not cascaded, is also determined by superimposing the ellipses in the shower plane coordinates instead of the camera coordinates (see Figure 3.8). The impact parameter is then determined for each telescope, defined as the distance from the core position to the telescope projected into the plane perpendicular to the shower axis.

Energy reconstruction of the primary particle for a given image size and impact parameter is found with the use of lookup tables produced from Monte Carlo simulations. The simulations model the VERITAS instrument response functions (IRFs), and are generated for a variety of observing conditions (including NSBs, telescope elevations and azimuths, and incident angles). Monte Carlo simulations are also performed for incident hadronic particles, which make up over 99% of all Cherenkov showers that trigger VERITAS. The simulations reveal that γ-ray showers are imaged with an elongated, narrow shape while hadronic showers are imaged as relatively shorter and bulkier. In order to remove many of the hadronic

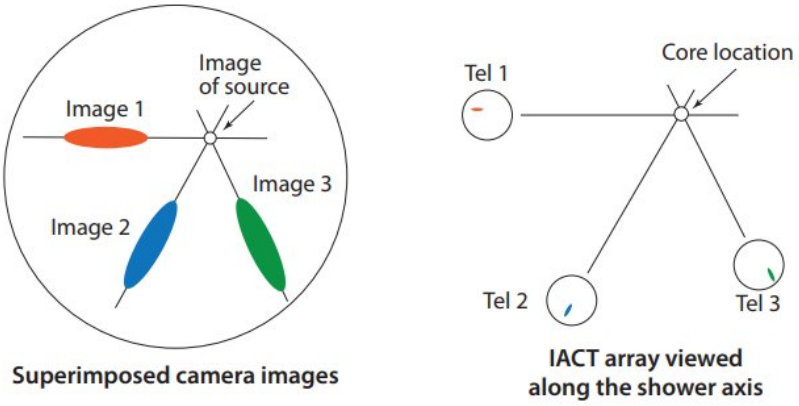

Figure 3.8: Left: The arrival direction of the shower is determined by superimposing the parameterized ellipses and intersecting the major axes. Right: The location where the shower core would have impacted the ground is determined by intersecting the major axes of the ellipses in the shower plane coordinates. Image taken from [DHH97].

showers, the images are characterized by two shape parameters: the mean scaled width (mscw) and mean scaled length (mscl). The mscw and mscl of an event are defined as

$$mscw = \frac{1}{N}\sum_{i=1}^{n}\frac{w_i - \bar{w}(S,D)}{\sigma_w(S,D)}$$

$$mscl = \frac{1}{N}\sum_{i=1}^{n}\frac{l_i - \bar{l}(S,D)}{\sigma_l(S,D)}$$

where N is the number of telescopes included in the analysis, and the simulated means and standard deviations $\bar{w}(S,D)$ and $\bar{l}(S,D)$ are the simulated mean width and length, respectively, for a given image size (S) and impact parameter (D), with $\sigma_w(S,D)$, $\sigma_l(S,D)$ being the simulated standard deviations. A simple "box cut" is performed which removes events with a mscw or mscl outside of an acceptable range associated with γ-ray events, typically being $-1.2 \leq mscw \leq 0.35$, and $-1.2 \leq mscl \leq 0.7$ (see Figure 3.9).

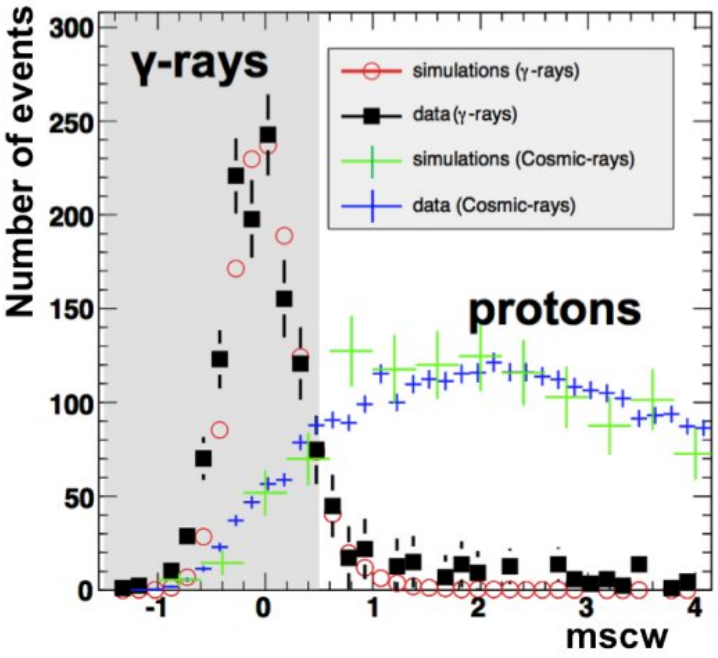

Figure 3.9: Distribution of mean-scaled widths for γ-rays and hadrons from simulated and real data. Events outside of the shaded region are discarded. A similar cut is also performed in the length parameter space. Image taken from [Hol15].

3.2.2.3 Background Determination Methods

A final discrimination on hadronic events is performed by defining the ON region where the expected γ-ray signal is coming from to a restricted solid angle in order to maximize the signal-to-noise ratio. This θ^2 cut, which is only applicable for compact sources for which angular extent does not significantly exceed the angular resolution of VERITAS, provides a strong reduction in background events from isotropic cosmic rays. After the sequence of cuts to remove hadronic-like events, there still remains a large number of events induced by primary particles other than source γ-rays. These background events consist primarily of electromagnetic showers from a primary electron or positron, and hadronic showers which appear γ-ray-like due to a strong electromagnetic component developing early in its shower. In order to extract a signal from the source, a sampling of the background rate is necessary. This is performed by observing background regions where no γ-ray signal expected, in addition to the source region. A significance calculation is then performed as described in Section 3.1.4.

The background region should be chosen to match the observing conditions of the source region as closely as possible to avoid introducing systematic errors. There are two conventional methods for selecting the background regions for compact sources: the reflected region (RR) method and the ring-background (RB) method (see Figure 3.10). Both methods measure the source and background regions simultaneously within a single observation, providing the major benefit of ensuring that the observing conditions are identical while requiring no additional observing time.

For the RR method, a compact source is observed in "wobble" mode with a slight pointing offset (typically 0.5°), such that the field of view contains multiple background regions of equal distance from the pointing direction and of the same size as the source region. This method assumes that the reflected regions are source-free. Since the background and source regions have equal area and are at equal distances from the pointing direction, no correction

is needed for the nonuniform probability of measuring events at different distances from the pointing direction. The RR method is not applicable for observations that are pointed directly at the source. The RB method uses an annulus around the source, with an adjustable inner and outer radii, as the background region. Unlike the RR method, the RB method is affected by the nonuniform probability of detecting events at different distances from the pointing direction, and an estimated correction is applied. However, the RB method can potentially use more of the telescope's field of view when generating a prediction.

Both RR and RB methods are not applicable for γ-ray sources which have an angular extent that is large compared to the γ-ray PSF of VERITAS, and for sources which have an unknown morphology. For especially extended sources which have an angular extent that exceeds the VERITAS field of view, a signal and background measurement cannot be simultaneously made. Therefore, for extended objects such as the Coma GCl, which is studied in this dissertation, an alternative background method is needed. Such a method is developed in chapter 4.

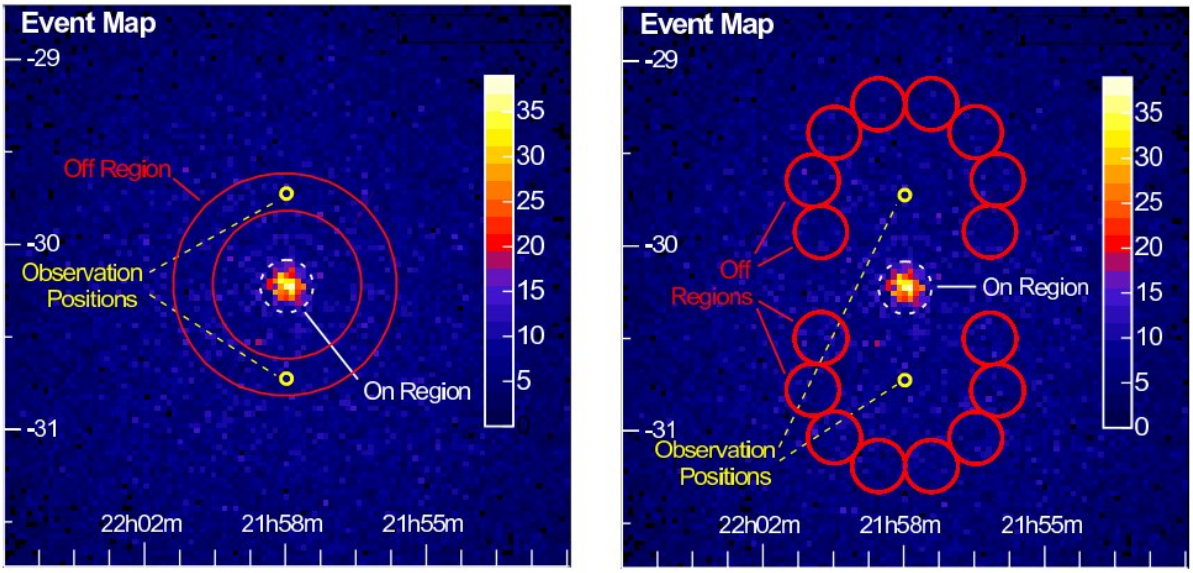

Figure 3.10: The ring-background (left) and reflected region (right) background prediction methods depicted on the γ-ray source PKS 2155-304. The solid angle contained within the solid red lines are the regions where background measurements are made, and the source region is contained in the dashed white line. Image taken from [BFH07].

CHAPTER 4

Data Analysis of the Coma Galaxy Cluster Extended Field

The genuine γ-ray signal in IACT data is masked by the overwhelming background of cosmic rays (CRs). Consequentially, the conventional approach to analyze sources with relatively small angular extension, with a characteristic angular scale considerably smaller than the field of view of the IACT, is a two stage process. First, the background is reduced by the application of cuts, collectively called "shape cuts", which capitalize on the differences between hadronic and electromagnetic cascades. The remaining sample of γ-ray-like events is still largely contaminated by CR initiated cascades, which can be hadronic or electromagnetic in origin. To detect compact sources, an excess of event counts is determined by comparing the integrated counts from the region where the putative source is located, and from a source-free region in the same observation field. Two conventional techniques for the background determination are typically used, known as the ring-background method and the reflected region method (see Section 3.2.2.3).

An IACT array acceptance is a function which represents the probability of an event being triggered and successfully reconstructed. The VERITAS acceptance is dependent on the angular distance from the pointing direction, especially beyond the central 1°. The implementation of the ring-background method requires knowledge of this angular acceptance, since the CR-induced γ-ray-like background for this method is sampled at different angular distances. The reflected region method utilizes the axial symmetry of the radial acceptance and therefore does not require the exact knowledge of this function at the cost of

a larger relative statistical error since the axial-symmetry-constrained region for background determination is limited in the field of view. The ring-background method was used in the original VERITAS publication to test several hypotheses of $\leq 0.4^\circ$ radius γ-ray emission in the Coma GCl [AAB12]. This method is dependent on the putative source morphology and the null detection conclusions of the paper are valid only under the assumption that the Coma GCl emission is limited to a $\leq 0.6^\circ$ radius region around the cluster center. Given that the evidence for the virial shocks has been claimed [KKL17] at radii larger than 0.6° based on the skymap provided in this publication, it is essential to design a new analysis method which could verify the presence of such an emission in the the entire field of view of VERITAS.

This chapter describes a non-conventional data analysis which was specifically developed to evaluate the existence of γ-ray emission with a very large angular extension (possibly larger than the VERITAS IACT field of view) in the Coma GCl field utilizing a number of mosaic pointings using VERITAS V4 and V6 data.

This analysis can be viewed as an elaborated version of what is known as the "matched runs" method in which a large set of archival VERITAS observations is used to estimate the CR induced γ-ray-like background from believed source-free observation fields with matched observational conditions. Unfortunately, the variations of these observing conditions inevitably introduce a systematic error into the analysis due to the fact that the background counts are no longer sampled from the same field of view as the source region. Data selection and calibration procedures utilizing the isotropic CR signal are purposely developed to reduce the magnitude of the residual variance and bias introduced by this method. To correctly evaluate the significance of detection in this method, the residual systematic variance is determined, and the associated mathematical procedures based on the maximum likelihood methodology have been developed to combine this variance with the Poisson count variance to generate a corrected significance.

The mosaic of VERITAS observations over the Coma GCl field is unprecedentedly large

($\sim 5^\circ \times 5^\circ$) meaning that with a total exposure of ~ 20 hours in V6 data, the exposure per ($\sim 0.2^\circ \times 0.2^\circ$) sky bin is expected to be small, non-uniform and have limited sensitivity within each bin. With this limitation in mind, an attempt is made in this dissertation to search for the presence of a γ-ray signal in the form of deviations in the significance distribution of individual sky bins associated with the specific theoretically motivated emission regions in the sky [KKL17, PP10].

In addition to the creation of a significance sky map, a single significance is generated over integrated solid angle regions corresponding to the two theoretically motivated emission morphologies. Given that the γ-ray emission from the Coma GCl has a potentially unprecedented extension for a detection by IACTs so far, this strategy provides the most sensitive tool to test a few specifically motivated morphologies of VHE γ-ray emission without diluting the methodology by the large trial factors.

There is one important consideration in designing the VERITAS data analysis chain which is uniquely adopted in this dissertation. Namely, an effort is made to design an analysis of the excess counts in each sky bin or in an integrated sky bin over a given morphology to be independent of the VERITAS angular acceptance function. Instead of re-scaling background values based on the VERITAS angular acceptance function, the background is assembled from source-free observational fields exactly mocking the real observations of a given sky bin or integrated region in the Coma GCl. This procedure dramatically reduces potential errors in the excess count determination, which is the motivation for this strategy. Once a significant number of excess counts is established with confidence, then a determination of the extended γ-ray source's flux properties can be made with the use of the VERITAS acceptance function. However, these considerations are treated as a task of future analysis development and is not considered in this dissertation.

Finally, at the end of this chapter the Coma GCl member galaxy Dragonfly 44 is analyzed as a potential Dark Matter candidate source.

4.1 Analysis of Extended Emission in the Coma GCl

In VHE γ-ray astronomy the overwhelming majority ($> 99\%$) of triggered events originate from the isotropic cosmic ray background. A small percentage ($< 10\%$) of these cosmic-ray-originated events appear like γ-ray events, either because a strong electromagnetic branch develops early on in the hadronic shower or because the primary particle is actually an electron. In this analysis these events which appear like γ rays are called *γ-ray-like* events, and the remaining cosmic-ray events are called *cosmic-ray-like* events. In order to measure a source region's γ-ray emission, a measurement of the background is necessary. Then a significance can be determined from the excess counts above the background level as was described in Section 3.1.4.

The acceptance of VERITAS depends on the various conditions in which the array operates, and therefore a background measurement made with a different acceptance than the source measurement contains both a bias error of mean value and an increased variance. Typically, as with observations of compact sources, the telescope field of view simultaneously contains the source region and source-free background regions, commonly called ON and OFF regions, respectively, which allow for a sampling of the background with nearly identical observing conditions, and thus acceptances. This strategy is incompatible with an analysis of an angular extended source such as the suggested virial shock emission in the Coma GCl, which has an angular extension within and beyond 5°. The analysis presented in this thesis develops a method to estimate the background over the full field of view of Coma GCl observations using a large collection of archival VERITAS data. This method inevitably introduces a systematic error in the background estimation because of the different acceptances of the data. The principle contributors to the variations in run acceptance are: weather conditions, telescope pointing direction (elevation and azimuth), night-sky background (NSB) brightness affecting the pedestal variation (pedvar), and different configuration and hardware states of the telescope array. The mechanism through

which these parameters affect the acceptance is described later in this chapter. In general cosmic-ray-like and γ-ray-like events have different acceptances, due to their different image shapes, which are affected differently by these parameters.

The VERITAS acceptance is also dependent on the energy of the primary particle through a variety of mechanisms. The telescope trigger plays a critical role in the detection of low energy events; for example, low energy showers which are just bright enough to trigger the data readout can elude detection if the Cherenkov light is attenuated, either by cloudy weather or an increased atmospheric depth at lower pointing elevations. The acceptance is also sensitive at higher energies. In general higher energy showers are more likely to have larger shower images recorded on the camera plane, since more pixels will trigger on the brighter Cherenkov shower. As the energy of the primary particle becomes larger, and the shower becomes brighter, there is a greater chance that the shower will be detected partially outside of the camera field of view and be truncated, in which case the event will be discarded during the image cleaning stage of the event reconstruction. Since the acceptance is energy dependent, this analysis is performed on energy binned sets of data. The set of data is divided into three equal logarithmically-spaced energy bins per decade, with four total energy bins analyzed starting from 215 GeV up to 4.64 TeV. In addition, a set of data over the full energy range considered ($0.2 - 4.6$ TeV) is analyzed.

The first step of the analysis procedure presented in this chapter is to apply the "matched runs" method by evaluating the notable acceptance-affecting observing parameters of the available Coma GCl data. With the balance in mind of maximizing exposure while constraining the acceptance-sensitive parameter space, a cut range is defined for all considered parameters which results in a large range of pointing elevations surviving the selection process. The archival VERITAS data which survive these cuts have their solid angle which contains sources removed and are considered source-free runs. The selection details, including descriptions of the mechanisms through which the considered parameters affect the VERITAS acceptance, is explained in Section 4.1.1.

After the conventional "matched runs" method is performed, the systematic error, both bias and variance, caused by the different acceptances in still varying observing conditions is known to be substantial. The analysis method developed in this dissertation further builds on the "matched runs" method by using the cosmic-ray-like events as a calibration source of the individual observing run acceptances. The calibration procedure consists of two steps. First, a linear regression is performed to correct for the dependence of the cosmic-ray-like acceptance on pointing elevation. Then, once the elevation bias has been removed, an attenuation calibration is performed by matching the cosmic-ray-like event rate above a cutoff energy for all runs. The adjustment of the cosmic-ray-like event rate for each run is made by modifying the gain of the telescopes in the data processing software, which has the effect comparable to adding or removing a neutral density filter to the cameras. The procedure is iteratively applied until settling on the targeted cutoff energy, defined by applying the same procedure to the Crab Nebula, the standard candle in VHE astronomy. Since the event rate of cosmic-ray-like events is approximately independent of a real γ-ray source in the field of view, this procedure has the major advantage of being able to simultaneously calibrate both the Coma GCl runs and the source-free runs. After this attenuation calibration on cosmic-ray-like events is performed, only the γ-ray-like events are considered, which are selected by the application of the "shape" cuts. A pointing elevation dependence is expected for the γ-ray-like event rates and the same linear regression procedure used on the cosmic-ray-like events is performed on the γ-ray-like events using only the source-free data, and all (Coma GCl and source-free) runs are corrected to remove potential bias. The calibration procedures outlined in this paragraph are explained in Section 4.1.2.

The acceptance is dependent on the event's position in the camera field of view with respect to the pointing direction. A major contributor to this dependence is the truncation of images at the edge of the camera which are subsequently rejected during image reconstruction. This dependence can be characterized predominantly by the angular distance from the pointing direction, with a minor second order dependence on the axial angle due to elevation

across the camera field of view. The second order correction is negligible for a single run, but it becomes important when considering large solid angles and exposures which this analysis incorporates. A linear regression is performed and a relatively small elevation ("Y-position") correction is made by weighting the events (typically $\sim 5\%$ in magnitude). The remaining angular acceptance depends only on the radial distance from the pointing direction. Since this analysis uses the full VERITAS field of view (up to $\sim 1.9^\circ$ in radius considered), and the angular acceptance rapidly decreases past the central 1°, measuring and correcting for the angular acceptance would introduce significant errors in determining the background. Instead, events and exposures are binned in their radial distance from the pointing direction. For a given solid angle in the Coma GCl region the angular binned amount of exposure each Coma GCl run has in the region is determined, defined as the exposure profile, which is mocked by the source-free runs to determine a background measurement. The angular acceptance considerations are explained in Section 4.1.3.

Since a defined exposure profile corresponds to its measured ON counts, the same exposure profile assigned to source-free runs can produce a measurement of the background. Given that the available source-free dataset has many more runs than the Coma GCl dataset, multiple samples of the background can be created. A significance is then determined using an adapted probability density distribution function which is modeled to incorporate a residual variance. Details of generating background measurements and computing a significance of the excess counts are explained in Section 4.1.4, which completes the description of the method. The method is then applied to the available Coma GCl data in two ways. First, skymaps are produced with significances determined for square solid angle bins, and the distribution of the skymap bin significances can be evaluated. Second, two specific Coma GCl γ-ray emitting morphologies are tested by creating a single solid angle bin which traces the tested region and a corresponding singular significance is determined. Both methods are applied in Section 4.1.5 and the results are presented.

4.1.1 Data Selection

VERITAS has observed the Coma GCl region over two campaigns. The first set of observations occurred in the Spring of 2008, during the V4 configuration epoch of VERITAS. A second set of observations occurred more recently, in the Spring of 2017 and again in 2019 and 2020, both under the V6 configuration epoch of VERITAS. The V4 and V6 epochs have qualitatively different array configurations: the layout of the telescopes and the γ-ray camera are significantly different between epochs. Many of the procedures applied in this analysis are nontransferable between epochs and therefore this analysis is performed independently for both V4 and V6 epochs.

In order to select VERITAS runs which are suitable for a background estimation, having similar observing conditions as the Coma GCl runs, the Coma GCl dataset is first evaluated and constrained. The primary parameters expected to affect the VERITAS acceptance include the number of active telescopes, weather during observation, telescope pointing elevation and azimuth, and the pedvar level corresponding to the brightness of the sky during observation. For each parameter considered, its effect on the acceptance is described and a restriction is made.

The VERITAS acceptance is greatest under the ideal weather conditions of clear skies. The weather conditions for each run are examined by the observers and a letter grade is assigned based on their assessment. In addition, throughout the run far infrared (FIR) measurements are made towards the pointing direction to detect the cloud coverage by measuring the temperature of the night-sky. The RMS variation of the FIR measurements is determined for the run and converted into a letter grade (values of 0.3° C or lower are given A or B grades). Evaluation of the cloud coverage is critical; the presence of clouds in the atmosphere reduces the amount of light collected by the telescope and correspondingly reduces the trigger rate of the telescope array, as events which have a brightness just above the trigger threshold dip below it, and are irrecoverably lost. While the absent data preferentially

affects lower energy events, a subset of high energy events with large impact parameters is also affected. In general, worsening weather conditions lowers the acceptance across all energies unequally. The inclusion of data from all weather conditions would introduce large, energy dependent variations in the acceptance, while restricting the data to only ideal weather conditions would significantly limit the working exposure. In consideration of balancing these two factors, the threshold of a weather grade of "B" or better for *both* evaluations (observer assessment and FIR RMS) is decided. This threshold retains most ($> 80\%$, 40 hours) of the Coma GCl exposure while limiting the variations in acceptance due to poor weather. All Coma GCl observations were taken in the Winter atmosphere (ATM 21). Since only a few Coma GCl observations ($< 4\%$) occurred with fewer than four operating telescopes, only runs with four operational telescopes are included in this analysis.

The telescope pointing direction also affects the acceptance in an energy dependent way. When pointed at zenith, observed events travel through the smallest distance of the atmosphere. As the pointing elevation of the telescopes lowers, two effects occur: the footprint of the Cherenkov light pool increases as the propagation distance increases, and the attenuation of the Cherenkov shower increases. The result is that at lower pointing elevations, there is an increase in the effective area of the telescope and a decrease in sensitivity to events, especially lower energy events. In addition, the azimuth of the pointing direction also affects the acceptance. The array is not azimuthally symmetric (especially in the V4 epoch), meaning the stereoscopic sensitivity and resulting impact parameters change as the telescopes move across azimuthal pointing directions. A second azimuthal effect is caused by the Earth's magnetic field, which points from South to North with an inclination angle of 58° downwards at the VERITAS location. Electrons and positrons in the Cherenkov cascade are traveling perpendicular to the magnetic field when the telescope is pointing North, and parallel when pointed South. For this reason, as the azimuth direction points closer towards North, the Cherenkov shower broadens and is more likely to be truncated in the camera field of view, making event reconstruction less likely. The available Coma GCl observations are

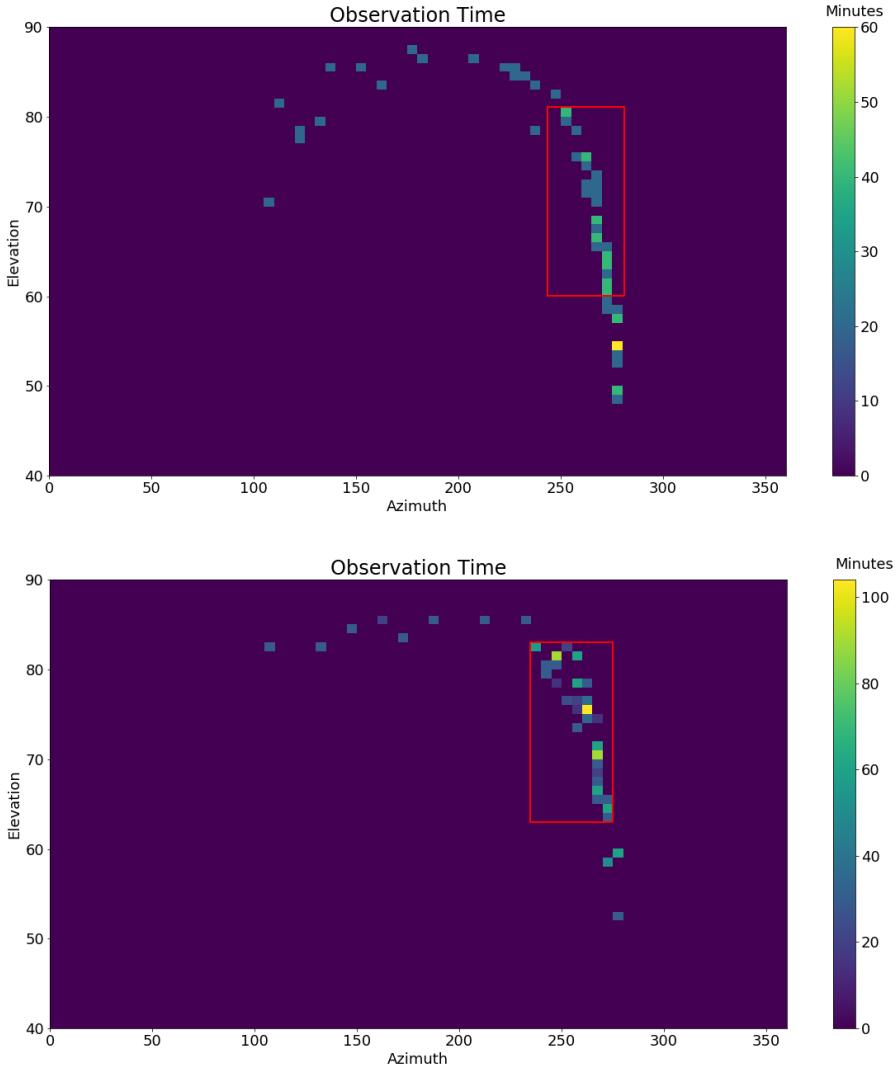

Figure 4.1: Available Coma GCl exposure by VERITAS for the V4 (top) and V6 (bottom) epochs with four operating telescopes and A or B weather. The x and y axes correspond to the pointing azimuth and elevation in degrees, respectively, where the VERITAS azimuth coordinate system runs clockwise from the North direction. The bin increments for elevation and azimuth are 1° and 5°, respectively. The red boxes highlight the telescope pointing cuts made, such that the selected observations are constrained to have similar observing conditions without the loss of excessive exposure.

analyzed and cut such that the pointing effects are consistent (the selected cuts for V4 and V6 are shown in Figure 4.1).

Another selection is made on the available data by filtering by average observation pedvar. The NSB varies across different regions of the sky, being brightest for pointings towards the Galactic Center and dimmest when pointing orthogonal to the Galactic plane. The NSB is also affected by weather conditions, moonlight brightness, and other forms of light pollution during observations. The image cleaning process uses the measured pedvar value in determining which pixels to retain. Since the pedvar, and thus the image cleaning process, is dependent on the brightness of the sky, the observations used in this analysis are restricted to a limited range of run-averaged pedvars. The pedvars of the Coma GCl observations are found to occupy narrow range of values, as shown in Figure 4.2, and therefore no Coma runs are removed on the basis of pedvar.

Once the range of observing conditions containing the Coma GCl data is defined, VERITAS archival observations which are within this range are selected to be used as background runs, hereafter called source-free data (field of view regions containing real or potential sources are removed). The amount of remaining exposure of the Coma GCl in the V4 and V6 epochs totals to 10.0 and 18.6 hours, respectively, and of source-free observations amounts to 37.7 and 116.5 hours, respectively. The restriction of the observing conditions presented thus far attempts to constrain the data to similar observing conditions and limit the bias and residual variance introduced from combining data from different observations, and the calibrations presented in the following sections aim to further reduce these systematic errors. The residual variance is modeled into the likelihood estimation under the assumption that the remaining acceptances, and thus event rates, are normally distributed (explained in detail in Section 4.1.4). This assumption is observed to be satisfied for data taken with the same instrument hardware, but it is not true over time periods where a significant, qualitative modification occurred to the hardware of the telescope array. For example the V4 and V6 array epochs have different telescope layouts and γ-ray cameras, and therefore

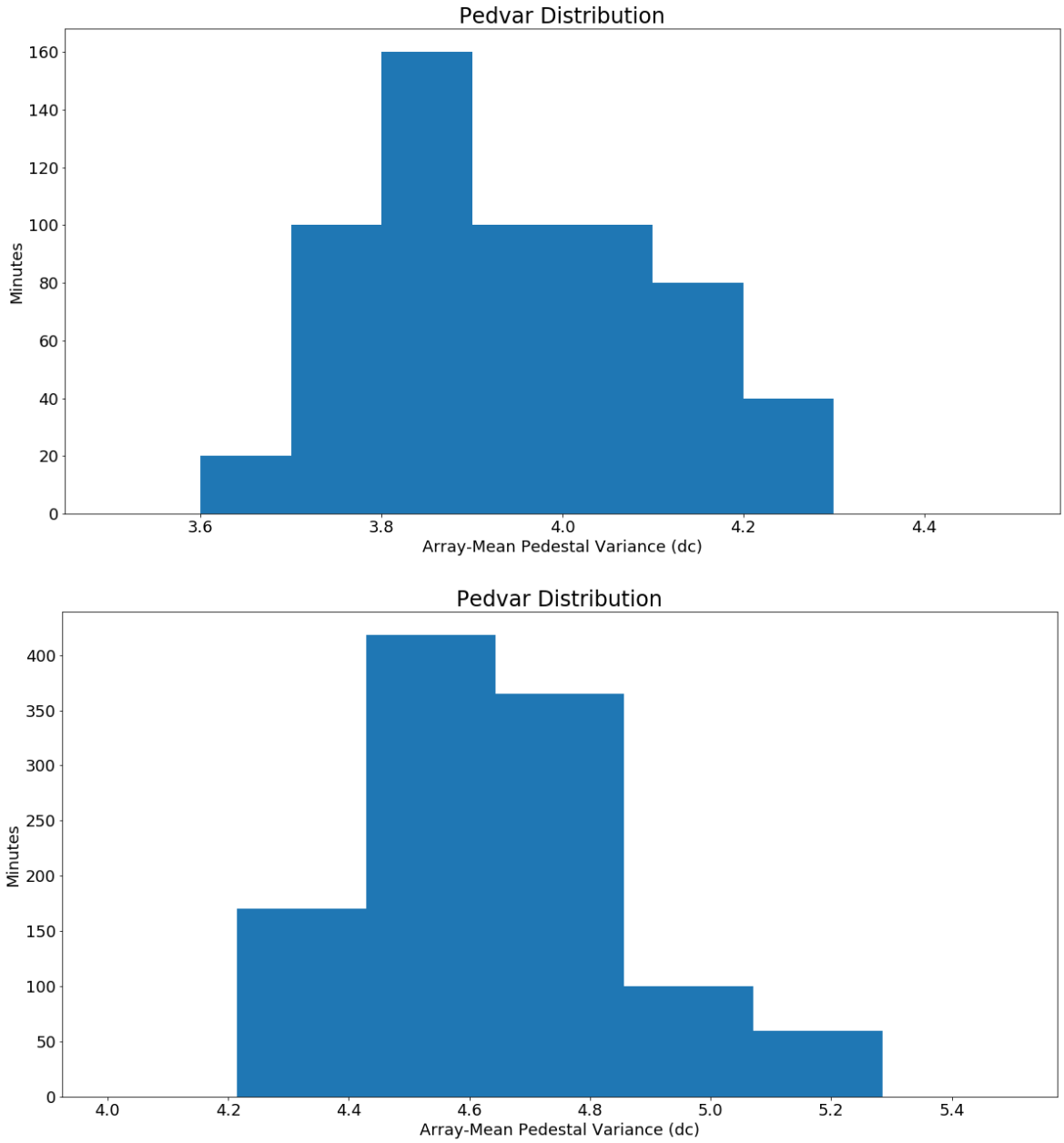

Figure 4.2: The resulting pedestal variance (pedvar) distributions of V4 (top) and V6 (bottom) Coma GCl observations after performing the elevation and azimuth selection. Since the distributions are already well constrained, therefore no additional pedvar selection is made on the Coma GCl observations. The background data selection requires V4 and V6 runs to have pedvars within the ranges shown.

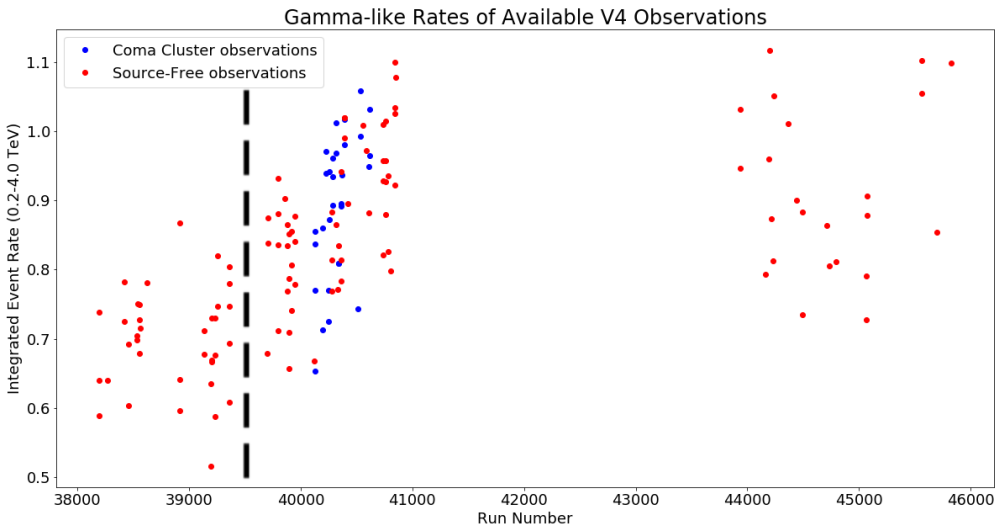

Figure 4.3: A scatter plot of the mean γ-ray-like event rates (in Hz) above 215 GeV for individual V4 runs passing the selection criteria after calibrations (described later) are performed. Energies below 215 GeV are not considered in this analysis because of their sensitivity to trigger effects. Coma GCl runs are shown in blue, while the source-free runs are shown in red. A jump in the calibrated rates can be seen between the runs before and after 39500 (marked by the dashed line) when significant hardware changes to the VERITAS array occurred, and therefore the runs before this date are removed from the source-free dataset. Note the gap in the data points is because these runs have an increased night-sky brightness (pedvar) value at the selected elevation and azimuth range.

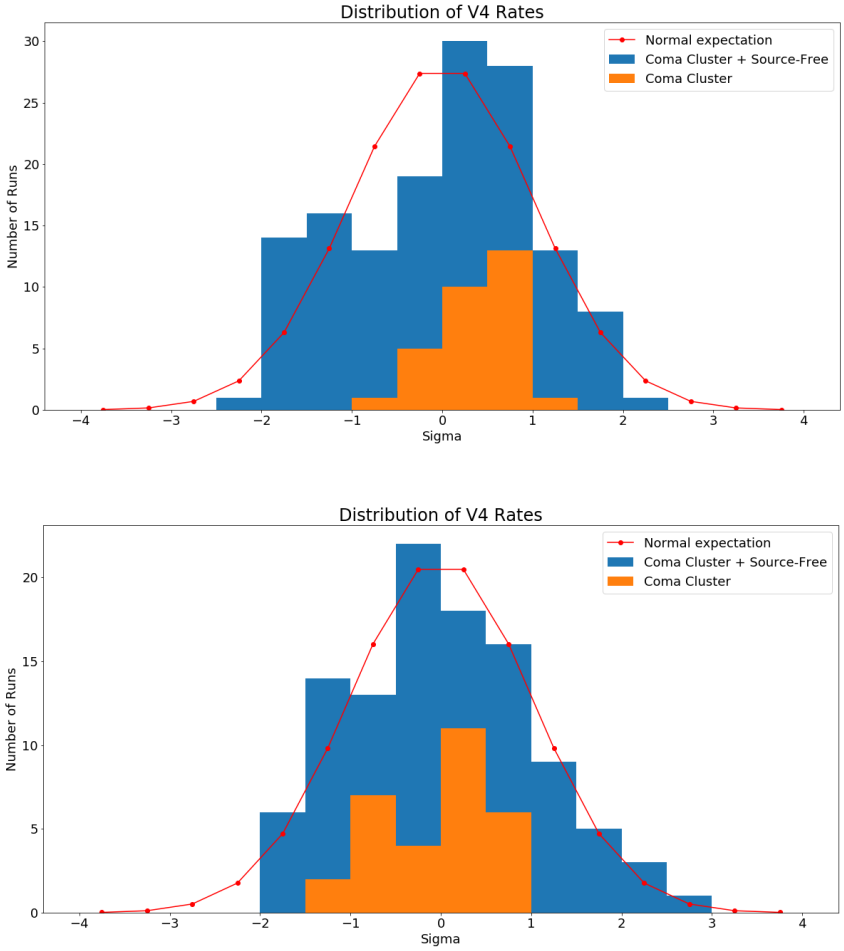

Figure 4.4: Histograms of the γ-ray-like event rates for V4 runs after calibrations (described later) are performed, before (top) and after (bottom) the outlier runs (runs before 39500) are removed. The event rate mean and standard deviation is determined for the dataset containing both Coma GCl and source-free runs, and the histogram is created in reference to these parameters with the red line displaying the normal distribution. The Coma GCl observations are shown in orange and the combined Coma GCl and source-free runs are shown in blue. The distribution of source-free runs is more representative of the Coma GCl distribution after the outlier runs are removed. Note that the mean and standard deviation changes between plots, since it is computed before and after the outlier runs are removed.

there is a qualitative difference in their data. A similar shift in the array acceptance caused by hardware changes is observed within the V4 epoch. In early 2008, 10 months after the VERITAS first light, numerous hardware upgrades and alterations were made, including a replacement of the L2 trigger system. The resulting array acceptance drastically changed around this time, shortly before the Coma GCl observations were performed, as can be seen in Figure 4.3. Even after the calibration procedures are performed on the data, the rates of the hardware-altered runs remain distinguished from the rest of the data. Therefore, in order for the source-free data to be representative of the Coma GCl data and obtain an approximately normal distribution of acceptances, the outlier runs are removed (see Figure 4.4). For the V4 data, runs before MJD 39500 are removed, which correspondingly reduces the source-free run exposure from 37.7 hours to 25.7 hours. The V6 rates, seen in Figure 4.5, do not have any obvious shifts in acceptances or significant hardware changes, and therefore no V6 observations are removed. Table 4.1 summarizes the list of observing conditions that are used to filter the data in conjunction with the accepted range, as well as the remaining exposure on the Coma GCl observations and the available exposure of source-free data.

4.1.2 Data Calibration

After the source-free runs are selected, they are processed with the Eventdisplay analysis software with the default cut parameters [MH18]. A trace summation window of 6 samples is used (2ns samples for a total of 12ns) for both V4 and V6 data to determine the charge (measured in digital counts) for each pixel. Camera images are then cleaned and the events are reconstructed geometrically (standard), with the requirement that at least two telescopes observe an event to be retained. The "standard" box cuts are performed on the surviving events, where the determined MSCW and MSCL are used to classify the event as either γ-ray-like or cosmic-ray-like (see Table 4.2 for a description of the standard cuts). The collection of event properties (image brightness, impact parameter, pointing elevation, etc.) are input into a simulation-derived lookup table to determine the primary particle's energy

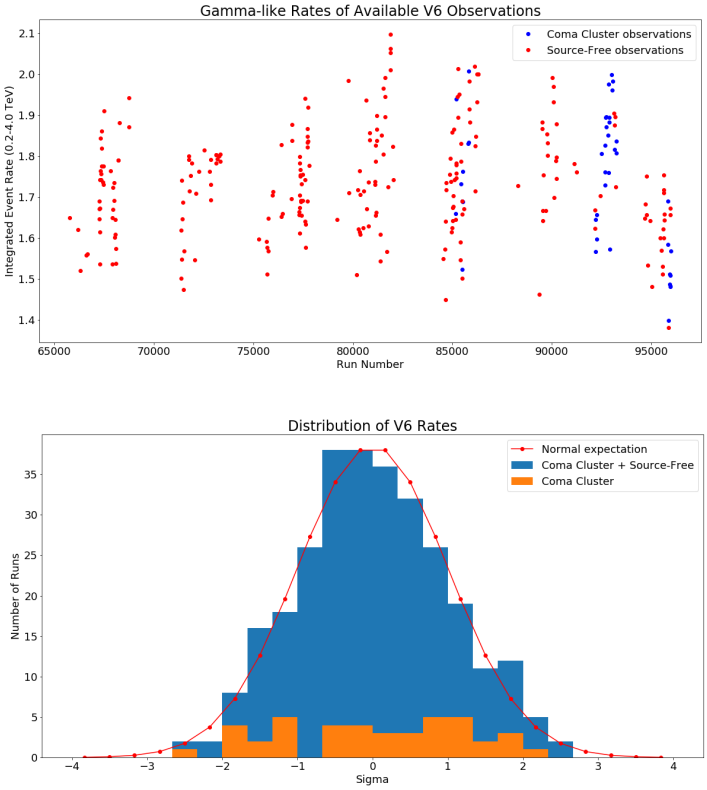

Figure 4.5: Top: A scatter plot of the mean γ-ray-like event rates (in Hz) above 215 GeV for individual V6 runs passing the selection criteria after calibrations (described later) are performed. Coma GCl runs are shown in blue, while the source-free runs are shown in red. Bottom: Histogram of the γ-ray-like event rates for V6 runs after calibrations are performed. The event rate mean and standard deviation is determined for the dataset containing both Coma GCl and source-free runs, and the histogram is created in reference to these parameters with the red line displaying the normal distribution. The Coma GCl observations are shown in orange and the combined Coma GCl and source-free runs are shown in blue. The distribution of rates of the source-free runs are approximately centered with respect to the Coma GCl runs, however the dispersion is not the same. While the variances of the Coma GCl and source-free runs are expected to match with more data, the discrepancy seen here may result in an overestimation of the significances later calculated which are based on a likelihood ratio with one degree of freedom.

Table 4.1: Observing Condition Selections

	Epoch	
	V4	V6
Minimum Run Duration	10 min	10 min
Weather Grade	A/B	A/B
Number of Telescopes	4	4
Pointing Elevation	$60° - 81°$	$62° - 82°$
Pointing Azimuth	$245° - 280°$	$235° - 275°$
Pedvar	$3.5 - 4.4$	$4.2 - 5.3$
Selected Coma Exposure	10.0 hr	18.6 hr
Selected Source-Free Exposure	25.7 hr	116.5 hr
Selected Crab Exposure	4.9 hr	7.9 hr

under the assumption that the event originated from a γ-ray primary. The mean deadtime of each run is measured ($\sim$10%), which is the percent of time where data acquisition is halted by the readout process and the exposures are correspondingly reduced.

The field of view of the runs are modified to remove regions, which contain astrophysical objects that are expected to significantly alter the telescope acceptance. There are two possible types of objects and corresponding impact on the acceptance: γ-ray sources and bright stars. The source-free runs are comprised of observations that do not contain extended γ-ray sources in the field of view. Once these runs are selected, a $0.1°$ radius region around putative and known sources are removed from the data, leaving the rest of the field of view source-free. In addition, bright stars are known to modify the reconstruction of events in the star region. For very bright stars imaged onto the camera plane, the pixel (or multiple pixels) containing the star are saturated with light and unable to capture Cherenkov photons and contribute to the IACT event reconstruction. This manifests as a divergence of events from the location of the star, and therefore a $0.25°$ radius region is removed around known

Table 4.2: Standard cuts used in this analysis

Cut Type	**Value**
NTel	≥ 2
MSCW	$-1.2 \rightarrow 0.5$
MSCL	$-1.2 \rightarrow 0.7$
Distance of Shower Core	≤ 350 m
Size Second Max	$\geq 400/600$ dc (V4/V6)
Emission Height	≥ 6 km

Table 4.3: The cut values made on triggered events for γ-ray-like events. Cosmic-ray-like events have the same cut parameters but with the complement values of MSCW and MSCL (which define the shape cut). At least two telescopes are required to have observed an event to activate stereoscopic reconstruction. Events landing far from the telescope array have poor stereoscopic reconstruction sensitivity, hence the distance to shower core cut. The size second max cut is a requirement that the second brightest pixel has a minimum number of digital counts. A minimum emission height is required, defined as the height of the air shower which contains the maximum number of Cherenkov emitting particles.

bright stars (Johnson B-magnitude < 5) for all data.

The data selection performed is expected to significantly limit the acceptance variations across runs for many of the selected parameters with the exception of elevation. The range of pointing elevations selected for this analysis is broad to accommodate the available Coma GCl data, and the acceptance is especially sensitive to changes in pointing elevation. Accordingly, a strong correlation (> 0.7) is observed between the event rates for the runs and their pointing elevations for most energy bins and for both γ-ray-like and cosmic-ray-like events. To calibrate for the effect that pointing elevation has on the acceptance, a linear regression is performed and the exposure of each run is adjusted according to the run's pointing elevation. For energy-binned data of a particular particle type (cosmic-ray-like or

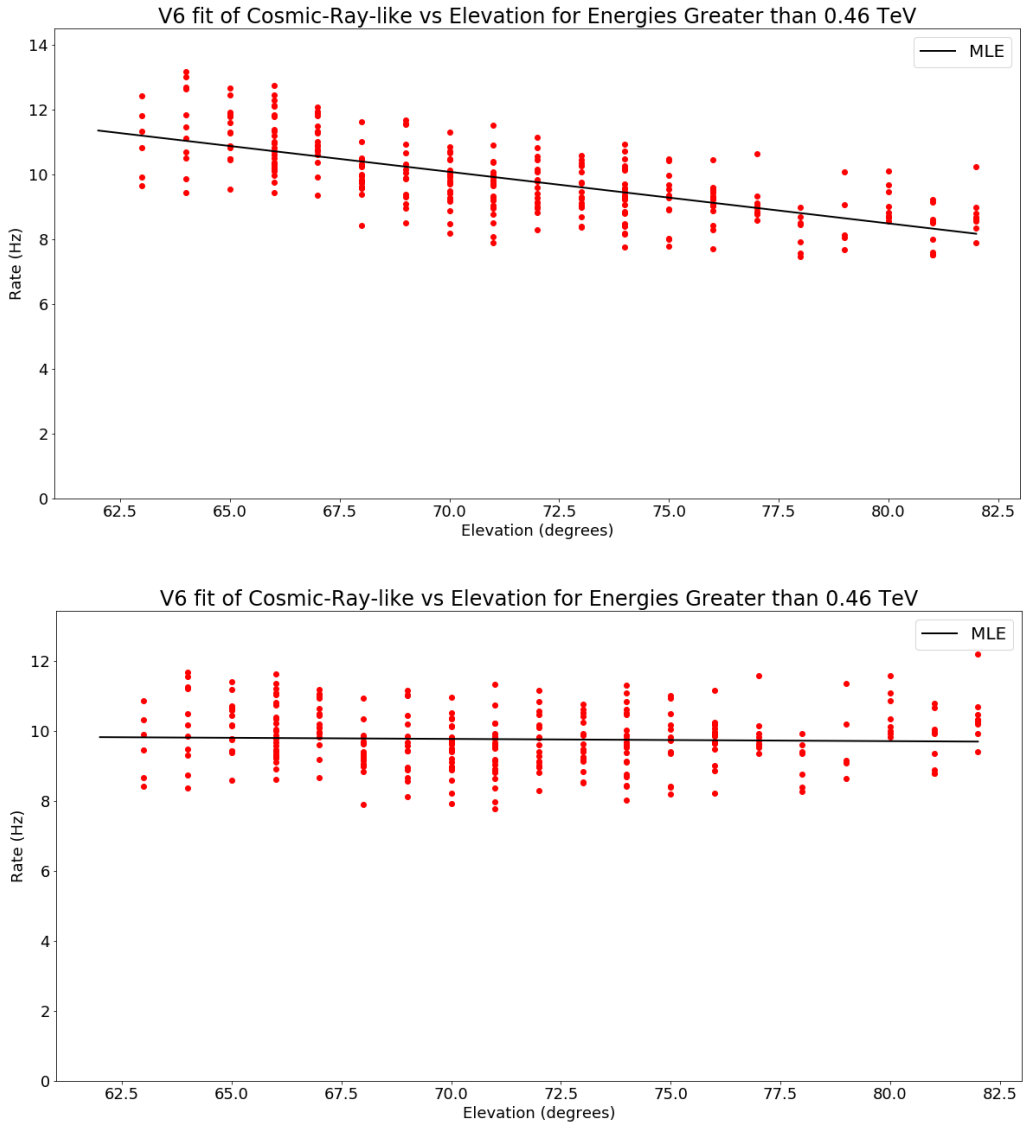

Figure 4.6: Top: A scatter plot of the CR event rates above 460 GeV vs pointing elevation for all selected V6 runs before gain calibration is performed. Since the cosmic-ray calibration of gain later performed uses only high energy cosmic-ray events, the elevation correction is determined for events with approximately the same energy range (above 460 GeV). A negative correlation is observed which is fitted by the maximum likelihood estimator (MLE) function described in the text. Bottom: After applying the fitted slope to correct the run exposures, the correlation is removed.

γ-ray-like), assuming a constant event rate R for all runs, to determine the correction slope m the Poisson probability distribution function is used in a maximum likelihood estimation:

$$\mathcal{L}(N_i, T_i, \Delta\phi_i | R, m) = \prod_i p(N_i, T_i, \Delta\phi_i | R, m) = \prod_i \frac{e^{-RT_i(1+m\Delta\phi_i)}[RT_i(1+m\Delta\phi_i)]^{N_i}}{N_i!}$$

where i is the run index, N_i is the observed counts in run i, T_i is the deadtime-weighted exposure of run i, and $\Delta\phi_i$ is the difference between the run elevation ϕ_i and pivot point ϕ_0 (for V4 $\phi_0 = 70°$, for V6 $\phi_0 = 72°$). The slope m is determined for cosmic-ray-like events (see Figure 4.6) and applied to remove the observed elevation dependence by changing $T_i(1 + m\Delta\phi_i) \to T_i$.

Once the elevation dependence has been removed, the cosmic-ray-like events are used to calibrate the run acceptances. Since the cosmic-ray background flux is widely believed to be isotropic with a stable power-law spectrum, different runs should measure approximately the same cosmic-ray event rate if their acceptances are equal, and therefore the measured cosmic rays may be useful as a calibration source. Consideration of the energy dependence of the cosmic-ray events acceptance is important. Varying weather conditions significantly contribute to differences in run acceptances. The light collected by a Cherenkov telescope for an event depends on the primary particle's energy, the distance between the shower core to the telescope array center (impact parameter), and the attenuation by the atmosphere due to weather conditions. This means that the high energy events may appear bright or dim, if the impact parameter is small or large, respectively, while the lowest energy events are only observed as dim showers with small impact parameters. During cloudy weather where the atmospheric opacity increases and the Cherenkov light is attenuated, dim events which are just bright enough to trigger the telescope in clear weather may fall below the trigger threshold and elude detection. Higher energy events are more likely to be bright events, and are therefore more likely to remain above the trigger threshold and be observed in all weather conditions considered, making them the preferred calibration sample. However, due to the power-law energy spectrum, a greatly increased statistical sample is acquired when considering lower energy cosmic-ray events.

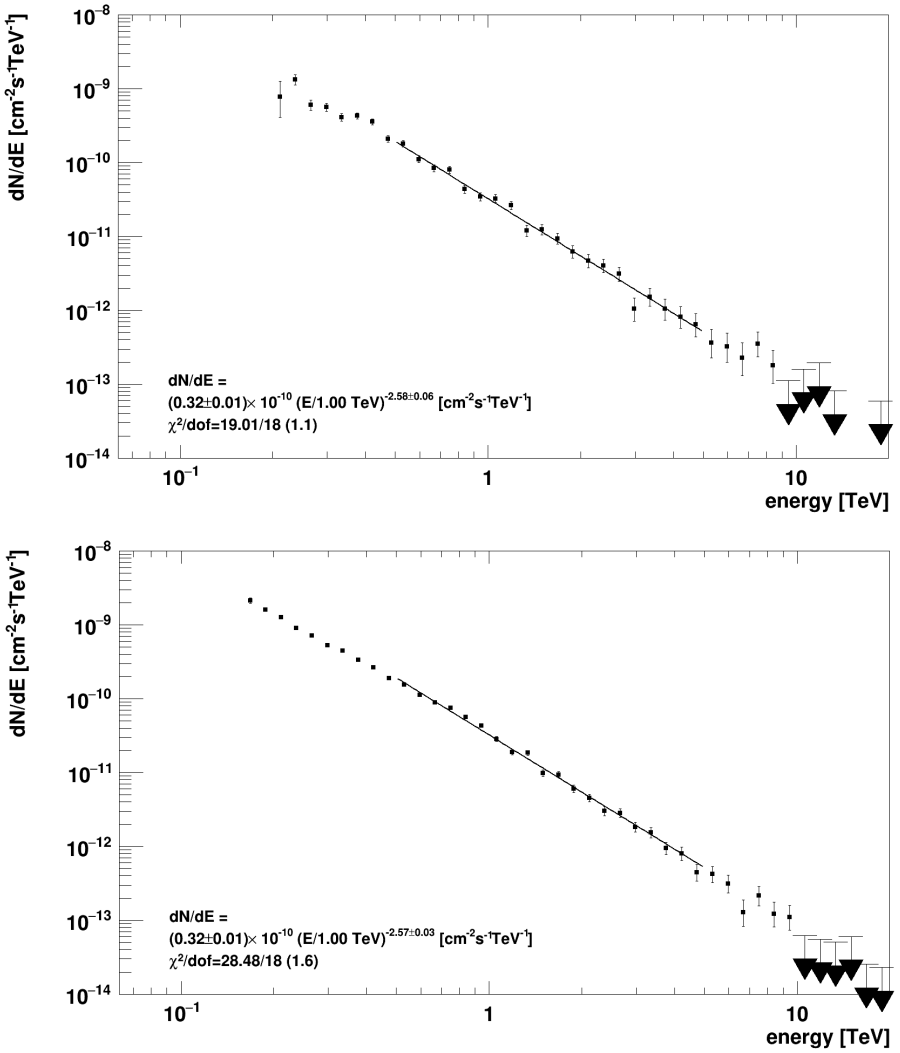

Figure 4.7: The resulting Crab energy spectrum for V4 (top) and V6 (bottom) after iterative gain adjustment. Both spectrums have an integrated flux above 1 TeV of 2.1×10^{-11} cm^{-2} s^{-1}, in agreement with the Crab's integrated flux published in [Hil98].

Motivated to achieve a reasonable balance of these two competing factors, a calibration on cosmic rays is performed such that all runs are reconstructed to have cosmic-ray rate of 15 Hz above a defined cutoff energy. Since atmospheric opacity is expected to be responsible for the acceptance variations, to counteract the light attenuation the calibration of a run is performed by adjusting the gain of the camera images during event reconstruction. The gain correction is iteratively applied until the measured 15 Hz energy is in good agreement with the defined cutoff energy ($< 0.1\%$), at which point all runs observe the same 15 Hz cosmic-ray rate above the cutoff energy (see Figure 4.8). This procedure is performed on high energy cosmic rays after the exposures of the individual runs are first corrected for elevation as previously described with the slope determined on high energy cosmic rays (> 500 GeV).

The Crab Nebula, the standard candle of γ-ray astronomy, is used to determine the cutoff energy by performing the same procedure and varying the cutoff energy until the resulting γ-ray flux above 1 TeV matches the published value (see Figure 4.7). The Crab data used had the same observing condition selection as previously defined with one exception: the pedvars of the Crab data are overall higher, yet with a similar tight range, and so no pedvar selection was made. Since the aim of this analysis is not to determine an energy dependent flux, but to inspect the existence of an event count excess from the region of interest in the Coma GCl, an approximate energy scale is deemed satisfactory. After the gain calibration is completed, then the reconstructed γ-ray-like event rates demonstrate a much smaller variance, indicating the calibration procedure efficiency (see Figure 4.9). At this point only the γ-ray-like events selected by applying "shape" cuts are used for the remainder of this analysis. The linear regression on elevation is performed again using γ-ray-like events from the source-free dataset. The slope correction is then applied to adjust the exposure of all run exposures, for both the Coma GCl runs and the source-free runs.

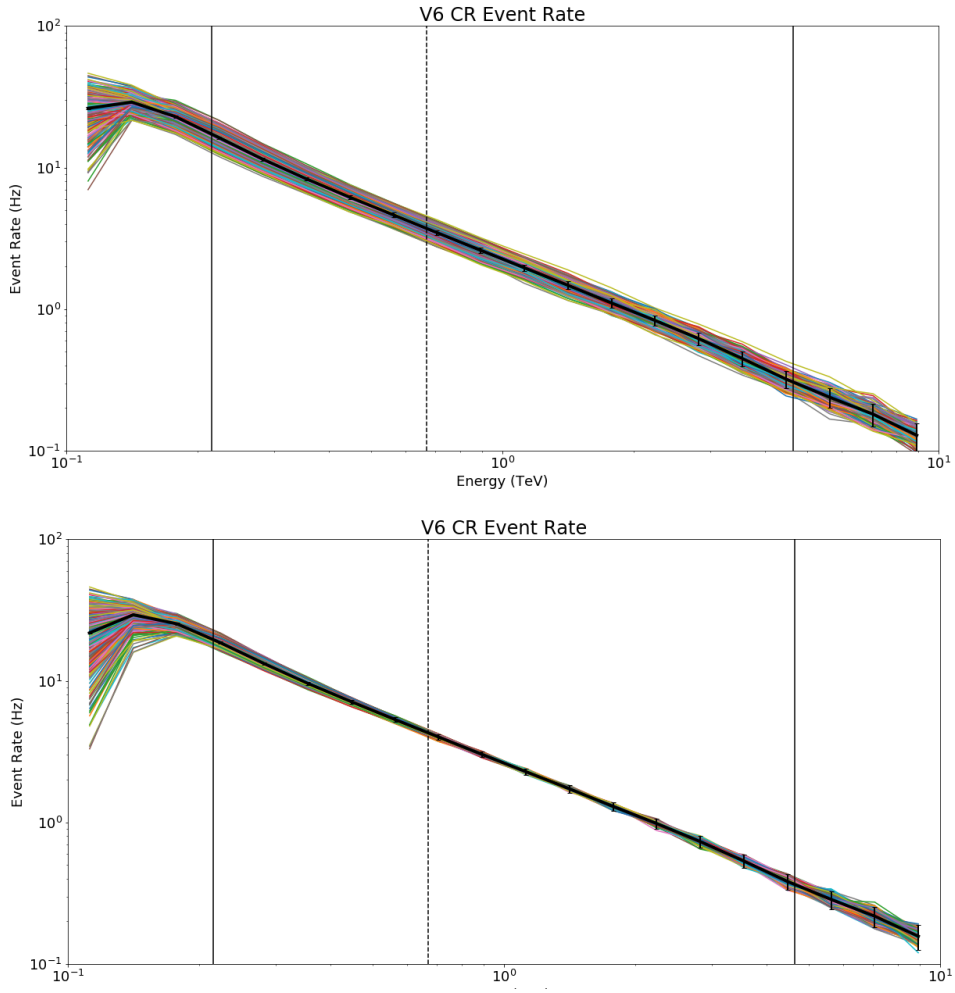

Figure 4.8: The distribution of the V6 event rates for cosmic-ray events of the 206 individual runs before (top) and after (bottom) gain calibration is performed. The cutoff energy for V6 (670 GeV) is shown by the dashed vertical line, and the energy range considered in the analysis is enclosed in the solid vertical lines ($0.2 - 4.6$ TeV). The mean rate is shown by the bold black line with the 3σ Poisson error bars for a ~ 20 minute exposure. The V4 data appears similar and are not shown.

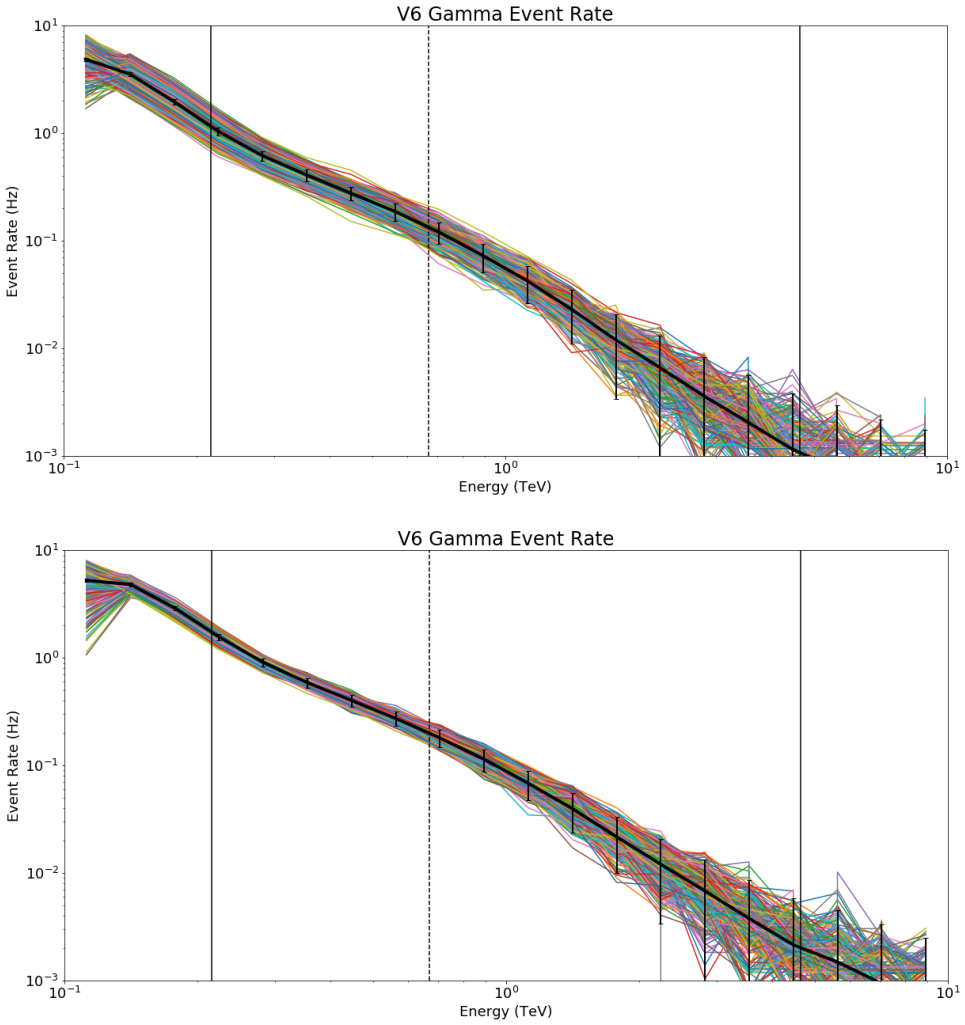

Figure 4.9: The distribution of the V6 event rates for γ-ray-like cosmic-ray events of the 164 individual **source-free** runs before (top) and after (bottom) gain calibration is performed. The cutoff energy for V6 (670 GeV) is shown by the dashed vertical line, and the energy range used in the analysis is enclosed in the solid vertical lines ($0.2 - 4.6$ TeV). The mean rate is shown by the bold black line with the 3σ error bars shown for the Poisson error for a 15 minute exposure. The dispersion in the rates is significantly reduced after the gain calibration procedure, especially at lower energies. The V4 data appears similar and are not shown.

4.1.3 Angular Acceptance Treatment

The VERITAS acceptance in the field of view is generally stable within 1° from the pointing direction, and then can increase or decrease beyond this distance depending on the energy of the event. This angular dependence originates from the finite camera size, which results in images being truncated and failing the reconstruction process. For standard point source analyses, observations are pointed such that events coming from outside the central 1° are not commonly used. In the creation of skymaps, an estimated angular acceptance is utilized which has significant errors far from the pointing directions. For this Coma GCl analysis, events coming from the full field of view are considered and therefore the varying angular acceptance with respect to the pointing direction is important to account for. To first order the angular dependence is a function depending on the radial distance from the pointing direction. Only a higher order correction to this approximation exists as a dependence on the axial angle around the pointing direction, which is caused by the elevation change across the field of view. Events observed below the pointing direction (towards the Earth's horizon) travel through a marginally thicker atmosphere compared to events above the pointing direction, and therefore the Cherenkov shower is relatively dimmer and less likely to be observed (especially at lower energies). In general the angular acceptance can be modeled as

$$f(r,\psi) \approx g(r)\left[1 + kr\sin(\psi)\right] = g(r) + kg(r)Y$$

where r is the radial distance from the pointing direction, ψ is the axial angle, k is a small scalar at the level of a few percent and $g(r)$ is often referred to as the axial angle independent radial acceptance. The axial angle dependence is calibrated for by replacing $r\sin(\psi)$ with Y, the displacement from the pointing direction along the elevation axis. To evaluate this "Y-position" term, the γ-ray-like events for each source-free run n are binned by their Y-position (horizontal slices across the field of view) in 0.25° bins for a total of 16 bins, where bins below the pointing direction are indexed from $-1 \rightarrow -8$, while bins above the pointing direction are indexed from $1 \rightarrow 8$. The relative difference between corresponding binned

event rates above and below the pointing direction is determined for run n, normalized by the mean of the two bins.

$$\Delta R_n(Y_i) = \frac{R_n(Y_i) - R_n(Y_{-i})}{R_n(Y_i) + R_n(Y_{-i})} = k_n Y_i$$

The average over the source-free runs is then found, which demonstrates a roughly linear dependence on the Y-distance from the pointing direction that is relatively weak (see Figure 4.10).

$$\langle \Delta R(Y_i) \rangle = \frac{1}{N} \sum_n^N \Delta R_n(Y_i) = \langle k_n \rangle Y_i = k Y_i$$

The slope of this dependence, k, is determined by a χ^2 minimization. Overall this is a small effect ($< 10\%$ for most events), and therefore a linear correction in the form of event weights is deemed sufficient. The error introduced into the Poisson uncertainty by scaling the event counts by $\sim 10\%$ is assumed to be minor and ignored in this analysis. The correction is applied by scaling individual event weights depending on their Y-position such that the total number of events are preserved to remove potential associated bias

$$w(Y > 0) = 1 + kY$$

$$w(Y < 0) = 1 - kY$$

This process is performed for each energy bin in the data of both V4 and V6 epochs. The relative difference demonstrates a linear dependence on Y-position for all binned datasets except for the V4 low energy bin ($220 - 460$ GeV). This is likely because the V4 array epoch had T1 and T4 telescopes in close proximity to each other, causing the majority of low energy events to be observed by only these two telescopes and possibly creating an angular bias in the event reconstruction direction from the pointing direction. Nevertheless the linear correction is still applied for the V4 low energy binned dataset.

Once the Y-position dependence is corrected, the remaining angular acceptance approximately depends only on the radial distance from the pointing direction. This radial dependent acceptance becomes especially important for events beyond 1°. Since this analysis

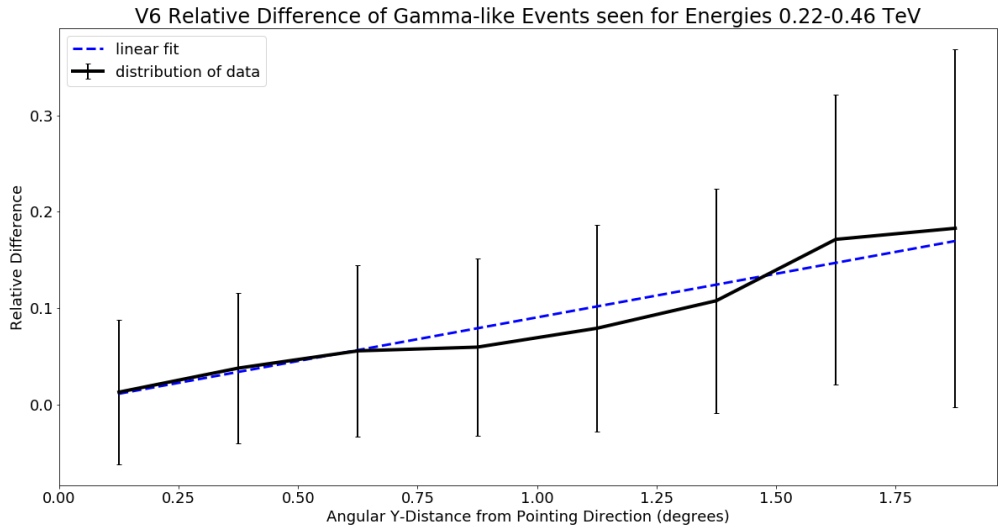

Figure 4.10: A plot of the relative difference (above and below the pointing direction) of γ-ray-like events as a function of the angular Y-position. The mean and 1-σ error bars of the distribution of the source-free runs is shown in black, with the linear fit shown by the blue line. A 0.25° bin size is used. For larger Y-positions where the effect is larger, the decreasing field of view compounded with the decreased radial acceptance significantly diminishes the effect's impact. The plot shown is for V6 source-free runs with events in the $220 - 460$ GeV range as an example.

utilizes the full field of view of observations, over 70% of the solid angle observed is beyond 1°. The radial acceptance therefore is critically important for this analysis. The radial acceptance is a complicated function with dependence on all of the observing conditions presented (elevation, weather, etc.). Simulated or modeled radial acceptance functions are subject to significant sources of error. Therefore, to avoid these errors, this analysis takes the approach of measuring the background from source-free runs with the same radial exposure. The field of view of all observations is separated into radial bins defined by six concentric rings of equal solid angle (0.6π deg^2 each, for a total solid angle of 3.6π deg^2). Events outside of the field of view ($> 1.9°$ from the pointing direction) are expected to be very rare and are therefore discarded from this analysis.

4.1.4 Excess Counts Significance Computation

For each region of interest in the Coma GCl field, such as a square bin with 0.2° length or an arbitrary shaped region containing proposed VHE γ-ray emission, an exposure profile q_{ji} is determined based on the observations for each run i and radial acceptance bin j:

$$q_{ji} = \Omega_{ji} t_i$$

The exposure profile is a product of the calibrated exposure t_i and solid angle Ω_{ji} partitioned into radial bins and has units of deg^2 $\cdot$ sec. The solid angle Ω_{ji} for each radial bin j is reduced from 0.6π deg^2 due to star and source removal earlier performed for each run i. An example of the computation of an exposure profile for a box region of interest is illustrated in Figure 4.11 for the case of two pointings in two runs of the observations and four radial bins, rather than six, for simplicity. Each run with the same pointing has the same partitioning of the solid angle Ω_{ji} and a total exposure profile can be viewed as an assembly of all runs, each represented by a column (a component) in the q_{ji} matrix.

The total number of counts observed from a region of interest is naturally computed as

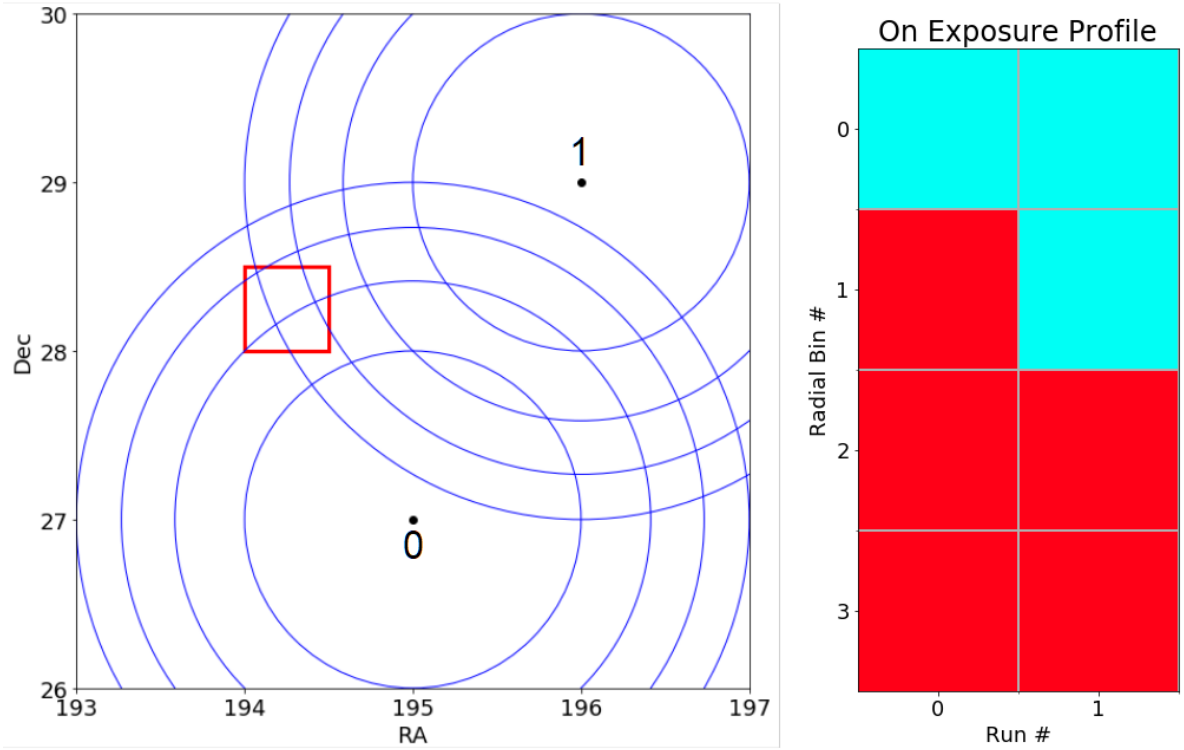

Figure 4.11: Exposure profile partitioning example showing two pointings and using four radial bins for simplicity of illustration. The region of interest is outlined by the red box. The field of view of the pointings are divided into equal area radial bins and the exposure profile q_{ji} is partioned into each bin for each run. Numbers are not shown in the exposure profile, but nonzero values are colored red while zero values are colored blue.

a sum over all observation runs

$$N^{ON} = \sum_i N_i^{ON}$$

Given the Poisson statistics of the N_i^{ON} random results of observations, we denote as λ the mean value of N^{ON} or

$$\lambda = \langle N^{ON} \rangle = \sum_i \langle N_i^{ON} \rangle$$

The variance of N^{ON} is then given by

$$\langle \left(N^{ON}\right)^2 \rangle - \langle N^{ON} \rangle^2 = \sum_i \left[\langle \left(N_i^{ON}\right)^2 \rangle - \langle N_i^{ON} \rangle^2 \right] = \sum_i \langle N_i^{ON} \rangle = \lambda$$

and it is Poisson distributed

$$P(N^{ON}|\lambda) = e^{-\lambda} \frac{\lambda^{N^{ON}}}{N^{ON}!}.$$

In the regime of the large number of counts, $N^{ON} \gg 1$, to later validate the application of Wilks' theorem for the computation of a significance from excess counts, the Poisson distribution is Gaussian

$$P(N^{ON}|\lambda) \to G(N^{ON}|\lambda, \lambda) = \frac{1}{\sqrt{2\pi\lambda}} e^{-\frac{\left(N^{ON}-\lambda\right)^2}{2\lambda}}$$

with the variance λ. The variance of the rate of counts coming from a region of interest is zero for this distribution in the case of an infinitely long exposure, which is not representative of the expected non-vanishing variance associated with the varying observing conditions in different runs. To account for this residual variance, the probability density distribution of N^{ON} is modified to $G(N^{ON}|\lambda, \lambda + s^2\lambda^2)$ in which s is the nuisance parameter modeling the strength of cumulative systematic effects causing a finite residual variance of the observed rates due to varying acceptances. This variance is assumed to be uncorrelated with the Poisson variance represented by the λ term. In the absence of a genuine γ-ray source in the region of interest, λ is entirely due to background counts. If a very weak source is presented, such as potentially in the case of the Coma GCl, the mean value $\langle N^{ON} \rangle = \lambda + N_\gamma$ will be perturbed by $N_\gamma \ll \lambda$. With this assumption, a Gaussian function

$$G(N^{ON}|\lambda + N_\gamma, \lambda + s^2\lambda^2)$$

with three parameters (N_γ, λ, s^2) is adopted as the probability density function in the presence of a weak signal in the ON dataset.

The exposure profile q_{ji} for N^{ON} counts and the probability density distribution function are necessary ingredients to determine the background counts N^{OFF} from the source-free runs, from which the excess counts can be computed and a significance based on the excess counts is evaluated. The source-free runs are used to assemble mock-up observations with matching exposure profiles to the real N^{ON} data. First the selected archival VERITAS runs, which are used as the source-free runs, are processed to remove regions with bright stars and potential γ-ray sources. The removal of these regions reduces the default solid angle bin size from 0.6π deg^2 for the affected radial bins j, resulting in the remaining solid angle Ω_{jl} for a given run l. For each source-free run its exposure profile Q_{jl} is determined by combining its solid angle coverage Ω_{jl} with its calibrated exposure t_l,

$$Q_{jl} = \Omega_{jl} t_l$$

For an isotropic background of γ-ray-like cosmic rays, it is then anticipated that the expected number of the observed counts N_{jl} depends on the exposure profile as,

$$\langle N_{jl} \rangle = R_j Q_{jl}$$

where R_j is the run-independent mean value of the background rate in the radial bin j. It is important to note that for evaluation of a small solid angle region, such as a $0.2^\circ \times 0.2^\circ$ skybin, the default solid angle Ω_{jl} exceeds the size of the sky bin by about a factor of 50, which allows for significantly more accurate determination of the mean background rates from samplings of $\frac{N_{jl}}{Q_{jl}}$.

Using the source-free data, N_{jl} and Q_{jl}, the measured background which mocks the actual observed ON counts can be generated as

$$N_n^{OFF} = \sum_{l,i} M_{il}^n \sum_j \frac{N_{jl}}{Q_{jl}} q_{ji},$$

where M_{il}^n is the mapping flag matrix containing values of 0 or 1 only. Since the number of source-free runs is larger than the number of ON runs in an exposure profile, multiple sets of OFF data are often capable of being generated for each ON set. To denote this, the index n is introduced enumerating different mock-up observing datasets. For each ON run i in an exposure profile, a single source-free run l is assigned by M_{il}^n in a given set n, ($\sum_l M_{il}^n = 1$). Each set provides a sampling of the background with an identical radial binned exposure and expected number of counts as in the ON dataset

$$\langle N_n^{OFF} \rangle = \sum_{l,i} M_{il}^n \sum_j \frac{\langle N_{jl} \rangle}{Q_{jl}} q_{ji} = \sum_{i,j} R_j q_{ji} = \lambda$$

The Poisson error of each dataset, however, is different and is given by

$$\langle \left(N_n^{OFF}\right)^2 \rangle - \langle N_n^{OFF} \rangle^2 = \sum_{i,k,l,j} M_{il}^n M_{kl}^n \frac{q_{ji}}{Q_{jl}} \frac{q_{jk}}{Q_{jl}} \langle N_{jl} \rangle = \sum_{i,l,j} R_j M_{il}^n \frac{q_{ji}^2}{Q_{jl}} = \alpha_n \lambda$$

in which a property of mapping matrix

$$M_{il}^n M_{kl}^n = M_{kl}^n \delta_{ik}$$

has been used since any given source-free run l is mapped only into a single ON run, i, in any given set. The parameter

$$\alpha_n = \frac{\sum_{i,l,j} R_j M_{il}^n \frac{q_{ji}^2}{Q_{jl}}}{\sum_{i,j} R_j q_{ji}}$$

describes the reduction of the Poisson variance of the OFF measurement compared to the ON dataset due to the larger background sampling exposure profile. In general, $\alpha_n(R_j; j = 1, 6)$ is a function of unknown background rates; however, it is independent of the overall normalization factor of the rates. The use of this fact will be made later in the discussion of the significance computation from the excess counts.

The construction of the mapping matrix is performed in a way that maximizes the number of OFF sets created given the available source-free runs. The OFF sets are randomly assembled to match the ON exposure profile from the source-free runs under two restrictions: data from each radial bin in a source-free run can only be used once, and a source-free run

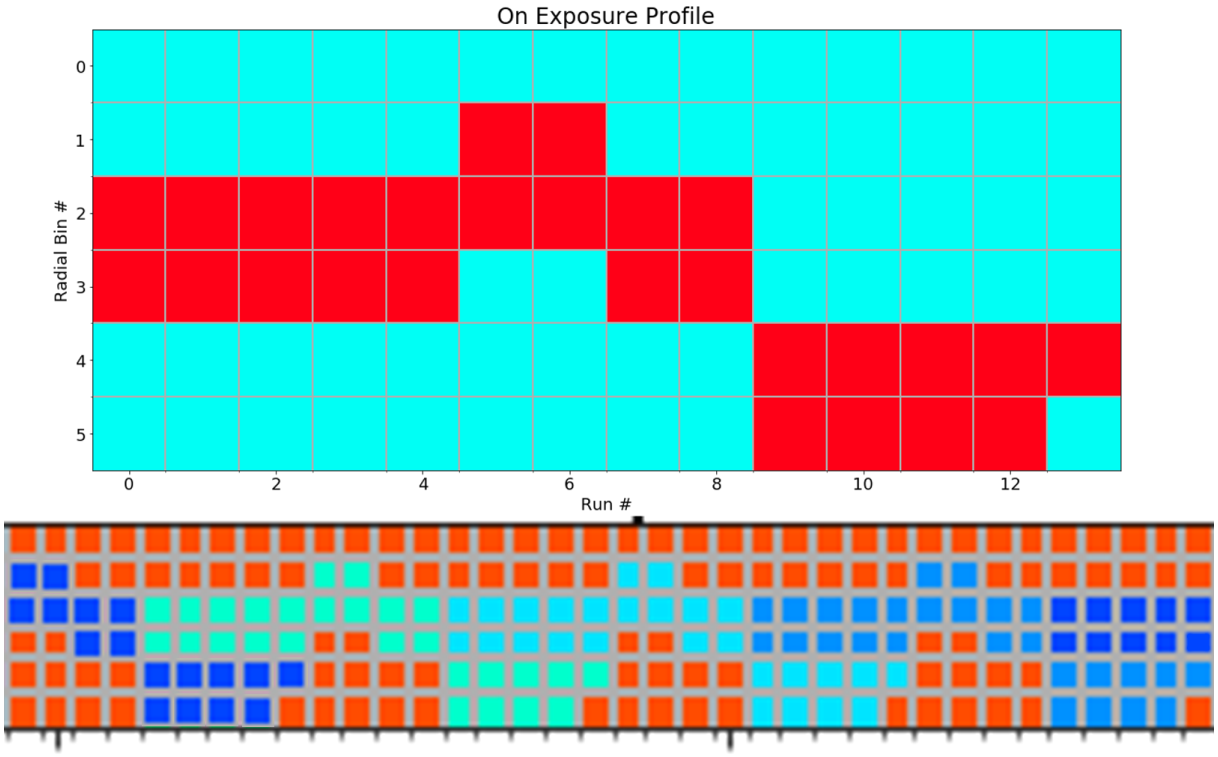

Figure 4.12: Top: An exposure profile consisting of 14 runs whose order has been rearranged in order to overlap their assembly. The used and unused radial bins are colored red and cyan, respectively. Bottom: An example of the above exposure profile being assembled into four sets of data (identified by the four shades of blue, where the red bins are unused). The x-axis corresponds to the source-free run index l, while the y-axis is the radial bin number. Four off sets with 14 runs each are able to be created from only 36 source-free runs. Source-free data within a radial bin are not used more than once.

cannot be used for more than one ON run in a set. These restrictions ensure that the correlations are not introduced or removed in the background sampling. During the generation of the mapping matrix, source-free runs are assigned to ON runs for an ON exposure profile while following these restrictions. The ON runs in the exposure profile are rearranged in an order that enables it to tile with itself while maximizing the number of overlapping ON runs, which enables a single source-free run to be used in two different sets without reusing data within a radial bin. The collection of source-free runs are then randomly assigned to overlapping ON runs until the maximum number of OFF sets are created. If there are leftover source-free runs which have not been assigned, then the number of overlapping ON runs is reduced by one if doing so does not reduce the number of OFF sets created. See Figure 4.12 for an illustration of the mapping procedure.

To evaluate the significance of the excess in the measured N^{ON} counts, a likelihood-ratio test is performed for the two hypotheses as described in Chapter 3.1.4. The likelihood function for this study is given by

$$\mathcal{L} = G(N^{ON}|\lambda + N_\gamma, \lambda + s^2\lambda^2) \cdot \prod_n G(N_n^{OFF}|\lambda, \alpha_n\lambda + s^2\lambda^2)$$

and in general it depends on 3+5 parameters of which the first three are (N_γ, λ, s^2) and the remaining five $(\frac{R_j}{R_1}, j = 2, 6)$ enter through the rate scale independent parameters α_n, which determine the Poisson component of the variance in the OFF set n. To find the likelihood-ratio for the test, it is necessary to compute the conditional $(N_\gamma = 0)$ and unconditional maxima for the likelihood with respect to all seven remaining nuisance parameters. The relative value of the Poisson variance $\alpha_n\lambda$ compared to the residual variance $s^2\lambda^2$ is of the order of 10^{-3} for an ON exposure skybin with solid angle $0.2^\circ \times 0.2^\circ$ and of the order of 10^{-2} for the larger solid angle regions analyzed which are associated with tested morphologies. Even with a factor of 10 difference in the ratio of the background rates, R_j/R_1, the maximum effect in optimization of these R_j parameters on the Gaussian variance is at the level of $\sim 1\%$ or less. The difficulty of computations in 8-dimensional parameter space compared to 3-dimensional is not justified since other assumptions which are made, such as $N^{ON} \gg 1$

and $N_\gamma \ll \lambda$, probably contribute deviations with values larger than this. In fact, attempts to include the $(\frac{R_j}{R_1}, j = 2, 6)$ parameter space are found to be largely degenerate, making a numerical maximum likelihood estimate infeasible. For this reasoning when calculating the Poisson variances in the OFF sets only, the assumption is made that all R_j are equal and therefore α_n is independent of R_j and is given by

$$\alpha_n = \frac{\sum_{i,l,j} M_{il}^n \frac{q_{ji}^2}{Q_{jl}}}{\sum_{i,j} q_{ji}}.$$

The likelihood ratio is then computed in the 3-dimensional parameter space of which two parameters (λ, s^2) are nuisance parameters, with one degree of freedom due to the single N_γ parameter. The Test Statistic is then determined,

$$TS = -2 \ln \left(\frac{\mathcal{L}_0}{\mathcal{L}} \right),$$

where $\mathcal{L}_0$ is the maximum likelihood value assuming $N_\gamma = 0$ and $\mathcal{L}$ is the maximum likelihood value assuming that all three parameters (N_γ, λ, s^2) are varied.

According to Wilks' Theorem, in the asymptotic limit of the number of samples going to infinity, this Test Statistic is χ^2 distributed with one degree of freedom. For a normal variable u, since u^2 follows a χ^2 distribution with one degree of freedom, then the square root of the Test Statistic is interpreted as an absolute value of detection significance, if the maximum likelihood estimate of N_γ is an excess (positive). For convenience of plotting, the results in the S distribution (or the significance distribution) has a sign added to it based on the sign of N_γ

$$S = \text{sign}(N_\gamma) \cdot \sqrt{-2 \ln \left(\frac{\mathcal{L}_0}{\mathcal{L}} \right)}.$$

4.1.5 Results

Skymaps are created of the Coma GCl region which encompass the angular extension of the integrated exposures. The skymap is divided into $0.2^\circ \times 0.2^\circ$ angular skymap bins, roughly

equivalent to the size of the VERITAS point spread function (68% containment within $\sim 0.1^\circ$ radius), and a significance is produced for each skymap bin. To ensure that the Gaussian approximation of the Poisson probability distribution function is valid, the requirement is made that the reconstructed expected counts must be greater than 10. In order to avoid inefficient use of source-free runs in the assembly of OFF sets, a radial bin is not included in the exposure of an ON run unless it contributes enough exposure (> 0.12 s·deg^2, equivalent to 5 minutes over the skymap bin's solid angle).

As a test of this extended-region analysis method, two datasets of source-free runs are used as ON data with the expectation of an overall low significance. For each Coma GCl run in the ON set, a random source-free run is assigned the pointing direction of that run and also removed from the remaining OFF dataset. The collection of these source-free runs with artificial pointings constitutes a *mimic* dataset, containing the same number of runs as the Coma GCl dataset. Since the available V4 source-free runs are limited, creating a V4 mimic dataset would reduce the OFF exposure by approximately a factor of two, hence no V4 mimic dataset is created. However the V6 dataset contains roughly six times as many source-free runs as Coma GCl runs, and therefore two mimic datasets are created while retaining most of the OFF exposure.

The proposed virial shock evidence in the Coma GCl, which has the morphology presented in Section 2.1.2, is tested by evaluating the distribution of skymap bins which are contained inside of the ring in comparison to the distribution of skymap bins over the full skymap. In addition to examining the proposed virial shock region, a central 1.5° radius circular region (approximately equivalent to the Coma GCl virial radius) is also tested in the same way. This region approximately corresponds to the extension of the simulated γ-ray emission, as well as the Fermi-LAT observed weak emission (see Figures 2.9 and 2.10). The resulting skymaps and distributions of significances are presented for the full energy range (200 GeV$-$4.6 TeV) for the four datasets: V4 and V6 Coma GCl, and two V6 mimic datasets (see Figures 4.13$-$4.16).

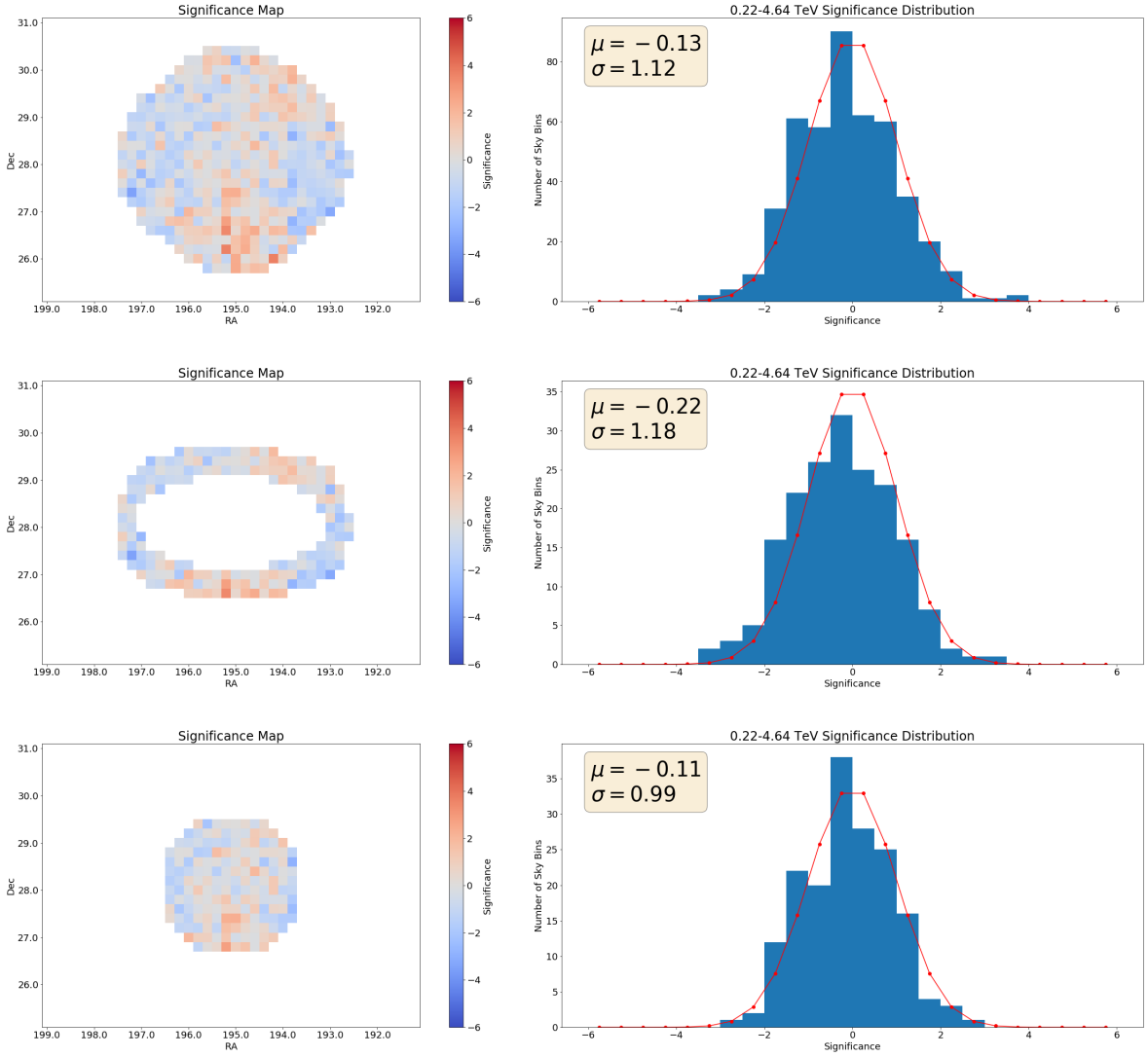

Figure 4.13: The significance skymap (left) and distribution of significance bins (right) for the V4 Coma GCl dataset over the full energy range (220 GeV−4.6 TeV) for three tested regions. Bins contained in the full skymap are shown in the first row, while only those contained in the tested virial shock ring and central 1.5° radius are shown in the second and third rows, respectively.

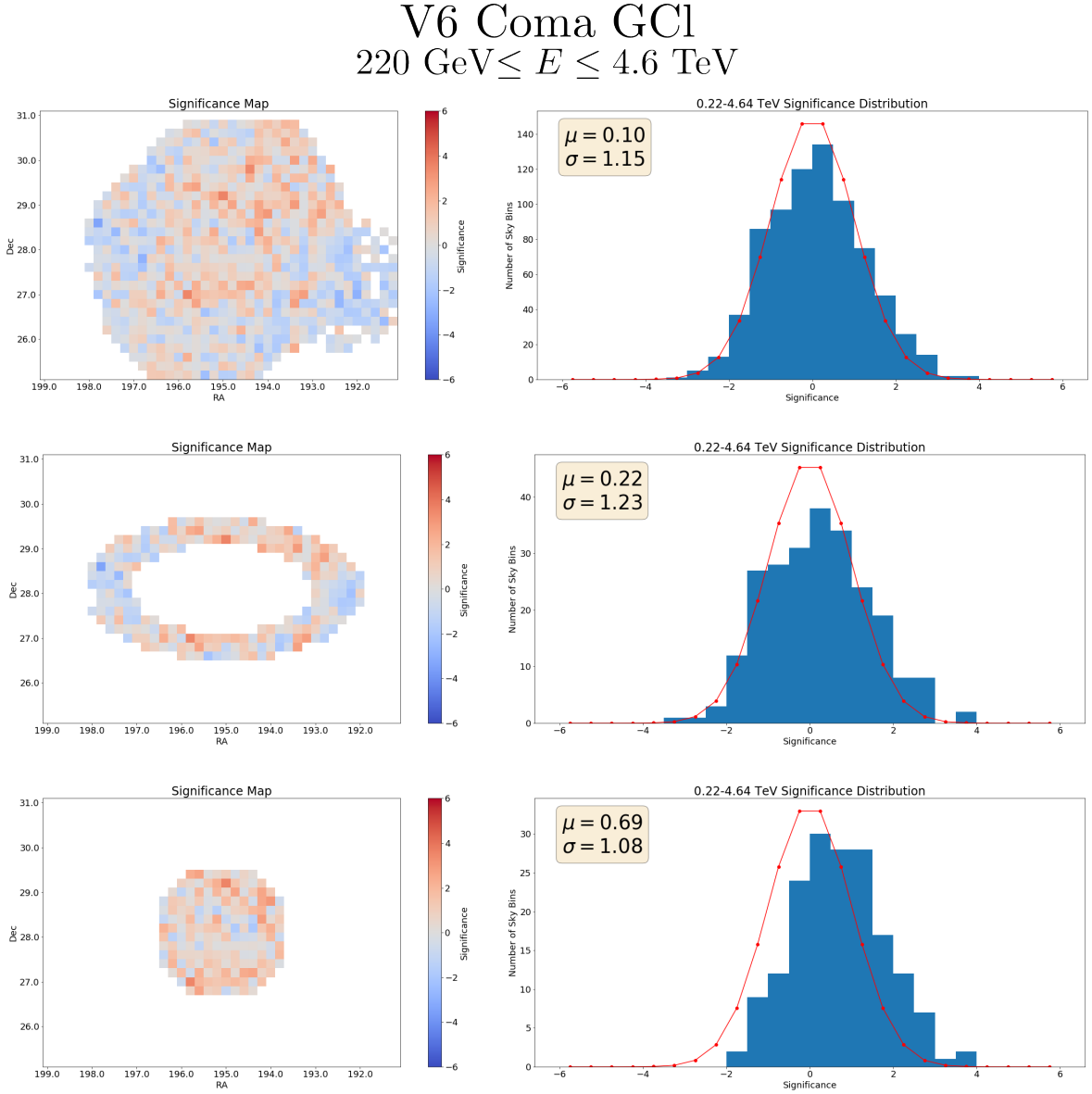

Figure 4.14: The significance skymap (left) and distribution of significance bins (right) for the V6 Coma GCl dataset over the full energy range (220 GeV−4.6 TeV) for three tested regions. Bins contained in the full skymap are shown in the first row, while only those contained in the tested virial shock ring and central 1.5° radius are shown in the second and third rows, respectively.

V6 Mimic #1
220 GeV$\leq E \leq$ 4.6 TeV

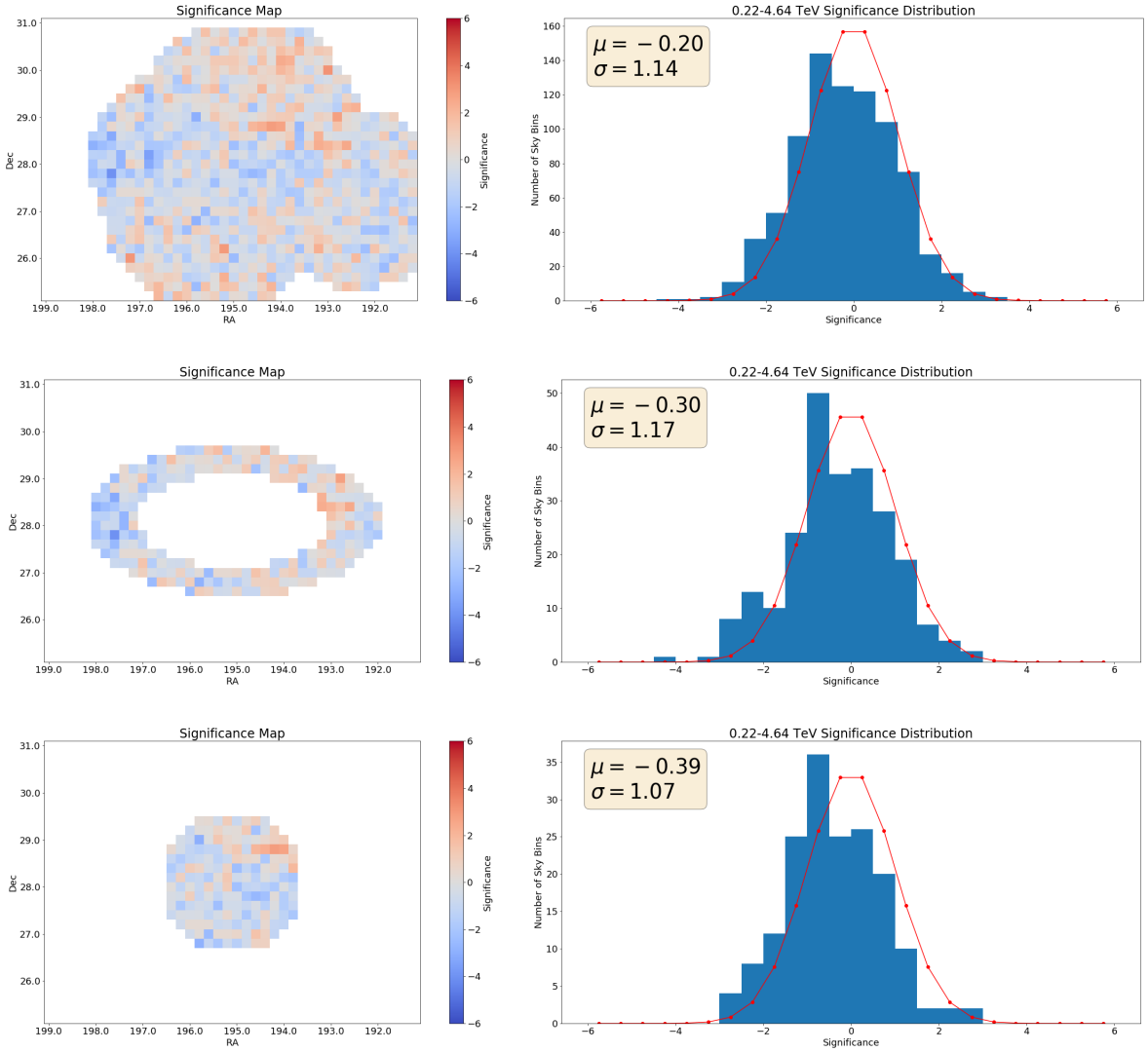

Figure 4.15: The significance skymap (left) and distribution of significance bins (right) for the V6 mimic #1 dataset over the full energy range (220 GeV−4.6 TeV) for three tested regions. Bins contained in the full skymap are shown in the first row, while only those contained in the tested virial shock ring and central 1.5° radius are shown in the second and third rows, respectively.

V6 Mimic #2

220 GeV$\leq E \leq$ 4.6 TeV

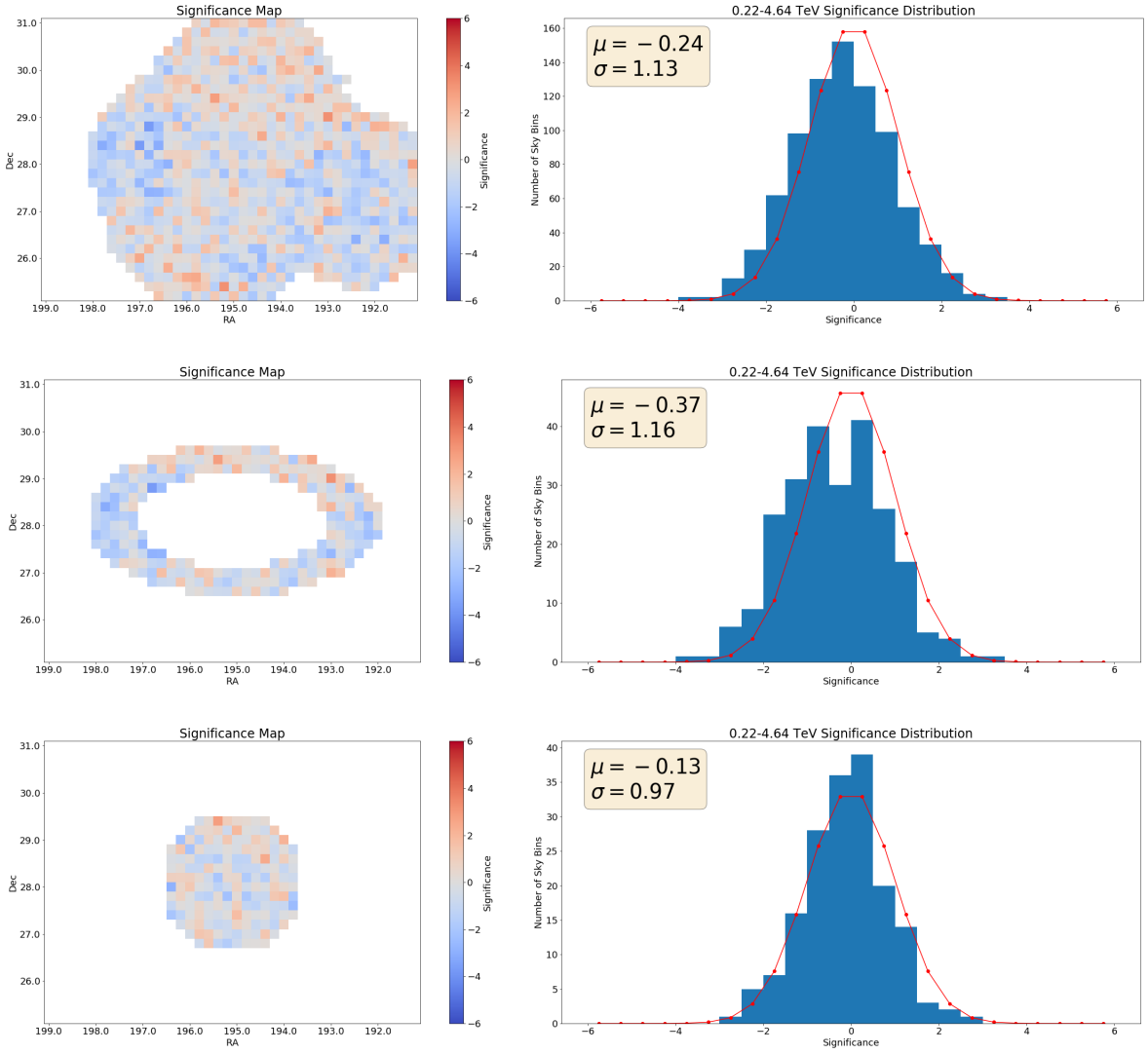

Figure 4.16: The significance skymap (left) and distribution of significance bins (right) for the V6 mimic #2 dataset over the full energy range (220 GeV−4.6 TeV) for three tested regions. Bins contained in the full skymap are shown in the first row, while only those contained in the tested virial shock ring and central 1.5° radius are shown in the second and third rows, respectively.

The results of the two mimic datasets provide examples of the expected significance distributions when a γ-ray source is not present, and therefore offer a scale for which the distributions can vary. Both mimic datasets are roughly normally distributed with some minor deviations in the mean and variance (see Figures 4.15,4.16). A slightly negative mean significance and larger standard deviation is found for the distributions of both mimic datasets, indicating that the mimic datasets may consist of runs which on average have a lower γ-ray-like event rate and larger dispersion compared to the remaining OFF runs. The deviations from normal may also be the result of approximations made which are not completely accurate (e.g. the Gaussian approximation of the Poisson distribution, Wilks' theorem). Overall the distributions are approximately normal, and there are no bins which have an exceptionally unlikely significance. Collections of neighboring bins with high and low significances can be seen, which are likely explained by a residual elevation dependence of the event rates which trace the pointing positions. The bins in the ring and circular regions have distributions which correspond to a subsample of the skymap bins, as expected for a random sample of bins.

The V4 Coma GCl skymap significances for the full energy range (see Figure 4.13) are distributed approximately normally for the full skymap, with no exceptionally significant bins present, and the ring and circular regions have distributions which are consistent with subsamples of the full skymap. The V6 Coma GCl full skymap (see Figure4.14) also demonstrates a roughly normal distribution of significance bins; however, the two models are not consistent with subsamples of the full skymap. The significance bins of the ring region appear to have a positive skew, while the circular region has a shift of the mean ($\mu = 0.69\sigma$). The energy binned results of the skymaps are shown in Figures 4.19$-$4.29 at the end of the section, where energy ranges that are not shown were unable to be computed due to the requirement that the expected number of counts be at least 10. The energy binned results indicate that the counts in the low energy bin (220 GeV$-$460 GeV) contribute the most to the positive skew seen for the ring region and the shift in the mean for the circular region.

Evaluation of the skymap bins offers a method of evaluating angular extended morphologies, but is not the most sensitive method for testing particular emission models such as the ring and circular regions. The amount of exposure which the skymap bins contain widely varies across the field of view, and hence the significances of the bins are determined with unequal sensitivities. However, when evaluating the significance distributions, the individual bins are misleadingly equally weighted.

Since the creation of an exposure profile is applicable to an arbitrary solid angle region, it is straightforward to produce a singular significance for an integrated region of any shape. Therefore, instead of evaluating square skymap bins, a single solid angle bin which matches either the proposed ring or circular morphology is created and evaluated. Because each Coma GCl observation has some exposure which lies within the ring and circular regions, the resulting exposure profiles end up consisting of the entirety of the ON data. Since an equal number of source-free runs are needed to produce an OFF set, only three V6 OFF sets are able to be created and just one V4 OFF set for the exposure profile of the ring and circle regions. This reduced sample size means that the maximum likelihood estimation of s^2, and therefore the resulting significance, is expected to be sensitive to the randomized arrangement of the source-free runs when assembling the OFF sets. Therefore, when evaluating significances of integrated regions, the OFF sets are randomly assembled 100 times with a significance calculated for each iteration. A histogram of the significances from these 100 iterations is then generated, and the median significance is used as the result.

The resulting distributions of integrated-region significances obtained from the 100 iterations are shown in Figure 4.17 for the full energy range (220 GeV$-$4.6 TeV) and are also summarized in Table 4.4. For the mimic datasets, a negative median significance is determined for both ring and circle regions in agreement with the negative shifted mean seen for the distributions of square skymap bins. The wide range of significances seen confirms that the order of assembly in generating the small number of OFF sets has a large impact on the determined significance. The limited number of OFF sets brings into question the

Table 4.4: Median Integrated-Region Significances

	Ring	**Circle**
V4 Coma	-0.1σ	-0.3σ
V6 Coma	1.9σ	2.7σ
V6 Mimic #1	-1.1σ	-1.6σ
V6 Mimic #2	-σ1.8	-0.8σ

interpretation of significance, as the working regime may be far from the asymptotic limit required to apply Wilks' theorem.

The V4 Coma GCl distribution of integrated-region significances has a median significance near 0σ for both ring and circle region. The V6 Coma GCl distribution, however, demonstrates a positive median significance of 1.9σ and 2.7σ for the ring and circle regions, respectively. The positive median significance for the ring region is consistent with the results for the square skymap bins. While the square bins in the ring region have a mean significance close to zero (see Figure 4.21 middle row), the bins with negative significance located at the left and right ends of the ring have much less exposure than the other bins, and are correspondingly weighted less in determination if a singular significance over the integrated ring region. Some square bins with positive significance are contained in both ring and circular regions, which may provide a large contribution to the positive median significance determined for both regions.

Unfortunately there is no straightforward method of combining the V4 and V6 datasets to produce an overall significance for the ring and circle regions. The V4 and V6 epochs operated with different telescope layouts and camera sensitivities (see Section 3.2), and the median significances were produced for the V4 epoch with considerably fewer source-free runs. Any attempt to combine the significances produced on the individual epochs would represent assumptions made in their combination more than a meaningful significance. Combination

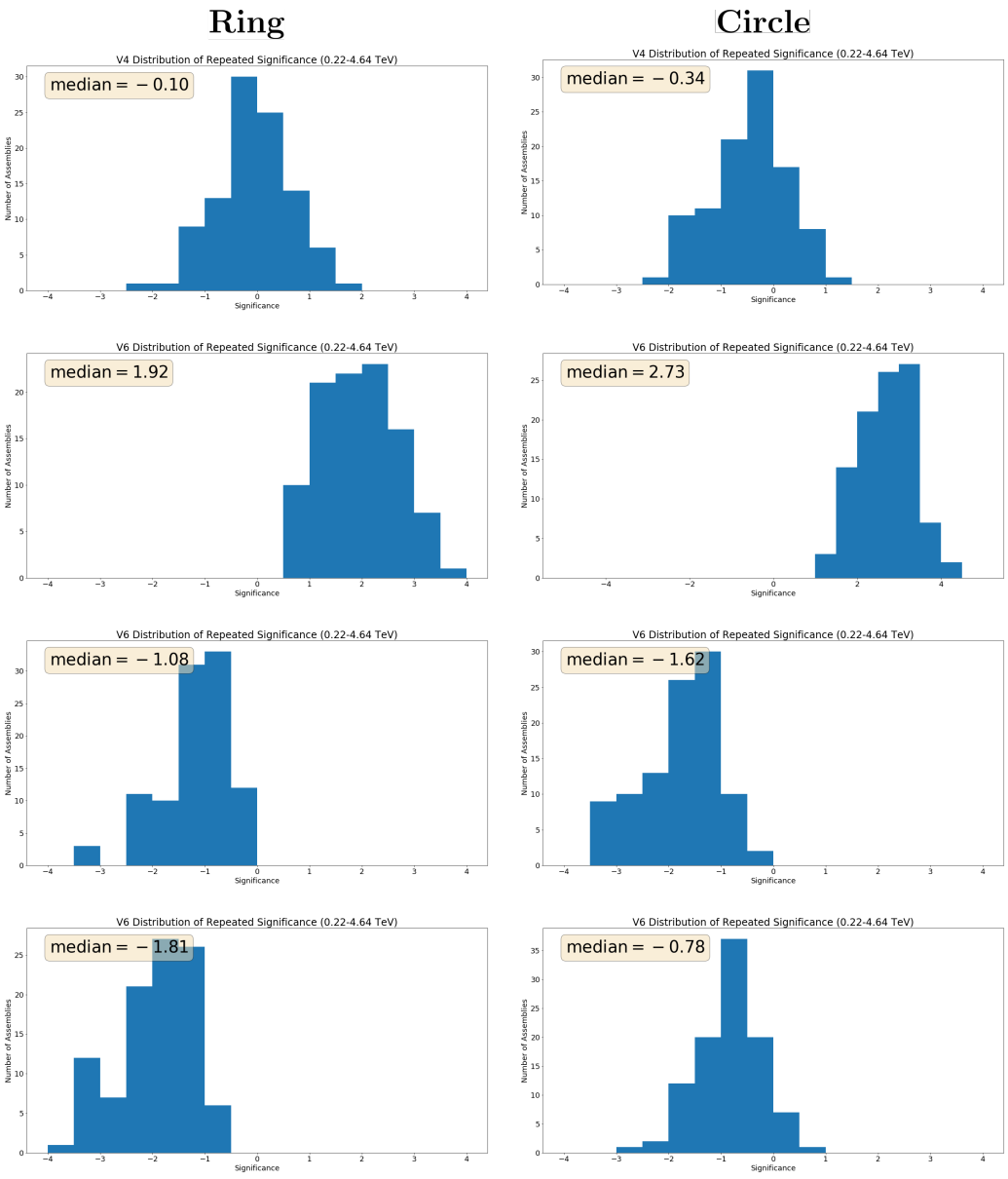

Figure 4.17: Histograms of 100 iterations determining the integrated-region significance of the ring and circle regions for different datasets over the full energy range (220 GeV−4.6 TeV). First row: V4 Coma GCl data. Second row: V6 Coma GCl data. Third row: V6 mimic dataset one. Fourth row: V6 mimic dataset two.

will, of course, reduce the 1.9σ and 2.7σ median significances obtained for the V6 dataset, but the reduction amount will be heavily dependent on the assumptions made in combining the epochs.

The 1.9σ and 2.7σ median significances for the ring and 1.5° radius circular regions, respectively, were obtained from a single trial. To check that the integrated significance is not associated with a systematic bias in solid angle, circular regions with radii of 1.0° and 2.0° were evaluated and demonstrated median significances of 1.8σ and 2.2σ, respectively, confirming that the dependence on solid angle is not monotonic.

In addition to the distribution of integrated-region significances for the full energy range, energy binned distributions are also produced for the V6 Coma GCl dataset and are shown in Figure 4.18.

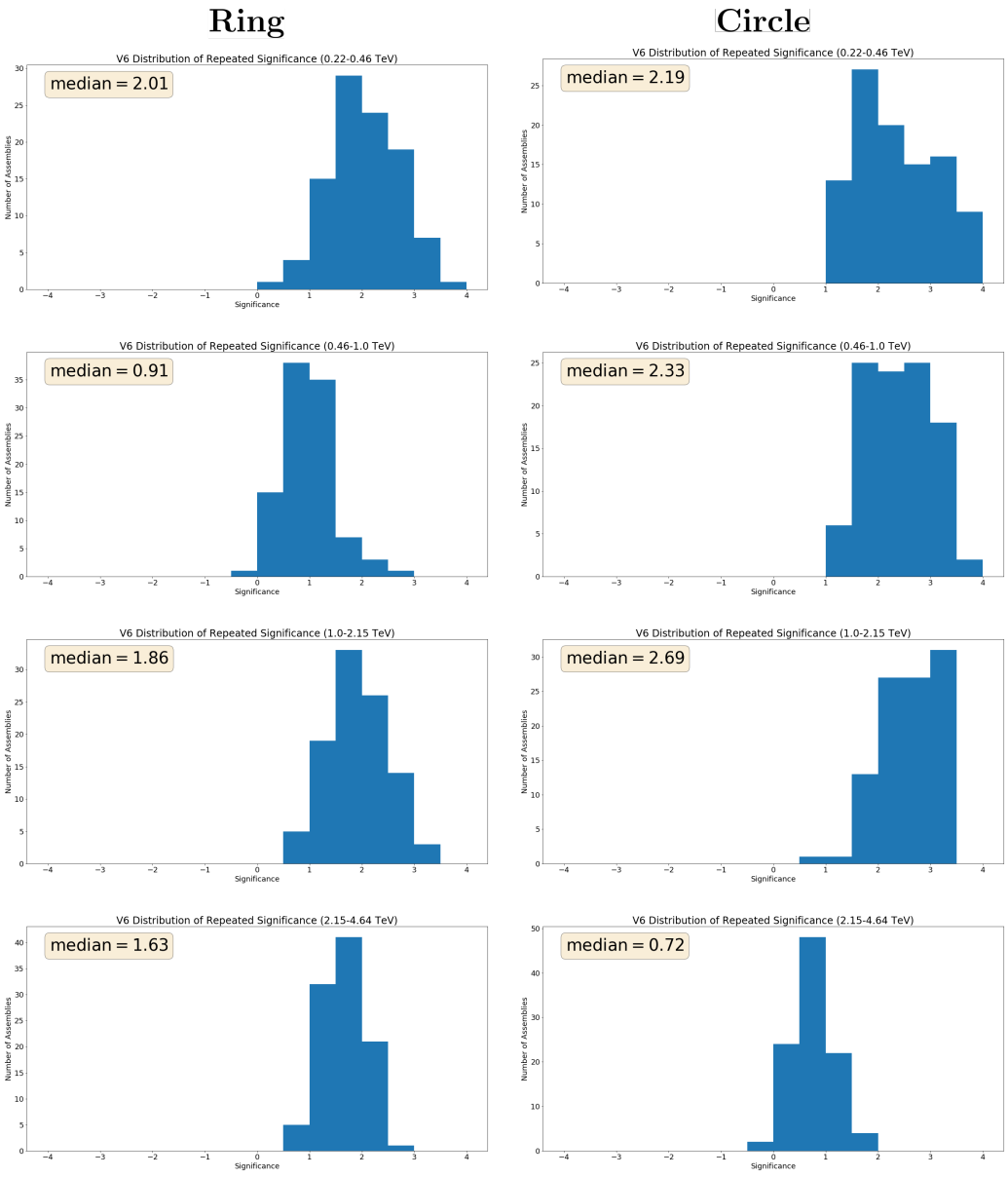

Figure 4.18: Histograms of 100 iterations determining the integrated significance of the ring and circle regions for the V6 Coma GCl dataset in different energy bins. First row: 220 GeV−460 GeV. Second row: 460 GeV−1 TeV. Third row: 1 TeV−2.2 TeV. Fourth row: 2.2 TeV−4.6 TeV.

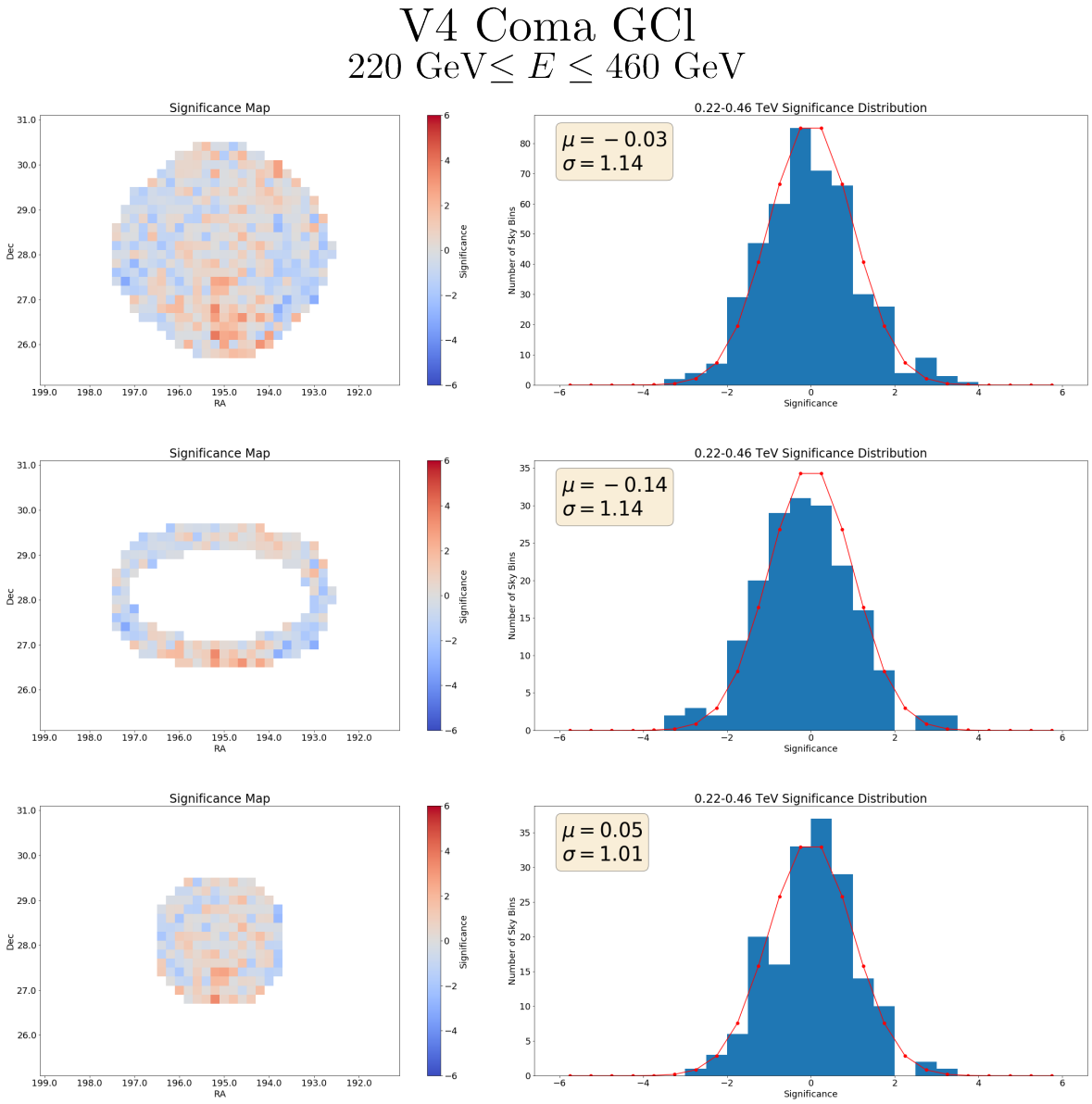

Figure 4.19: The significance skymap (left) and distribution of significance bins (right) for the V4 Coma GCl dataset over the energy range 220 GeV−460 GeV for three tested regions. Bins contained in the full skymap are shown in the first row, while only those contained in the tested virial shock ring and central 1.5° radius are shown in the second and third rows, respectively.

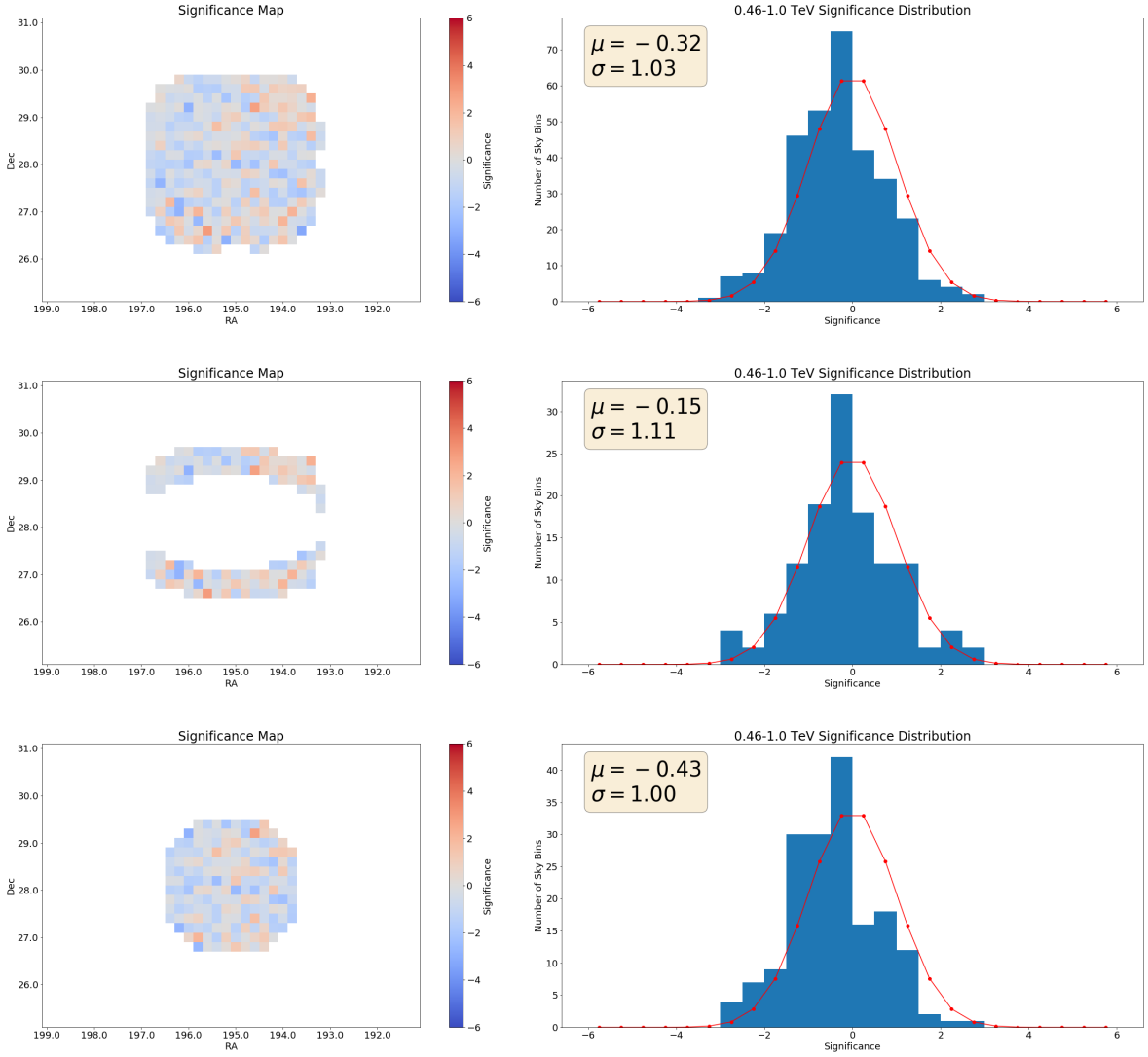

Figure 4.20: The significance skymap (left) and distribution of significance bins (right) for the V4 Coma GCl dataset over the energy range 460 GeV−1 TeV for three tested regions. Bins contained in the full skymap are shown in the first row, while only those contained in the tested virial shock ring and central 1.5° radius are shown in the second and third rows, respectively.

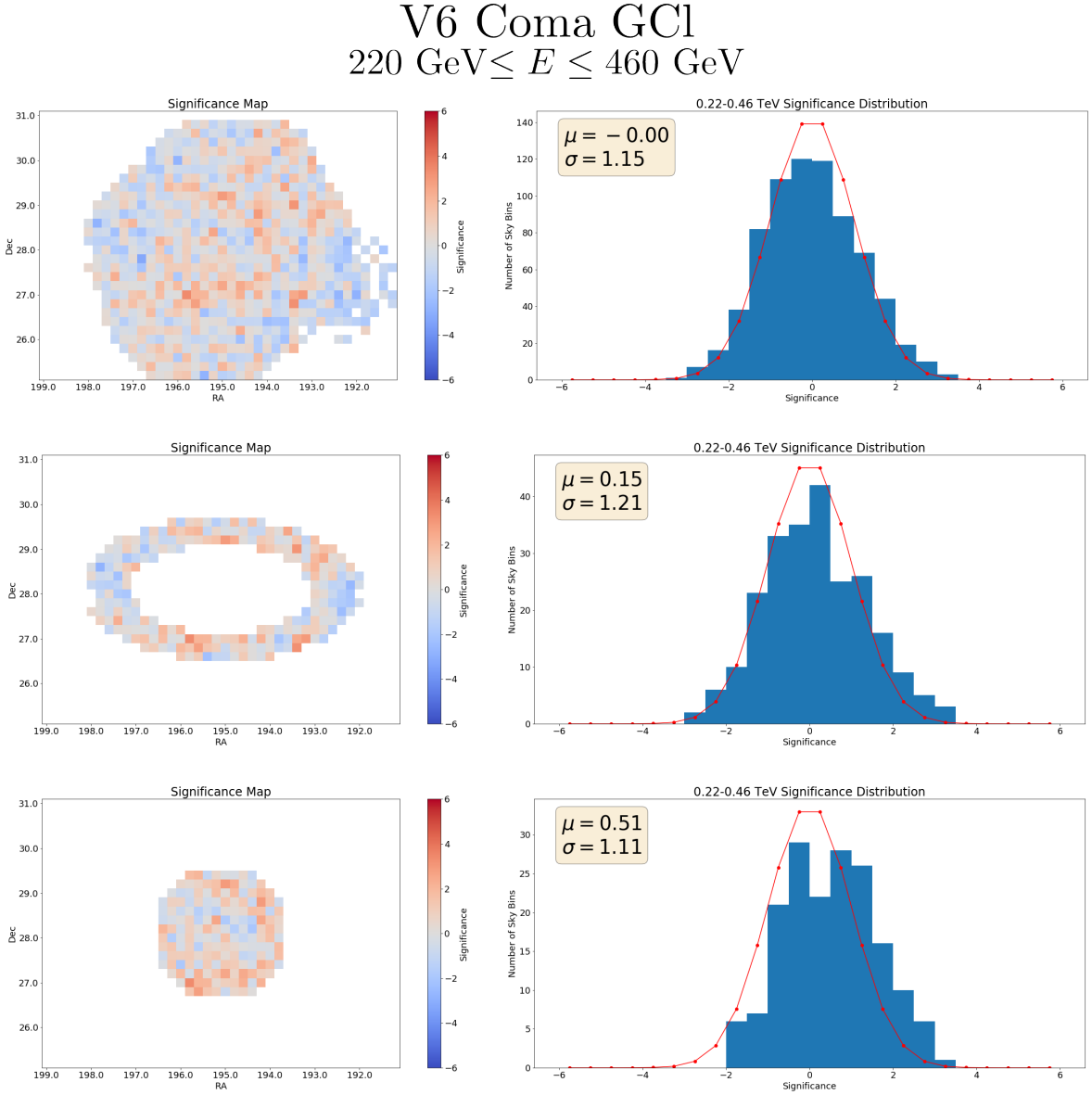

Figure 4.21: The significance skymap (left) and distribution of significance bins (right) for the V6 Coma GCl dataset over the energy range 220 GeV−460 GeV for three tested regions. Bins contained in the full skymap are shown in the first row, while only those contained in the tested virial shock ring and central 1.5° radius are shown in the second and third rows, respectively.

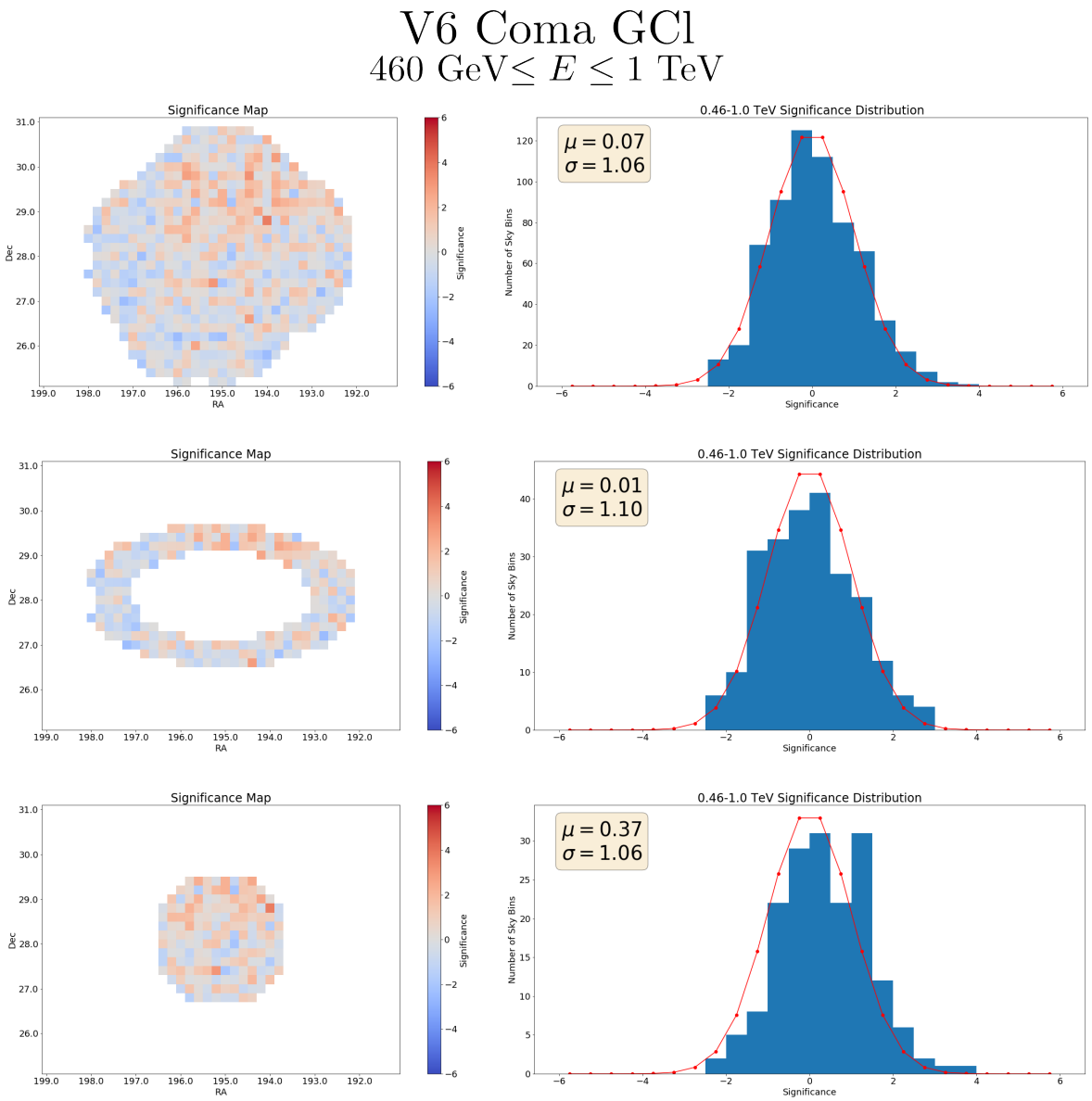

Figure 4.22: The significance skymap (left) and distribution of significance bins (right) for the V6 Coma GCl dataset over the energy range 460 GeV−1 TeV for three tested regions. Bins contained in the full skymap are shown in the first row, while only those contained in the tested virial shock ring and central 1.5° radius are shown in the second and third rows, respectively.

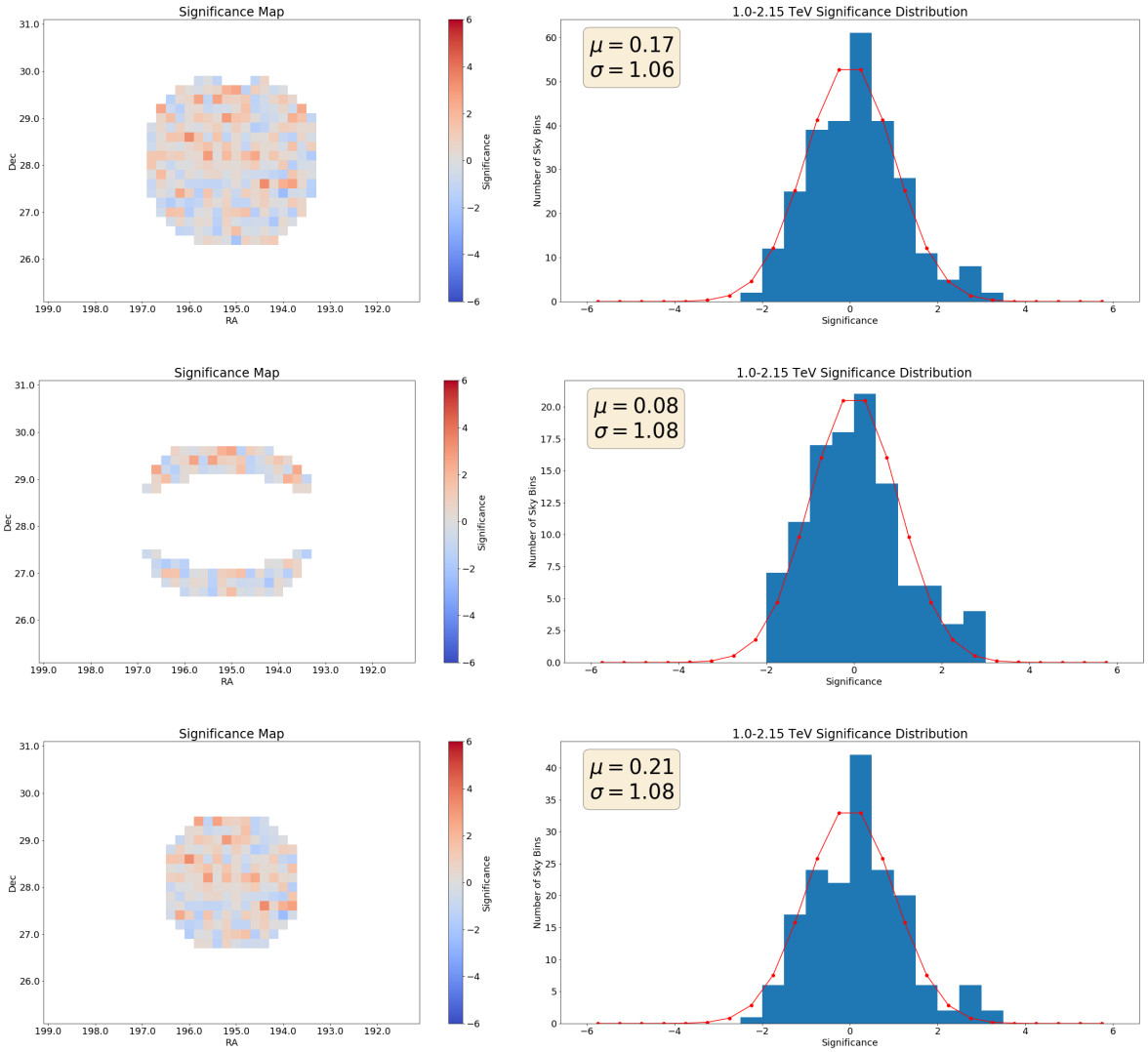

Figure 4.23: The significance skymap (left) and distribution of significance bins (right) for the V6 Coma GCl dataset over the energy range 1 TeV−2.2 TeV for three tested regions. Bins contained in the full skymap are shown in the first row, while only those contained in the tested virial shock ring and central 1.5° radius are shown in the second and third rows, respectively.

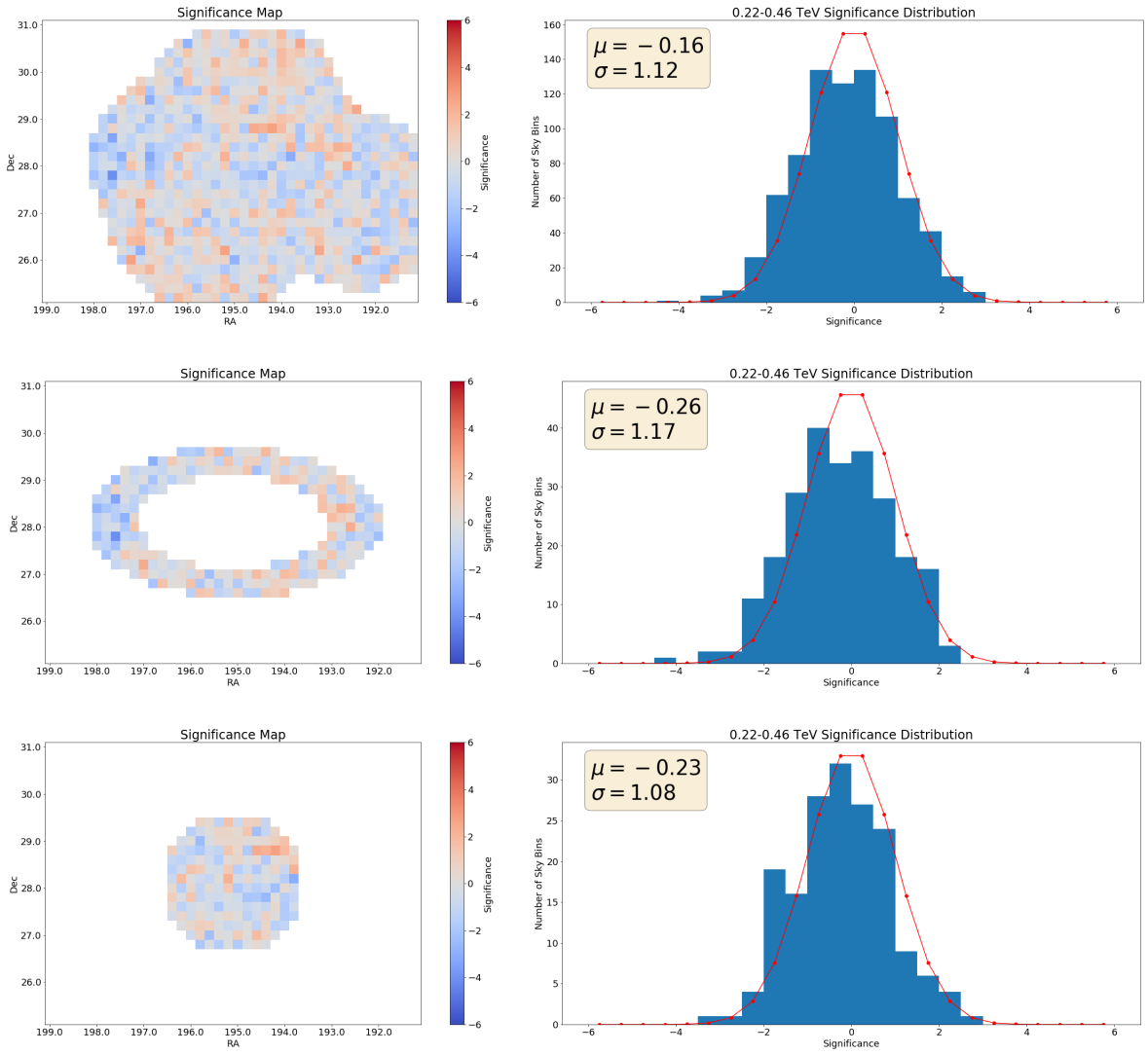

Figure 4.24: The significance skymap (left) and distribution of significance bins (right) for the V6 mimic #1 dataset over the energy range 220 GeV−460 GeV for three tested regions. Bins contained in the full skymap are shown in the first row, while only those contained in the tested virial shock ring and central 1.5° radius are shown in the second and third rows, respectively.

V6 Mimic #1
460 GeV$\leq E \leq$ 1 TeV

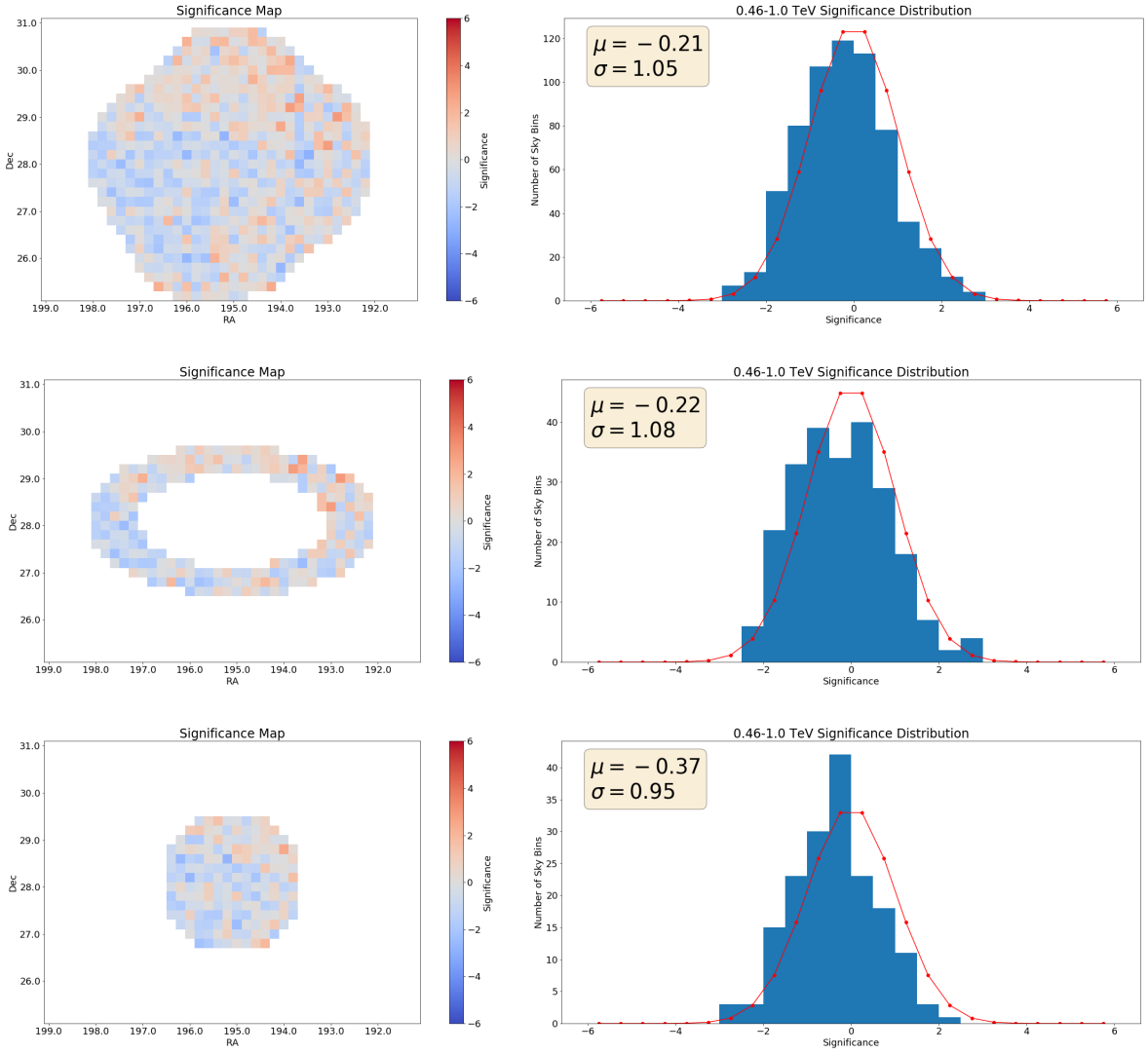

Figure 4.25: The significance skymap (left) and distribution of significance bins (right) for the V6 mimic #1 dataset over the energy range 460 GeV−1 TeV for three tested regions. Bins contained in the full skymap are shown in the first row, while only those contained in the tested virial shock ring and central 1.5° radius are shown in the second and third rows, respectively.

V6 Mimic #1
1 TeV$\leq E \leq$ 2.2 TeV

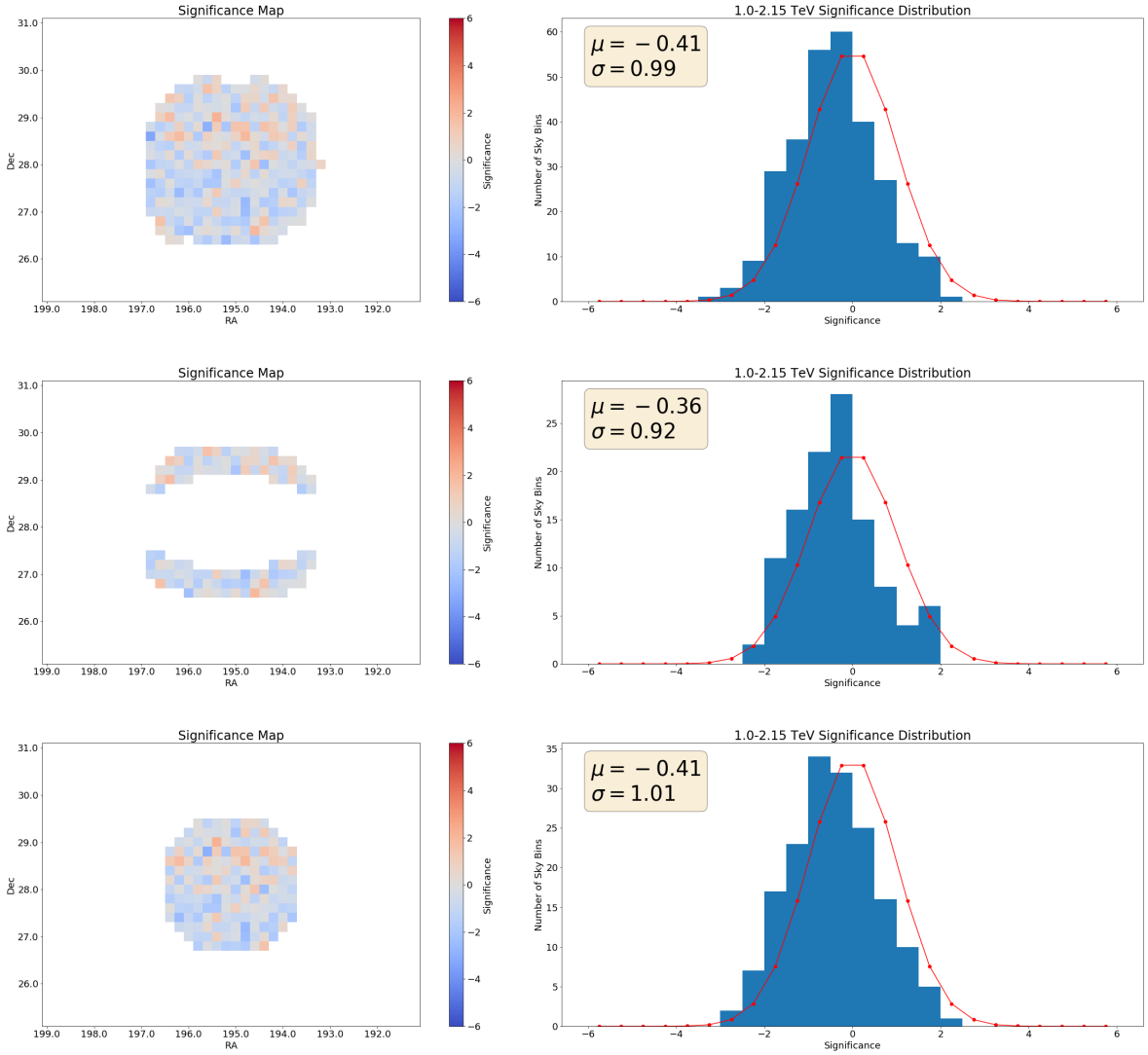

Figure 4.26: The significance skymap (left) and distribution of significance bins (right) for the V6 mimic #1 dataset over the energy range 1 TeV−2.2 TeV for three tested regions. Bins contained in the full skymap are shown in the first row, while only those contained in the tested virial shock ring and central 1.5° radius are shown in the second and third rows, respectively.

V6 Mimic #2

220 GeV$\leq E \leq$ 460 GeV

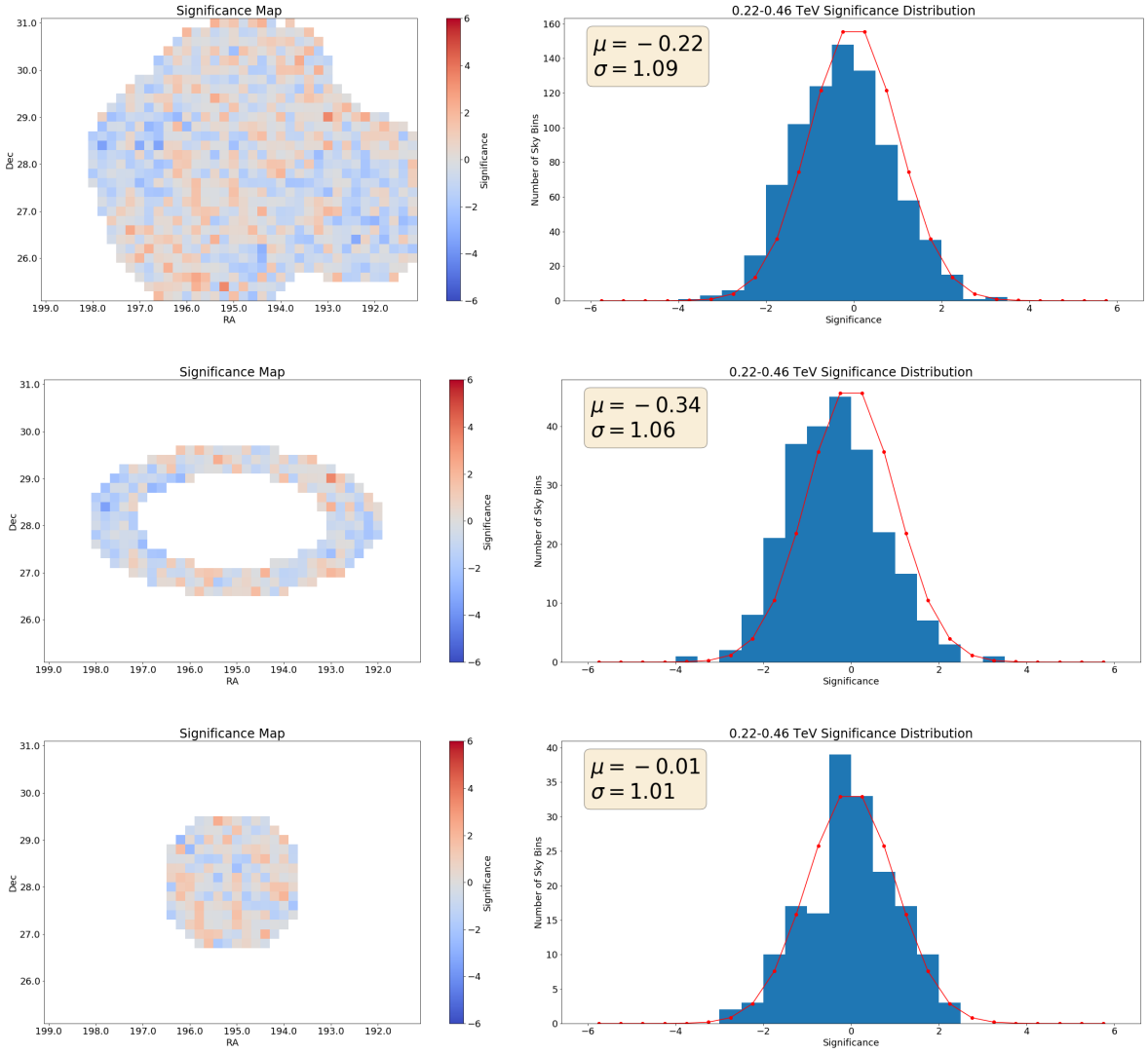

Figure 4.27: The significance skymap (left) and distribution of significance bins (right) for the V6 mimic #2 dataset over the energy range 220 GeV−460 GeV for three tested regions. Bins contained in the full skymap are shown in the first row, while only those contained in the tested virial shock ring and central 1.5° radius are shown in the second and third rows, respectively.

V6 Mimic #2
460 GeV$\leq E \leq$ 1 TeV

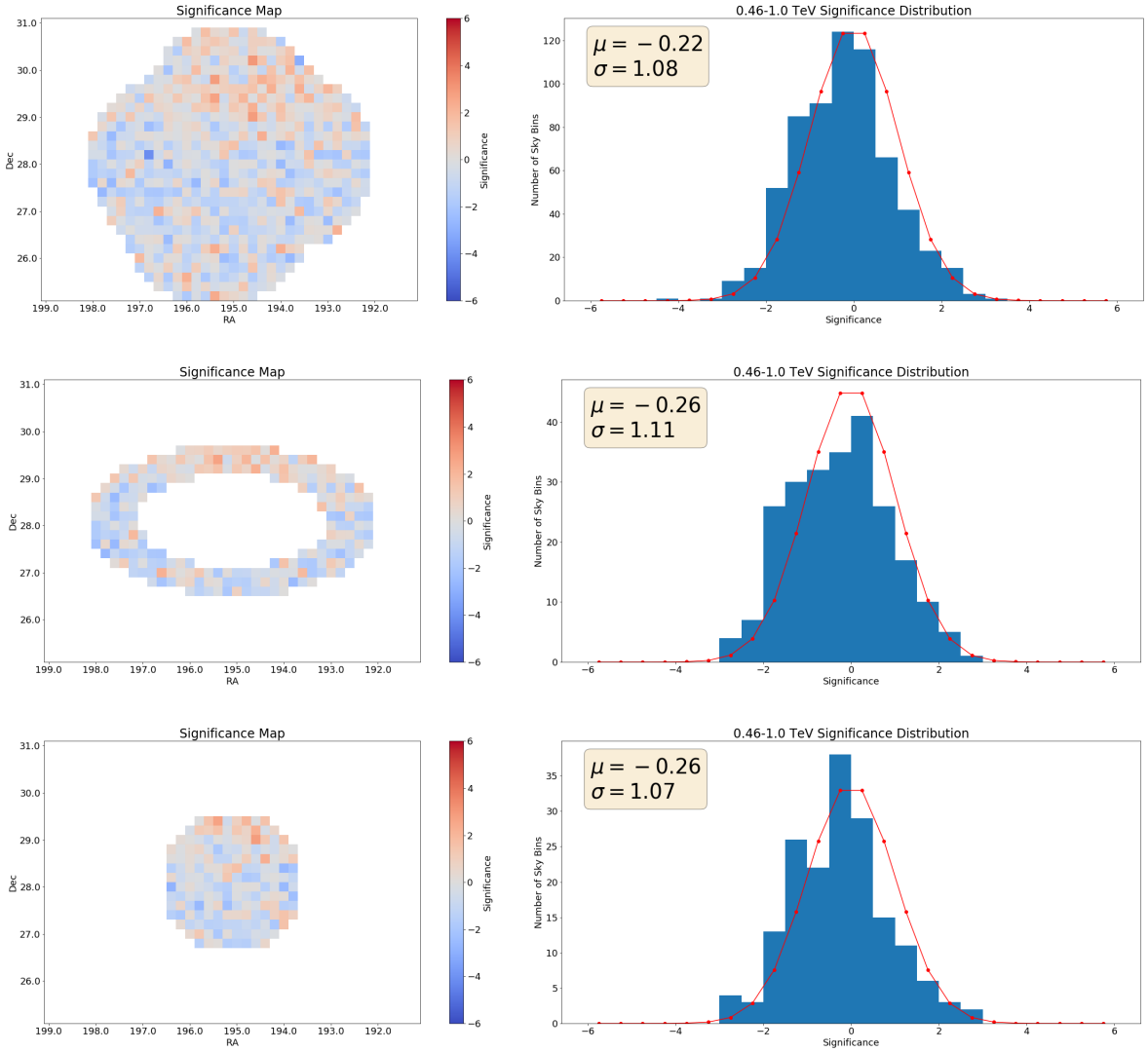

Figure 4.28: The significance skymap (left) and distribution of significance bins (right) for the V6 mimic #2 dataset over the energy range 460 GeV−1 TeV for three tested regions. Bins contained in the full skymap are shown in the first row, while only those contained in the tested virial shock ring and central 1.5° radius are shown in the second and third rows, respectively.

V6 Mimic #2
1 TeV$\leq E \leq$ 2.2 TeV

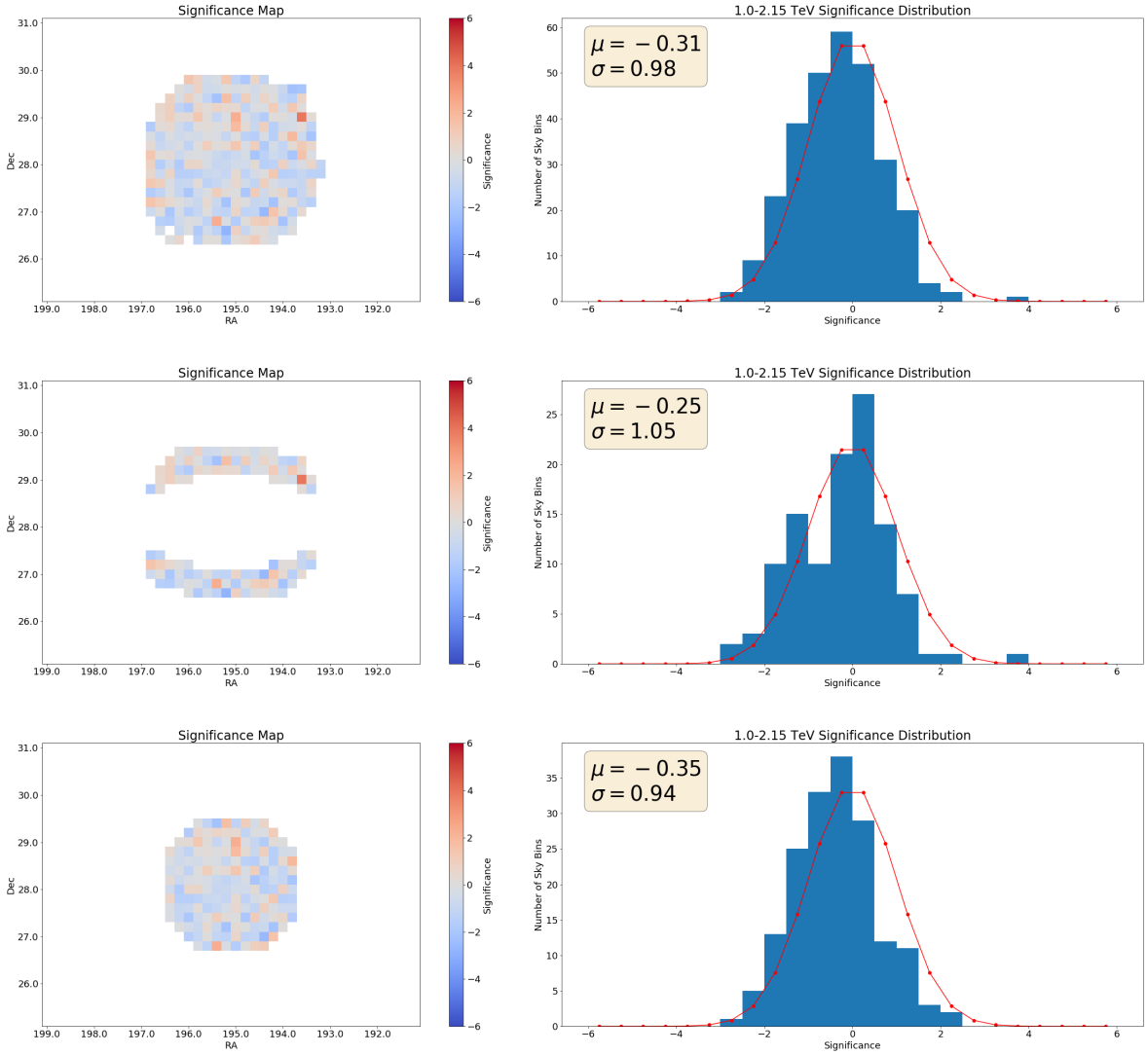

Figure 4.29: The significance skymap (left) and distribution of significance bins (right) for the V6 mimic #2 dataset over the energy range 1 TeV−2.2 TeV for three tested regions. Bins contained in the full skymap are shown in the first row, while only those contained in the tested virial shock ring and central 1.5° radius are shown in the second and third rows, respectively.

4.2 Dragonfly44

Dragonfly 44 is located nearby the Coma GCl's center ($\sim 1^\circ$ south in declination) and therefore some of the Coma GCl exposure overlaps. From 2017-2020, the VERITAS observations of the Coma GCl region had exposure within $\sim 1^\circ$ of Dragonfly 44 which amounts to 9 and 11.3 hours of quality data (A/B weather, four telescopes) in the V4 and V6 epochs, respectively. These observations are analyzed with the Eventdisplay software using "standard" box cuts simulated for a point source ($\sim 0.1^\circ$ radius) with at least two telescopes required to observe an event. Since some of the available observations have a pointing direction $\sim 1^\circ$ away from Dragonfly 44, and the radial acceptance is expected to be significantly affected beyond this distance, the use of the ring-background method for this data is sensitive to inaccuracies in the radial acceptance function used and therefore the reflected region background method is used with six regions selected in each observation from which to sample the background.

The 99% confidence level upper limit (assuming a Gaussian distribution) on excess γ-ray-like counts in a defined energy range is determined and translated into a flux upper limit from the formula

$$N_\gamma(E_{max} \geq E \geq E_{min}) = T_{obs} \times \frac{\int_{E_{min}}^{E_{max}} A_{eff}(E) \frac{dN_\gamma}{dE} dE}{\int_{E_{min}}^{E_{max}} \frac{dN_\gamma}{dE} dE} \times \Phi_\gamma(E_{max} \geq E \geq E_{min})$$

where T_{obs} is the total observing time, $\frac{dN_\gamma}{dE}$ is the differential energy spectrum, and A_{eff} is the simulated effective area of the telescope array which is dependent on zenith angle, pointing offset, and cut selections. The differential energy spectrum is assumed to obey a power-law spectrum with spectral index $\Gamma = 2.4$,

$$\frac{dN_\gamma}{dE} \propto E^{-\Gamma}$$

The resulting energy binned differential flux upper limits are shown in table 4.5. An analysis of the V6 data expectedly provides stronger upper limits than for the V4 data.

Constraints on the WIMP from indirect detection are derived from the differential flux observed, and the J-factor of the observation (see Section 2.2.3). The J-factor for Dragon-

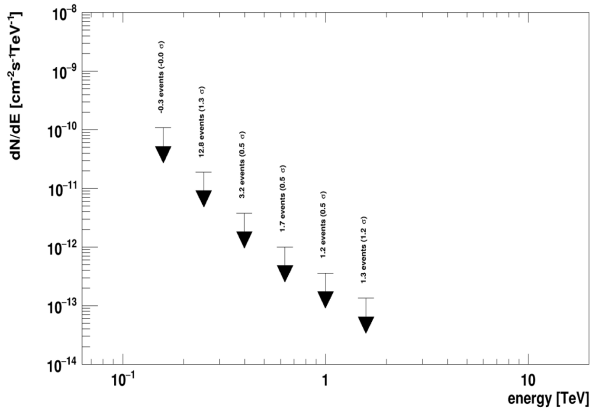

Figure 4.30: V6 upper limits on the differential flux are shown for an 0.1° integration radius around Dragonfly 44.

fly 44 is not known, and estimations would be subject to very large uncertainties. Therefore, a direct upper limit constraining the WIMP is not performed, and instead the differential flux upper limits are determined which are presented in Table 4.5 and shown in Figure 4.30. To compare the competitiveness of the observed γ-ray flux with other VERITAS observations of dark matter indirect detection targets, the 95% confidence level flux integral upper limits (above 300 GeV) are produced resulting in the values of 1.3×10^{-12} and 8.5×10^{-13} cm^{-2} s^{-1} for the V4 and V6 datasets, respectively. These upper limits are roughly $\sim 2-8$ times larger than those derived from local dwarf spheroidal galaxies (dSphs), and therefore in order to be competitive, the required J-factor must be larger than those of the dSphs by an equivalent factor [AAB17]. This means that an improved cross sectional upper limit requires Dragonfly 44 to have a J-factor approximately $\sim 2-8$ times larger than $\sim 10^{19}$ GeV^2 cm^{-5}. Since the dSph upper limits on the annihilation cross section are about two orders of magnitude away from the thermal relic abundance value ($\langle \sigma v \rangle \approx 10^{-26}$ cm^3 s^{-1}), then the DF44 J-factor would have to be approximately $\sim (2-8) \times 10^{21}$ GeV^2 cm^{-5} to reach the thermal relic value.

Table 4.5: Dragonfly 44 Results

	Epoch	
	V4	V6
Total Exposure	9 hr	11.3 hr
Weather Grade	A/B	A/B
Number of Telescopes	4	4
Differential Flux Upper Limits (99% CL)	$(\mathrm{cm}^2 \cdot \mathrm{s} \cdot \mathrm{TeV})^{-1}$	
$0.2 - 0.32$ TeV	9.6×10^{-11}	1.9×10^{-11}
$0.32 - 0.5$ TeV	8.0×10^{-12}	3.8×10^{-12}
$0.5 - 0.79$ TeV	1.1×10^{-12}	1.0×10^{-12}
$0.79 - 1.26$ TeV	9.1×10^{-13}	3.6×10^{-13}
$1.26 - 2.0$ TeV	3.1×10^{-13}	1.3×10^{-13}

CHAPTER 5

The Schwarzschild-Couder Telescope Optical Alignment System

5.1 The Cherenkov Telescope Array

The next generation IACT γ-ray observatory, the Cherenkov Telescope Array (CTA), is currently in development (see Figure 5.1). The CTA project is a multinational collaborative project designed to achieve an order of magnitude improvement in sensitivity for the current core energy range of 100 GeV-10 TeV compared to current IACT arrays such as VERITAS, as well as expand the energy range below 20 GeV and to more than 300 TeV [AAA13a]. CTA will make use of three sizes of Cherenkov telescopes: large size telescopes (LSTs) with a reflector diameter of $\sim$ 23m, medium size telescopes (MSTs) with a reflector diameter of $\sim 9 - 12$m, and small size telescopes (SSTs) with a reflector diameter of $\sim$ 4m. The LSTs provide sensitivity at the lowest energies by capturing enough of the dim Cherenkov light to reach a level above the trigger threshold, while the SSTs provide sensitivity at the highest energies by covering a large footprint ($\sim$ 10 km^2) to observe more of the low flux γ-rays which have Cherenkov showers that are bright enough to be observed with smaller dish diameters. The MSTs are responsible for the core energy range ($\sim$ 100 GeV$-$10 TeV) and are therefore the project's telescope class with an arguably guaranteed scientific return.

The CTA Observatory will operate as an open, proposal-driven observatory consisting of an array in each of the northern and southern hemispheres in order to provide full sky coverage. The northern hemisphere array is located at the Observatorio del Roque de los

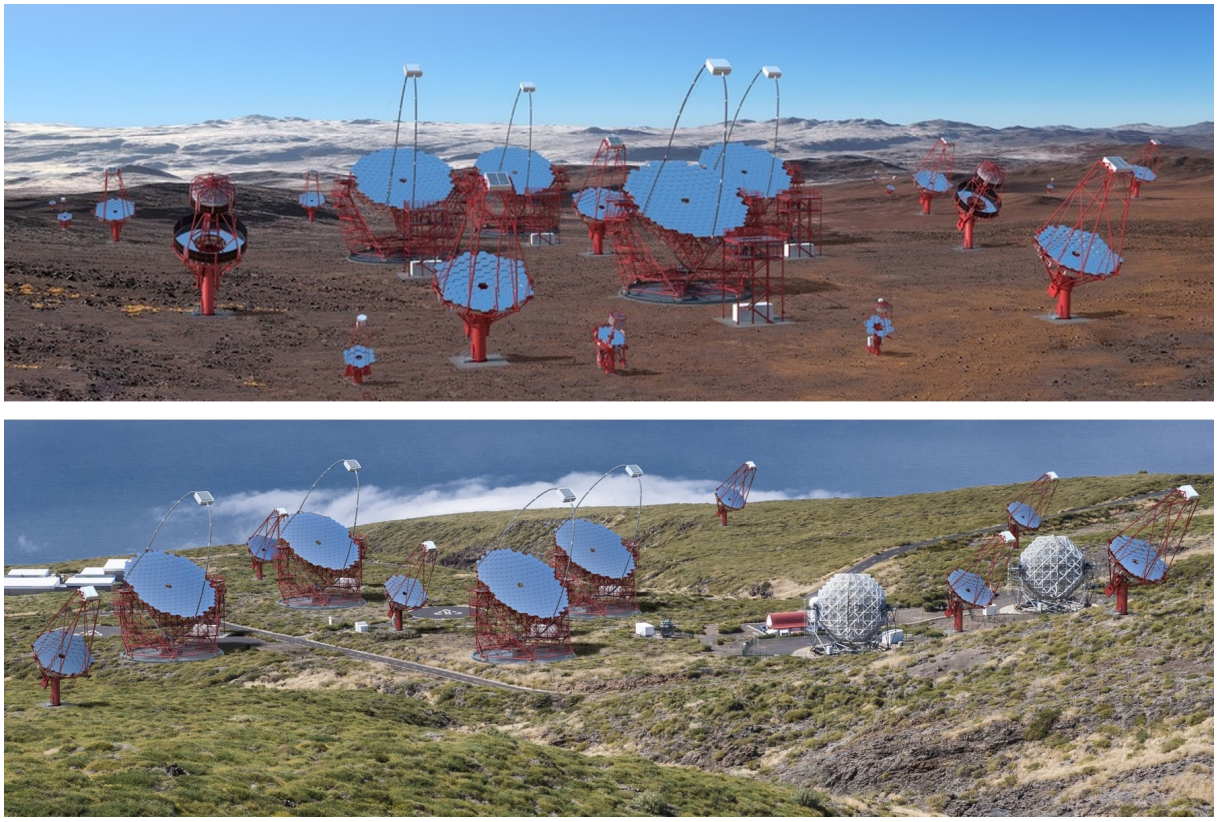

Figure 5.1: An artist's rendition of the CTA southern (top) and northern (bottom) sites which includes the various telescope candidates shown in the south, including the pSCT. Image taken from the CTA webpage (https://www.cta-observatory.org/).

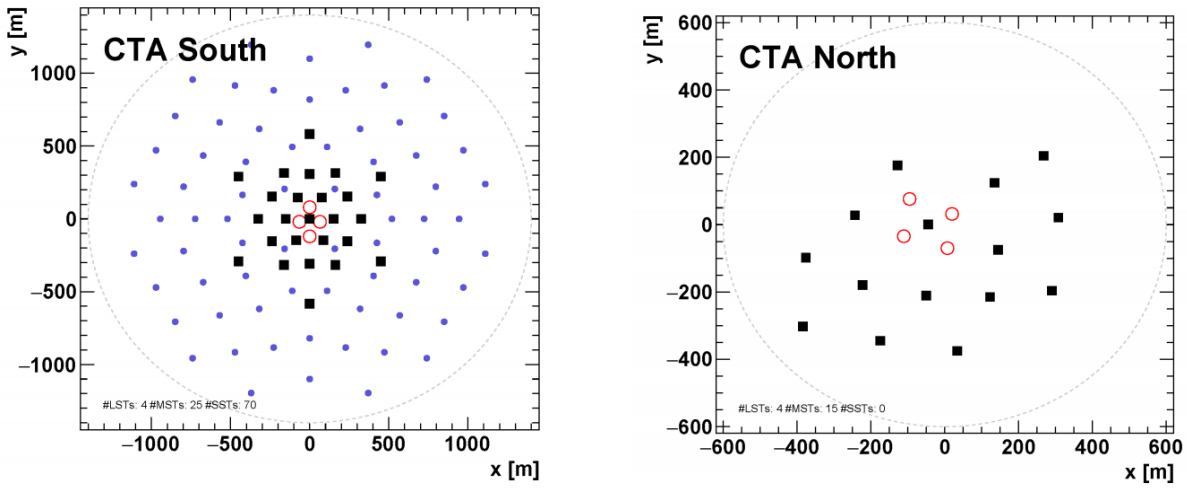

Figure 5.2: The proposed layouts of the southern and northern hemisphere CTA sites. The red circles are LSTs, the black square are MSTs, and the blue dots are SSTs. Both sites are designed to host MSTs, the workhorse telescope of the CTA observatory. The LSTs and MSTs are spaced apart approximately the radius of the Cherenkov light pool in order to ensure that contained events are sensitively observed by multiple telescopes. Image taken from [Ong18]

Muchachos on the island of La Palma, Spain (see Figure 5.1 bottom) and has already began construction efforts. The northern array is designed to be comprised of 4 LSTs and 15 MSTs and will focus on extragalactic science in the energy range of 20 GeV−20 TeV. The opacity of the Universe for γ-rays with energies larger than 20 TeV which travel cosmological distances (z$>$ 1) is much larger than 1 and, hence, the northern CTA site is not planned to host any SSTs (see Figure 5.2 right). The southern hemisphere array, which will have a view of the Galactic Center and concentrate on both, Galactic and extragalactic science, is set to be constructed near the Paranal Observatory in Chile (see Figure 5.1 top). The southern array site is planned to contain 4 LSTs, 25 MSTs, and 70 SSTs which will enable the array to span the full energy range of CTA. The layout of telescopes in the southern CTA observatory (CTAO) is shown in Figure 5.2 (left).

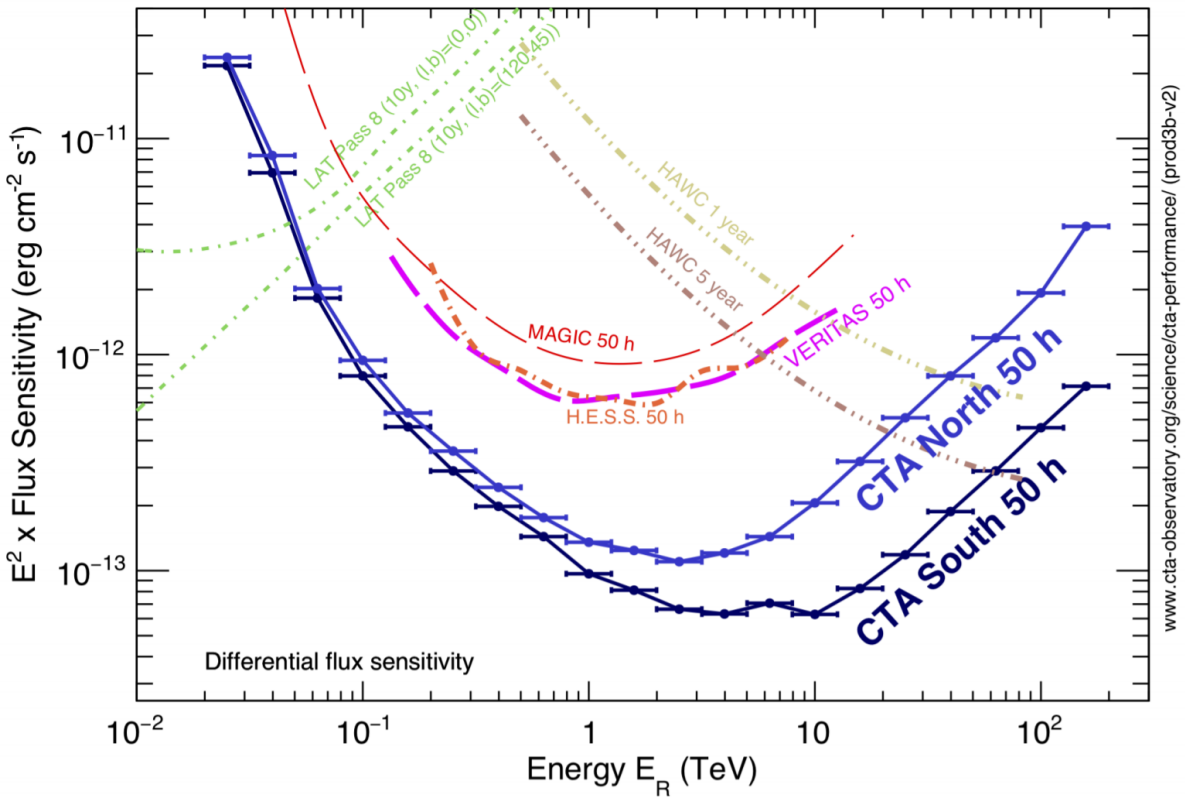

Figure 5.3: The simulated differential flux sensitivity of the CTA northern and southern arrays compared to other instruments. MAGIC and H.E.S.S. are IACT arrays like VERITAS, and HAWC is an array of water Cherenkov detectors. Only a rough comparison between IACTs & LAT and HAWC instruments is possible since the method of calculation and the criteria applied are not identical between different γ-ray detection technologies. For CTA, the differential sensitivity is defined as the minimum flux needed to obtain a 5-standard-deviation detection of a point-like source, calculated in five logarithmic energy bins per decade. At least ten detected γ-rays per energy bin are also required. Image taken from the CTA webpage (https://www.cta-observatory.org/).

In addition to increasing sensitivity and widening the observable energy range, key goals of the CTA project are to improve the angular resolution and field of view (FoV) in comparison to current IACT arrays, and to enhance sky survey and monitoring capabilities (see Figures 5.3 and 5.4). To help achieve these goals, the LSTs, MSTs, and SSTs cameras are designed to have FoVs greater than 4.5°, 7° and 8°, respectively. A wide camera FoV with high resolution imaging unaffected by aberrations has many benefits, the most obvious of which is an increased observing FoV. The angular acceptance also improves with a wider camera FoV, becoming more uniform over larger regions and reducing systematic errors. The observation of on-axis events at large impact parameters also becomes more likely, increasing the overall collecting area as well as improving the stereoscopic reconstruction process by including more telescopes. With the increased number of telescopes in CTA compared to current generation IACT arrays, the fraction of observed events with the EAS core position contained inside of the array footprint is dramatically increased. Since the photon density of γ-ray Cherenkov showers is nearly flat up to a radius of $\sim$ 130 m before falling off as roughly $1/r^2$, IACTs are spaced approximately this distance in order to simultaneously observe an event from different viewing angles and exploit stereoscopic observations to achieve high angular resolution and sensitivity. Containing an event allows for precise event triangulation and reconstruction of the arrival direction of the primary γ-ray photon compared to events which land outside of the array, assuming that the camera imaging resolution is high enough to take advantage of the stereoscopic reconstruction.

It is for these reasons that the innovative 9.7m Schwarzschild-Couder Telescope (SCT) is an especially suitable medium-sized telescope for CTA (see Figure 5.5). The SCT has a two-mirror, aplanatic optical system (OS) which corrects spherical and comatic aberrations, obtaining a nearly constant point spread function (PSF) over its 8° FoV. The SCT's demagnifying secondary mirror also significantly reduces the plate scale compared to the conventional Davies-Cotton Telescope (DCT), enabling the use of a smaller camera (0.8m vs 2.5m) which is compatible with the less expensive silicon photo-multipliers (SiPM) compared

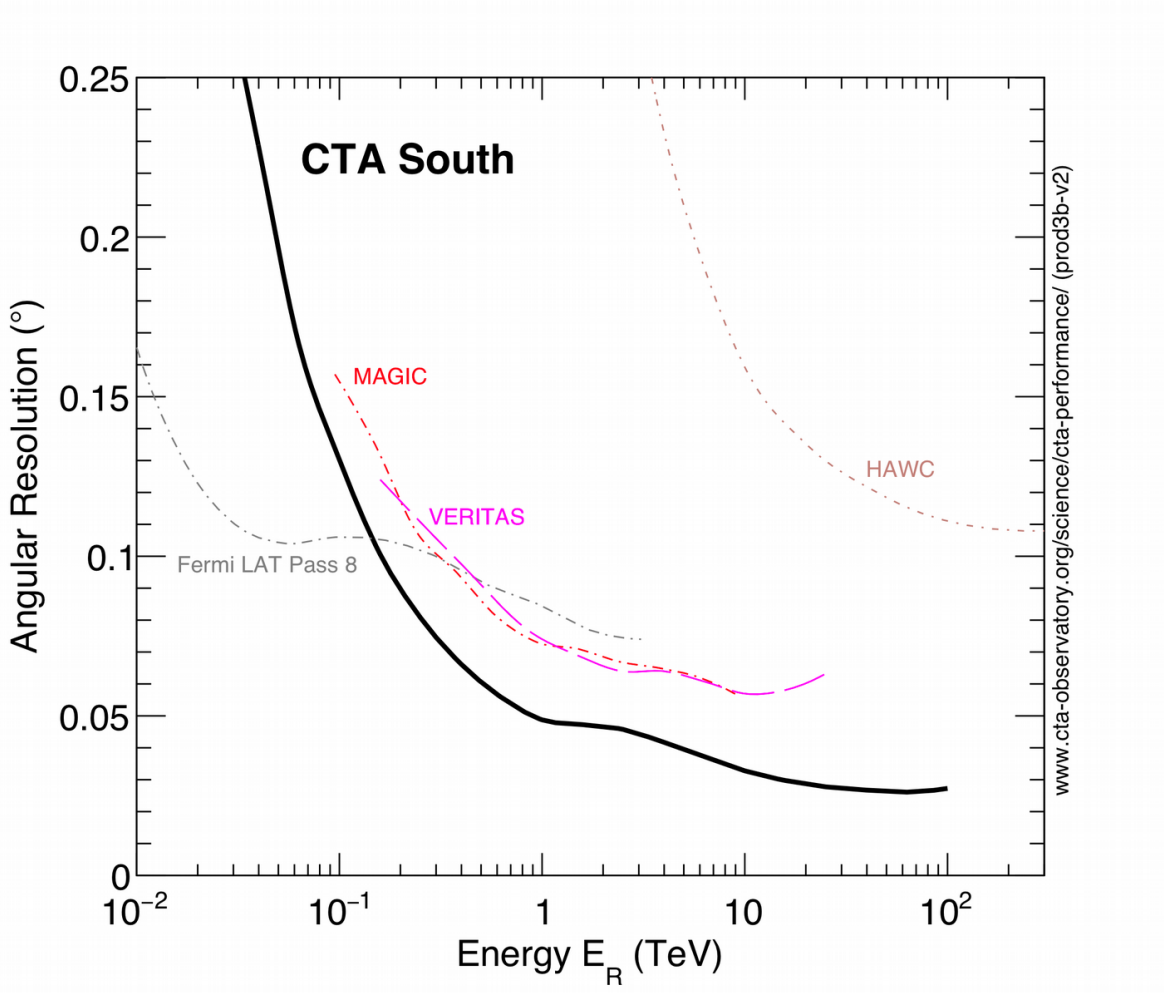

Figure 5.4: The simulated angular resolution of the CTA southern array vs. the reconstructed energy, where angular resolution here is defined to be the angle within which 68% of γ-ray events are reconstructed. Image taken from the CTA webpage (https://www.cta-observatory.org/).

to the PMTs used in the DCT. The SCT camera is composed of 11,328 pixels of angular size 0.067° for a competitive, slightly higher price than the DCT camera which has ∼1,800 pixels of angular size 0.17°. The superior imaging resolution of the SCT camera in CTA results in an improved angular resolution of γ-ray events, especially for the large fraction of events in CTA which are contained, as well as a reduced amount of night-sky background noise per pixel. In addition, the SCT optical design also has a greatly improved off-axis PSF compared to the DCT, which suffers from severe comatic aberrations leading to the degradation of imaging at large field angles (see Figure 5.5). These unique characteristics, in combination with a smaller pixel size, makes an array of SCTs exceptionally suitable to achieve the CTA goals of analyzing objects with large angular extensions, performing sky surveys, and observing poorly localized VHE transients. The SCT design, which has never been implemented for an IACT, is being investigated to determine the performance benefits of such an instrument in the CTA installation. To do this, a prototype SCT (pSCT) has been constructed at the site of VERITAS observatory and is currently undergoing commissioning and performance validation and verification (see Figure 5.6).

5.2 pSCT Introduction

IACTs are relatively inexpensive astronomical instruments, however a consideration of cost-to-performance trade-offs is critically important for the construction of large arrays such as CTA. The following examines the cost-relevant features of the CTA MSTs, the 10 m aperature class instruments. The MSTs collect photons with wavelengths in the range $290-700$ nm; however, they do not operate in the diffraction limit, they do not integrate light over long exposures into individual camera pixels, and they do not have protection domes. MSTs collect incoherent Cherenkov light from atmospheric cascades at distances of $5-20$ km, with the goal to collect as much light as possible into a single pixel of the γ-ray camera during an EAS event. Despite being instruments operating with $\sim$ 400 nm photons, the optical

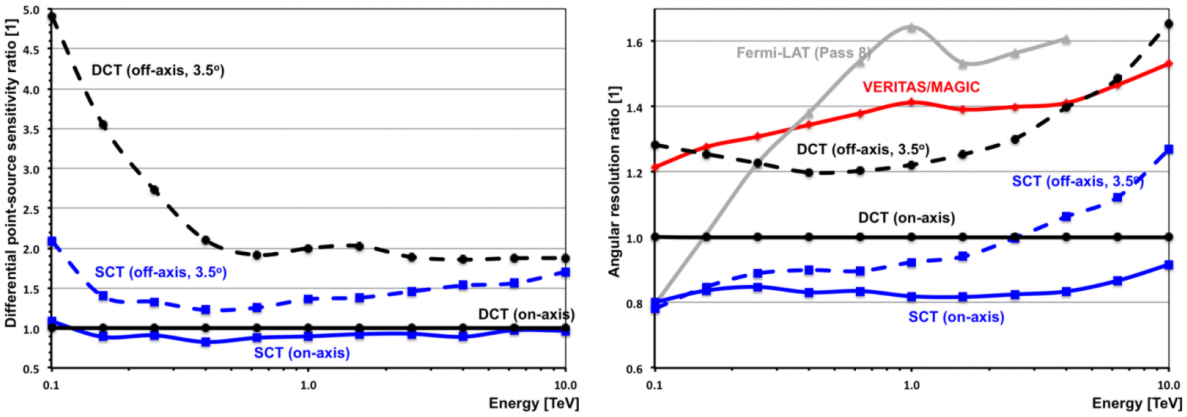

Figure 5.5: Left: The ratio of differential point source sensitivities simulated for the CTA southern array layout with the 25 MSTs as either DCTs or SCTs. The SCT configuration demonstrates significantly improved off-axis point source sensitivity at low energies. Right: The ratio of angular resolutions of different instruments compared to the CTA southern array layout with DCTs. The use of SCTs instead of DCTs offers an improvement in angular resolution similar to the CTA improvement over current generation IACT arrays.

tolerances of conventional MSTs are in the range of several mm, somewhat comparable to those of radio telescopes with several millimeters wavelength. The SCT in particular has the more demanding alignment requirement for some of its degrees of freedom in the sub-mm level, around 0.1 mm. Unlike radio telescopes, however, MSTs do not require precise pointing over a long exposure integration window. The Cherenkov light flash lasts only several nanoseconds, and therefore accurate pointing information of the telescope only needs to be known at the time of the event. The design goal of the MST optical support structure (OSS) is to maintain a stable optical PSF during 20-minute observation runs at a reduced cost, but not necessarily have high precision pointing over long exposures. This requirement can be achieved inexpensively with the use of sky cameras and an application of offline pointing corrections, meaning the constraints on the MST's OSS and telescope positioning system are significantly relaxed. The SCT's OSS is designed to maintain an acceptable PSF under various loads (gravity, wind, etc.) and allow for re-alignment of mirrors between runs as needed. For cost considerations the pSCT's currently implemented alignment system is not a true closed-loop alignment system since it utilizes lookup tables to correct for telescope deformations and maintain the PSF. A goal of the current commissioning of the pSCT is to determine the refresh rate requirement for corrective re-alignment of the SCT optical system and determine the balance between OSS rigidity and optical system re-alignment needs. IACTs also save on costs by not using a protective telescope dome, placing more importance on the longevity and maintenance costs of the mirrors and their coating and over-coating technologies. The mirror fabrication technologies suitable for the SCT implementation have only recently reached the necessary level of sophistication and relatively low cost. The pSCT will be used to evaluate the longevity of the hybrid mirror segments, as well as the two over-coating technologies.

The development of the SCT is naturally motivated by the pursuit to improve future generation IACT arrays such as CTA. Designed to achieve a performance near the theoretical limit of the IACT stereoscopic technique, the SCT's optical system has significantly improved

imaging in the wide 8° FoV by correcting comatic aberrations and minimizing astigmatism (see Figure 5.7). The SCT has a very fast optical system with the ratio of focal length to the primary mirror diameter equal to 0.58. The plate scale of the SCT is reduced by a factor of 2.86 in comparison to the DCT, making it possible to construct the telescope camera using semiconductor photo-sensors integrated with the electronics within a small camera placed between the primary and secondary mirrors (see Figure 5.6). In addition, the SCT's optical system is isochronous, which not only meets the timing requirement for the IACT technique, but may improve Cherenkov shower reconstruction capabilities compared to the asynchronous conventional DC telescopes. However these improvements come at a cost: the mirrors are highly curved and aspherical which presents a fabrication challenge, and the alignment tolerances of the optical system are stricter than in the DC design by more than a factor of ten.

This chapter of the thesis briefly describes the technical implementation of the SCT, particularly focusing on the optical system elements of both hardware and software which I provided significant contribution to while working on the project. The goal of this detailed description is to document the design choices, details of implementation, and the calibration procedures adapted for actuator modules, Stewart platforms of mirror panels, and several elements of the global alignment system.

5.3 pSCT Optical System Hardware

A full scale prototype SCT (pSCT) has been constructed at FLWO, adjacent to the VERITAS telescopes, where it is currently undergoing commissioning and evaluation. The pSCT is composed of a 9.7 m aperature primary mirror with a 4.4 m central hole, a 5.4 m demagnifying secondary mirror, and a 0.8m diameter focal plane at the effective focal length of 5.6 m. The optical system has a curved, convex focal plane in order to minimize astigmatism at the edge of the FoV [VFB07]. The mirrors, camera, and auxiliary systems are supported

Figure 5.6: The constructed prototype Schwarzschild-Couder Telescope at the Fred Lawrence Whipple Observatory near Tucson, Arizona. Image provided by photographer Deivid Ribeiro.

by a steel optical support structure, which is mounted onto the telescope positioner. The pSCT's positioner, which provides elevation and azimuth motion, is nearly identical to the positioner used in the CTA medium sized DC telescope design with the difference being a slightly shorter tower height to accommodate the already existing FLWO foundation tolerances. Baffles are mounted around both primary and secondary mirrors in order to reduce NSB contamination during observations and to protect the telescope from sunlight and safely park the pSCT during the daytime without the need for a dome. The pSCT camera is rigidly mounted to the camera frame of the OSS located between the primary and secondary mirrors. The SCT camera has a modular design with 177 slots inside its 0.8 m diameter, with each slot capable of fitting a camera module containing an 8×8 grid of SiPM pixels with pixel size 6.5×6.5 mm^2, corresponding to a pixel angular size of $0.067^\circ \times 0.067^\circ$. A prototype camera has been installed in the central 5×5 set of modules, corresponding to a square FoV with side length 2.68°, which has met the challenging requirements of delivering a high channel density with low power consumption. A camera upgrade project is now underway which will upgrade the prototype camera to the full 177 module, $11,328$ pixel camera with an 8° FoV [Meu19].

5.3.1 Mirror Panel Alignment Hardware

Producing the pSCT's primary (M1) or secondary (M2) mirrors in a monolithic fashion would be prohibitively expensive, and therefore they are segmented. The 9.7 m primary mirror is divided into 48 mirror panels positioned along two concentric rings, an inner ring (P1) consisting of 16 panels and an outer ring (P2) consisting of 32 panels. Similarly, the 5.4 m secondary mirror is made up of 24 mirror panels with the inner ring (S1) containing 8 panels and the outer ring (S2) containing 16 panels. A separation between mirror panels of 14 mm is introduced for ease of installation and mirror alignment. The alignment tolerance of the pSCT mirror panels, determined by extensive ray tracing simulations, requires a tip-tilt precision of $\sim 100\mu$rad in order for the PSF to be compatible with the pixel size of the

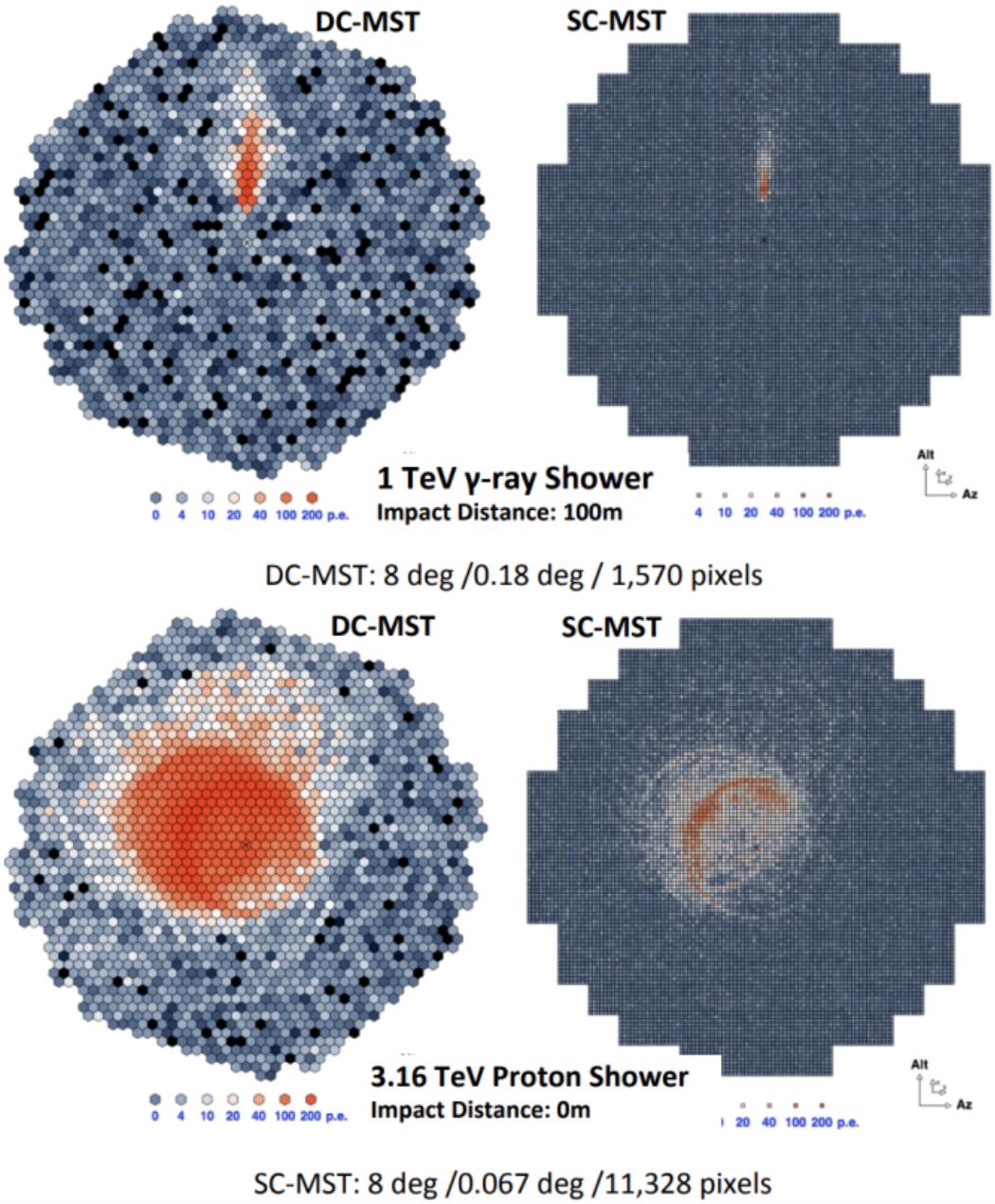

Figure 5.7: Comparison between the simulated focal plane images of the Davies-Cotton (left) and Schwarzschild-Couder (right) telescopes for 1 TeV γ-ray (top) and 3 TeV proton (bottom) primary particles. Images based on simulations performed in [WJD16].

camera [OBD15]. To achieve this, each mirror panel is mounted onto a hexapod Stewart platform (SP) which itself is mounted onto an aluminum triangular base that interfaces to the telescope OSS. The SP enables the mirror panel to be positioned freely throughout the space of its three translational and three rotational degrees of freedom (DoF), limited only by the 3 μm motion increment and 63 mm range of the six actuators which comprise it, corresponding to a tip-tilt angular resolution of ~ 1 arcsec. A magnetic encoder attached to the actuator motor is capable of detecting relative motion of the motor, but has a degenerate voltage reading every two hundred steps (one revolution or ~ 0.6 mm motor shaft motion) and, therefore, software tracking is required to maintain the absolute actuator state. Both the actuator stepping motor and the encoder are housed in a waterproof aluminum cylinder. The six SP actuators interface with the backside of the mirror panel and the triangle base through six Cardan joints, precisely machined from aluminum to minimize hysteresis effects. A table with details of the SP hardware is shown in Table 5.1.

Table 5.1: Stewart Platform Hardware Elements

Device	**Description**
Actuator	Manufacturer: Haydon Kerk Hybrid Stepper Captive Linear Actuator 3 μm step size, 50 mm travel range
Encoder and Cabling	Manufacturer: Binder USA 1.8° angular resolution (200 steps per revolution)
Controller Board	Manufacturer: UCLA custom design Includes Gumstix Overo microcomputer
Machined Parts	Manufacturer: Share Machine Actuator and MPCB housing, Cardan joints, triangle base

To guide the panel-to-panel alignment system (P2PAS) in assembling the primary and secondary mirror surfaces, each panel is equipped with mirror panel edge sensors (MPES),

	Primary mirror	Secondary mirror
Global alignment	Value	Value
Translation $\perp$ to optical axis	10 mm	10 mm
Translation $\parallel$ to optical axis	17 mm	0.5 mm
Tilt	15 mrad	0.15 mrad
Panel-to-panel alignment	Standard deviation	Standard deviation
Translation $\perp$ to optical axis	2.2 mm	1.1 mm
Translation $\parallel$ to optical axis	17mm	4 mm
Rotation around tangent axis	0.1 mrad	0.2 mrad
Rotation around radial axis	0.1 mrad	0.3 mrad
Rotation around normal axis	16.2 mrad	118 mrad

Table 5.2: A list of the isolated transformations of pSCT optical system elements corresponding to an increase in the PSF to 1 arcmin on-axis. The most sensitive degrees of freedom are the tip and tilt of the individual panels in both M1 & M2, and also the tip and tilt of M2 as a whole.

which consist of a laser-camera pair of units mounted across neighboring panel edges. The laser unit contains a laser diode directed through a 300 μm diameter pinhole towards the camera unit, which contains a 12 mm opal diffuser screen and a 0.3 Megapixel web camera. The MPES provides a measurement of the position of the laser light centroid with $< 10\mu$m resolution over an imaging screen area of ~ 1 cm^2. Both units have a weatherproof enclosure and are powered by the same USB connection used to communicate with the camera. The MPES coordinate measurements provide a two dimensional projection of the relative positions between panels. Three MPES are mounted in mutually orthogonal orientations along each long edge, such that all six degrees of freedom are measured with ~ 10 μm resolution, sufficient to measure the relative alignment between neighboring panels. Additional MPES are placed along short edges interconnecting the two rings of different panel types in both M1 & M2 to further constrain alignment (see Figure 5.8). The total number of MPES per mirror (208 for the M1, 104 for the M2) overconstrains the P2PAS system by roughly 40%, providing flexibility and redundancy in achieving alignment in the event of malfunctioning MPES hardware. The MPES measurements are used to guide the initial alignment of the mirror surfaces once the mirrors are attached to the OSS and are also available to monitor and correct for misalignments which may originate from a variety of causes, including OSS deformations from thermal expansion, varying gravitational loads for different pointing directions, hysteresis of SP actuators, and possibly other sources. The pSCT project will investigate these sources of misalignment and determine the cases which require realignment of the panels as well as the necessary realignment frequency.

Communication with a panel's actuators and MPES is performed through a mirror panel controller board (MPCB) which is locally attached to the triangular base of each panel. The MPCB contains a Gumstix Overo microcomputer with Ethernet connectivity, six USB input connections for communication with and powering of the MPES, an additional USB connection with a USB-to-Ethernet adapter, six actuator interfacing ports through which actuator motion output signals are sent and encoder voltage measurements are performed,

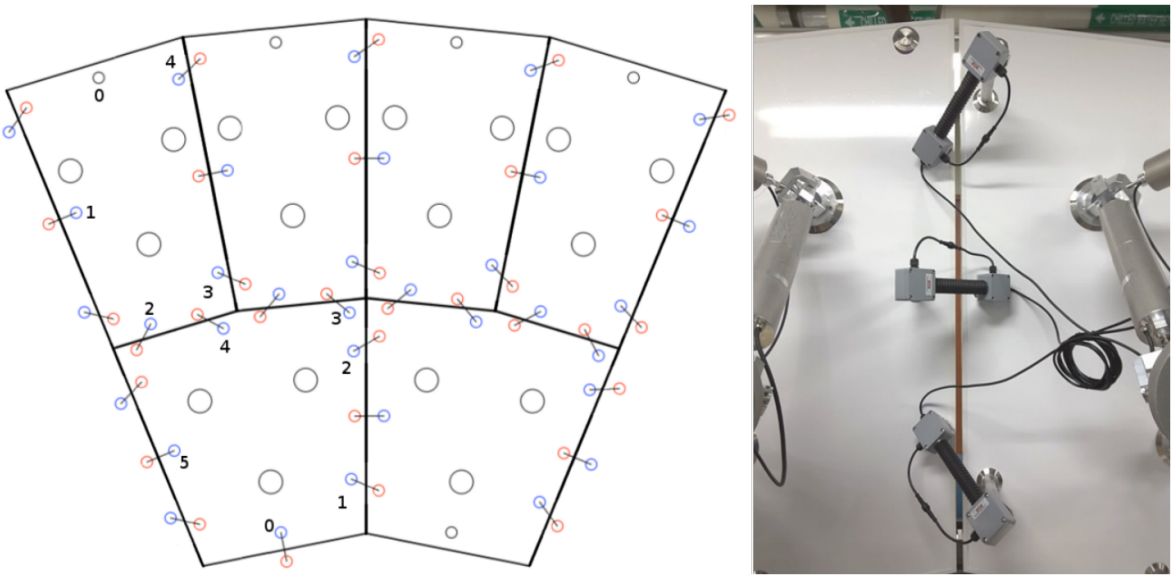

Figure 5.8: Left: Schematic showing the orientation and numbering of MPES mounted on the backside of the primary mirror panels. Blue circles correspond to the camera side of the MPES, while red circles correspond to the laser side. Right: Image of a long edge between two mirror panels. The MPES are oriented in mutually orthogonal directions, such that all six degrees of freedom between the panel positions are sensitively measured.

and a port to measure the voltage of a connected external temperature sensor. The collection of a mirror panel with its accompanied SP, MPES, MPCB, and triangle base is defined as a mirror panel module (MPM). The MPMs are modular in design, such that each panel's MPCB is responsible for the signal processing and software control of its local actuators, MPES, and temperature, and each MPM is capable of operating independently from other MPMs. MPM components which have a hardware failure can simply be individually replaced in order to resume a healthy state of the MPM. Alignment of the overall primary and secondary mirror surfaces is performed by a central computer which communicates directions to the individual MPCB microcomputers which control their respective MPMs.

5.3.2 Global Alignment Hardware

While the P2PAS is responsible for achieving continuous primary and secondary mirror figures from the individual mirror panels, the global alignment system (GAS) is designed to mutually align M1, M2 and the focal plane of the γ-ray camera and continuously monitor their relative positioning with respect to the sky for offline pointing corrections. To achieve the designed optical PSF, the alignment tolerances on these global elements are modest (in the several mm range, see Table 5.2). The only relatively demanding requirements are on the M2 tip and tilt, and the relative positioning of the M2 and the camera focal plane along the optical axis. These stricter requirements are necessary to point the telescope with an accuracy of 10 arcsec averaged over a period of a few seconds in order to accumulate an image of the sky for offline astrometry.

The GAS schematic is shown in Figure 5.9 (left). It consists of two optical tables (OTs) with optical equipment (see Figure 5.10) mounted on the OSS at the centers of the M1 (OT1) and M2 (OT2) mirrors, the γ-ray camera optical module (COM), and a system of LEDs placed on three special panels for each M1 and M2. Each OT is equipped with a SP and MPCB, identical to those used for MPMs, but with an interfacing aluminum plate mounted on the SP instead of a mirror panel to allow for OT positioning in the telescope

OS. Both plates are machined to mount three CCD cameras and an autocollimator (AC) used to measure the tip and tilt alignment of the opposing mirror surface to the OT plane. In addition, OT1 is equipped with a laser and OT2 contains a laser rangefinder, a rear facing CCD sky camera, and two transparent targets each with a position sensitive device (PSD) to measure the OT1 laser beam position's x and y coordinates.

The GAS system is used to achieve an initial global alignment and the designed optical PSF. In particular the rangefinder, installed on the OT2 with a resolution of 0.3mm, is used to align the γ-ray camera focal plane and M2. The CCD camera installed on OT2 which views the focal plane of the γ-ray camera is the main instrument to conduct optical alignment of individual M1 and M2 panels by utilizing defocused images of bright stars (see Figure 5.16). This CCD camera is also used to track bright stars and determine the relative motion of their images with respect to the γ-ray camera. The changing gravitational load on the SCT's global optical elements during observations induces small motions between them which does not notably degrade the optical PSF, but which does significantly affect the telescope pointing. The CCD camera images of bright stars is used to create the telescope bending model, which "corrects" the telescope pointing in the tracking system so that the displacement of the stellar images on the focal plane caused by repeatable telescope OSS deformations are removed to the first order. The GAS system is also designed to provide a data stream with information on the relative positioning of the global elements of the optical system with respect to the sky, used for higher order offline pointing corrections.

The SCT γ-ray camera does not have all active degrees of freedom and cannot be re-positioned during the observations; it moves together with the telescope structure subject to a relative displacement measured to be at the level of several millimeters. The COM, which has two transparent targets with PSDs, measures four degrees of freedom of the OT1 laser beam (tip, tilt, x and y) and provides data to continuously maintain the same position of the laser beam with respect to the γ-ray camera by adjusting the OT1. The OT2 concurrently measures the position of the OT1 laser beam to maintain its own alignment with OT1 with

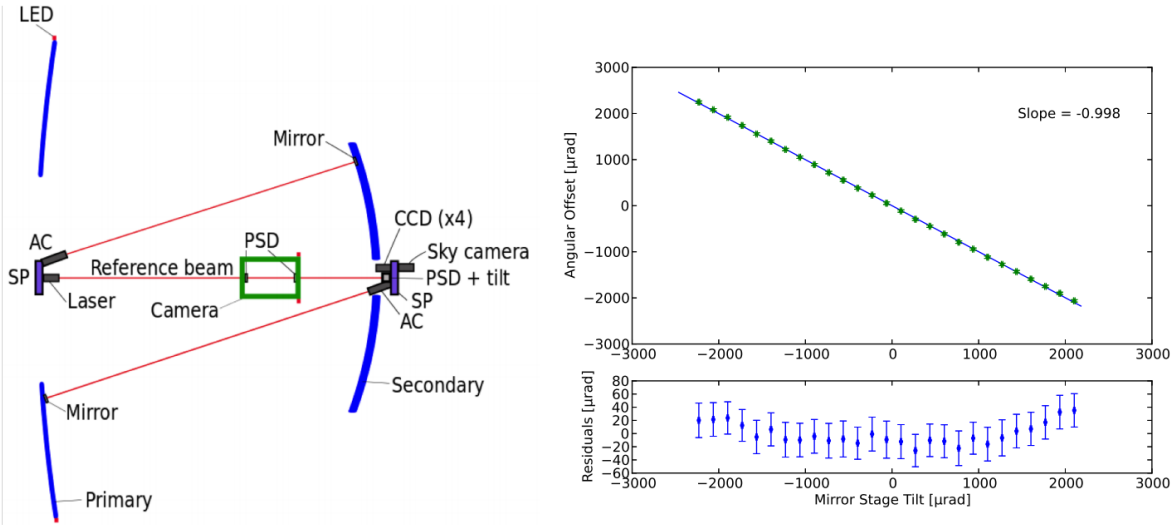

Figure 5.9: Left: A schematic of the pSCT Global Alignment System with all relevant devices as described in the text. Right: The performance of the autocollimator's ability to determine the tilt using a 5 cm circular mirror located 8 m away. The accuracy has a residual of $\lesssim 50$ μm, below the tolerance requirement of 150 μm .

four degrees of freedom. Hence, by moving only the two OTs during observations, the relative alignment of OT1, OT2, and the γ-ray camera is maintained during observations. The CCD cameras installed on OT1 and OT2 continuously measures the position of three specific GAS panels equipped with LEDs on each M1 and M2 as well as determines the global tip and tilt of M1 and M2 with respect to OT2 and OT1 using two ACs. The CCD sky camera, mounted on the backside of the OT2, images a $4.4^\circ \times 3.3^\circ$ FoV image of stars through which the center of the FoV can be calculated through astrometry. Since the sky camera is aligned with the laser beam and, therefore, with the γ-ray camera the data on the positioning of M1 and M2 with respect to the laser beam can be used to construct a model for offline pointing corrections which can be verified by the tracking of the stars. These activities are part of the planned telescope commissioning scheduled to take place during the upcoming observing season.

Power and Ethernet connectivity to all MPMs, OTs, COM, and LEDs are wired directly

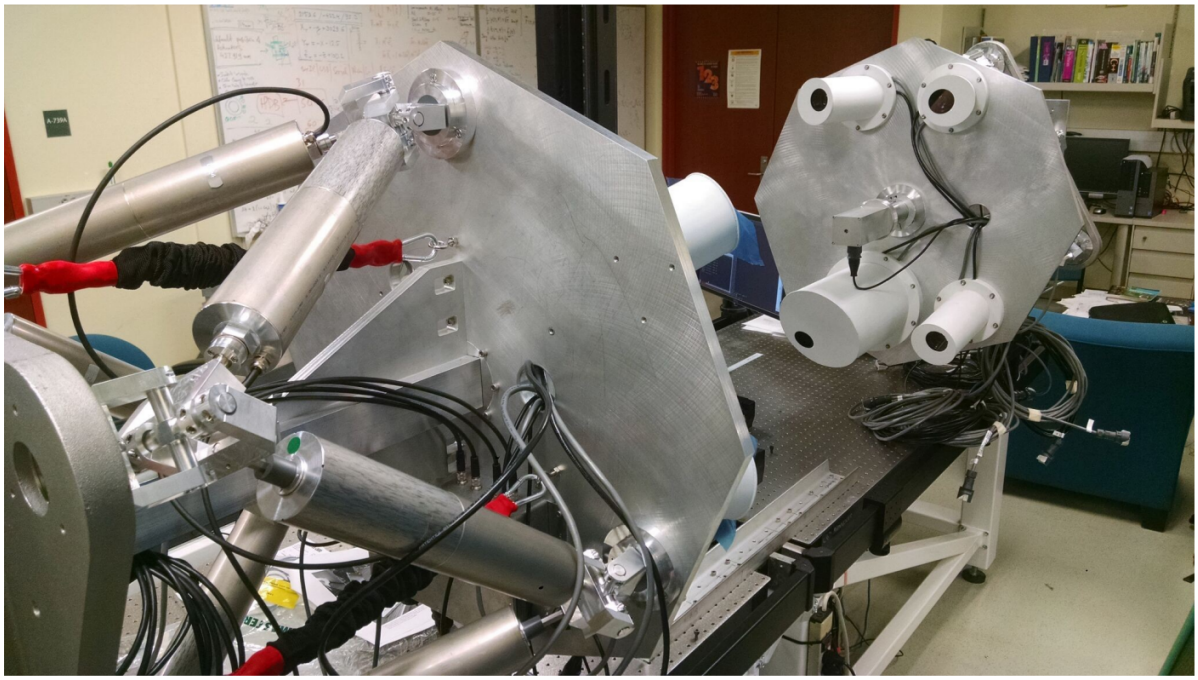

Figure 5.10: Optical Tables being calibrated in the UCLA laboratory. Each table contains a SP which enables motion for alignment. Three CCD cameras and one AC are located on each table (located in the white enclosures). The primary OT laser can be seen at the center of the far table. Not shown is the secondary OT rangefinder, PSD enclosure, and the sky camera.

on the OSS and delivered from two power and Ethernet distribution boxes (PEDBs), one responsible for the 48 primary MPMs and another for the 24 secondary MPMs. The PEDBs provide 24 VDC power to the MPCBs as well as 24 VDC and 12 VDC power to auxiliary global alignment and COD hardware. The PEDB housing consists of outdoor rated enclosures with temperature control and air cooling capabilities. Ethernet is directed through the PEDBs by way of commercial grade network switches. Monitoring of the voltage and currents, as well as powering of the PEDB power supplies is performed through Arduino microcomputers housed inside the PEDBs. All of the pSCT hardware elements are designed and tested to be weatherproof and withstand the environment conditions at FLWO.

5.4 pSCT Optical System Software and Calibrations

Being the first-of-its-kind medium sized telescope employing the SC optical system, the pSCT is equipped with a multitude of hardware elements providing resilience from unforeseen obstacles in order to achieve the strict alignment requirements. The sophisticated alignment system, while providing an enormous amount of flexibility, requires just as much control and therefore presents a significant software challenge. Matching the modular hardware framework, an object-oriented programming design is adopted. Classes of objects are developed from the lowest level hardware elements (Controller Board Computer, Actuator, MPES classes) up to the highest level (Telescope class), with the lower level objects being created as children of the parent objects. This hierarchical software structure, with classes of objects developed to mirror the hardware elements (see Figure 5.11), facilitates software development by enabling parallel, localized code progression of the classes. In addition, any updates or alterations made to the pSCT hardware for implementation in CTA do not require a complete overhaul of the software, but simply an adjustment to that hardware element's class. Network communication between objects is performed through OPC Unified Architecture (OPC-UA), a standard communication protocol adopted by CTA. The software development

of the pSCT is designed with integration with CTA in mind, such that minimal alterations of the software structure are required to satisfy CTA software requirements.

5.4.1 Mirror Panel Controller Board Software

At the lowest level of the alignment branch of software is the mirror panel controller board computer (CBC) class, which is responsible for all MPCB hardware functions including: powering on and off the six actuator ports and the six MPES USB ports, measuring the encoder voltage of the six actuator ports, measuring both temperature sensors, sending stepping pulse signals to the actuator ports, and additional auxiliary functions not listed. The MPCB contains a multi channel ADC with an independent channel for each of the six MPCB actuator ports, as well as two additional channels for the internal and external temperature sensors measuring the temperatures of the MPCB and MPM triangle, respectively. The shaping of the input voltage by the voltage conditioning circuit before it reaches the ADC causes slight changes in the six individual actuator ports of the MPCB which require calibration. These voltage deviations are not significant enough to prevent alignment by the SPs, as they result in a maximum discrepancy of an actuator's length of ~ 30 μm. Nevertheless, the voltages are better represented after a linear correction is performed on the measured values. The observed voltage is modeled to be a linearly dependent function of both the true voltage and the temperature of the circuit board, as measured by the internal temperature sensor:

$$V_{obs} = V_0 + (1+\alpha)V_{true} + (T - T_0)(\beta + \gamma V_{true})$$

Solving for V_{true},

$$V_{true} = \frac{V_{obs} - V_0 - \beta(T - T_0)}{1 + \alpha + \gamma(T - T_0)}$$

The four correction parameters (V_0,α,β,γ) are determined during a calibration process after assembly of the MPCBs. Six reference voltages spanning the full voltage range of the encoder are read through the actuator ports and observed at three MPCB temperatures

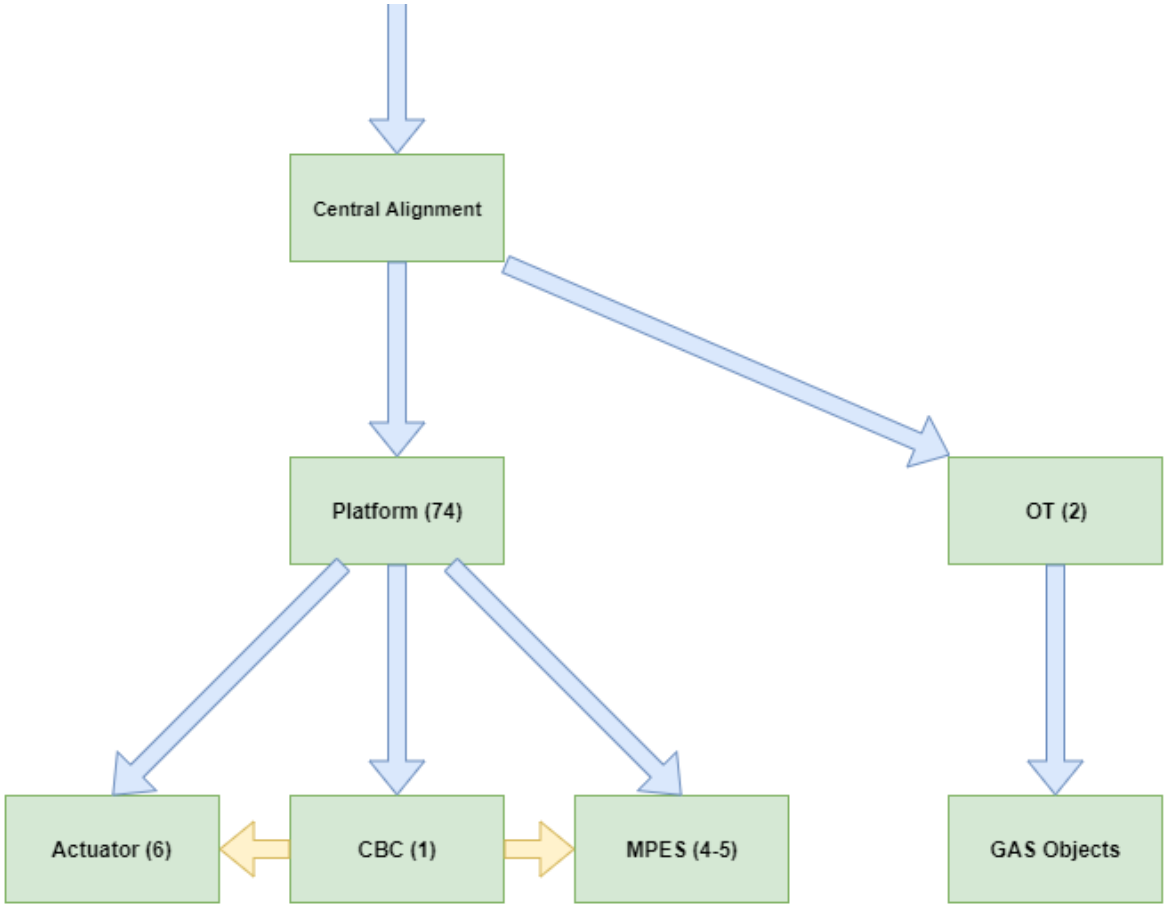

Figure 5.11: The alignment branch of the pSCT software structure. The Central Alignment computer aggregates the platform and GAS alignment status, processes this information and determines how the individual platforms should move to achieve alignment. The platform objects, corresponding to each SP in the optical system, consist of one Controller Board Computer (CBC) object, six actuator objects, and four to five MPES objects depending on the location of the platform. The actuator and MPES objects communicate with the local CBC object in order to read and move the actuators via the actuator ports, as well as read the MPES position via the USB ports.

(roughly 0° C, 20° C, and 40° C), totaling 18 measurements which are included in a χ^2 minimization to determine the four correction parameters. Each MPCB has four correction parameters for each of its six actuator ports stored in the pSCT SQL database to be loaded by the CBC class during initialization of the alignment software, such that the voltage measurements are automatically adjusted during operation.

5.4.2 Actuator Software and Calibration

Also existing at the base of the alignment branch is the actuator class, which is responsible for precisely moving an actuator, determining the length of an actuator, and detecting improper behavior of an actuator (e.g. improper stepping, stuck). The actuator is comprised of a magnetic rotor with 200 steps per revolution mounted on an internal nut which rotates around a threaded drive screw attached to a spline. The thread spacing of the drive screw is roughly 0.6 mm, corresponding to a linear step size for the actuator of ~ 3 μm. A magnetic encoder is attached to the rotating internal nut, producing a voltage which changes linearly with the rotation of the rotor and enabling the linear distance traveled by the actuator to be determined by tracking the encoder voltage. Since the encoder voltage produces a degenerate reading every full rotation, determining the exact position of an actuator requires tracking of the number of rotations performed. Careful tracking of the actuator revolution count is one of the key functions performed by the actuator software, which enables the complete determination of the length of the actuators and consequently the exact positions of the mirror panels mounted on the SPs. In order to achieve this, a calibration procedure is implemented which determines the hardware limits of an actuator module, sets the software limits, and measures an actuator's voltage profile.

The actuator hardware limits are found by repeatably stepping the motor a small number of steps and measuring the change in the encoder voltage. When the motor reaches the end of its range of motion, the change in encoder voltage will reveal that the motor moved fewer steps than the amount ordered, possibly moving in the opposite direction from a recoil of the

spring in the motor observed at the hardware limits. Careful consideration of the stepping increment when probing the hardware limits is required: too small of a stepping increment can produce a change in the encoder voltage that appears like the limit is reached when it is not, while too large of a stepping increment lowers the accuracy in determining the position of the hardware limit. In addition, stepping with too large of an increment into the hardware limit may cause the motor to get stuck at the limit, requiring considerable manual force to repair. In consideration of balancing these effects, the increment size of 15 steps is selected in the current iteration of the software and is shown to repeatably find the hardware limits with $\theta < 30^\circ$ accuracy. During assembly of the actuators, the extension hardware limit is probed and the encoder's voltage is read by the MPCB. If the measurement is near the voltage discontinuity of the encoder (the conservative definition of "near" adopted during assembly is $\Delta\theta < 90^\circ$), the encoder is unfixed and reattached in an altered position until the criterion is satisfied. This procedure ensures that an actuator's extension hardware limit will be repeatedly probed to exist on the same encoder revolution, since the magnitude of the uncertainty is well below the distance to the discontinuity. An actuator's "Home" position can then be uniquely defined with respect to this repeatable reference point: from the extension hardware limit the actuator is retracted until the encoder voltage jumps the discontinuity, and then it is retracted two more complete revolutions (see Figure 5.12).

The "software range" of an actuator, which is the allowed range of motion during operation, is set to 100 revolutions (20000 steps $\approx$ 61 mm), while the mechanical "hardware range" of the actuator is roughly 105 revolutions, hence the additional two revolutions added in the definition. The shaft length of an actuator in the Home position is measured during calibration with $\sim 10\ \mu m$ accuracy. The length of any position can be found by determining the number of steps away from the Home position, since the actuator moves a constant length per step. After finding the Home position during calibration, the positions of the extension and retraction hardware limits are then probed and found in reference to the Home position.

The actuator is made with an approximately uniform step size of 3.048μm corresponding

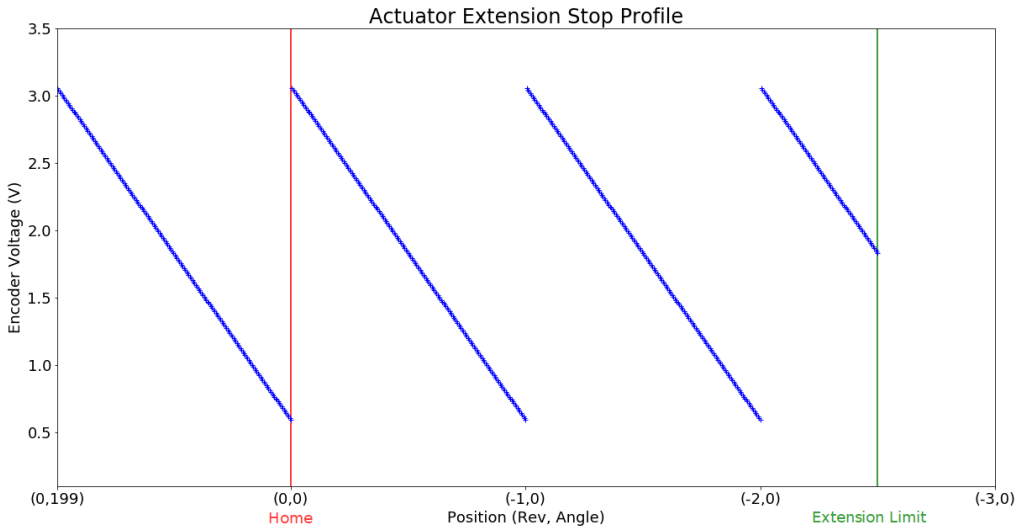

Figure 5.12: Schematic demonstrating how an actuator's Home position is defined. An actuator is extended until the hardware limit is reached (green line). At this mechanical position, the encoder is fixed at a rotation angle such that the corresponding voltage of the extension limit position is roughly in the central half of the range of voltages ($\sim 1.2 - 2.4$ V). The actuator is then retracted until it observes three discontinuity jumps of the encoder, at which point it is in the Home position. Further retraction increments the angular position until another discontinuity is reached, and then the angular position is reset to zero and the revolution position is incremented by one.

to a rotation of the rotor of 1.8°. Deviations from equal spacing are observed at the 0.1° level, which accumulated over many steps can be of the same order as the step amount. Representing the captive position of the motor assembly, these deviations are consistent across revolutions and therefore a motor profile of an actuator can be found by measuring the encoder voltages of all 200 angular positions. Comparison of an actuator's encoder voltage reading with the set of 200 voltages allows a more accurate determination of the angle which the motor exhibits. The profile is measured during calibration, once the Home position is found and the shaft length is measured (see Figure 5.13), by stepping an actuator over many revolutions, with the encoder voltage measured and recorded at each position. The encoder voltages for each of the 200 angular position are averaged over the revolutions and the standard deviations are computed and required to be adequately small (< 3 mV). Instances where the standard deviation is too large most commonly occur if the actuator missed a step during calibration, or if the encoder voltage discontinuity is aligned with one of the 200 angular positions, such that small fluctuations cause both sides of the discontinuity to be measured for a single angular position. Once reliably determined, the set of 200 voltage measurements defining the motor profile, along with the positions of the hardware limits and the shaft length of the Home position, are saved into the pSCT SQL database where they can be loaded during software construction of an actuator object.

To save on costs for the implementation of the pSCT, the actuator module's design has an encoder measurement of only the current angle of the rotor, which produces a degenerate hardware reading for more than 100 possible revolutions. It is important to maintain the complete position of the actuator through software implementation in order to know its shaft length, as each revolution corresponds to a displacement of 610μm. The strict alignment tolerances of the optical system require precise adjustment of the SPs, which use the actuator lengths as inputs into the calculation to determine the motion to perform, and therefore incorrect actuator lengths would cause improper SP motion. Maintaining the actuator's position also enables the tracking of the available range of motion, making it possible to

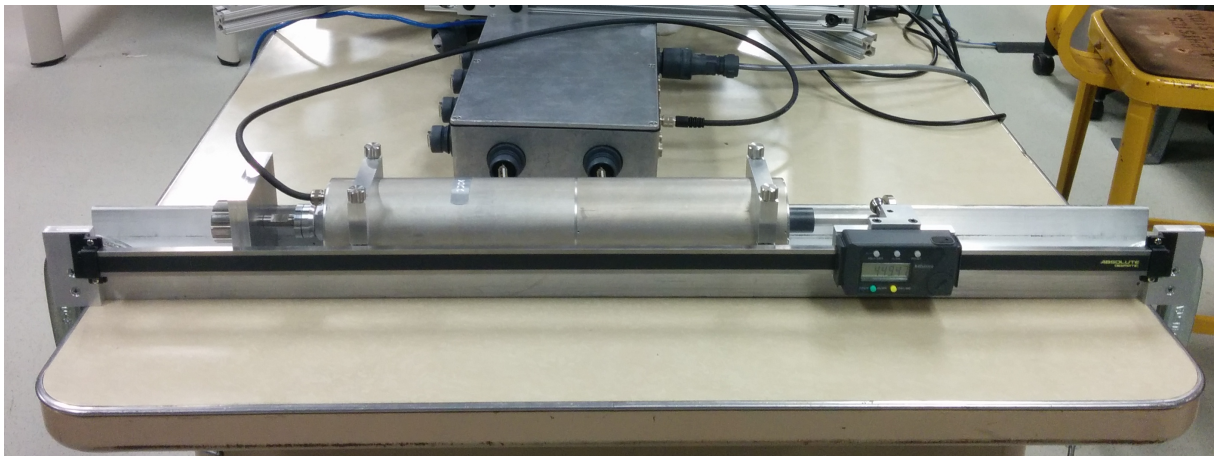

Figure 5.13: The actuator calibration setup at the UCLA lab. Once an actuator is assembled, the Home position is found and the actuator's length at this position is measured using a caliper with 10μm resolution. The actuator is then unfixed and finishes its calibration procedure.

predict the motions available to the SPs when aligning the full mirrors, as well as preventing possible damage to an actuators motor from pushing it against its hardware limit. For these reasons, the actuator class is designed to keep track of the revolution state of an actuator. The Home position of an actuator is defined to have a coordinate of zero revolutions and an angular position of zero. Each retraction step from this Home position increments the angular position by one, and after 200 steps a full revolution is completed and the revolution counter is incremented. The actuator class is designed such that it keeps internal track of these positions, and it also records them locally on its MPCB in an actuator status file (ASF) such that a reinstantiation of an actuator object can reload its position from this file. To insure against the loss of an actuator's position information, the actuator class requires that all motion is broken into steps which are less than half of the number of steps in a revolution (80 steps in the current software version). In the instance where an actuator was commanded to move but did not, or did move but the position was not correctly recorded on the local ASF, the software can detect the discrepancy between the measured encoder

voltage and the recorded position. Since the actuator's motion is small enough, the incorrect position can be accurately recovered by rounding to the nearest position.

A number of errors can occur during an actuator's operation which the actuator class is designed to detect, alert the user, and have functions to remedy the error when guided by the user. The list of errors include: improper motor motion detected by encoder readings, mismatching between the measured encoder position and the last known recorded position, failure to communicate with the SQL database, and irregularities in determining the Home position. Each error has its own triggering criterion and is given a severity distinction of either "operable" or "fatal". Operable errors simply report to the user that the error occurred, while fatal errors report the error and disable the actuator from moving. Each error has its trigger state recorded in the ASF along with the actuator position and a timestamp, allowing the actuators to retain its error state when the actuator software objects are instantiated. Functions are available for the user to handle the error appropriately and clear the triggered error. Overall the actuator class is designed to detect any improper functionality in its motion or measurement, and maintain the exact position of the actuator.

5.4.3 Platform Software

Existing one level above the actuator class in the software hierarchy is the platform class, which consists of one CBC, six actuator, and four to five MPES children. The platform class is responsible for integrating its six component actuators into a unified motion of the SP. The designed gap between mirror panels is 14 mm, and it can be significantly smaller than this when panels are installed and the mirror is yet to be aligned. Initial alignment methods require motion of the panels greater than this gap size, which means that collisions are a possibility for some of the routes which the SP actuators can take to reach the target position. The safest path is along the projection from the current position to the target position, and therefore the platform class determines the projection vector and orders the six actuators of the SP to step approximately along it. To speed up the motion time, actuators are moved

only when their queued number of steps is above the stepping increment of the actuators. The maximum deviation of the SP from the projection direction which this queuing can cause is less than 1 mm, well below the expected gap size.

Included in the integrated motion of the SP actuators is a hysteresis-reducing action. The SP joints and actuators are designed with high precision in order to reduce hysteresis, however a small amount remains as measured by a test setup. For this test, an assembled SP remained in a fixed position with repeated MPES measurements taken as a control sample. Then the SP iterated movement away from and returning to the fixed position. The movements were performed in a variety of ways, with different actuator stepping lengths and order each time, and an MPES measurement was taken each time the original position was reached (see Figure 5.14). The MPES measurements show that platform hysteresis is present at a small scale, with a standard deviation in MPES pixel position of ~ 0.5 px, corresponding to a tilt of a panel of less than 10 μrad, roughly an order of magnitude below the tolerance requirements. The observed hysteresis may be caused by some remaining friction in the lubricated joint, or a directional dependence of an actuator's captive locking mechanism. The magnitude of the hysteresis effect is found to be significantly alleviated by applying a small motion ($\sim$ 100 μm) to the actuators before reaching the destination, such that the panel approaches the target position from the same direction. This hysteresis motion is built into the platform class such that it repeatedly follows any SP motion made, ensuring that all actuators which are moved end their motion by extending a number of steps.

In addition to integrated SP motion, the platform class monitors and aggregates the individual error status of its six actuator children objects and subsequently sets its own error state. An error algebra exists which associates the set of actuator errors to platform errors, ensuring that in the event of a "fatal" actuator error the SP does not move, while for "operable" actuator errors the platform remains capable of motion. An integrated platform error state also simplifies the higher level error handling, reducing the number of objects which require their error states to be monitored by a factor of six. The platform class also performs

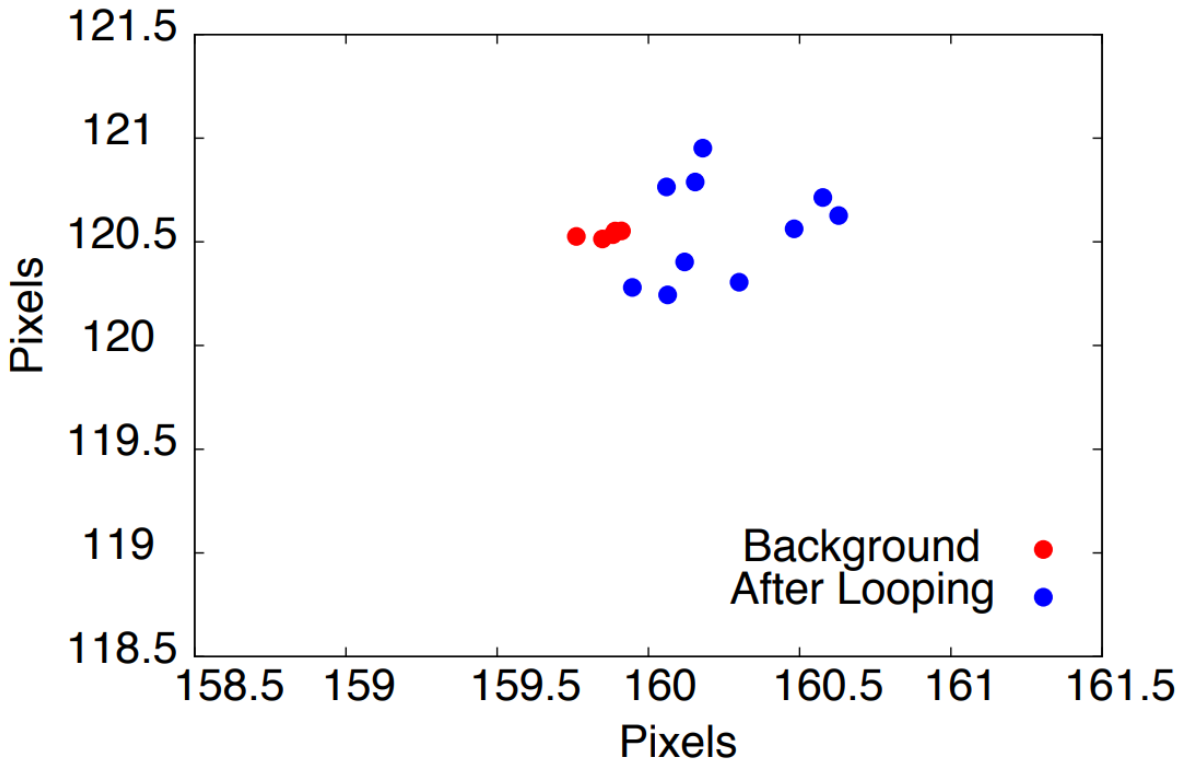

Figure 5.14: The magnitude of hysteresis present in the P2PAS alignment as measured by MPES position (44 μm per pixel). The red dots demonstrate the position of an MPES without moving actuators. The actuators are then moved in random directions and return to the original positions, at which point a measurement is made. These measurements are shown by the blue dots.

a number of auxiliary responsibilities, including: reading the MPCB calibration information from the SQL database and directing its CBC child object to load this information, loading MPES objects, and reading the internal and external temperatures.

5.4.4 Telescope Software

At the highest level of the alignment software tree is the telescope class, which is responsible for the correct construction of the individual alignment software objects and performing intelligent alignment of the entire telescope. In general, alignment methods in the telescope class can be split into two categories: methods for the panel-to-panel alignment system (P2PAS), which construct continuous primary and secondary mirror surfaces from the mirror panel constituents, and methods for the global alignment system (GAS), which mutually align the two assembled mirrors and the γ-ray camera. The telescope class is designed to interface with the user through a GUI, and as such contains objects and methods with user input in mind. The platform and GAS objects are constructed in the telescope class with the correct hardware mapping by reading from a mapping table in the database. The development of the telescope class is ongoing, with new methods being implemented as their importance is revealed during the commissioning of the optical system. The alignment of the SCT optical system is a three step process: first, initial calibration MPES measurements of all aligned mirror panel edges is obtained in the UCLA lab using a coordinate measuring machine (step 1), then the MPMs are installed onto the SCT and initially aligned based on the MPES calibration measurements (step 2), and finally they are aligned utilizing images of defocused bright stars (step 3). What follow below provides a general description of the MPES-based alignment algorithm (step 2), which incorporates both P2PAS and GAS data.

The P2PAS is guided by measurements of the MPES, which are mounted across the edges of neighboring panels. The camera component of each MPES measures the position of the laser spot incident on it originating from its corresponding laser component mounted on the neighboring panel, such that a two dimensional projection of the relative position between

the two panels is observed. The small translations and rotations of a panel, and therefore the corresponding change in MPES measurement, can be represented as a Taylor series expansion in powers of changes in SP actuator lengths. For small displacements a linear approximation is sufficient. That is, for the set of MPES measurements $\vec{\sigma}_{jk}$ along the edge which joins panels j and k with actuator lengths $\vec{L}_j$ and $\vec{L}_k$, respectively, a response matrix $\hat{R}_{jk}(\vec{L}_j, \vec{L}_k)$ is defined by $\delta\vec{\sigma}_{jk} = \hat{R}_{jk}\delta\vec{L}_k$ which transforms small actuator displacements into corresponding changes in the MPES readings. The "vector" notations used in this formula are for six actuators of a SP, hence $\vec{L}$ is six dimensional, and for all measurements of the MPES on the j-k edge, which is number of sensors on the edge times two (x and y positions). A response matrix can be obtained by simply moving the six actuators individually and measuring the corresponding change in MPES measurements. Once obtained, the response matrix can be used to determine the actuator motion necessary to adjust the set of MPES positions to a reference position corresponding to alignment between the panels. That is, once the reference MPES positions $\vec{\sigma}_{jk}^{ref}$ are known, the necessary displacement in MPES coordinates can be calculated ($\Delta\vec{\sigma}_{jk} = \vec{\sigma}_{jk}^{ref} - \vec{\sigma}_{jk}$) and the inverse of the response matrix can be used to determine the actuator motion needed to reach the reference position ($\Delta\vec{L}_k = \hat{R}_{jk}^{-1}\Delta\vec{\sigma}_{jk}$). The P2PAS has more MPES degrees of freedom than the actuator degrees of freedom; in other words it is an overdetermined linear system. The additional degrees of freedom provide robustness in the event of MPES hardware failure, allowing the MPES-based alignment to still be achieved. In general, the P2PAS motion is governed by a χ^2 minimization for each mirror,

$$\chi^2_{P2PAS} = \sum_{j,k} w_{jk} \left[\hat{R}_{jk}\Delta\vec{L}_k + \hat{R}_{kj}\Delta\vec{L}_j - \Delta\vec{\sigma}_{jk}\right]^2$$

where the sum is over all mirror panels which compose of the mirror surface, and the weights can be adjusted to give higher confidence MPES measurements more impact, and vice versa. The basis representation presented here is most intuitive, as the elements directly correspond to individual actuator lengths and MPES measurements; however different representations may be more advantageous to work in. For example, in the basis of eigenvectors of the

mirror-wide response matrix there are loosely or even entirely unconstrained perturbations with small or zero eigenvalues. Motion of the M1 or M2 as a whole has six eigenvectors with zero eigenvalues and therefore is not constrained by P2PAS MPES measurements alone. Similarly the dipole and quadrupole large spatial scale distortions of the entire M1 or M2 have very small perturbations at each individual edge but accumulate over many edges, and are therefore also loosely constrained, requiring various methods of regularization such as inclusion of GAS data or constraining some degrees of freedom with respect to OSS itself.

The global alignment methodology is analogous to the P2PAS alignment, but instead of using MPES measurements and individual actuator motions to guide and adjust the alignment, the various GAS measurements are used to direct the alignment while adjustments are performed by the γ-ray camera and specific combinations of actuator motions corresponding to motion of the mirror surfaces as a whole. Just like with the P2PAS, the global alignment instructions are calculated by a χ^2 minimization,

$$\chi^2_{GAS} = \sum_n w_n \left[\hat{R}_n \Delta\vec{r} - \Delta d_n \right]^2$$

where the sum is over the n degrees of freedom measured by the GAS components (PSDs, LEDs, ACs, etc.), the single vector $\Delta\vec{r}$ represents deviations to the 18 degrees of freedom corresponding to the positions of the primary, secondary, and γ-ray camera with respect to the telescope OSS, $\hat{R}_n$ is the response of the n GAS DoF by adjusting $\vec{r}$, and Δd_n is the adjustment sought for the n DoF to reach the aligned position. The weight factors w_n can be adjusted to the confidence of the hardware elements, as well as in accordance with the alignment tolerances of the system (for example placing higher weights on the tip-tilt AC measurements while placing lower weight on transverse motion of the γ-ray camera). Adjustments of the primary and secondary mirrors as a whole, represented by elements of $\Delta\vec{r}$, can be substituted with the P2PAS eigenvectors with zero eigenvalues corresponding to motion of the entire mirror surface. Simultaneous alignment of the P2PAS and the GAS can

therefore be performed through a combined χ^2 minimization to solve for $\Delta\vec{L}_k$,

$$\chi^2 = \chi^2_{primary} + \chi^2_{secondary} + \chi^2_{GAS}$$

5.5 pSCT Status and Future

All hardware elements of the pSCT project have been installed and commissioning and performance validation and verification tasks are currently underway. In early 2019 the pSCT camera and mirrors were simultaneously uncovered and the telescope was inaugurated. Shortly thereafter, its first light and first EAS were observed (see Figure 5.15). In July of 2019 the γ-ray camera was aligned to the center of the mechanical structure and then subsequently aligned with the M1 and M2 mirrors. Significant development of alignment software and SCT optical system alignment procedures occurred in the fall of 2019 culminating in an initial alignment of the optical system, which focused on-axis a bright star by the 72 mirror segments into a 68% containment ellipsoid with major and minor axes of 4.2 arcmin (6.8 mm) and 3.8 arcmin (6.2 mm), respectively, surpassing the designed performance baseline requirements. The result was obtained after implementation of the third step of the alignment process utilizing defocused optical images of bright stars (see Figure 5.16). 75.5% of the PSF is contained within a 4 arcmin (6.5 mm) square imaging SiPM pixel centered at the peak, and 99.5% of the PSF is contained within a 8 arcmin "trigger" pixel defined as 2×2 imaging pixels for the pSCT. While evaluation of individual alignment tolerances has not yet been completed, this result demonstrates that the cumulative alignment tolerance has been achieved. A further improvement of the alignment is achievable by including higher order corrections to the alignment calculations as well as by accounting for deviations in focal length of the individual mirror panels from the designed focal length. A measurement of the off-axis PSF is in progress and efforts to improve it are underway.

The Global Alignment system was used for initial alignment between M1, M2 and the γ-ray camera and to perform optical alignment of the OS. The hardware of the GAS sys-

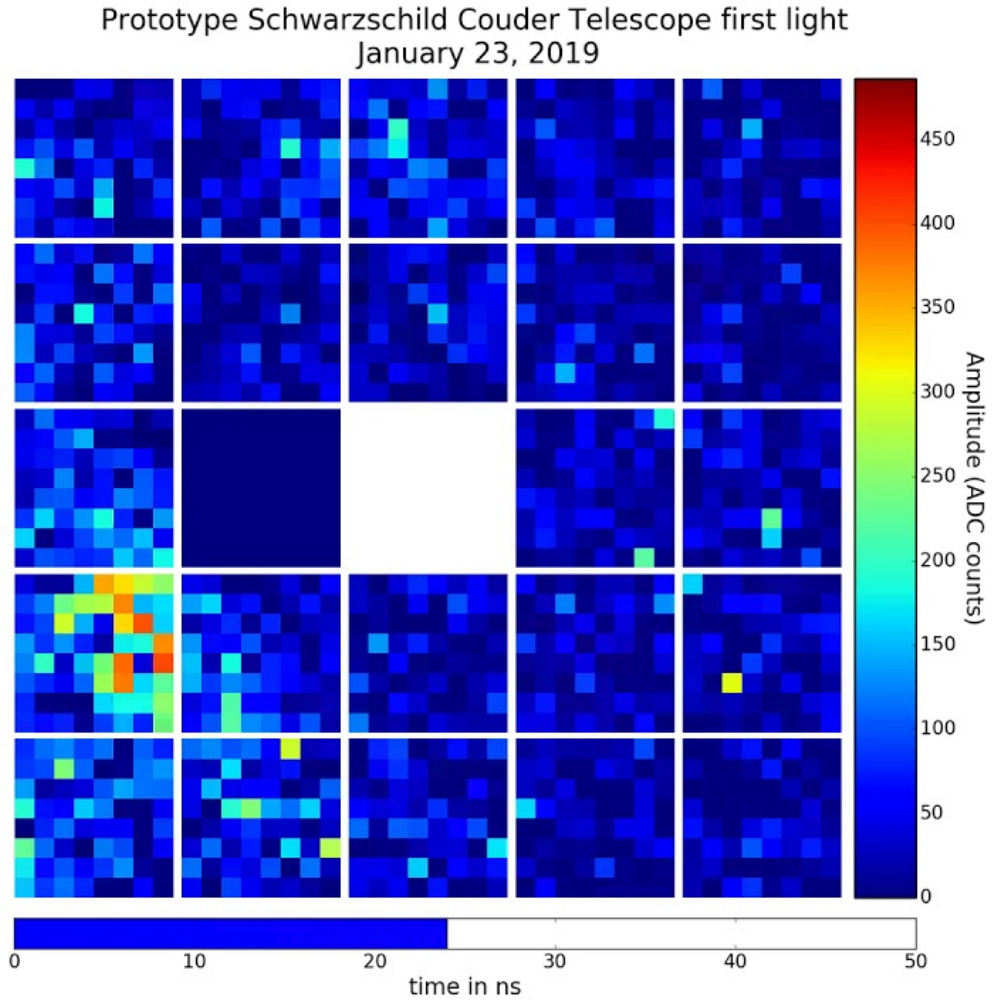

Figure 5.15: Camera snapshot of a single event for the pSCT's first light. The white square in the center is because the COM is temporary replacing the front end electronics module. The module left of the center is dark because it did not connect after the prototype SCT camera was turned on the first time. The optical system of the SCT in this image is only coarsely aligned. The data shown in this picture do not include pedestal subtraction or data processing and has only historical value.

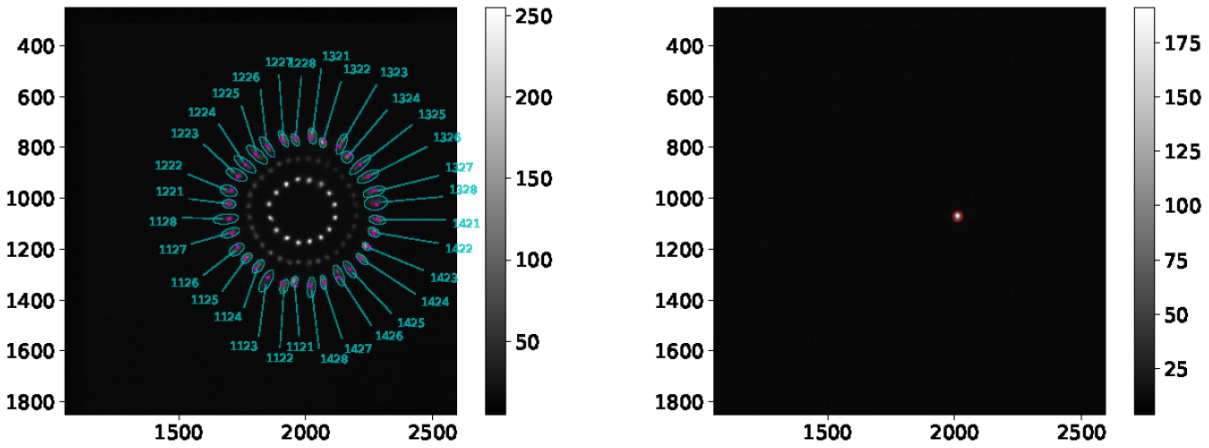

Figure 5.16: Left: The de-focused image of a star on-axis to the pSCT optical system. The individual points correspond to focused light by pairs of individual primary (annotated) and secondary mirror panels. Right: Each mirror panel is adjusted to bring the points into focus, producing a rough alignment of the optical system. Further improvements are expected when including higher order corrections to the alignment algorithm and structure deformations are accounted for. These images were taken by a CCD camera placed near the focal plane.

tem, which will be used to acquire data for off-line telescope pointing corrections, has been activated and tests were performed to initially assess the GAS pointing monitoring capabilities. First, the ability of GAS CCDs to determine a panel's position was tested by moving a panel 3 mm forward and backward from a starting position and making a measurement, which demonstrated a position reconstruction accuracy of better than 0.25 mm. To test the stability of the structure, 23 images, each with 0.5 second exposures, were taken of moving stars using the CCD sky camera and the position of the center of the FoV was reconstructed using astrometry, resulting in a standard deviation of the pointing position below 3" (see Figure 5.17). Further tests will be performed to determine the extent of the deformations in the structure as the telescope moves through different elevations and from thermal expansion of the structure. Since the pSCT is designed with awareness of potential occurrences of misalignment of the OS, the alignment system is capable of monitoring and correcting the misalignment at a refresh rate of several minutes. The exact refresh rate needed for alignment corrections is still to be determined, if at all necessary. For significant pointing elevation changes, where a necessary correction is expected, measurements of the misalignment can be made and the necessary alignment correction can be predicted. In addition to structure deformations, hysteresis of the alignment components is expected which will be measured to determine the magnitude and methods of alleviation. Overall there are sources of misalignment to the optical system which will be measured, and methods will be developed which attempt to minimize their effect. Ultimately the pSCT's optical system is capable of monitoring and fixing misalignments between runs if necessary. Further investigation and significant software development of the alignment system is planned for the $2020 - 2021$ observing season.

The initial commissioning of the $2.68^\circ \times 2.68^\circ$ partially populated pSCT camera was completed in January 2020 and it was followed by observations of the Crab Nebula which took place in February and early March of 2020. The pSCT technology was validated by the detection of the Crab Nebula, an established γ-ray source. The co-located VER-

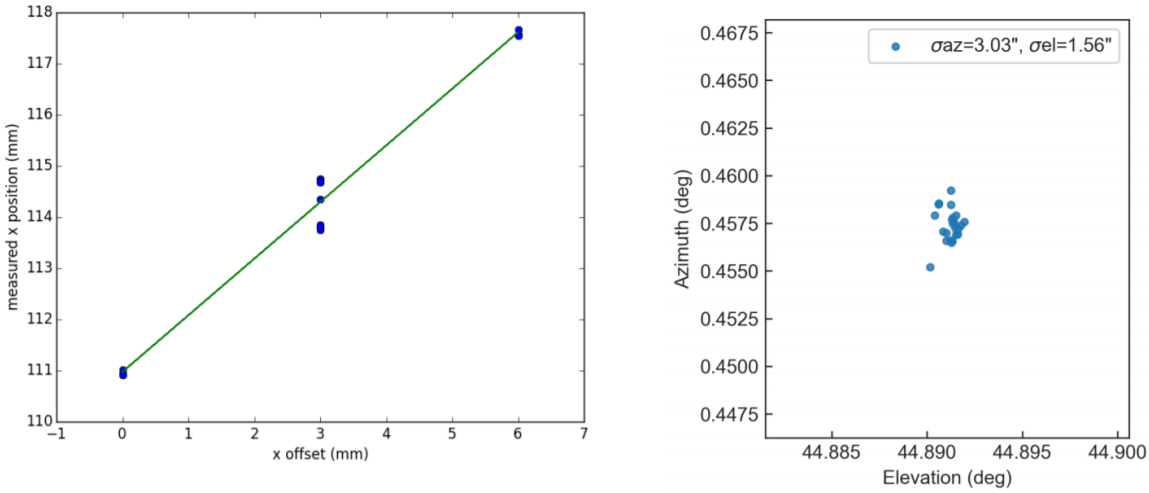

Figure 5.17: Left: GAS CCD determination of a panel's position along one direction. Right: The CCD sky camera FOV center position as determined by astrometry, demonstrating the stability of the pointing. Image taken from [AAA19].

ITAS simultaneously observed the Crab Nebula with pSCT for a few hours, allowing for the cross-calibration of γ-ray events observed with both instruments and the optimization of background rejection for the stand-alone pSCT data. The analysis methods refined on the pSCT-VERITAS combined dataset were applied to an independent sample of about 20 hours of pSCT-only data, yielding a more than 8 standard deviation (sigma) detection of the γ-ray signal from the Crab Nebula, shown in Figure 5.18. This initial detection of a γ-ray source verifies the end-to-end performance of the pSCT as a new design of an IACT for CTA, capable of recording images of γ-ray showers with unsurpassed precision.

The upgrade of the pSCT camera to the fully instrumented 8° FoV is already underway. This project will not only increase the number of camera modules from 25 to 177, but will also improve the camera hardware elements. The individual camera modules will use next generation SiPMs which have an improved photon detection efficiency and a reduced temperature dependence. In addition, the electronics layout of the modules are revised in order to reduce electromagnetic interference and provide a cleaner readout with reduced

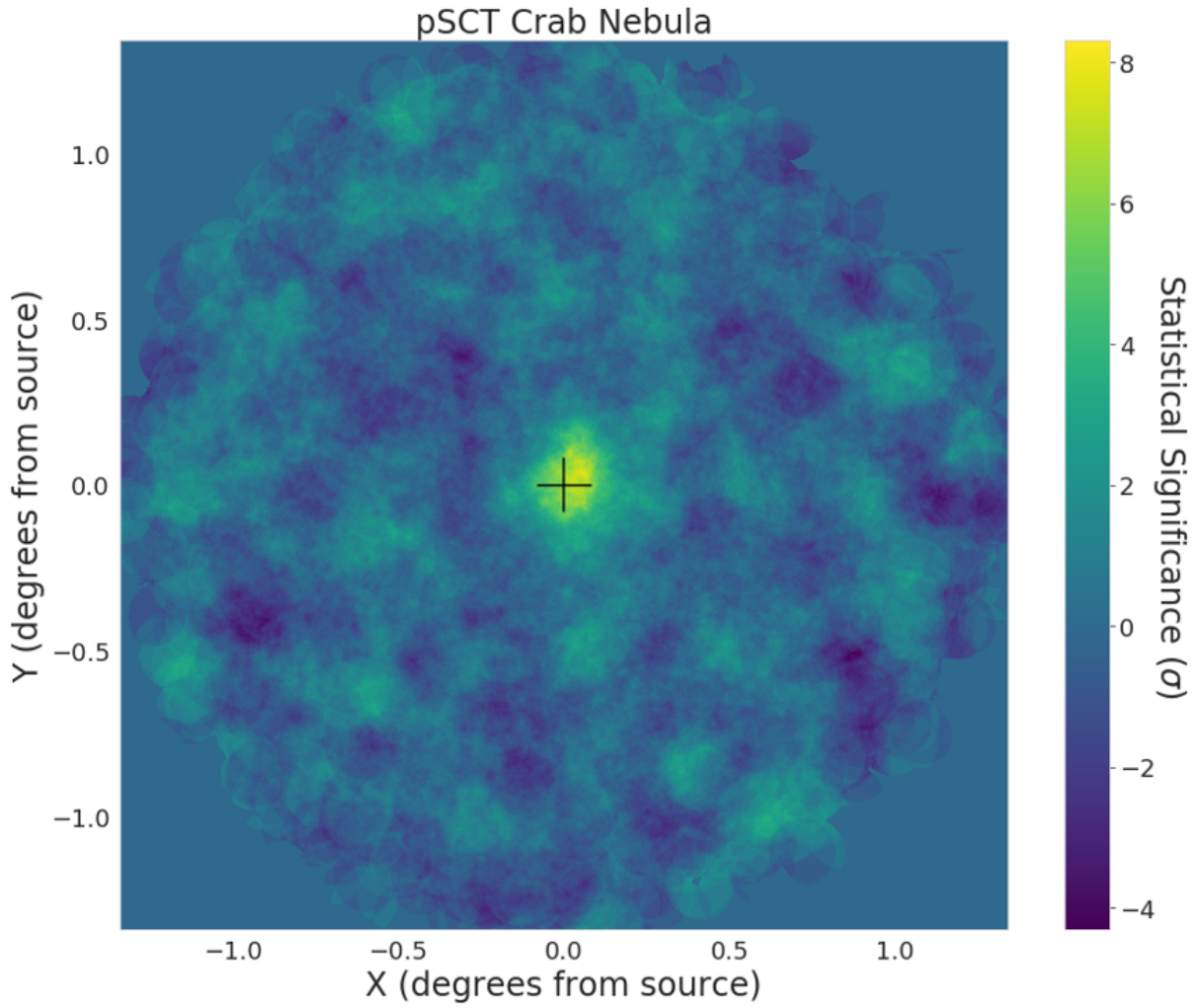

Figure 5.18: The preliminary map of γ-ray events recorded by the pSCT from the direction of the Crab Nebula, marked with the cross at the center of the map. The data analysis was optimized on a few hours of joint observations with the VERITAS observatory and applied to an independent 20-hour dataset with the pSCT operating in stand-alone mode.

noise [Meu19]. The camera backplane, the main circuit board which interfaces the individual camera modules, is also redesigned to accommodate the full 177 module camera and its increased network communication requirements. Furthermore, many auxiliary systems will also be upgraded, including an improved camera shutter and weatherproof seal. The camera upgrade project is expected to be completed by the end of 2021, at which point the fully functional SCT will take data in conjunction with VERITAS, adding the scientifically important wide FoV observing capabilities to the VERITAS observatory.

Verification and validation of the SCT technology on the pSCT prototype is ongoing, however the largest known anticipated challenge in the realization of this novel telescope design - the demanding optical system and its tolerances - has been met. While the performance of off-axis optics and the fully populated camera still need to be verified, the results so far are promising. In the context of constructing an array of SCTs for CTA, an effort is underway to identify potential improvements to the SCT design, and areas where cost can be reduced and large scale industrialization can be achieved. The implementation of SCTs in CTA offers superior imaging resolution, especially off-axis, and pushes the array to the near theoretical limit of the IACT stereoscopic technique.

CHAPTER 6

Discussion

The work presented in this dissertation was motivated by the strong observational and theoretical foundations which together firmly argue for the existence of a non-thermal population of particles in GCls known to have radio halos. The high energy electrons which produce radio synchrotron radiation, and in some cases possibly a soft X-ray excess, can originate from either the interaction of VHE protons with the ICM or from *in situ* re-acceleration to very high energies. The ultimate source of energy for both of these processes is provided by the enormous gravitational binding energy of the cluster and inflow or accretion of matter into it through the history of the cluster's evolution. VHE electrons produced in both scenarios must be accompanied by the generation of VHE γ-rays either via decay of neutral pions in the hadronic channel, or via inverse Compton scattering of the CMB in the QED channel. There is strong motivation to believe that it is only a matter of time before detection and establishment of galaxy clusters as a new class of VHE γ-ray emitters, once the sensitivity level of new analysis methods and/or new instrumentation becomes adequate. Although no conclusive detection of γ-ray emission from the Coma GCl has been made to date, there are signs that it may be just "around the corner". Fermi-LAT observations have found weak ($\sim 3\sigma$) emission within the 1.5° virial radius, and this dissertation's analysis found a 2.7σ median significance within the same region for the V6 dataset. The IACT data analysis of the very extended $5° \times 5°$ Coma GCl field is very challenging since this angular extension significantly exceeds the VERITAS observatory's field of view. In this dissertation I have undertaken an effort to either reject the previously made claim of "evidence", or detect, the γ-ray signal from the Coma GCl by developing a novel method of data analysis applicable

for an extended field of view with consideration of the nonuniform VERITAS instrument response function. The method is based on the background determination from source-free observations of dark fields, and it utilizes cosmic-ray-like events as a calibration source to reduce the dispersion in run acceptance for γ-ray-like events. The method can be viewed as a variant of what is known as the matched runs approach to the background determination, supplemented by original ideas to improve it using cosmic rays and adjusting the data analysis strategy for a significance determination on excess counts.

The VERITAS collaboration observed the Coma GCl previously and published the null detection result of a signal coming from the central region with a radius less than 0.4°, as well as a significance skymap of the Coma GCl field [AAB12], derived from the V4 dataset. This map was used by researchers independent of VERITAS to propose evidence of an extended virial shock associated with heightened γ-ray emission in the outer regions of the Coma GCl with distances exceeding 1° from the cluster center [KKL17]. The morphology of emission region presented by the researchers is modeled as an extended elongated ellipsoidal ring associated with shock acceleration of local electrons by the virialization of matter infalling into the cluster from adjacent cosmic filaments (see Figure 2.12).

The VERITAS collaboration has communicated to the researchers the possibility of instrumental effects in the published map at large radii from the center and, hence, we have not accepted the claimed evidence. The desire to settle the question of whether or not the γ-ray evidence is real is also a motivation of the study presented in this dissertation. This required an entirely different analysis chain from that originally published, as the significance would have to be assessed in the outer regions of the cluster which was not the goal of the original VERITAS publication. The VERITAS sky map which was published explicitly assumed that extended emission of the Coma GCl is not present at distances father than 0.4° from the cluster center. This assumption is vital in order to accurately determine the CR background, which is measured from an annulus $\sim 0.7^\circ$ around the targeted region. This technique, known as ring-background method, requires the explicit assumption of the

morphology of the region with and without γ-ray emission.

The ring-background method is subject to two significant sources of error if applied incorrectly, such as in the case of creating the extended skymap of the Coma GCl away from the center. The first source of error is created from the dependence of the VERITAS acceptance on angular distance from the pointing direction, which degrades quickly beyond $\sim 1^\circ$ and is modeled with significant error due to specific observing conditions impacting the VERITAS performance in this regime. The modeled angular acceptance function is included into the VERITAS analysis to correct for this error, but the function is highly dependent on pointing elevation, weather, energy, night-sky background and other observing properties. For example, if the angular acceptance at large angular distances from the VERITAS pointing direction is overestimated, then the normalized background measurement will be reduced and an artificial ring structure can emerge. The scale of the significance determination is also overestimated at large angular distances because the run-dependent variations of the acceptance function are not included into the significance computation.

The second potential source of error in applying the ring-background method to the extended Coma GCl skymap is caused by the contamination of the background measurement by the extended γ-ray emission. An assumption of the ring-background method is that the measured background region contains no signal. For an analysis of a source with an extension larger than the annulus distance ($\sim 0.7^\circ$), this assumption is not valid. The published VERITAS skymap was generated under the assumption that only the central 0.4° region was properly analyzed, and that areas outside of this region are subject to large systematic errors. For example, if one considers a putative γ-ray source with a declining gradient extension of a degree or so, the ring-background method will generate an artificial ring-like feature in the skymap.

The explained difficulties of the application of the ring-background method to the Coma GCl datasets motivates the development of an entirely different analysis chain from the original VERITAS publication. The proposed ring morphology has been directly analyzed

in this dissertation by two methods. First, a skymap of square solid angle bins of $0.2^\circ \times 0.2^\circ$ was produced with a significance determined for each bin. The distribution of significances from the bins contained in the supposed emission ring appears to be consistent with a subsample of the distribution of the full skymap, demonstrating that the set of "ringed" bins is no more significant than an arbitrary selection of bins. Second, a single integrated solid angle bin was defined which traces the ring morphology, and a singular significance was produced. Since this significance is sensitive to the assembly arrangement of the OFF data, 100 iterations with randomized assemblies were performed and the median significance of the resulting distribution was determined for the ring model. This technique demonstrated a median significance of -0.1σ and 1.9σ in the V4 and V6 datasets, respectively, the latter of which had approximately double the exposure. The VERITAS observatory had very different configurations during the V4 and V6 epochs, with a significantly higher sensitivity in V6 dataset. No attempt to combine these datasets was made given the difficulties of dealing with potentially different instrumentation dependent errors outweighing the likely marginal increase in significance from adding V4 data to V6. The nearly 0σ result for the original V4 dataset indicates that the proposed virial shock signal with a ring morphology in the VERITAS published skymap is rejected. The V6 1.9σ result, however, tentatively indicates that an excess of emission may exist within the proposed ring region, although this region has some overlap with the central 1.5° circular region.

When evaluating the simple central 1.5° radius region for excess counts, an even greater significance of 2.7σ is observed in the V6 dataset. These results seem to indicate that, if an extended VHE γ-ray excess does exist in the Coma GCl, the model of emission being distributed in the central 1.5° radius of the Coma GCl is preferential to the emission coming from the proposed ring morphology. In fact, this result arguably aligns with the central extended γ-ray excess seen by Fermi-LAT ($\sim 3\sigma$), which has emission extending out to a similar radius (see Figure 2.10). This result is also consistent with the expected γ-ray emission morphology from simulations (see Figure 6.1). While a 2.7σ result alone may not

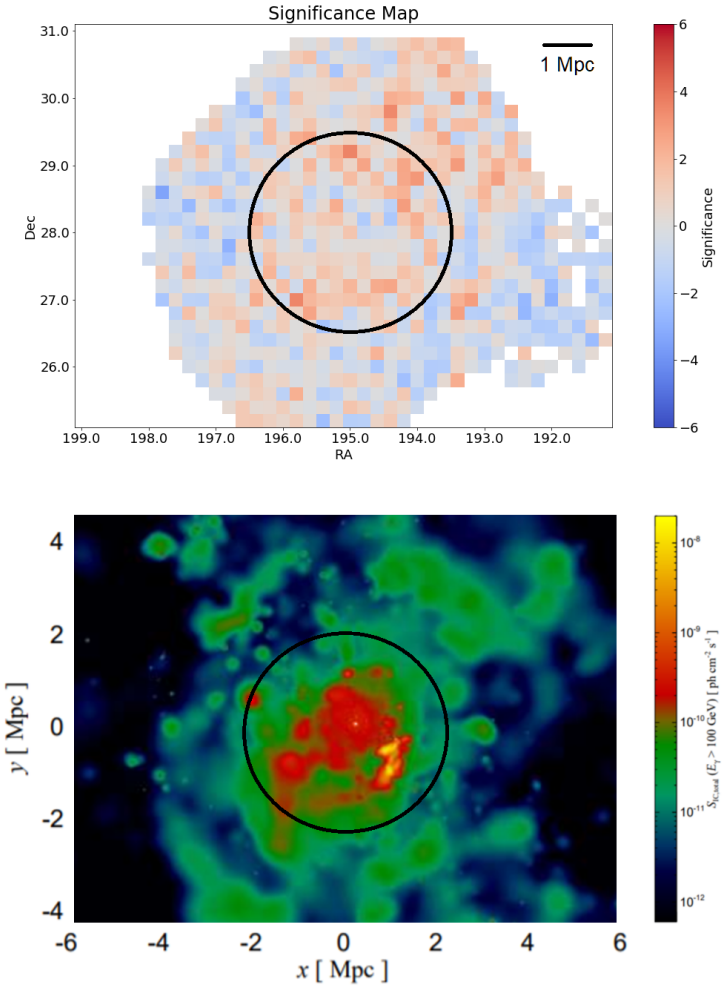

Figure 6.1: Top: The significance map determined in this analysis on the V6 Coma GCl dataset. Bottom: The simulated secondary acceleration γ-ray emission (above 100 GeV) for a Coma-like cluster scaled to match the top figure (see Figure 2.9 for the original). The central 1.5° (approximately 2.5 Mpc) radius region (circled) demonstrates a median significance of 2.7σ for the V6 Coma GCl dataset, which approximately corresponds to the simulated emission central extension in the secondary acceleration model shown in the bottom figure, as well as the hadronic model shown in Figure 2.9.

be an important result, in the context of the Fermi-LAT result and simulated expectation, it may warrant further investigation. This result is encouraging for the future prospects of γ-ray detection from the Coma GCl and other galaxy clusters.

If the 2.7σ result obtained from 18 hours of VERITAS V6 exposure is genuine, then an additional $\sim$ 40 hours exposure of the Coma GCl in the wobble observing mode with a standard offset of 0.5° around the cluster center is enough to reach the 5σ detection requirement. This estimation assumes that the sensitivity scales with the square root of exposure. In fact, the 18 hours of V6 observation time of the Coma GCl field has pointings far from the 1.5° region, and thus the amount of sensitive exposure in the central region is actually less than 18 hours. Observations with a 0.5° wobble offset would maintain exposure of the 1.5° radius central region with nearly maximum sensitivity (the radial acceptance has a strong impact past 1° from the pointing direction). While increasing the wobble offsets up to 0.7° or 0.8° would lower the sensitivity in the central region, it would also improve sensitivity for the study of the potential emission boundary. Consideration of such trade-offs may be important if an observed significance becomes near the detection threshold, at which point a more sophisticated observing strategy to resolve the emission morphology will become desirable.

In addition to improving the statistical sensitivity with more Coma GCl exposure, the analysis procedure presented also benefits from increased exposure of both the Coma GCl and source-free fields. Additional Coma GCl exposure is expected to increase the detection significance if the 2.7σ result is genuine. The number of source-free runs available will also increase as VERITAS continues to observe other sources. This will enable more OFF sets to be assembled, which is particularly important in accurately estimating the residual variance and will result in a reduced sampling variance for the integrated-region median significances.

With CTA coming online in approximately five years, boasting an improved sensitivity and wider field of view, a definitive detection of γ-ray emission from galaxy clusters may be just over the horizon. Under the assumption that the nonthermal electrons in GCls are of

hadronic origin, simulations predict that the Perseus GCl is the brightest GCl to observe γ-ray emission coming from pion decay due to its denser core [PP10]. These simulations predict (see Figure 6.2) that with the improved CTA sensitivity, detection of γ-ray emission can be reached in 300 hours for the least optimal configuration of parameter space considered ($B = 20\mu$G, centrally peaked model) [CAA19]. A much more modest exposure of 60 hours is expected to be enough for detection of γ-ray emission for the more favorable parameter space configuration ($B = 10\mu$G, extended model). These predictions are generated for an investigated central region of 0.15° radius, as the γ-ray emission for the hadronic model is expected to be strongly concentrated near the cluster core.

When considering a significant component of γ-ray emission *not* from pion decay, but instead from inverse Compton scattering of re-accelerated nonthermal electrons, then the Coma GCl may become a more appealing target to investigate extended emission out to the virial radius due to its giant radio halo and recent merger history. The physics of turbulent re-acceleration has large uncertainties, and hence it may be a possible mechanism through which the nonthermal electrons are energized at a cluster-wide scale. While observing the Coma GCl is not currently a key science project of CTA, exposure for the Coma GCl may be allocated by CTA through a submission of a proposal to the CTA Guest Observer Programme. The use of an extended analysis method, such as the one presented in this dissertation, can be adapted for CTA observations to possibly detect diffuse γ-ray emission associated with the re-acceleration model. The specific method presented in this dissertation utilized the large archive of VERITAS observations which CTA does not yet have, and so a direct adaptation to CTA is not possible before a large collection of source-free observations has been established. However, the increased field of view of CTA permits new observing strategies for angular extended objects, such as the possibility of simultaneously observing an extended Coma GCl region and a background region in an 8° field of view.

An array of SCTs in CTA would be especially suitable for the investigation of extended γ-ray emission in all astrophysical objects, such as the Coma GCl. The prototype SCT

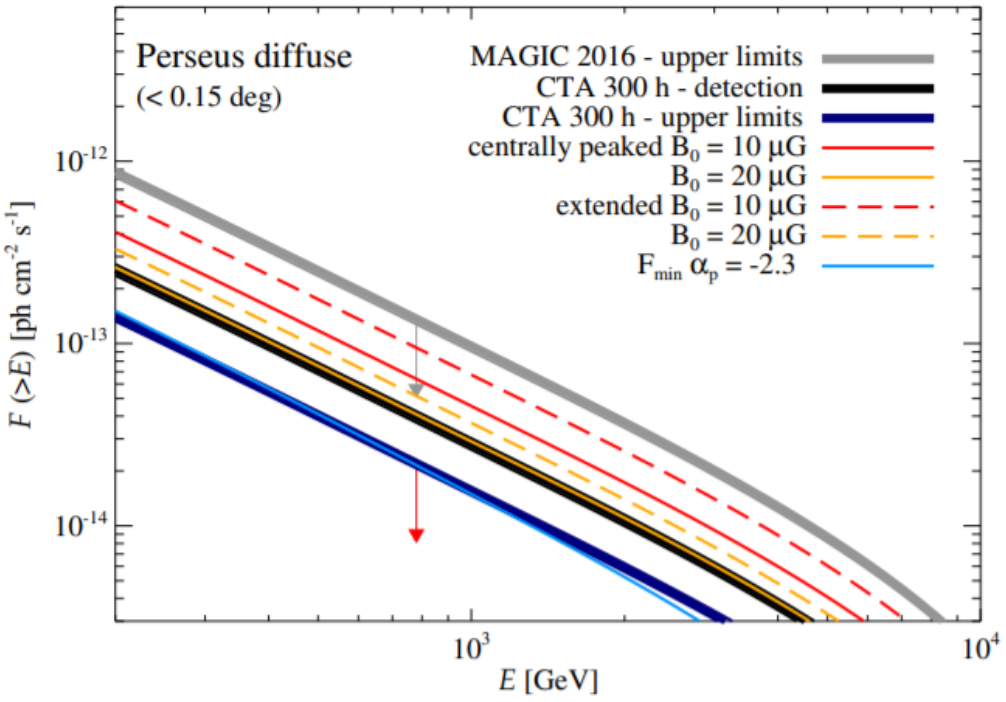

Figure 6.2: The predicted intensity of the γ-ray emission of hadronic origin in the Perseus GCl integrated within a 0.15° radius from the center. The centrally peaked (solid line) and extended (dashed line) models of the cosmic-ray profile is taken from [PP10]. Intensities for central magnetic field strengths of 10 μG and 20 μG are shown by the red and yellow lines, respectively. The grey band shows the current upper limits from MAGIC observations. The dark blue band is an estimate of the 95% CL upper limit from 300 hours of observation by CTA, while the black band is an estimate of the corresponding detectability level. The light blue line is an estimate of the minimum γ-ray flux for a nonthermal proton spectral index of 2.3. Image taken from [CAA19]

has undergone significant development and construction tasks in recent years, validated SCT technology by detecting the Crab Nebula, and is currently in the late commissioning stages. So far the pSCT has demonstrated an on-axis optical performance which satisfies its design specifications, and various alignment improvements are being implemented to further improve it and verify off-axis capabilities. With the 8° field of view fully instrumented camera in development with a scheduled completion date by the end of 2021, the pSCT is soon expected to validate its potential for a CTA-like installation.

[AAA12] A. Abramowski, F. Acero, F. Aharonian, A. G. Akhperjanian, G. Anton, A. Balzer, A. Barnacka, U. Barres de Almeida, Y. Becherini, J. Becker, B. Behera, K. Bernlöhr, E. Birsin, J. Biteau, A. Bochow, C. Boisson, J. Bolmont, P. Bordas, J. Brucker, F. Brun, P. Brun, T. Bulik, I. Büsching, S. Carrigan, S. Casanova, M. Cerruti, P. M. Chadwick, A. Charbonnier, R. C. G. Chaves, A. Cheesebrough, A. C. Clapson, G. Coignet, G. Cologna, J. Conrad, M. Dalton, M. K. Daniel, I. D. Davids, B. Degrange, C. Deil, H. J. Dickinson, A. Djannati-Ataï, W. Domainko, L. O'C. Drury, G. Dubus, K. Dutson, J. Dyks, M. Dyrda, K. Egberts, P. Eger, P. Espigat, L. Fallon, C. Farnier, S. Fegan, F. Feinstein, M. V. Fernand es, A. Fiasson, G. Fontaine, A. Förster, M. Füßling, Y. A. Gallant, H. Gast, L. Gérard, D. Gerbig, B. Giebels, J. F. Glicenstein, B. Glück, P. Goret, D. Göring, S. Häffner, J. D. Hague, D. Hampf, M. Hauser, S. Heinz, G. Heinzelmann, G. Henri, G. Hermann, J. A. Hinton, A. Hoffmann, W. Hofmann, P. Hofverberg, M. Holler, D. Horns, A. Jacholkowska, O. C. de Jager, C. Jahn, M. Jamrozy, I. Jung, M. A. Kastendieck, K. Katarzyński, U. Katz, S. Kaufmann, D. Keogh, D. Khangulyan, B. Khélifi, D. Klochkov, W. Kluźniak, T. Kneiske, Nu. Komin, K. Kosack, R. Kossakowski, H. Laffon, G. Lamanna, D. Lennarz, T. Lohse, A. Lopatin, C. C. Lu, V. Marandon, A. Marcowith, J. Masbou, D. Maurin, N. Maxted, M. Mayer, T. J. L. McComb, M. C. Medina, J. Méhault, R. Moderski, E. Moulin, C. L. Naumann, M. Naumann-Godo, M. de Naurois, D. Nedbal, D. Nekrassov, N. Nguyen, B. Nicholas, J. Niemiec, S. J. Nolan, S. Ohm, E. de Oña Wilhelmi, B. Opitz, M. Ostrowski, I. Oya, M. Panter, M. Paz Arribas, G. Pedaletti, G. Pelletier, P. O. Petrucci, S. Pita, G. Pühlhofer, M. Punch, A. Quirrenbach, M. Raue, S. M. Rayner, A. Reimer, O. Reimer, M. Renaud, R. de los Reyes, F. Rieger, J. Ripken, L. Rob, S. Rosier-Lees, G. Rowell, B. Rudak, C. B. Rulten, J. Ruppel, V. Sahakian, D. A. Sanchez, A. Santangelo, R. Schlickeiser, F. M. Schöck, A. Schulz, U. Schwanke, S. Schwarzburg, S. Schwemmer, F. Sheidaei, J. L. Skilton, H. Sol, G. Spengler, Ł. Stawarz, R. Steenkamp, C. Stegmann, F. Stinzing, K. Stycz, I. Sushch, A. Szostek, J. P. Tavernet, R. Terrier, M. Tluczykont, K. Valerius, C. van Eldik, G. Vasileiadis, C. Venter, J. P. Vialle, A. Viana, P. Vincent, H. J. Völk, F. Volpe, S. Vorobiov, M. Vorster, S. J. Wagner, M. Ward, R. White, A. Wierzcholska, M. Zacharias, A. Zajczyk, A. A. Zdziarski, A. Zech, H. S. Zechlin, and H. E. S. S. Collaboration. "Search for Dark Matter Annihilation Signals from the Fornax Galaxy Cluster with H.E.S.S." *ApJ*, **750**(2):123, May 2012.

[AAA13a] B.S. Acharya, M. Actis, T. Aghajani, G. Agnetta, J. Aguilar, F. Aharonian, M. Ajello, A. Akhperjanian, M. Alcubierre, J. Aleksić, R. Alfaro, E. Aliu, A.J. Allafort, D. Allan, I. Allekotte, E. Amato, J. Anderson, E.O. Angüner, L.A. Antonelli, P. Antoranz, A. Aravantinos, T. Arlen, T. Armstrong, H. Arnaldi, L. Arrabito, K. Asano, T. Ashton, H.G. Asorey, Y. Awane, H. Baba,

A. Babic, N. Baby, J. Bähr, A. Bais, C. Baixeras, S. Bajtlik, M. Balbo, D. Balis, C. Balkowski, A. Bamba, R. Bandiera, A. Barber, C. Barbier, M. Barceló, A. Barnacka, J. Barnstedt, U. Barres de Almeida, J.A. Barrio, A. Basili, S. Basso, D. Bastieri, C. Bauer, A. Baushev, J. Becerra, Y. Becherini, K.C. Bechtol, J. Becker Tjus, V. Beckmann, W. Bednarek, B. Behera, M. Belluso, W. Benbow, J. Berdugo, K. Berger, F. Bernard, T. Bernardino, K. Bernlöhr, N. Bhat, S. Bhattacharyya, C. Bigongiari, A. Biland, S. Billotta, T. Bird, E. Birsin, E. Bissaldi, J. Biteau, M. Bitossi, S. Blake, O. Blanch Bigas, P. Blasi, A. Bobkov, V. Boccone, M. Boettcher, L. Bogacz, J. Bogart, M. Bogdan, C. Boisson, J. Boix Gargallo, J. Bolmont, G. Bonanno, A. Bonardi, T. Bonev, P. Bonifacio, G. Bonnoli, P. Bordas, A. Borgland, J. Borkowski, R. Bose, O. Botner, A. Bottani, L. Bouchet, M. Bourgeat, C. Boutonnet, A. Bouvier, S. Brau-Nogué, I. Braun, T. Bretz, M. Briggs, T. Bringmann, P. Brook, P. Brun, L. Brunetti, T. Buanes, J. Buckley, R. Buehler, V. Bugaev, A. Bulgarelli, T. Bulik, G. Busetto, S. Buson, K. Byrum, M. Cailles, R. Cameron, J. Camprecios, R. Canestrari, S. Cantu, M. Capalbi, P. Caraveo, E. Carmona, A. Carosi, J. Carr, P.-H. Carton, S. Casanova, M. Casiraghi, O. Catalano, S. Cavazzani, S. Cazaux, M. Cerruti, E. Chabanne, P. Chadwick, C. Champion, A. Chen, J. Chiang, L. Chiappetti, M. Chikawa, V.R. Chitnis, F. Chollet, J. Chudoba, M. Cieślar, A. Cillis, J. Cohen-Tanugi, S. Colafrancesco, P. Colin, J. Colome, S. Colonges, M. Compin, P. Conconi, V. Conforti, V. Connaughton, J. Conrad, J.L. Contreras, P. Coppi, P. Corona, D. Corti, J. Cortina, L. Cossio, H. Costantini, G. Cotter, B. Courty, S. Couturier, S. Covino, G. Crimi, S.J. Criswell, J. Croston, G. Cusumano, M. Dafonseca, O. Dale, M. Daniel, J. Darling, I. Davids, F. Dazzi, A. De Angelis, V. De Caprio, F. De Frondat, E.M. de Gouveia Dal Pino, I. de la Calle, G.A. De La Vega, R. de los Reyes Lopez, B. De Lotto, A. De Luca, J.R.T. de Mello Neto, M. de Naurois, Y. de Oliveira, E. de Oña Wilhelmi, V. de Souza, G. Decerprit, G. Decock, C. Deil, E. Delagnes, G. Deleglise, C. Delgado, D. Della Volpe, P. Demange, G. Depaola, A. Dettlaff, A. Di Paola, F. Di Pierro, C. Díaz, J. Dick, R. Dickherber, H. Dickinson, V. Diez-Blanco, S. Digel, D. Dimitrov, G. Disset, A. Djannati-Ataï, M. Doert, M. Dohmke, W. Domainko, D. Dominis Prester, A. Donat, D. Dorner, M. Doro, J.-L. Dournaux, G. Drake, D. Dravins, L. Drury, F. Dubois, R. Dubois, G. Dubus, C. Dufour, D. Dumas, J. Dumm, D. Durand, J. Dyks, M. Dyrda, J. Ebr, E. Edy, K. Egberts, P. Eger, S. Einecke, C. Eleftheriadis, S. Elles, D. Emmanoulopoulos, D. Engelhaupt, R. Enomoto, J.-P. Ernenwein, M. Errando, A. Etchegoyen, P. Evans, A. Falcone, D. Fantinel, K. Farakos, C. Farnier, G. Fasola, B. Favill, E. Fede, S. Federici, S. Fegan, F. Feinstein, D. Ferenc, P. Ferrando, M. Fesquet, A. Fiasson, E. Fillin-Martino, D. Fink, C. Finley, J.P. Finley, M. Fiorini, R. Firpo Curcoll, H. Flores, D. Florin, W. Focke, C. Föhr, E. Fokitis, L. Font, G. Fontaine, M. Fornasa, A. Förster, L. Fortson, N. Fouque, A. Franckowiak, C. Fransson, G. Fraser, R. Frei, I.F.M. Albuquerque, L. Fresnillo, C. Fruck, Y. Fujita, Y. Fukazawa, Y. Fukui, S. Funk,

W. Gäbele, S. Gabici, R. Gabriele, A. Gadola, N. Galante, D. Gall, Y. Gallant, J. Gámez-García, B. García, R. Garcia López, D. Gardiol, D. Garrido, L. Garrido, D. Gascon, M. Gaug, J. Gaweda, L. Gebremedhin, N. Geffroy, L. Gerard, A. Ghedina, M. Ghigo, E. Giannakaki, F. Gianotti, S. Giarrusso, G. Giavitto, B. Giebels, V. Gika, P. Giommi, N. Girard, E. Giro, A. Giuliani, T. Glanzman, J.-F. Glicenstein, N. Godinovic, V. Golev, M. Gomez Berisso, J. Gómez-Ortega, M.M. Gonzalez, A. González, F. González, A. González Muñoz, K.S. Gothe, M. Gougerot, R. Graciani, P. Grandi, F. Grañena, J. Granot, G. Grasseau, R. Gredig, A. Green, T. Greenshaw, T. Grégoire, O. Grimm, J. Grube, M. Grudzinska, V. Gruev, S. Grünewald, J. Grygorczuk, V. Guarino, S. Gunji, G. Gyuk, D. Hadasch, R. Hagiwara, J. Hahn, N. Hakansson, A. Hallgren, N. Hamer Heras, S. Hara, M.J. Hardcastle, J. Harris, T. Hassan, K. Hatanaka, T. Haubold, A. Haupt, T. Hayakawa, M. Hayashida, R. Heller, F. Henault, G. Henri, G. Hermann, R. Hermel, A. Herrero, N. Hidaka, J. Hinton, D. Hoffmann, W. Hofmann, P. Hofverberg, J. Holder, D. Horns, D. Horville, J. Houles, M. Hrabovsky, D. Hrupec, H. Huan, B. Huber, J.-M. Huet, G. Hughes, T.B. Humensky, J. Huovelin, A. Ibarra, J.M. Illa, D. Impiombato, S. Incorvaia, S. Inoue, Y. Inoue, K. Ioka, E. Ismailova, C. Jablonski, A. Jacholkowska, M. Jamrozy, M. Janiak, P. Jean, C. Jeanney, J.J. Jimenez, T. Jogler, T. Johnson, L. Journet, C. Juffroy, I. Jung, P. Kaaret, S. Kabuki, M. Kagaya, J. Kakuwa, C. Kalkuhl, R. Kankanyan, A. Karastergiou, K. Kärcher, M. Karczewski, S. Karkar, J. Kasperek, D. Kastana, H. Katagiri, J. Kataoka, K. Katarzyński, U. Katz, N. Kawanaka, B. Kellner-Leidel, H. Kelly, E. Kendziorra, B. Khélifi, D.B. Kieda, T. Kifune, T. Kihm, T. Kishimoto, K. Kitamoto, W. Kluźniak, C. Knapic, J. Knapp, J. Knödlseder, F. Köck, J. Kocot, K. Kodani, J.-H. Köhne, K. Kohri, K. Kokkotas, D. Kolitzus, N. Komin, I. Kominis, Y. Konno, H. Köppel, P. Korohoda, K. Kosack, G. Koss, R. Kossakowski, P. Kostka, R. Koul, G. Kowal, S. Koyama, J. Kozioł, T. Krähenbühl, J. Krause, H. Krawczynski, F. Krennrich, A. Krepps, A. Kretzschmann, R. Krobot, P. Krueger, H. Kubo, V.A. Kudryavtsev, J. Kushida, A. Kuznetsov, A. La Barbera, N. La Palombara, V. La Parola, G. La Rosa, K. Lacombe, G. Lamanna, J. Lande, D. Languignon, J. Lapington, P. Laporte, C. Lavalley, T. Le Flour, A. Le Padellec, S.-H. Lee, W.H. Lee, M.A. Leigui de Oliveira, D. Lelas, J.-P. Lenain, D.J. Leopold, T. Lerch, L. Lessio, B. Lieunard, E. Lindfors, A. Liolios, A. Lipniacka, H. Lockart, T. Lohse, S. Lombardi, A. Lopatin, M. Lopez, R. López-Coto, A. López-Oramas, A. Lorca, E. Lorenz, P. Lubinski, F. Lucarelli, H. Lüdecke, J. Ludwin, P.L. Luque-Escamilla, W. Lustermann, O. Luz, E. Lyard, M.C. Maccarone, T.J. Maccarone, G.M. Madejski, A. Madhavan, M. Mahabir, G. Maier, P. Majumdar, G. Malaguti, S. Maltezos, A. Manalaysay, A. Mancilla, D. Mandat, G. Maneva, A. Mangano, P. Manigot, K. Mannheim, I. Manthos, N. Maragos, A. Marcowith, M. Mariotti, M. Marisaldi, S. Markoff, A. Marszałek, C. Martens, J. Martí, J.-M. Martin, P. Martin, G. Martínez, F. Martínez, M. Martínez,

A. Masserot, A. Mastichiadis, A. Mathieu, H. Matsumoto, F. Mattana, S. Mattiazzo, G. Maurin, S. Maxfield, J. Maya, D. Mazin, L. Mc Comb, N. McCubbin, I. McHardy, R. McKay, C. Medina, C. Melioli, D. Melkumyan, S. Mereghetti, P. Mertsch, M. Meucci, J. Michałowski, P. Micolon, A. Mihailidis, T. Mineo, M. Minuti, N. Mirabal, F. Mirabel, J.M. Miranda, R. Mirzoyan, T. Mizuno, B. Moal, R. Moderski, I. Mognet, E. Molinari, M. Molinaro, T. Montaruli, I. Monteiro, P. Moore, A. Moralejo Olaizola, M. Mordalska, C. Morello, K. Mori, F. Mottez, Y. Moudden, E. Moulin, I. Mrusek, R. Mukherjee, P. Munar-Adrover, H. Muraishi, K. Murase, A. Murphy, S. Nagataki, T. Naito, D. Nakajima, T. Nakamori, K. Nakayama, C. Naumann, D. Naumann, M. Naumann-Godo, P. Nayman, D. Nedbal, D. Neise, L. Nellen, V. Neustroev, N. Neyroud, L. Nicastro, J. Nicolau-Kukliński, A. Niedźwiecki, J. Niemiec, D. Nieto, A. Nikolaidis, K. Nishijima, S. Nolan, R. Northrop, D. Nosek, N. Nowak, A. Nozato, P. O'Brien, Y. Ohira, M. Ohishi, S. Ohm, H. Ohoka, T. Okuda, A. Okumura, J.-F. Olive, R.A. Ong, R. Orito, M. Orr, J. Osborne, M. Ostrowski, L.A. Otero, N. Otte, E. Ovcharov, I. Oya, A. Ozieblo, L. Padilla, S. Paiano, D. Paillot, A. Paizis, S. Palanque, M. Palatka, J. Pallota, K. Panagiotidis, J.-L. Panazol, D. Paneque, M. Panter, R. Paoletti, A. Papayannis, G. Papyan, J.M. Paredes, G. Pareschi, G. Parks, J.-M. Parraud, D. Parsons, M. Paz Arribas, M. Pech, G. Pedaletti, V. Pelassa, D. Pelat, M.d.C. Perez, M. Persic, P.-O. Petrucci, B. Peyaud, A. Pichel, S. Pita, F. Pizzolato, Ł. Platos, R. Platzer, L. Pogosyan, M. Pohl, G. Pojmanski, J.D. Ponz, W. Potter, J. Poutanen, E. Prandini, J. Prast, R. Preece, F. Profeti, H. Prokoph, M. Prouza, M. Proyetti, I. Puerto-Gimenez, G. Pühlhofer, I. Puljak, M. Punch, R. Pyzioł, E.J. Quel, J. Quinn, A. Quirrenbach, E. Racero, P.J. Rajda, P. Ramon, R. Rando, R.C. Rannot, M. Rataj, M. Raue, P. Reardon, O. Reimann, A. Reimer, O. Reimer, K. Reitberger, M. Renaud, S. Renner, B. Reville, W. Rhode, M. Ribó, M. Ribordy, M.G. Richer, J. Rico, J. Ridky, F. Rieger, P. Ringegni, J. Ripken, P.R. Ristori, A. Riviére, S. Rivoire, L. Rob, U. Roeser, R. Rohlfs, G. Rojas, P. Romano, W. Romaszkan, G.E. Romero, S. Rosen, S. Rosier Lees, D. Ross, G. Rouaix, J. Rousselle, S. Rousselle, A.C. Rovero, F. Roy, S. Royer, B. Rudak, C. Rulten, M. Rupiński, F. Russo, F. Ryde, B. Sacco, E.O. Saemann, A. Saggion, V. Sahakian, K. Saito, T. Saito, Y. Saito, N. Sakaki, R. Sakonaka, A. Salini, F. Sanchez, M. Sanchez-Conde, A. Sandoval, H. Sandaker, E. Sant'Ambrogio, A. Santangelo, E.M. Santos, A. Sanuy, L. Sapozhnikov, S. Sarkar, N. Sartore, H. Sasaki, K. Satalecka, M. Sawada, V. Scalzotto, V. Scapin, M. Scarcioffolo, J. Schafer, T. Schanz, S. Schlenstedt, R. Schlickeiser, T. Schmidt, J. Schmoll, P. Schovanek, M. Schroedter, C. Schultz, J. Schultze, A. Schulz, K. Schure, T. Schwab, U. Schwanke, J. Schwarz, S. Schwarzburg, T. Schweizer, S. Schwemmer, A. Segreto, J.-H. Seiradakis, G.H. Sembroski, K. Seweryn, M. Sharma, M. Shayduk, R.C. Shellard, J. Shi, T. Shibata, A. Shibuya, E. Shum, L. Sidoli, M. Sidz, J. Sieiro, M. Sikora, J. Silk, A. Sillanpää, B.B. Singh, J. Sitarek, C. Skole, R. Smareglia, A. Smith, D. Smith, J. Smith, N. Smith, D. Sobczyńska,

H. Sol, G. Sottile, M. Sowiński, F. Spanier, D. Spiga, S. Spyrou, V. Stamatescu, A. Stamerra, R. Starling, Ł. Stawarz, R. Steenkamp, C. Stegmann, S. Steiner, N. Stergioulas, R. Sternberger, M. Sterzel, F. Stinzing, M. Stodulski, U. Straumann, E. Strazzeri, L. Stringhetti, A. Suarez, M. Suchenek, R. Sugawara, K.-H. Sulanke, S. Sun, A.D. Supanitsky, T. Suric, P. Sutcliffe, J. Sykes, M. Szanecki, T. Szepieniec, A. Szostek, G. Tagliaferri, H. Tajima, H. Takahashi, K. Takahashi, L. Takalo, H. Takami, G. Talbot, J. Tammi, M. Tanaka, S. Tanaka, J. Tasan, M. Tavani, J.-P. Tavernet, L.A. Tejedor, I. Telezhinsky, P. Temnikov, C. Tenzer, Y. Terada, R. Terrier, M. Teshima, V. Testa, D. Tezier, D. Thuermann, L. Tibaldo, O. Tibolla, A. Tiengo, M. Tluczykont, C.J. Todero Peixoto, F. Tokanai, M. Tokarz, K. Toma, K. Torii, M. Tornikoski, D.F. Torres, M. Torres, G. Tosti, T. Totani, F. Toussenel, G. Tovmassian, P. Travnicek, M. Trifoglio, I. Troyano, K. Tsinganos, H. Ueno, K. Umehara, S.S. Upadhya, T. Usher, M. Uslenghi, J.F. Valdes-Galicia, P. Vallania, G. Vallejo, W. van Driel, C. van Eldik, J. Vandenbrouke, J. Vanderwalt, H. Vankov, G. Vasileiadis, V. Vassiliev, D. Veberic, I. Vegas, S. Vercellone, S. Vergani, C. Veyssiére, J.P. Vialle, A. Viana, M. Videla, P. Vincent, S. Vincent, J. Vink, N. Vlahakis, L. Vlahos, P. Vogler, A. Vollhardt, H.-P. von Gunten, S. Vorobiov, C. Vuerli, V. Waegebaert, R. Wagner, R.G. Wagner, S. Wagner, S.P. Wakely, R. Walter, T. Walther, K. Warda, R. Warwick, P. Wawer, R. Wawrzaszek, N. Webb, P. Wegner, A. Weinstein, Q. Weitzel, R. Welsing, M. Werner, H. Wetteskind, R. White, A. Wierzcholska, S. Wiesand, M. Wilkinson, D.A. Williams, R. Willingale, K. Winiarski, R. Wischnewski, Ł. Wiśniewski, M. Wood, A. Wörnlein, Q. Xiong, K.K. Yadav, H. Yamamoto, T. Yamamoto, R. Yamazaki, S. Yanagita, J.M. Yebras, D. Yelos, A. Yoshida, T. Yoshida, T. Yoshikoshi, V. Zabalza, M. Zacharias, A. Zajczyk, R. Zanin, A. Zdziarski, A. Zech, A. Zhao, X. Zhou, K. Zietara, J. Ziolkowski, P. Ziolkowski, V. Zitelli, C. Zurbach, and P. Zychowski. "Introducing the CTA concept." *Astroparticle Physics*, **43**:3 – 18, 2013. Seeing the High-Energy Universe with the Cherenkov Telescope Array - The Science Explored with the CTA.

[AAA13b] M. Ackermann, M. Ajello, A. Albert, A. Allafort, L. Baldini, G. Barbiellini, D. Bastieri, K. Bechtol, R. Bellazzini, E. Bissaldi, E. D. Bloom, E. Bonamente, E. Bottacini, T. J. Brand t, J. Bregeon, M. Brigida, P. Bruel, R. Buehler, S. Buson, G. A. Caliandro, R. A. Cameron, P. A. Caraveo, J. M. Casandjian, C. Cecchi, E. Charles, R. C. G. Chaves, A. Chekhtman, J. Chiang, S. Ciprini, R. Claus, J. Cohen-Tanugi, J. Conrad, S. Cutini, F. D'Ammand o, A. de Angelis, F. de Palma, C. D. Dermer, S. W. Digel, L. Di Venere, P. S. Drell, A. Drlica-Wagner, R. Essig, C. Favuzzi, S. J. Fegan, E. C. Ferrara, W. B. Focke, A. Franckowiak, Y. Fukazawa, S. Funk, P. Fusco, F. Gargano, D. Gasparrini, S. Germani, N. Giglietto, F. Giordano, M. Giroletti, T. Glanzman, G. Godfrey, G. A. Gomez-Vargas, I. A. Grenier, S. Guiriec, M. Gustafsson, D. Hadasch, M. Hayashida, A. B. Hill, D. Horan, X. Hou, R. E. Hughes, Y. Inoue, E. Izaguirre, T. Jogler, T. Kamae,

J. Knödlseder, M. Kuss, J. Lande, S. Larsson, L. Latronico, F. Longo, F. Loparco, M. N. Lovellette, P. Lubrano, D. Malyshev, M. Mayer, M. N. Mazziotta, J. E. McEnery, P. F. Michelson, W. Mitthumsiri, T. Mizuno, A. A. Moiseev, M. E. Monzani, A. Morselli, I. V. Moskalenko, S. Murgia, T. Nakamori, R. Nemmen, E. Nuss, T. Ohsugi, A. Okumura, N. Omodei, M. Orienti, E. Orlando, J. F. Ormes, D. Paneque, J. S. Perkins, M. Pesce-Rollins, F. Piron, G. Pivato, S. Rainò, R. Rando, M. Razzano, S. Razzaque, A. Reimer, O. Reimer, R. W. Romani, M. Sánchez-Conde, A. Schulz, C. Sgrò, J. Siegal-Gaskins, E. J. Siskind, A. Snyder, G. Spand re, P. Spinelli, D. J. Suson, H. Tajima, H. Takahashi, J. G. Thayer, J. B. Thayer, L. Tibaldo, M. Tinivella, G. Tosti, E. Troja, Y. Uchiyama, T. L. Usher, J. Vandenbroucke, V. Vasileiou, G. Vianello, V. Vitale, B. L. Winer, K. S. Wood, M. Wood, Z. Yang, G. Zaharijas, and S. Zimmer. "Search for gamma-ray spectral lines with the Fermi Large Area Telescope and dark matter implications." *Phys. Rev. D*, **88**(8):082002, October 2013.

[AAA18a] H. Abdalla, F. Aharonian, F. Ait Benkhali, E. O. Angüner, M. Arakawa, C. Arcaro, C. Armand , M. Arrieta, M. Backes, M. Barnard, Y. Becherini, J. Becker Tjus, D. Berge, S. Bernhard, K. Bernlöhr, R. Blackwell, M. Böttcher, C. Boisson, J. Bolmont, S. Bonnefoy, P. Bordas, J. Bregeon, F. Brun, P. Brun, M. Bryan, M. Büchele, T. Bulik, T. Bylund, M. Capasso, S. Caroff, A. Carosi, S. Casanova, M. Cerruti, N. Chakraborty, S. Chand ra, R. C. G. Chaves, A. Chen, S. Colafrancesco, B. Condon, I. D. Davids, C. Deil, J. Devin, P. deWilt, L. Dirson, A. Djannati-Ataï, A. Dmytriiev, A. Donath, V. Doroshenko, L. O'C. Drury, J. Dyks, K. Egberts, G. Emery, J. P. Ernenwein, S. Eschbach, S. Fegan, A. Fiasson, G. Fontaine, S. Funk, M. Füßling, S. Gabici, Y. A. Gallant, F. Gaté, G. Giavitto, D. Glawion, J. F. Glicenstein, D. Gottschall, M. H. Grondin, J. Hahn, M. Haupt, G. Heinzelmann, G. Henri, G. Hermann, J. A. Hinton, W. Hofmann, C. Hoischen, T. L. Holch, M. Holler, D. Horns, D. Huber, H. Iwasaki, A. Jacholkowska, M. Jamrozy, D. Jankowsky, F. Jankowsky, L. Jouvin, I. Jung-Richardt, M. A. Kastendieck, K. Katarzyński, M. Katsuragawa, U. Katz, D. Kerszberg, D. Khangulyan, B. Khélifi, J. King, S. Klepser, W. Kluźniak, Nu. Komin, K. Kosack, S. Krakau, M. Kraus, P. P. Krüger, G. Lamanna, J. Lau, J. Lefaucheur, A. Lemière, M. Lemoine-Goumard, J. P. Lenain, E. Leser, T. Lohse, M. Lorentz, R. López-Coto, I. Lypova, D. Malyshev, V. Marandon, A. Marcowith, C. Mariaud, G. Martí-Devesa, R. Marx, G. Maurin, P. J. Meintjes, A. M. W. Mitchell, R. Moderski, M. Mohamed, L. Mohrmann, E. Moulin, T. Murach, S. Nakashima, M. de Naurois, H. Ndiyavala, F. Niederwanger, J. Niemiec, L. Oakes, P. O'Brien, H. Odaka, S. Ohm, M. Ostrowski, I. Oya, M. Padovani, M. Panter, R. D. Parsons, C. Perennes, P. O. Petrucci, B. Peyaud, Q. Piel, S. Pita, V. Poireau, A. Priyana Noel, D. A. Prokhorov, H. Prokoph, G. Pühlhofer, M. Punch, A. Quirrenbach, S. Raab, R. Rauth, A. Reimer, O. Reimer, M. Renaud, F. Rieger, L. Rinchiuso, C. Romoli, G. Rowell,

B. Rudak, E. Ruiz-Velasco, V. Sahakian, S. Saito, D. A. Sanchez, A. Santangelo, M. Sasaki, R. Schlickeiser, F. Schüssler, A. Schulz, U. Schwanke, S. Schwemmer, M. Seglar-Arroyo, M. Senniappan, A. S. Seyffert, N. Shafi, I. Shilon, K. Shiningayamwe, R. Simoni, A. Sinha, H. Sol, F. Spanier, A. Specovius, M. Spir-Jacob, Ł. Stawarz, R. Steenkamp, C. Stegmann, C. Steppa, T. Takahashi, J. P. Tavernet, T. Tavernier, A. M. Taylor, R. Terrier, L. Tibaldo, D. Tiziani, M. Tluczykont, C. Trichard, M. Tsirou, N. Tsuji, R. Tuffs, Y. Uchiyama, D. J. van der Walt, C. van Eldik, C. van Rensburg, B. van Soelen, G. Vasileiadis, J. Veh, C. Venter, A. Viana, P. Vincent, J. Vink, F. Voisin, H. J. Völk, T. Vuillaume, Z. Wadiasingh, S. J. Wagner, R. M. Wagner, R. White, A. Wierzcholska, R. Yang, D. Zaborov, M. Zacharias, R. Zanin, A. A. Zdziarski, A. Zech, F. Zefi, A. Ziegler, J. Zorn, N. Żywucka, M. Cirelli, P. Panci, F. Sala, J. Silk, and M. Taoso. "Searches for gamma-ray lines and 'pure WIMP' spectra from Dark Matter annihilations in dwarf galaxies with H.E.S.S." *J. Cosmology Astropart. Phys.*, **2018**(11):037, November 2018.

[AAA18b] V.A. Acciari, S. Ansoldi, L.A. Antonelli, A. Arbet Engels, C. Arcaro, D. Baack, A. Babić, B. Banerjee, P. Bangale, U. Barres de Almeida, J.A. Barrio, J. Becerra González, W. Bednarek, E. Bernardini, A. Berti, J. Besenrieder, W. Bhattacharyya, C. Bigongiari, A. Biland, O. Blanch, G. Bonnoli, R. Carosi, G. Ceribella, S. Cikota, S.M. Colak, P. Colin, E. Colombo, J.L. Contreras, J. Cortina, S. Covino, V. D'Elia, P. Da Vela, F. Dazzi, A. De Angelis, B. De Lotto, M. Delfino, J. Delgado, F. Di Pierro, E. Do Souto Espiñera, A. Domínguez, D. Dominis Prester, D. Dorner, M. Doro, S. Einecke, D. Elsaesser, V. Fallah Ramazani, A. Fattorini, A. Fernández-Barral, G. Ferrara, D. Fidalgo, L. Foffano, M.V. Fonseca, L. Font, C. Fruck, D. Galindo, S. Gallozzi, R.J. García López, M. Garczarczyk, M. Gaug, P. Giammaria, N. Godinović, D. Guberman, D. Hadasch, A. Hahn, T. Hassan, J. Herrera, J. Hoang, D. Hrupec, S. Inoue, K. Ishio, Y. Iwamura, H. Kubo, J. Kushida, D. Kuveždić, A. Lamastra, D. Lelas, F. Leone, E. Lindfors, S. Lombardi, F. Longo, M. López, A. López-Oramas, C. Maggio, P. Majumdar, M. Makariev, G. Maneva, M. Manganaro, K. Mannheim, L. Maraschi, M. Mariotti, M. Martínez, S. Masuda, D. Mazin, M. Minev, J.M. Miranda, R. Mirzoyan, E. Molina, A. Moralejo, V. Moreno, E. Moretti, P. Munar-Adrover, V. Neustroev, A. Niedzwiecki, M. Nievas Rosillo, C. Nigro, K. Nilsson, D. Ninci, K. Nishijima, K. Noda, L. Nogués, S. Paiano, J. Palacio, D. Paneque, R. Paoletti, J.M. Paredes, G. Pedaletti, P. Peñil, M. Peresano, M. Persic, P.G. Prada Moroni, E. Prandini, I. Puljak, J.R. Garcia, W. Rhode, M. Ribó, J. Rico, C. Righi, A. Rugliancich, L. Saha, T. Saito, K. Satalecka, T. Schweizer, J. Sitarek, I. Šnidarić, D. Sobczynska, A. Somero, A. Stamerra, M. Strzys, T. Surić, F. Tavecchio, P. Temnikov, T. Terzić, M. Teshima, N. Torres-Albà, S. Tsujimoto, G. Vanzo, M. Vazquez Acosta, I. Vovk, J.E. Ward, M. Will, and D. Zarić. "Constraining dark matter lifetime with a deep gamma-ray survey

of the Perseus galaxy cluster with MAGIC." *Physics of the Dark Universe*, **22**:38 – 47, 2018.

[AAA19] C. Adams, G. Ambrosi, M. Ambrosio, C. Aramo, W. Benbow, B. Bertucci, E. Bissaldi, M. Bitossi, A. Boiano, C. Bonavolontà, R. Bose, A. Brill, J. H. Buckley, M. Caprai, C. E. Covault, L. Di Venere, S. Fegan, Q. Feng, E. Fiandrini, A. Gent, N. Giglietto, F. Giordano, R. Halliday, O. Hervet, G. Hughes, T. B. Humensky, M. Ionica, W. Jin, P. Kaaret, D. Kieda, B. Kim, F. Licciulli, S. Loporchio, V. Masone, T. Meures, B. A. W. Mode, R. Mukherjee, A. Okumura, N. Otte, F. R. Pantaleo, R. Paoletti, A. Petrashyk, J. Powell, K. Powell, D. Ribeiro, J. Rousselle, A. Rugliancich, M. Santander, R. Shang, B. Stevenson, L. Stiaccini, L. P. Taylor, L. Tosti, V. Vagelli, M. Valentino, J. Vand enbroucke, V. Vassiliev, P. Wilcox, and D. A. Williams. "Prototype Schwarzschild-Couder Telescope for the Cherenkov Telescope Array: Commissioning Status of the Optical System." *arXiv e-prints*, p. arXiv:1909.11403, September 2019.

[AAA20] V. A. Acciari, S. Ansoldi, L. A. Antonelli, A. Arbet Engels, D. Baack, A. Babić, B. Banerjee, U. Barres de Almeida, J. A. Barrio, J. Becerra González, W. Bednarek, L. Bellizzi, E. Bernardini, A. Berti, J. Besenrieder, W. Bhattacharyya, C. Bigongiari, A. Biland, O. Blanch, G. Bonnoli, Ž. Bošnjak, G. Busetto, R. Carosi, G. Ceribella, Y. Chai, A. Chilingarian, S. Cikota, S. M. Colak, U. Colin, E. Colombo, J. L. Contreras, J. Cortina, S. Covino, V. D'Elia, P. da Vela, F. Dazzi, A. de Angelis, B. de Lotto, M. Delfino, J. Delgado, D. Depaoli, F. di Pierro, L. di Venere, E. Do Souto Espiñeira, D. Dominis Prester, A. Donini, D. Dorner, M. Doro, D. Elsaesser, V. Fallah Ramazani, A. Fattorini, G. Ferrara, D. Fidalgo, L. Foffano, M. V. Fonseca, L. Font, C. Fruck, S. Fukami, R. J. García López, M. Garczarczyk, S. Gasparyan, M. Gaug, N. Giglietto, F. Giordano, P. Gliwny, N. Godinović, D. Green, J. G. Green, D. Guberman, D. Hadasch, A. Hahn, J. Herrera, J. Hoang, D. Hrupec, M. Hütten, T. Inada, S. Inoue, K. Ishio, Y. Iwamura, L. Jouvin, D. Kerszberg, H. Kubo, J. Kushida, A. Lamastra, D. Lelas, F. Leone, E. Lindfors, S. Lombardi, F. Longo, M. López, R. López-Coto, A. López-Oramas, S. Loporchio, B. Machado de Oliveira Fraga, C. Maggio, P. Majumdar, M. Makariev, M. Mallamaci, G. Maneva, M. Manganaro, K. Mannheim, L. Maraschi, M. Mariotti, M. Martínez, D. Mazin, S. Mićanović, D. Miceli, T. Miener, M. Minev, J. M. Miranda, R. Mirzoyan, E. Molina, A. Moralejo, D. Morcuende, V. Moreno, E. Moretti, P. Munar-Adrover, V. Neustroev, C. Nigro, K. Nilsson, D. Ninci, K. Nishijima, K. Noda, L. Nogués, S. Nozaki, S. Paiano, J. Palacio, M. Palatiello, D. Paneque, R. Paoletti, J. M. Paredes, P. Peñil, M. Peresano, M. Persic, P. G. Prada Moroni, E. Prandini, I. Puljak, W. Rhode, M. Ribó, J. Rico, C. Righi, A. Rugliancich, L. Saha, N. Sahakyan, T. Saito, S. Sakurai, K. Satalecka, F. G. Saturni, K. Schmidt, T. Schweizer, J. Sitarek, I. Šnidarić, D. Sobczynska, A. Somero, A. Stamerra, D. Strom, Y. Suda, T. Surić, M. Takahashi, F. Tavecchio, P. Temnikov, T. Terzić, M. Teshima, N. Torres-Albà,

L. Tosti, V. Vagelli, J. van Scherpenberg, G. Vanzo, M. Vazquez Acosta, C. F. Vigorito, V. Vitale, I. Vovk, M. Will, D. Zarić, and MAGIC Collaboration. "A search for dark matter in Triangulum II with the MAGIC telescopes." *Physics of the Dark Universe*, **28**:100529, May 2020.

[AAB12] T. Arlen, T. Aune, M. Beilicke, W. Benbow, A. Bouvier, J. H. Buckley, V. Bugaev, K. Byrum, A. Cannon, A. Cesarini, L. Ciupik, E. Collins-Hughes, M. P. Connolly, W. Cui, R. Dickherber, J. Dumm, A. Falcone, S. Federici, Q. Feng, J. P. Finley, G. Finnegan, L. Fortson, A. Furniss, N. Galante, D. Gall, S. Godambe, S. Griffin, J. Grube, G. Gyuk, J. Holder, H. Huan, G. Hughes, T. B. Humensky, A. Imran, P. Kaaret, N. Karlsson, M. Kertzman, Y. Khassen, D. Kieda, H. Krawczynski, F. Krennrich, K. Lee, A. S Madhavan, G. Maier, P. Majumdar, S. McArthur, A. McCann, P. Moriarty, R. Mukherjee, T. Nelson, A. O'Faoláin de Bhróit, R. A. Ong, M. Orr, A. N. Otte, N. Park, J. S. Perkins, M. Pohl, H. Prokoph, J. Quinn, K. Ragan, L. C. Reyes, P. T. Reynolds, E. Roache, J. Ruppel, D. B. Saxon, M. Schroedter, G. H. Sembroski, C. Skole, A. W. Smith, I. Telezhinsky, G. Tešić, M. Theiling, S. Thibadeau, K. Tsurusaki, A. Varlotta, M. Vivier, S. P. Wakely, J. E. Ward, A. Weinstein, R. Welsing, D. A. Williams, B. Zitzer, C. Pfrommer, and A. Pinzke. "CONSTRAINTS ON COSMIC RAYS, MAGNETIC FIELDS, AND DARK MATTER FROM GAMMA-RAY OBSERVATIONS OF THE COMA CLUSTER OF GALAXIES WITH VERITAS AND-FERMI." *The Astrophysical Journal*, **757**(2):123, sep 2012.

[AAB13] W. Atwood, A. Albert, L. Baldini, M. Tinivella, J. Bregeon, M. Pesce-Rollins, C. Sgrò, P. Bruel, E. Charles, A. Drlica-Wagner, A. Franckowiak, T. Jogler, L. Rochester, T. Usher, M. Wood, J. Cohen-Tanugi, and S. Zimmer. "Pass 8: Toward the Full Realization of the Fermi-LAT Scientific Potential." *arXiv e-prints*, p. arXiv:1303.3514, March 2013.

[AAB17] S. Archambault, A. Archer, W. Benbow, R. Bird, E. Bourbeau, T. Brantseg, M. Buchovecky, J. H. Buckley, V. Bugaev, K. Byrum, M. Cerruti, J. L. Christiansen, M. P. Connolly, W. Cui, M. K. Daniel, Q. Feng, J. P. Finley, H. Fleischhack, L. Fortson, A. Furniss, A. Geringer-Sameth, S. Griffin, J. Grube, M. Hütten, N. Hâkansson, D. Hanna, O. Hervet, J. Holder, G. Hughes, B. Hummensky, C. A. Johnson, P. Kaaret, P. Kar, N. Kelley-Hoskins, M. Kertzman, D. Kieda, S. Koushiappas, M. Krause, F. Krennrich, M. J. Lang, T. T. Y. Lin, S. McArthur, P. Moriarty, R. Mukherjee, D. Nieto, S. O'Brien, R. A. Ong, A. N. Otte, N. Park, M. Pohl, A. Popkow, E. Pueschel, J. Quinn, K. Ragan, P. T. Reynolds, G. T. Richards, E. Roache, C. Rulten, I. Sadeh, M. Santander, G. H. Sembroski, K. Shahinyan, A. W. Smith, D. Staszak, I. Telezhinsky, S. Trepanier, J. V. Tucci, J. Tyler, S. P. Wakely, A. Weinstein, P. Wilcox, D. A. Williams, B. Zitzer, and VERITAS Collaboration. "Dark matter constraints from a joint analysis of dwarf Spheroidal galaxy observations with VERITAS." *Phys. Rev. D*,

95(8):082001, April 2017.

[Abr14] A. Abramowski et al. "Search for dark matter annihilation signatures in H.E.S.S. observations of Dwarf Spheroidal Galaxies." *Phys. Rev.*, **D90**:112012, 2014.

[ACH14] Kevork N. Abazajian, Nicolas Canac, Shunsaku Horiuchi, and Manoj Kaplinghat. "Astrophysical and Dark Matter Interpretations of Extended Gamma-Ray Emission from the Galactic Center." *Phys. Rev.*, **D90**(2):023526, 2014.

[Ack14] M. Ackermann et al. "Search for cosmic-ray induced gamma-ray emission in Galaxy Clusters." *Astrophys. J.*, **787**:18, 2014.

[Ack15] M. Ackermann et al. "Searching for Dark Matter Annihilation from Milky Way Dwarf Spheroidal Galaxies with Six Years of Fermi Large Area Telescope Data." *Phys. Rev. Lett.*, **115**(23):231301, 2015.

[Ack16] M. Ackermann et al. "Search for gamma-ray emission from the Coma Cluster with six years of Fermi-LAT data." *Astrophys. J.*, **819**(2):149, 2016. [Erratum: Astrophys. J.860,no.1,85(2018)].

[Ack17] M. Ackermann et al. "The Fermi Galactic Center GeV Excess and Implications for Dark Matter." *Astrophys. J.*, **840**(1):43, 2017.

[Ahn16] M. L. Ahnen et al. "Deep observation of the NGC 1275 region with MAGIC: search of diffuse γ-ray emission from cosmic rays in the Perseus cluster." *Astron. Astrophys.*, **589**:A33, 2016.

[Alb15] Andrea Albert. "Indirect Searches for Dark Matter with the Fermi Large Area Telescope1." *Physics Procedia*, **61**:6 – 12, 2015. 13th International Conference on Topics in Astroparticle and Underground Physics, TAUP 2013.

[Ale13] Jelena Aleksić. *Optimized Dark Matter Searches in Deep Observations of Segue 1 with MAGIC*. PhD thesis, Barcelona U., 2013.

[BAT08] M. Bradač, S. W. Allen, T. Treu, H. Ebeling, R. Massey, R. G. Morris, A. von der Linden, and D. Applegate. "Revealing the Properties of Dark Matter in the Merging Cluster MACS J0025.4-1222." *ApJ*, **687**:959–967, November 2008.

[BBR12] Marcus Brüggen, Andrei Bykov, Dongsu Ryu, and Huub Röttgering. "Magnetic Fields, Relativistic Particles, and Shock Waves in Cluster Outskirts." *Space Sci. Rev.*, **166**(1-4):187–213, May 2012.

[BCD09] G. Brunetti, R. Cassano, K. Dolag, and G. Setti. "On the evolution of giant radio halos and their connection with cluster mergers." *A&A*, **507**(2):661–669, Nov 2009.

[BFH07] David Berge, S. Funk, and J. Hinton. "Background Modelling in Very-High-Energy gamma-ray Astronomy." *Astron. Astrophys.*, **466**:1219–1229, 2007.

[BGB16] Luca Bravi, Myriam Gitti, and Gianfranco Brunetti. "Do radio mini-halos and gas heating in cool-core clusters have a common origin?" *Mon. Not. Roy. Astron. Soc.*, **455**(1):L41–L45, 2016.

[BGC08] G. Brunetti, S. Giacintucci, R. Cassano, W. Lane, D. Dallacasa, T. Venturi, N. Kassim, G. Setti, W. D. Cotton, and M. Markevitch. "A low-frequency radio halo associated with a cluster of galaxies." *Nature*, **455**:944, 2008.

[BJ14] Gianfranco Brunetti and Thomas W. Jones. "Cosmic rays in galaxy clusters and their nonthermal emission." *Int. J. Mod. Phys.*, **D23**:1430007, 2014.

[BZZ17] G. Brunetti, S. Zimmer, and F. Zandanel. "Relativistic protons in the Coma galaxy cluster: first gamma-ray constraints ever on turbulent reacceleration." *Mon. Not. Roy. Astron. Soc.*, **472**(2):1506–1525, 2017.

[CAA19] Cherenkov Telescope Array Consortium, B. S. Acharya, I. Agudo, I. Al Samarai, R. Alfaro, J. Alfaro, C. Alispach, R. Alves Batista, J. P. Amans, E. Amato, G. Ambrosi, E. Antolini, L. A. Antonelli, C. Aramo, M. Araya, T. Armstrong, F. Arqueros, L. Arrabito, K. Asano, M. Ashley, M. Backes, C. Balazs, M. Balbo, O. Ballester, J. Ballet, A. Bamba, M. Barkov, U. Barres de Almeida, J. A. Barrio, D. Bastieri, Y. Becherini, A. Belfiore, W. Benbow, D. Berge, E. Bernardini, M. G. Bernardini, M. Bernardos, K. Bernlöhr, B. Bertucci, B. Biasuzzi, C. Bigongiari, A. Biland, E. Bissaldi, J. Biteau, O. Blanch, J. Blazek, C. Boisson, J. Bolmont, G. Bonanno, A. Bonardi, C. Bonavolontà, G. Bonnoli, Z. Bosnjak, M. Böttcher, C. Braiding, J. Bregeon, A. Brill, A. M. Brown, P. Brun, G. Brunetti, T. Buanes, J. Buckley, V. Bugaev, R. Bühler, A. Bulgarelli, T. Bulik, M. Burton, A. Burtovoi, G. Busetto, R. Canestrari, M. Capalbi, F. Capitanio, A. Caproni, P. Caraveo, V. Cárdenas, C. Carlile, R. Carosi, E. Carquín, J. Carr, S. Casanova, E. Cascone, F. Catalani, O. Catalano, D. Cauz, M. Cerruti, P. Chadwick, S. Chaty, R. C. G. Chaves, A. Chen, X. Chen, M. Chernyakova, M. Chikawa, A. Christov, J. Chudoba, M. Cieślar, V. Coco, S. Colafrancesco, P. Colin, V. Conforti, V. Connaughton, J. Conrad, J. L. Contreras, J. Cortina, A. Costa, H. Costantini, G. Cotter, S. Covino, R. Crocker, J. Cuadra, O. Cuevas, P. Cumani, A. D'Aì, F. D'Ammando, P. D'Avanzo, D. D'Urso, M. Daniel, I. Davids, B. Dawson, F. Dazzi, A. De Angelis, R. de Cássia dos Anjos, G. De Cesare, A. De Franco, E. M. de Gouveia Dal Pino, I. de la Calle, R. de los Reyes Lopez, B. De Lotto, A. De Luca, M. De Lucia, M. de Naurois, E. de Oña Wilhelmi, F. De Palma, F. De Persio, V. de Souza, C. Deil, M. Del Santo, C. Delgado, D. della Volpe, T. Di Girolamo, F. Di Pierro, L. Di Venere, C. Díaz, C. Dib, S. Diebold, A. Djannati-Ataï, A. Domínguez, D. Dominis Prester, D. Dorner, M. Doro, H. Drass, D. Dravins, G. Dubus, V. V. Dwarkadas, J. Ebr, C. Eckner, K. Egberts, S. Einecke, T. R. N.

Ekoume, D. Elsässer, J. P. Ernenwein, C. Espinoza, C. Evoli, M. Fairbairn, D. Falceta-Goncalves, A. Falcone, C. Farnier, G. Fasola, E. Fedorova, S. Fegan, M. Fernand ez-Alonso, A. Fernández-Barral, G. Ferrand, M. Fesquet, M. Filipovic, V. Fioretti, G. Fontaine, M. Fornasa, L. Fortson, L. Freixas Coromina, C. Fruck, Y. Fujita, Y. Fukazawa, S. Funk, M. Füßling, S. Gabici, A. Gadola, Y. Gallant, B. Garcia, R. Garcia López, M. Garczarczyk, J. Gaskins, T. Gasparetto, M. Gaug, L. Gerard, G. Giavitto, N. Giglietto, P. Giommi, F. Giordano, E. Giro, M. Giroletti, A. Giuliani, J. F. Glicenstein, R. Gnatyk, N. Godinovic, P. Goldoni, G. Gómez-Vargas, M. M. González, J. M. González, D. Götz, J. Graham, P. Grand i, J. Granot, A. J. Green, T. Greenshaw, S. Griffiths, S. Gunji, D. Hadasch, S. Hara, M. J. Hardcastle, T. Hassan, K. Hayashi, M. Hayashida, M. Heller, J. C. Helo, G. Hermann, J. Hinton, B. Hnatyk, W. Hofmann, J. Holder, D. Horan, J. Hörandel, D. Horns, P. Horvath, T. Hovatta, M. Hrabovsky, D. Hrupec, T. B. Humensky, M. Hütten, M. Iarlori, T. Inada, Y. Inome, S. Inoue, T. Inoue, Y. Inoue, F. Iocco, K. Ioka, M. Iori, K. Ishio, Y. Iwamura, M. Jamrozy, P. Janecek, D. Jankowsky, P. Jean, I. Jung-Richardt, J. Jurysek, P. Kaaret, S. Karkar, H. Katagiri, U. Katz, N. Kawanaka, D. Kazanas, B. Khélifi, D. B. Kieda, S. Kimeswenger, S. Kimura, S. Kisaka, J. Knapp, J. Knödlseder, B. Koch, K. Kohri, N. Komin, K. Kosack, M. Kraus, M. Krause, F. Krauß, H. Kubo, G. Kukec Mezek, H. Kuroda, J. Kushida, N. La Palombara, G. Lamanna, R. G. Lang, J. Lapington, O. Le Blanc, S. Leach, J. P. Lees, J. Lefaucheur, M. A. Leigui de Oliveira, J. P. Lenain, R. Lico, M. Limon, E. Lindfors, T. Lohse, S. Lombardi, F. Longo, M. López, R. López-Coto, C. C. Lu, F. Lucarelli, P. L. Luque-Escamilla, E. Lyard, M. C. Maccarone, G. Maier, P. Majumdar, G. Malaguti, D. Mandat, G. Maneva, M. Manganaro, S. Mangano, A. Marcowith, J. Marín, S. Markoff, J. Martí, P. Martin, M. Martínez, G. Martínez, N. Masetti, S. Masuda, G. Maurin, N. Maxted, D. Mazin, C. Medina, A. Melandri, S. Mereghetti, M. Meyer, I. A. Minaya, N. Mirabal, R. Mirzoyan, A. Mitchell, T. Mizuno, R. Moderski, M. Mohammed, L. Mohrmann, T. Montaruli, A. Moralejo, D. Morcuende-Parrilla, K. Mori, G. Morlino, P. Morris, A. Morselli, E. Moulin, R. Mukherjee, C. Mundell, T. Murach, H. Muraishi, K. Murase, A. Nagai, S. Nagataki, T. Nagayoshi, T. Naito, T. Nakamori, Y. Nakamura, J. Niemiec, D. Nieto, M. Nikołajuk, K. Nishijima, K. Noda, D. Nosek, B. Novosyadlyj, S. Nozaki, P. O'Brien, L. Oakes, Y. Ohira, M. Ohishi, S. Ohm, N. Okazaki, A. Okumura, R. A. Ong, M. Orienti, R. Orito, J. P. Osborne, M. Ostrowski, N. Otte, I. Oya, M. Padovani, A. Paizis, M. Palatiello, M. Palatka, R. Paoletti, J. M. Paredes, G. Pareschi, R. D. Parsons, A. Pe'er, M. Pech, G. Pedaletti, M. Perri, M. Persic, A. Petrashyk, P. Petrucci, O. Petruk, B. Peyaud, M. Pfeifer, G. Piano, A. Pisarski, S. Pita, M. Pohl, M. Polo, D. Pozo, E. Prandini, J. Prast, G. Principe, D. Prokhorov, H. Prokoph, M. Prouza, G. Pühlhofer, M. Punch, S. Pürckhauer, F. Queiroz, A. Quirrenbach, S. Rainò, S. Razzaque, O. Reimer, A. Reimer, A. Reisenegger, M. Renaud, A. H. Rezaeian, W. Rhode, D. Ribeiro,

M. Ribó, T. Richtler, J. Rico, F. Rieger, M. Riquelme, S. Rivoire, V. Rizi, J. Rodriguez, G. Rodriguez Fernandez, J. J. Rodríguez Vázquez, G. Rojas, P. Romano, G. Romeo, J. Rosado, A. C. Rovero, G. Rowell, B. Rudak, A. Rugliancich, C. Rulten, I. Sadeh, S. Safi-Harb, T. Saito, N. Sakaki, S. Sakurai, G. Salina, M. Sánchez-Conde, H. Sandaker, A. Sandoval, P. Sangiorgi, M. Sanguillon, H. Sano, M. Santand er, S. Sarkar, K. Satalecka, F. G. Saturni, E. J. Schioppa, S. Schlenstedt, M. Schneider, H. Schoorlemmer, P. Schovanek, A. Schulz, F. Schussler, U. Schwanke, E. Sciacca, S. Scuderi, I. Seitenzahl, D. Semikoz, O. Sergijenko, M. Servillat, A. Shalchi, R. C. Shellard, L. Sidoli, H. Siejkowski, A. Sillanpää, G. Sironi, J. Sitarek, V. Sliusar, A. Slowikowska, H. Sol, A. Stamerra, S. Stanič, R. Starling, Ł. Stawarz, S. Stefanik, M. Stephan, T. Stolarczyk, G. Stratta, U. Straumann, T. Suomijarvi, A. D. Supanitsky, G. Tagliaferri, H. Tajima, M. Tavani, F. Tavecchio, J. P. Tavernet, K. Tayabaly, L. A. Tejedor, P. Temnikov, Y. Terada, R. Terrier, T. Terzic, M. Teshima, V. Testa, S. Thoudam, W. Tian, L. Tibaldo, M. Tluczykont, C. J. Todero Peixoto, F. Tokanai, J. Tomastik, D. Tonev, M. Tornikoski, D. F. Torres, E. Torresi, G. Tosti, N. Tothill, G. Tovmassian, P. Travnicek, C. Trichard, M. Trifoglio, I. Troyano Pujadas, S. Tsujimoto, G. Umana, V. Vagelli, F. Vagnetti, M. Valentino, P. Vallania, L. Valore, C. van Eldik, J. Vand enbroucke, G. S. Varner, G. Vasileiadis, V. Vassiliev, M. Vázquez Acosta, M. Vecchi, A. Vega, S. Vercellone, P. Veres, S. Vergani, V. Verzi, G. P. Vettolani, A. Viana, C. Vigorito, J. Villanueva, H. Voelk, A. Vollhardt, S. Vorobiov, M. Vrastil, T. Vuillaume, S. J. Wagner, R. Wagner, R. Walter, J. E. Ward, D. Warren, J. J. Watson, F. Werner, M. White, R. White, A. Wierzcholska, P. Wilcox, M. Will, D. A. Williams, R. Wischnewski, M. Wood, T. Yamamoto, R. Yamazaki, S. Yanagita, L. Yang, T. Yoshida, S. Yoshiike, T. Yoshikoshi, M. Zacharias, G. Zaharijas, L. Zampieri, F. Zand anel, R. Zanin, M. Zavrtanik, D. Zavrtanik, A. A. Zdziarski, A. Zech, H. Zechlin, V. I. Zhdanov, A. Ziegler, and J. Zorn. *Science with the Cherenkov Telescope Array.* 2019.

[CBG06] D. Clowe, M. Bradač, A. H. Gonzalez, M. Markevitch, S. W. Randall, C. Jones, and D. Zaritsky. "A Direct Empirical Proof of the Existence of Dark Matter." *ApJ*, **648**:L109–L113, September 2006.

[CCW15] Francesca Calore, Ilias Cholis, and Christoph Weniger. "Background Model Systematics for the Fermi GeV Excess." *JCAP*, **1503**:038, 2015.

[CFO16] Richard H. Cyburt, Brian D. Fields, Keith A. Olive, and Tsung-Han Yeh. "Big Bang Nucleosynthesis: 2015." *Rev. Mod. Phys.*, **88**:015004, 2016.

[Con18] Christopher J. Conselice. "Ultra-diffuse Galaxies Are a Subset of Cluster Dwarf Elliptical/Spheroidal Galaxies." *Research Notes of the AAS*, **2**(1):43, mar 2018.

[CS14] Damiano Caprioli and Anatoly Spitkovsky. "Simulations of Ion Acceleration at Non-relativistic Shocks. II. Magnetic Field Amplification." *Astrophys. J.*,

794(1):46, 2014.

[DC57] John M. Davies and Eugene S. Cotton. "Design of the quartermaster solar furnace." *Solar Energy*, **1**(2):16 – 22, 1957. The Proceedings of the Solar Furnace Symposium.

[DFH16] Tansu Daylan, Douglas P. Finkbeiner, Dan Hooper, Tim Linden, Stephen K. N. Portillo, Nicholas L. Rodd, and Tracy R. Slatyer. "The characterization of the gamma-ray signal from the central Milky Way: A case for annihilating dark matter." *Phys. Dark Univ.*, **12**:1–23, 2016.

[DHH97] A. Daum, G. Hermann, M. Heß, W. Hofmann, H. Lampeitl, G. Pühlhofer, F. Aharonian, A.G. Akhperjanian, J.A. Barrio, A.S. Beglarian, K. Bernlöhr, J.J.G. Beteta, S.M. Bradbury, J.L. Contreras, J. Cortina, T. Deckers, E. Feigl, J. Fernandez, V. Fonseca, A. Fraß, B. Funk, J.C. Gonzalez, G. Heinzelmann, M. Hemberger, A. Heusler, I. Holl, D. Horns, R. Kankanyan, O. Kirstein, C. Köhler, A. Konopelko, D. Kranich, H. Krawczynski, H. Kornmayer, A. Lindner, E. Lorenz, N. Magnussen, H. Meyer, R. Mirzoyan, H. Möller, A. Moralejo, L. Padilla, M. Panter, D. Petry, R. Plaga, J. Prahl, C. Prosch, G. Rauterberg, W. Rhode, A. Röhring, V. Sahakian, M. Samorski, J.A. Sanchez, D. Schmele, W. Stamm, M. Ulrich, H.J. Völk, S. Westerhoff, B. Wiebel-Sooth, C.A. Wiedner, M. Willmer, and H. Wirth. "First results on the performance of the HEGRA IACT array." *Astroparticle Physics*, **8**(1):1 – 11, 1997.

[Fab94] A. C. Fabian. "Cooling Flows in Clusters of Galaxies." *ARA&A*, **32**:277–318, 1994.

[Feg97] D. J. Fegan. "gamma/hadron separation at TeV energies." *J. Phys.*, **G23**:1013–1060, 1997.

[FO13] Yutaka Fujita and Yutaka Ohira. "Radio mini-halo emission from cosmic rays in galaxy clusters and heating of the cool cores." *MNRAS*, **428**(1):599–608, Jan 2013.

[Git16] Myriam Gitti. "Radio mini-halos and AGN heating in cool core clusters of galaxies." *PoS*, **EXTRA-RADSUR2015**:043, 2016.

[GKW15] Alex Geringer-Sameth, Savvas M. Koushiappas, and Matthew Walker. "Dwarf galaxy annihilation and decay emission profiles for dark matter experiments." *Astrophys. J.*, **801**(2):74, 2015.

[Han07] David Hanna. "Calibration Techniques for VERITAS." In *Proceedings, 30th International Cosmic Ray Conference (ICRC 2007): Merida, Yucatan, Mexico, July 3-11, 2007*, volume 3, pp. 1417–1420, 2007.

[Hil85] A. M. Hillas. "Cerenkov light images of EAS produced by primary gamma." *International Cosmic Ray Conference*, **3**, August 1985.

[Hil98] A. M. Hillas et al. "Spectrum of TeV gamma-rays from the Crab nebula." *Astrophys. J.*, **503**:744–759, 1998.

[Hol06] Jamie Holder et al. "The first VERITAS telescope." *Astropart. Phys.*, **25**:391–401, 2006.

[Hol11] Jamie Holder. "VERITAS: Status and Highlights." *International Cosmic Ray Conference*, **11**:137, Jan 2011.

[Hol15] Jamie Holder. "Atmospheric Cherenkov Gamma-ray Telescopes." *arXiv e-prints*, p. arXiv:1510.05675, Oct 2015.

[HTE13] B. Huber, C. Tchernin, D. Eckert, C. Farnier, A. Manalaysay, U. Straumann, and R. Walter. "Probing the cosmic-ray content of galaxy clusters by stacking Fermi-LAT count maps." *Astron. Astrophys.*, **560**:A64, 2013.

[KB12] Andrey V. Kravtsov and Stefano Borgani. "Formation of Galaxy Clusters." *ARA&A*, **50**:353–409, Sep 2012.

[Kes17] U. Keshet. "X-ray to gamma-ray virial shock signal from the Coma cluster." In *Proceedings of the 7th International Fermi Symposium*, p. 151, October 2017.

[Kie13] Dave B. Kieda. "The Gamma Ray Detection sensitivity of the upgraded VERITAS Observatory." In *Proceedings, 33rd International Cosmic Ray Conference (ICRC2013): Rio de Janeiro, Brazil, July 2-9, 2013*, p. 0700, 2013.

[KKL17] Uri Keshet, Doron Kushnir, Abraham Loeb, and Eli Waxman. "Preliminary Evidence for a Virial Shock around the Coma Galaxy Cluster." *ApJ*, **845**(1):24, Aug 2017.

[KSP19] Ruta Kale, Krishna M. Shende, and Viral Parekh. "A radio halo surrounding the Brightest Cluster Galaxy in RXCJ0232.2–4420: a mini-halo in transition?" *Mon. Not. Roy. Astron. Soc.*, **486**(1):L80–L84, 2019.

[LM83] T.-P. Li and Y.-Q. Ma. "Analysis methods for results in gamma-ray astronomy." *ApJ*, **272**:317–324, September 1983.

[Mar10] Maxim Markevitch. "Intergalactic shock fronts." *arXiv e-prints*, p. arXiv:1010.3660, Oct 2010.

[Mat05] J. Matthews. "A Heitler model of extensive air showers." *Astroparticle Physics*, **22**:387–397, January 2005.

[MCE90] J. C. Mather, E. S. Cheng, R. E. Eplee, Jr., R. B. Isaacman, S. S. Meyer, R. A. Shafer, R. Weiss, E. L. Wright, C. L. Bennett, N. W. Boggess, E. Dwek, S. Gulkis, M. G. Hauser, M. Janssen, T. Kelsall, P. M. Lubin, S. H. Moseley, Jr., T. L. Murdock, R. F. Silverberg, G. F. Smoot, and D. T. Wilkinson. "A preliminary measurement of the cosmic microwave background spectrum by the Cosmic Background Explorer (COBE) satellite." *ApJ*, **354**:L37–L40, May 1990.

[Meu19] T. Meures. "Upgrading the Prototype Schwarzschild-Couder Telescope Camera to a Wide-Field, High-Resolution Instrument." In *36th International Cosmic Ray Conference (ICRC2019)*, volume 36 of *International Cosmic Ray Conference*, p. 742, July 2019.

[MG08] P. Mazzotta and S. Giacintucci. "Do Radio Core-Halos and Cold Fronts in Non-Major-Merging Clusters Originate from the Same Gas Sloshing?" *ApJ*, **675**:L9, March 2008.

[MGB12] Oscar Macías-Ramírez, Chris Gordon, Anthony M. Brown, and Jenni Adams. "Evaluating the gamma-ray evidence for self-annihilating dark matter from the Virgo cluster." *Phys. Rev. D*, **86**:076004, Oct 2012.

[MH18] Gernot Maier and Jamie Holder. "Eventdisplay: An Analysis and Reconstruction Package for Ground-based Gamma-ray Astronomy." *PoS*, **ICRC2017**:747, 2018. [35,747(2017)].

[MHK10] A. McCann, D. Hanna, J. Kildea, and M. McCutcheon. "A new mirror alignment system for the VERITAS telescopes." *Astroparticle Physics*, **32**:325–329, Jan 2010.

[Min03] Francesco Miniati. "Numerical modeling of gamma radiation from galaxy clusters." *Mon. Not. Roy. Astron. Soc.*, **342**:1009, 2003.

[MN07] B. R. McNamara and P. E. J. Nulsen. "Heating Hot Atmospheres with Active Galactic Nuclei." *Ann. Rev. Astron. Astrophys.*, **45**:117–175, 2007.

[MV07] Maxim Markevitch and Alexey Vikhlinin. "Shocks and cold fronts in galaxy clusters." *Phys. Rept.*, **443**:1–53, 2007.

[MVR11] Michael McDonald, Sylvain Veilleux, David S. N. Rupke, Richard Mushotzky, and Christopher Reynolds. "Star Formation Efficiency in the Cool Cores of Galaxy Clusters." *ApJ*, **734**(2):95, Jun 2011.

[OB13] G. A. Ogrean and M. Brüggen. "First X-ray evidence for a shock at the Coma relic." *MNRAS*, **433**(2):1701–1708, Aug 2013.

[OBD15] A. N. Otte, J. Biteau, H. Dickinson, S. Funk, T. Jogler, C. A. Johnson, P. Karn, K. Meagher, H. Naoya, T. Nguyen, A. Okumura, M. Santander, L. Sapozhnikov, A. Stier, H. Tajima, L. Tibaldo, J. Vandenbroucke, S. Wakely, A. Weinstein, and D. A. Williams. "Development of a SiPM Camera for a Schwarzschild-Couder Cherenkov Telescope for the Cherenkov Telescope Array." *arXiv e-prints*, p. arXiv:1509.02345, Sep 2015.

[Ong18] Rene A. Ong. "Cherenkov Telescope Array: The Next Generation Gamma-ray Observatory." *PoS*, **ICRC2017**:1071, 2018.

[PAA11] Planck Collaboration, P. A. R. Ade, N. Aghanim, M. Arnaud, M. Ashdown, J. Aumont, C. Baccigalupi, A. Balbi, A. J. Banday, R. B. Barreiro, M. Bartelmann, J. G. Bartlett, E. Battaner, R. Battye, K. Benabed, A. Benoît, J. P. Bernard, M. Bersanelli, R. Bhatia, J. J. Bock, A. Bonaldi, J. R. Bond, J. Borrill, F. R. Bouchet, M. L. Brown, M. Bucher, C. Burigana, P. Cabella, C. M. Cantalupo, J. F. Cardoso, P. Carvalho, A. Catalano, L. Cayón, A. Challinor, A. Chamballu, R. R. Chary, L. Y. Chiang, C. Chiang, G. Chon, P. R. Christensen, E. Churazov, D. L. Clements, S. Colafrancesco, S. Colombi, F. Couchot, A. Coulais, B. P. Crill, F. Cuttaia, A. da Silva, H. Dahle, L. Danese, R. J. Davis, P. de Bernardis, G. de Gasperis, A. de Rosa, G. de Zotti, J. Delabrouille, J. M. Delouis, F. X. Désert, C. Dickinson, J. M. Diego, K. Dolag, H. Dole, S. Donzelli, O. Doré, U. Dörl, M. Douspis, X. Dupac, G. Efstathiou, P. Eisenhardt, T. A. Enßlin, F. Feroz, F. Finelli, I. Flores-Cacho, O. Forni, P. Fosalba, M. Frailis, E. Franceschi, S. Fromenteau, S. Galeotta, K. Ganga, R. T. Génova-Santos, M. Giard, G. Giardino, Y. Giraud-Héraud, J. González-Nuevo, R. González-Riestra, K. M. Górski, K. J. B. Grainge, S. Gratton, A. Gregorio, A. Gruppuso, D. Harrison, P. Heinämäki, S. Henrot-Versillé, C. Hernández-Monteagudo, D. Herranz, S. R. Hildebrand t, E. Hivon, M. Hobson, W. A. Holmes, W. Hovest, R. J. Hoyland, K. M. Huffenberger, G. Hurier, N. Hurley-Walker, A. H. Jaffe, W. C. Jones, M. Juvela, E. Keihänen, R. Keskitalo, T. S. Kisner, R. Kneissl, L. Knox, H. Kurki-Suonio, G. Lagache, J. M. Lamarre, A. Lasenby, R. J. Laureijs, C. R. Lawrence, M. Le Jeune, S. Leach, R. Leonardi, C. Li, A. Liddle, P. B. Lilje, M. Linden-Vørnle, M. López-Caniego, P. M. Lubin, J. F. Macías-Pérez, C. J. MacTavish, B. Maffei, D. Maino, N. Mandolesi, R. Mann, M. Maris, F. Marleau, E. Martínez-González, S. Masi, S. Matarrese, F. Matthai, P. Mazzotta, S. Mei, P. R. Meinhold, A. Melchiorri, J. B. Melin, L. Mendes, A. Mennella, S. Mitra, M. A. Miville-Deschênes, A. Moneti, L. Montier, G. Morgante, D. Mortlock, D. Munshi, A. Murphy, P. Naselsky, F. Nati, P. Natoli, C. B. Netterfield, H. U. Nørgaard-Nielsen, F. Noviello, D. Novikov, I. Novikov, M. Olamaie, S. Osborne, F. Pajot, F. Pasian, G. Patanchon, T. J. Pearson, O. Perdereau, L. Perotto, F. Perrotta, F. Piacentini, M. Piat, E. Pierpaoli, R. Piffaretti, S. Plaszczynski, E. Pointecouteau, G. Polenta, N. Ponthieu, T. Poutanen, G. W. Pratt, G. Prézeau, S. Prunet, J. L. Puget, J. P. Rachen, W. T. Reach, R. Rebolo,

M. Reinecke, C. Renault, S. Ricciardi, T. Riller, I. Ristorcelli, G. Rocha, C. Rosset, J. A. Rubiño-Martín, B. Rusholme, E. Saar, M. Sandri, D. Santos, R. D. E. Saunders, G. Savini, B. M. Schaefer, D. Scott, M. D. Seiffert, P. Shellard, G. F. Smoot, A. Stanford, J. L. Starck, F. Stivoli, V. Stolyarov, R. Stompor, R. Sudiwala, R. Sunyaev, D. Sutton, J. F. Sygnet, N. Taburet, J. A. Tauber, L. Terenzi, L. Toffolatti, M. Tomasi, J. P. Torre, M. Tristram, J. Tuovinen, L. Valenziano, L. Vibert, P. Vielva, F. Villa, N. Vittorio, L. A. Wade, B. D. Wandelt, J. Weller, S. D. M. White, M. White, D. Yvon, A. Zacchei, and A. Zonca. "Planck early results. VIII. The all-sky early Sunyaev-Zeldovich cluster sample." *A&A*, **536**:A8, Dec 2011.

[PAA18] Planck Collaboration, N. Aghanim, Y. Akrami, M. Ashdown, J. Aumont, C. Baccigalupi, M. Ballardini, A. J. Banday, R. B. Barreiro, N. Bartolo, S. Basak, R. Battye, K. Benabed, J. P. Bernard, M. Bersanelli, P. Bielewicz, J. J. Bock, J. R. Bond, J. Borrill, F. R. Bouchet, F. Boulanger, M. Bucher, C. Burigana, R. C. Butler, E. Calabrese, J. F. Cardoso, J. Carron, A. Challinor, H. C. Chiang, J. Chluba, L. P. L. Colombo, C. Combet, D. Contreras, B. P. Crill, F. Cuttaia, P. de Bernardis, G. de Zotti, J. Delabrouille, J. M. Delouis, E. Di Valentino, J. M. Diego, O. Doré, M. Douspis, A. Ducout, X. Dupac, S. Dusini, G. Efstathiou, F. Elsner, T. A. Enßlin, H. K. Eriksen, Y. Fantaye, M. Farhang, J. Fergusson, R. Fernandez-Cobos, F. Finelli, F. Forastieri, M. Frailis, E. Franceschi, A. Frolov, S. Galeotta, S. Galli, K. Ganga, R. T. Génova-Santos, M. Gerbino, T. Ghosh, J. González-Nuevo, K. M. Górski, S. Gratton, A. Gruppuso, J. E. Gudmundsson, J. Hamann, W. Hand ley, D. Herranz, E. Hivon, Z. Huang, A. H. Jaffe, W. C. Jones, A. Karakci, E. Keihänen, R. Keskitalo, K. Kiiveri, J. Kim, T. S. Kisner, L. Knox, N. Krachmalnicoff, M. Kunz, H. Kurki-Suonio, G. Lagache, J. M. Lamarre, A. Lasenby, M. Lattanzi, C. R. Lawrence, M. Le Jeune, P. Lemos, J. Lesgourgues, F. Levrier, A. Lewis, M. Liguori, P. B. Lilje, M. Lilley, V. Lindholm, M. López-Caniego, P. M. Lubin, Y. Z. Ma, J. F. Macías-Pérez, G. Maggio, D. Maino, N. Mandolesi, A. Mangilli, A. Marcos-Caballero, M. Maris, P. G. Martin, M. Martinelli, E. Martínez-González, S. Matarrese, N. Mauri, J. D. McEwen, P. R. Meinhold, A. Melchiorri, A. Mennella, M. Migliaccio, M. Millea, S. Mitra, M. A. Miville-Deschênes, D. Molinari, L. Montier, G. Morgante, A. Moss, P. Natoli, H. U. Nørgaard-Nielsen, L. Pagano, D. Paoletti, B. Partridge, G. Patanchon, H. V. Peiris, F. Perrotta, V. Pettorino, F. Piacentini, L. Polastri, G. Polenta, J. L. Puget, J. P. Rachen, M. Reinecke, M. Remazeilles, A. Renzi, G. Rocha, C. Rosset, G. Roudier, J. A. Rubiño-Martín, B. Ruiz-Granados, L. Salvati, M. Sandri, M. Savelainen, D. Scott, E. P. S. Shellard, C. Sirignano, G. Sirri, L. D. Spencer, R. Sunyaev, A. S. Suur-Uski, J. A. Tauber, D. Tavagnacco, M. Tenti, L. Toffolatti, M. Tomasi, T. Trombetti, L. Valenziano, J. Valiviita, B. Van Tent, L. Vibert, P. Vielva, F. Villa, N. Vittorio, B. D. Wand elt, I. K. Wehus, M. White, S. D. M. White, A. Zacchei, and A. Zonca. "Planck 2018 results. VI. Cosmological param-

eters." *arXiv e-prints*, p. arXiv:1807.06209, Jul 2018.

[PP10] Anders Pinzke and Christoph Pfrommer. "Simulating the γ-ray emission from galaxy clusters: a universal cosmic ray spectrum and spatial distribution." *MNRAS*, **409**(2):449–480, December 2010.

[PW65] A. A. Penzias and R. W. Wilson. "A Measurement of Excess Antenna Temperature at 4080 Mc/s." *ApJ*, **142**:419–421, July 1965.

[RF70] V. C. Rubin and W. K. Ford, Jr. "Rotation of the Andromeda Nebula from a Spectroscopic Survey of Emission Regions." *ApJ*, **159**:379, February 1970.

[Rin19] Lucia Rinchiuso. "Latest results on dark matter searches with H.E.S.S." In *7th Roma International Conference on Astroparticle Physic (RICAP18) Rome, Italy, September 4-7, 2018*, 2019.

[RIP08] E. Roache, R. Irvin, J. S. Perkins, K. Harris, A. Falcone, J. Finley, and T. Weeks. "Mirror Facets for the VERITAS Telescopes." *International Cosmic Ray Conference*, **3**:1397–1400, 2008.

[RKC08] Dongsu Ryu, Hyesung Kang, Jungyeon Cho, and Santabrata Das. "Turbulence and Magnetic Fields in the Large Scale Structure of the Universe." *Science*, **320**:909, 2008.

[RLC05] Wolfgang A. Rolke, Angel M. Lopez, and Jan Conrad. "Limits and confidence intervals in the presence of nuisance parameters." *Nucl. Instrum. Meth.*, **A551**:493–503, 2005.

[RSM94] H. Rottgering, I. Snellen, G. Miley, J. P. de Jong, R. J. Hanisch, and R. Perley. "VLA observations of the rich X-ray cluster Abell 2256." *ApJ*, **436**:654–668, December 1994.

[SB87] J. Silk and H. Bloemen. "A gamma-ray constraint on the nature of dark matter." *ApJ*, **313**:L47–L51, February 1987.

[SBB18] F. Savini, A. Bonafede, M. Brüggen, R. van Weeren, G. Brunetti, H. Intema, A. Botteon, T. Shimwell, A. Wilber, D. Rafferty, S. Giacintucci, R. Cassano, V. Cuciti, F. de Gasperin, H. Röttgering, M. Hoeft, and G. White. "First evidence of diffuse ultra-steep-spectrum radio emission surrounding the cool core of a cluster." *MNRAS*, **478**(2):2234–2242, Aug 2018.

[Sof17] Y. Sofue. "Rotation and mass in the Milky Way and spiral galaxies." *PASJ*, **69**:R1, February 2017.

[vAB16] Pieter van Dokkum, Roberto Abraham, Jean Brodie, Charlie Conroy, Shany Danieli, Allison Merritt, Lamiya Mowla, Aaron Romanowsky, and Jielai Zhang. "A High Stellar Velocity Dispersion and 100 Globular Clusters for the Ultra-diffuse Galaxy Dragonfly 44." *ApJ*, **828**(1):L6, Sep 2016.

[vAD17] Reinout J. van Weeren, Felipe Andrade-Santos, William A. Dawson, Nathan Golovich, Dharam V. Lal, Hyesung Kang, Dongsu Ryu, Marcus Brìggen, Georgiana A. Ogrean, William R. Forman, Christine Jones, Vinicius M. Placco, Rafael M. Santucci, David Wittman, M. James Jee, Ralph P. Kraft, David Sobral, Andra Stroe, and Kevin Fogarty. "The case for electron re-acceleration at galaxy cluster shocks." *Nature Astronomy*, **1**:0005, Jan 2017.

[vAM15] Pieter G. van Dokkum, Roberto Abraham, Allison Merritt, Jielai Zhang, Marla Geha, and Charlie Conroy. "Forty-seven Milky Way-sized, Extremely Diffuse Galaxies in the Coma Cluster." *ApJ*, **798**(2):L45, Jan 2015.

[VEB15] F. Vazza, D. Eckert, M. Brüggen, and B. Huber. "Electron and proton acceleration efficiency by merger shocks in galaxy clusters." *Mon. Not. Roy. Astron. Soc.*, **451**(2):2198–2211, 2015.

[Ven17] T. Venturi et al. "The two-component giant radio halo in the galaxy cluster Abell 2142." *Astron. Astrophys.*, **603**:A125, 2017.

[VFB07] V. V. Vassiliev, Stephen Fegan, and Pierre Brousseau. "Schwarzschild-Couder two-mirror telescope for ground-based γ-ray astronomy." In *Proceedings, 30th International Cosmic Ray Conference (ICRC 2007): Merida, Yucatan, Mexico, July 3-11, 2007*, volume 3, pp. 1445–1448, 2007. [3,1445(2007)].

[vHM17] Remco F. J. van der Burg, Henk Hoekstra, Adam Muzzin, Cristóbal Sifón, Massimo Viola, Malcolm N. Bremer, Sarah Brough, Simon P. Driver, Thomas Erben, and Catherine Heymans. "The abundance of ultra-diffuse galaxies from groups to clusters. UDGs are relatively more common in more massive haloes." *A&A*, **607**:A79, Nov 2017.

[WBB02] T. C. Weekes, H. Badran, S. D. Biller, I. Bond, S. Bradbury, J. Buckley, D. Carter-Lewis, M. Catanese, S. Criswell, W. Cui, P. Dowkontt, C. Duke, D. J. Fegan, J. Finley, L. Fortson, J. Gaidos, G. H. Gillanders, J. Grindlay, T. A. Hall, K. Harris, A. M. Hillas, P. Kaaret, M. Kertzman, D. Kieda, F. Krennrich, M. J. Lang, S. LeBohec, R. Lessard, J. Lloyd-Evans, J. Knapp, B. McKernan, J. McEnery, P. Moriarty, D. Muller, P. Ogden, R. Ong, D. Petry, J. Quinn, N. W. Reay, P. T. Reynolds, J. Rose, M. Salamon, G. Sembroski, R. Sidwell, P. Slane, N. Stanton, S. P. Swordy, V. V. Vassiliev, and S. P. Wakely. "VERITAS: the Very Energetic Radiation Imaging Telescope Array System." *Astroparticle Physics*, **17**(2):221–243, May 2002.

[WCF89] T. C. Weekes, M. F. Cawley, D. J. Fegan, K. G. Gibbs, A. M. Hillas, P. W. Kowk, R. C. Lamb, D. A. Lewis, D. Macomb, N. A. Porter, P. T. Reynolds, and G. Vacanti. "Observation of TeV Gamma Rays from the Crab Nebula Using the Atmospheric Cerenkov Imaging Technique." *ApJ*, **342**:379, July 1989.

[Wei08] A. Weinstein. "The VERITAS Trigger System." In *International Cosmic Ray Conference*, volume 3 of *International Cosmic Ray Conference*, pp. 1539–1542, January 2008.

[WGA19] R. J. van Weeren, F. de Gasperin, H. Akamatsu, M. Brüggen, L. Feretti, H. Kang, A. Stroe, and F. Zandanel. "Diffuse Radio Emission from Galaxy Clusters." *Space Sci. Rev.*, **215**(1):16, 2019.

[Wil38] S. S. Wilks. "The Large-Sample Distribution of the Likelihood Ratio for Testing Composite Hypotheses." *Ann. Math. Statist.*, **9**(1):60–62, 03 1938.

[WJD16] M. Wood, T. Jogler, J. Dumm, and S. Funk. "Monte Carlo studies of medium-size telescope designs for the Cherenkov Telescope Array." *Astroparticle Physics*, **72**:11–31, January 2016.

[ZA14] Fabio Zandanel and Shin'ichiro Ando. "Constraints on diffuse gamma-ray emission from structure formation processes in the Coma cluster." *Mon. Not. Roy. Astron. Soc.*, **440**(1):663–671, 2014.

[ZCS14] I. Zhuravleva, E. Churazov, A. A. Schekochihin, S. W. Allen, P. Arévalo, A. C. Fabian, W. R. Forman, J. S. Sanders, A. Simionescu, R. Sunyaev, A. Vikhlinin, and N. Werner. "Turbulent heating in galaxy clusters brightest in X-rays." *Nature*, **515**:85–87, November 2014.

[Zim15] S. Zimmer. "Galaxy Clusters with the Fermi-LAT: Status and Implications for Cosmic Rays and Dark Matter Physics." In *5th International Fermi Symposium Nagoya, Japan, October 20-24, 2014*, volume C141020.1, 2015.

[Zit16] Benjamin Zitzer. "A Search for Dark Matter from Dwarf Galaxies using VERITAS." *PoS*, **ICRC2015**:1225, 2016.

[ZMB13] J. A. ZuHone, M. Markevitch, G. Brunetti, and S. Giacintucci. "Turbulence and Radio Mini-halos in the Sloshing Cores of Galaxy Clusters." *ApJ*, **762**:78, January 2013.

[ZPP14] Fabio Zandanel, Christoph Pfrommer, and Francisco Prada. "On the physics of radio haloes in galaxy clusters: scaling relations and luminosity functions." *Mon. Not. Roy. Astron. Soc.*, **438**(1):124–144, 2014.

[Zwi37] F. Zwicky. "On the Masses of Nebulae and of Clusters of Nebulae." *ApJ*, **86**:217, October 1937.